A new spectrometer to measure the molar Planck constant

Jochen Krempel

München 2010

A new spectrometer to measure the molar Planck constant

Jochen Krempel

Dissertation

an der Fakultät für Physik

der Ludwig-Maximilians-Universität

München

vorgelegt von

Jochen Krempel

aus Heidelberg.

München, den 23. Dezember 2010.

Erstgutachter: Prof. Dr. Dietrich Habs

Zweitgutachter: Prof. Dr. Ronald Frahm, Bergische Universität Wuppertal

Tag der mündlichen Prüfung: 21. Januar 2011

Zusammenfassung

Entwicklung eines neuen Spektrometers
zur Bestimmung der molaren Planck-Konstante.

Die SI-Einheit Kilogramm soll in den nächsten Jahren neu definiert werden. Bei dem Versuch die Einheit auf eine fundamentale Naturkonstante zurückzuführen, insbesondere die Planck- und die Avogadro-Konstante, traten widersprüchliche Ergebnisse auf. Durch eine direkte Bestimmung der molaren Planck-Konstanten können die Gründe für die Diskrepanz eruiert werden. Eine direkte Bestimmung der molaren Planck-Konstanten unterstützt die Suche nach der Ursache der Diskrepanz. Eine solche Messung kann mit dem γ-Spektrometer *Gams* durchgeführt werden. Dieses Instrument ist am ILL in Betrieb, allerdings ist es nicht stabil genug, um die benötigte Genauigkeit von relativ 2×10^{-8} zu liefern. Um die Stabilität und somit die Genauigkeit um einen Faktor 20 zu verbessern, wurde ein neues Instrument entworfen und gebaut. Es war nötig das Kernstück des Instruments, ein Winkelinterferometer, im Vakuum zu betreiben. Desweiteren wurden drift-freie Befestigungsmethoden entwickelt.

Für optische Elemente, wie zum Beispiel hohle Retroreflektoren, wurde ein neues Design konzipiert. Darüberhinaus wurde ein neues Datennahmesystem entwickelt, ebenso die dazu nötige Theorie zur Auswertung. Die Planung wurde vollständig abgeschlossen und das Instrument aufgebaut. Erste Tests mit diesem Aufbau belegen eine gute Stabilität.

Während der Entwicklung des neuen Instruments wurde das alte *Gams4* optimiert. Dadurch konnte die Neutronenbindungsenergie von Chlor-36 neu bestimmt werden mit dem Ergebnis (8579797.4 ± 1.8) eV. Die relative Ungenauigkeit konnte somit um einen Faktor 2.7 verbessert werden. Sie ist weniger als halb so groß wie die Ungenauigkeit irgendeiner anderen, vergleichbaren Neutronenbindungsenergie.

Abstract

A new spectrometer to measure the molar Planck constant.

The SI-unit kilogram is scheduled to be re-defined within the next years. In the attempt to link it to a fundamental constant of nature – namely the Planck constant or the Avogadro constant – some discrepancies appeared. A direct determination of the molar Planck constant helps to trace this discrepancy. Such a determination can be done with the γ-spectrometer *Gams*, that exists at the ILL. However, the instrument is not stable enough to provide the required accuracy of 2×10^{-8} (relative). To improve stability and accuracy, a complete new instrument was designed and built. For this purpose, the instrument core, an angle interferometer, had to be set up in vacuum. Drift-free fixation-methods and new designs for the optical elements, like corner-cube retro-reflectors, were developed. A new data acquisition system was elaborated, and also the mathematical theory to evaluate the acquired data. The new concepts for the instrument were completed, manufactured and assembled. First performance tests showed a quite convincing result in terms of stability.

During the development of the new instrument, the old instrument *Gams4* was optimized. The neutron binding energy of chlorine-36 was determined to be $(8579797.4\pm1.8)\,\mathrm{eV}$. The relative uncertainty is 2.7 times smaller than the previous value. It is two times smaller than the uncertainty of any other comparable binding energy.

Contents

Chapter 1

Introduction

The "Système international d'unités" (SI) is the basis of all units used by modern measurements. Only this common standard allows a comparison of experiments performed around the world.

It is derived from seven base units. One of them is the kilogram. Due to deficiencies in the present definition of the kilogram, this definition is envisaged to be changed within the next years. However, comparisons of the necessary measurements revealed inconsistencies. An independently measured molar Planck constant $N_\mathrm{A}h$ may help to trace the origin of these inconsistencies.

The γ-spectrometer "*Gams*" can do such a measurement. However, in its present configuration, it is not stable enough to provide the required accuracy. This work describes the upgrade of *Gams4* towards *Gams6* which will provide the required accuracy of 0.1 eV at a transition energy of 6 MeV. The independent spectrometer *Gams5* will remain almost unchanged, even though it was tempararily used for test purposes. See section 1.6 for details.

The new instrument will provide the most accurate angle measurement device in the world. All experimental techniques presently practiced at *Gams* will profit from the improvements:

- Nuclear state lifetime measurements via the Gamma Ray Induced Doppler broadening technique (GRID) can be extended to longer lifetime values and to weaker transitions. This allows probing nuclear structure calculations in a wider range [Jen+10].

- Experimental studies on the diffraction properties of various crystals for the realization of a soft γ-ray Laue lens were performed recently at *Gams5* [Bar+09]. A more stable instrument increases the characterization speed for the numerous crystals that will be used for the final lens.

- The new instrument will allow to carry out a direct comparison of lattice constants on a 10^{-8} level. Solid state research related to the study of micro strain in crystals will become possible. Furthermore, due to the high penetration depth of γ-rays, many metrological measurements, that have been carried out on crystals with X-rays and being essentially sensitive to surface effects, can now be extended to bulk studies [Mas+09; Mas+10].

- Recently developed very intense laser-driven γ-ray sources would profit from a feedback device allowing to resolve γ-rays with eV resolution [HK10]. The technologies developed for *Gams6* can be directly extended for this purpose. Due to the double Laue-Diffraction geometry, it provides a constant energy resolution $\Delta E/E \simeq 10^{-6}$ over an energy range from 0.01–10 MeV. The newly developed angle interferometer techniques should provide stable Bragg angle measurements over a time period of several days.

- The structure factor at high energies is so far not known experimentally for high photon energies. Theoretical density functional calculations based on predictions of the electron density distribution differ on a 10^{-7} level. *Gams6* will allow to contribute in this field.

The structure of this work is the following:

Chapter 1 gives an overview of the physical constants that is related to a redefinition of the kilogram. It is described why this re-definition is necessary and how it may be done. The role of the Molar Planck constant $N_{\mathrm{A}}h$ will be clarified. Also the measurement methods for the relevant constants will be discussed briefly. The measurement method for $N_{\mathrm{A}}h$ is presented in detail, this includes the physics that is investigated with the *Gams* spectrometer.

Chapter 2 illustrates the spectrometer itself, starting with an overview, then giving the detailed functioning and defining all mathematics that is necessary for the data evaluation. This includes a new algorithm for correcting environmental influences, for example the temperature. The instrument calibration procedure is eluded in detail.

Chapter 3 contains a measurement of the chlorine-36 binding energy that was performed with the *Gams4* spectrometer after careful tuning and applying the newly developed spectrometer mathematics that is described in chapter 2. The uncertainty of

the result is a factor three smaller than that of the previous value. It is a factor two smaller than any other binding energy in the 8 MeV range that has ever been measured.

Chapter 4 explains the new developments that have been integrated in the construction of *Gams6*. It focuses on the interferometer, its components and mounting methods; but vibration damping concepts of the vacuum chamber are presented as well. The development of a complete new data acquisition system is described. This includes the new phase detection module as well as the necessary mathematics for data evaluation.

Chapter 5 presents the new design of the diffraction crystals and the absolute determination of the lattice constant, as well as the comparison of the lattice constant at different spots.

Chapter 6 presents further optimization possibilities of *Gams4*. Also new fields of applications for the *Gams*-technology are explained.

The Appendix describes the characterisation of some crucial components that were built into the spectrometer. A list of abbreviations and an explanation of used symbols can be found there.

Before motivating this work, it should be remembered that its task is the development of a new instrument to measure the molar Planck constant. The challenge is to combine the accuracy of metrology-instruments with the shaky environment of a fission neutron source.

1.1 Motivation to measure the molar Planck constant $N_\mathrm{A}h$

The value for the molar Planck constant, suggested by the Committee on Data for Science and Technology (CODATA), is currently $N_\mathrm{A}h = 3.990\,312\,6821(57) \times 10^{-10}\,\mathrm{J\,s\,mol^{-1}}$, corresponding to a relative uncertainty of $u_\mathrm{r} = 1.4 \times 10^{-9}$ [CoData06]. This value is obtained by taking into account all published measurements until the 31st of December 2006. The values from individual measurements are combined to an uncertainty weighted average value. In case of contradictions during the global adjustment of *all* fundamental constants, the uncertainty of the affected values is increased to obtain a consistent set of fundamental constants. The current value for the molar Planck constant is extracted

from its relation to the Rydberg constant R_∞, the relative atomic mass of the electron $A_r(e)$ and the fine structure constant α from the relation:

$$N_A h = \alpha^2 \frac{A_r(e) M_u c}{2 R_\infty} \tag{1.1}$$

as explained in more detail in subsection 1.1.1. R_∞ and $A_r(e)$ are measured very accurately in electronic transitions of the hydrogen atom and in Penning traps, respectively. α provides the largest contribution to the uncertainty. The fine structure constant itself is derived from several measurements where the one from the electron magnetic moment is the most accurate and thus dominating. Therefore, it has currently the largest impact on the uncertainty of the molar Planck constant as M_u and c are defined values (See Table 1.1).

Of course the molar Planck constant can be obtained from its multiplicands, the Avogadro constant N_A and the Planck constant h, but both are known less precisely than the fine structure constant. At the start of this work, however, even within this uncertainty the product mismatched with the value obtained from the electron magnetic moment measurements. The mismatch was about 1.2×10^{-6}, while each quantity involved was measured at least once with an uncertainty of 2.9×10^{-8} or better.

These constants are important for an aspired redefinition of the SI-unit kilogram. Any independent measurement of a relation between these constants is therefore highly welcome.

Notation of masses

In the following sections, we recall some definitions of the SI-unit system, in particular for masses, and introduce a formalism to denote them. This follows the usual conventions as for example in [CoData06]. The relative atomic mass $A_r(X)$ of an entity X is defined by

$$A_r(X) = \frac{m(X)}{m_u} , \tag{1.2}$$

where $m(X)$ is the mass of one particle, atom or molecule of X and m_u is the atomic mass constant defined by $m_u = \frac{1}{12} m(^{12}C) = 1\,u \approx 1.66 \times 10^{-27}$ kg, where u is the unified atomic mass unit and $m(^{12}C)$ is the mass of an unbound atom of carbon 12 atom at rest and in the ground state. m_X may be used as abbreviation for $m(X)$ if X is a fundamental particle like an electron or a neutron.

The molar mass $M(X)$ of entity X, which is the mass of one mole of X with SI unit kg/mol, is given by

$$M(X) = N_A \cdot m(X) = A_r(X) \cdot M_u , \tag{1.3}$$

Quantity	Symbol	Value
speed of light in vacuum	c	$299\,792\,458\,\mathrm{m\,s^{-1}}$
magnetic constant	μ_0	$4\pi \times 10^{-7}\,\mathrm{N\,A^{-2}}$
		$= 12.566\,370\ldots \times 10^{-7}\,\mathrm{N\,A^{-2}}$
electric constant	ϵ_0	$(\mu_0 c^2)^{-1}$
		$= 8.854\,187\ldots \times 10^{-12}\,\mathrm{F\,m^{-1}}$
relative atomic mass of $^{12}\mathrm{C}$	$A_\mathrm{r}(^{12}\mathrm{C})$	12
molar mass constant	M_u	$10^{-3}\,\mathrm{kg\,mol^{-1}}$
molar mass of $^{12}\mathrm{C}$: $A_\mathrm{r}(^{12}\mathrm{C})M_\mathrm{u}$	$M(^{12}\mathrm{C})$	$12 \times 10^{-3}\,\mathrm{kg\,mol^{-1}}$
conventional value of Josephson constant	$K_{\mathrm{J}\text{-}90}$	$483\,597.9\,\mathrm{GHz\,V^{-1}}$
conventional value of von Klitzing constant	$R_{\mathrm{K}\text{-}90}$	$25\,812.807\,\Omega$

Table 1.1: Some exact quantities relevant to this work. Taken from [CoData06].

where $N_\mathrm{A} \approx 6.02 \times 10^{23}/\mathrm{mol}$ is the Avogadro constant and $M_\mathrm{u} = 10^{-3}\,\mathrm{kg/mol}$ is the molar mass constant. The numerical value of N_A is the number of entities in one mole. Since the definition of the mole states that one mole contains the same number of entities as there are in $0.012\,\mathrm{kg}$ of carbon 12, $M(^{12}\mathrm{C}) = 0.012\,\mathrm{kg/mol}$ exactly. Table 1.1 lists some further quantities whose numerical values are exactly defined.

1.1.1 Relation between $N_\mathrm{A}h$ and the fine structure constant α

The fine structure constant α is a dimensionless fundamental constant with a value of $\approx \frac{1}{137}$. It is also known as the coupling constant of the electromagnetic interaction in the low energy limit. It was first introduced by Sommerfeld to extend the Bohr model. In this semi-classical model, the fine structure constant corresponds to the "orbital speed" of the first ground state electron around the hydrogen nucleus in fractions of the speed of light. It relates to the Planck constant, the charge of the electron e, the electric constant ϵ_0 and the speed of light as:

$$\alpha = \frac{e^2}{2\epsilon_0 hc} \ . \tag{1.4}$$

The Rydberg constant R_∞ is related to the transition in atoms and can be determined experimentally from that. It is defined as:

$$R_\infty = \frac{e^4 m_\mathrm{e}}{8\epsilon_0^2 h^3 c} = \alpha^2 \frac{m_\mathrm{e} c}{2h} \ . \tag{1.5}$$

The electron mass m_e can be expressed as an relative atomic mass following (1.2), using the atomic mass constant. Replacing the latter via (1.3) introduces the Avogadro constant:

$$N_{\mathrm{A}}h = \alpha^2 \frac{A_{\mathrm{r}}(\mathrm{e})M_{\mathrm{u}}c}{2R_\infty} \tag{1.6}$$

Since M_{u} and c are known exactly and R_∞ as well as $A_{\mathrm{r}}(\mathrm{e})$ are known rather precisely, the relative uncertainties u_{r} behave like:

$$u_{\mathrm{r}}(N_{\mathrm{A}}h) \approx 2u_{\mathrm{r}}(\alpha) \ . \tag{1.7}$$

1.1.2 Relation of α to other constants

The values of fundamental constants are not always directly accessible by experiments. However, various relations between different constants can be measured experimentally. While a single measurement may not be very accurate, each provides some additional trust in the consistency of the underlying physical theory, and they all contribute to reducing the uncertainty in the knowledge of all constants via global adjustment.

Here, a small fraction of relations is given to illustrate the mesh of relations between the constants.

α and magnetic moment of electron μ_{e}: The magnetic moment of the electron can be measured very accurately in units of the Bohr magneton

$$\mu_{\mathrm{B}} = \frac{eh}{4\pi m_{\mathrm{e}}} \ , \tag{1.8}$$

where e is the elementary charge.

The measured value of μ_{B} can be compared with the theoretical value which is derived from quantum electrodynamics (QED) calculations and depends on α via:

$$\begin{aligned}
\frac{\mu_{\mathrm{e}}}{\mu_{\mathrm{B}}} =& 1 + a_{\mu\tau} + a_{\mathrm{hadronic}} + a_{\mathrm{weak}} \\
& + C_2 \cdot \left(\frac{\alpha}{\pi}\right)^1 + C_4 \cdot \left(\frac{\alpha}{\pi}\right)^2 + C_6 \cdot \left(\frac{\alpha}{\pi}\right)^3 + C_8 \cdot \left(\frac{\alpha}{\pi}\right)^4 + C_{10} \cdot \left(\frac{\alpha}{\pi}\right)^5 + \cdots \ .
\end{aligned} \tag{1.9}$$

QED calculations give exact values for C_2, C_4, and C_6, a numerical value and uncertainty for C_8, and a small $a_{\mu\tau}$. C_{10} is expected to be so small as to have lesser influence than the present experimental uncertainty of μ_{e}. a_{hadronic} and a_{weak} are hadronic and weak contributions. Assuming no electron substructure, they are known accurately enough, so that from a determination of the electron magnetic moment μ_{e}, a value for the fine structure constant of $\frac{1}{\alpha} = 137.035\,999\,084(51)$ corresponding to $u_{\mathrm{r}} = 3.7\times10^{-10}$ could be obtained [HFG08]. Today, this is the most accurate method to determine α.

α **to** $h/m(X)$**:**   The definition of the Rydberg constant (1.5) can be used to derive a relation between α and the ratio of the Planck constant and the mass $m(X)$ of a particle X:

$$\alpha^2 = R_\infty \frac{2h}{m_{\mathrm{e}}c} = \frac{2R_\infty}{c} \frac{m(X)}{m_{\mathrm{e}}} \frac{h}{m(X)} \ . \tag{1.10}$$

The relative uncertainties of R_∞ and $A_{\mathrm{r}}(\mathrm{e})$ are less than $7{\times}10^{-12}$ and $5{\times}10^{-10}$, respectively, and the relative uncertainties u_{r} of $A_{\mathrm{r}}(X)$ are less than that of $A_{\mathrm{r}}(\mathrm{e})$ for many particles and atoms. Since c is known exactly, α can thus be determined precisely from a measurement of $h/m(X)$.
This has been done with high precision for $\frac{h}{m_{\mathrm{n}}}$, $\frac{h}{m(^{133}\mathrm{Cs})}$ and $\frac{h}{m(^{87}\mathrm{Rb})}$. See Figures 1.1 and 1.2.

α **to von Klitzing constant** R_{K}**:**   The quantum hall effect provides a quantized hall resistance $R = R_{\mathrm{K}}/n$, where n is an integer number. It is found that R_{K} is a fundamental constant of nature, called the von Klitzing constant. More details are given in subsection 1.1.5. If one assumes the validity of $R_{\mathrm{K}} = h/e^2$, then R_{K} is related to α by:

$$\alpha = \frac{\mu_0 c}{2} \frac{1}{R_{\mathrm{K}}} \ . \tag{1.11}$$

The so-called "calculable capacitor" [TL56] provides a way to determine R_{K} with an accuracy of some parts of 10^{-8}. However, different measurements provide varying values, so the total relative uncertainty is at the 10^{-7} level (see Figure 1.1).

α **to Josephson constant** K_{J} **and gyromagnetic ratio:**   The gyromagnetic ratio γ of a bound particle of spin quantum number i and magnetic moment μ is given by

$$\gamma = \frac{2\pi f}{B} = \frac{|\mu| \, 2\pi}{h \cdot i} \ . \tag{1.12}$$

where f is the spin-flip frequency of the particle in the magnetic flux density B. Experimentally, the gyromagnetic ratio of a proton is better accessible if shielded by a spherical water sample. Thus, the shielded gyromagnetic ratio $\gamma_{\mathrm{p}'}$ of the proton is of interest. It is given by:

$$\gamma_{\mathrm{p}'} = \frac{2 \cdot 2\pi}{h} \mu_{\mathrm{p}'} \ . \tag{1.13}$$

Together with the definition of the g_{e}-factor of the electron

$$\mu_e = \frac{g_{\mathrm{e}}}{2} \mu_{\mathrm{B}} \tag{1.14}$$
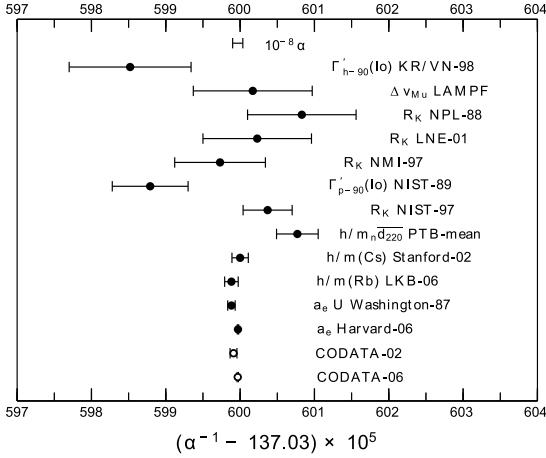
Figure 1.1: Values of the fine-structure constant α with $u_{\mathrm{r}} < 10^{-7}$, in order of decreasing uncertainty from top to bottom, and the 2002 and 2006 CODATA recommended values of α. Data and Graph from [CoData06].
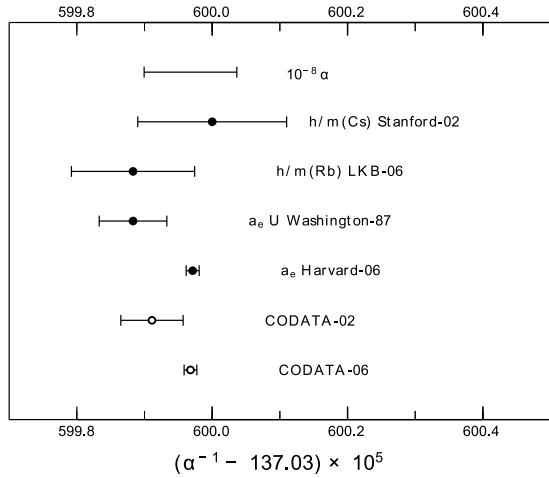
Figure 1.2: Values of the fine-structure constant α with $u_{\mathrm{r}} < 10^{-8}$, in order of decreasing uncertainty from top to bottom. The data are identical to those in Figure 1.1.

and equations (1.8), (1.5), (1.4), (1.26) and (1.27) one can derive α as:

$$\alpha^{-3} = \frac{\mu_{\mathrm{p}\prime}}{\mu_{\mathrm{e}}} \frac{K_{\mathrm{J}} R_{\mathrm{K}}}{4 R_{\infty}} g_{\mathrm{e}} \frac{1}{\gamma_{\mathrm{p}\prime}} \ . \tag{1.15}$$

The relative uncertainty of the $\gamma_{\mathrm{p}\prime}$ measurement is about 1.1×10^{-7} [Wil+89] and thus dominating here. Due to the negative third power, the relative uncertainty $U_{\mathrm{r}}(\alpha)$ is smaller by a factor 3 and hence 3.7×10^{-8}. Hence, this experimental value is in disagreement by two standard deviations with the adjusted value of the fine structure constant obtained with other measurement methods. This is of importance, as the determination of h via the watt balance relies on the correctness of the assumed relations between the Josephson constant, von Klitzing constant and fine structure constant, as explained in subsection 1.1.5.

1.1.3   Re-defining the kilogram

The kilogram is the unit of mass. It is one of the seven base units of the SI. Since 1889 it is defined to be equal to the mass of the international prototype of the kilogram, which is a block made of platinum-iridium. This artefact is kept with its six official copies in a vault at the Bureau International des Poids et Mesures in Sèvres (BIPM) in Paris. In addition, copies of the international prototype have been manufactured by the BIPM for use as national prototypes. For current use, the BIPM maintains some additional copies.

Figure 1.3: The kilogram prototype. Hosted at BIPM under 3 glass shields in standard air. Photograph from BIPM.
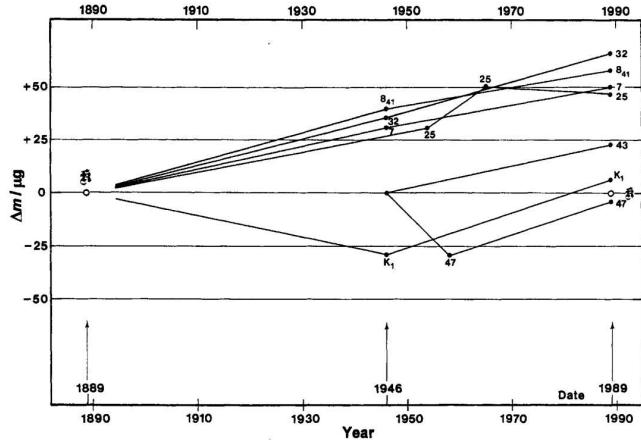
Figure 1.4: Drift of the six official copies relative to the international prototype of the kilogram. Graph from [Gir94].

More than eighty copies have been produced since 1880. However, only the international prototype defines the kilogram. All copies are only temporary replacements and have to be calibrated against the international prototype. Some of the national prototypes have already been destroyed or were lost.

As the prototypes are stored in air (usually under two or more nested bell jars – see Figure 1.3), they gain mass through adsorption of atmospheric contaminants onto their surfaces. These gains were found to be reversible and in the order of $1\,\mu g$ per year. For this reason, the CIPM declared that the reference mass of the international prototype is that immediately after cleaning and washing by a specified method. The reference mass thus defined is used to calibrate national standards of platinum-iridium alloy.

These comparisons of the national prototypes to the international prototype occur every 50 years. After the third and most recent comparison, it can be concluded that the copies gained on average about $25\,\mu g$ in mass compared to the international prototype within 100 years (see Figure 1.4 and [Gir94]). As 40 copies are made from the very same alloy as the prototype, and the six official copies are even stored under the same conditions, it is unclear where this deviation comes from. Furthermore, as the prototype is not different from its copies, it must be assumed that the international prototype has reduced in weight compared to its copies. It is important to note that there is no proof that the mass of the prototype – or its copies – stayed constant in absolute terms.

21

Therefore it is desired to change the definition of the kilogram for two reasons: to get rid of the artefact, which can be lost or damaged and is only available locally, and to relate the kilogram to a constant of nature that does not change over time within the measurement accuracy.

Just like the metre has been defined by fixing the speed of light as a constant, the kilogram is intended to be linked to a constant of nature. Currently there are two potential candidates, the Avogadro constant N_A and the Planck constant h. However, the change of the definition is only envisaged when the measurement accuracy of at least one of these constants is below or comparable to the current uncertainty of the prototype and when all measurements agree within their uncertainty. Hence, the aim is to perform measurements with relative uncertainties lower than two parts in 10^8.

A possible definition via the Avogadro constant may be:

> The kilogram is the mass of exactly $5.018\,451\,272\,5 \times 10^{25}$ unbound carbon-12 atoms at rest and in their ground state.

A possible definition via the Planck constant may be:

> The kilogram is the mass of a body at rest whose equivalent energy corresponds to a frequency of exactly $299\,792\,458/6\,626\,069\,311 \times 10^{43}$ hertz.

For details on the consequences of either of these definitions see [Mil+05].

Other domains of the SI are seeking for a revision, too. Hence a global change of the SI may involve the redefinition of the kilogram, ampere, kelvin and mole at the same time. In this suggestion by [Mil+06], the Planck constant would serve to define the kilogram, while the Avogadro constant would be used to define the mole.

The most recent schedule for this incisive change is the year 2011, when the 24th Conférence Générale des Poids et Mesures (CGPM) takes place. Hence every contributing experiment should provide sufficiently accurate results by 2010.

Hz

Watt balance

γ-ray spectroscopy

$Mgv = nh\nu^2/4$

$N_{\mathrm{A}} h \, \nu = mc^2$

kg

mol

$M = m N_{\mathrm{A}}$

X-ray crystal density
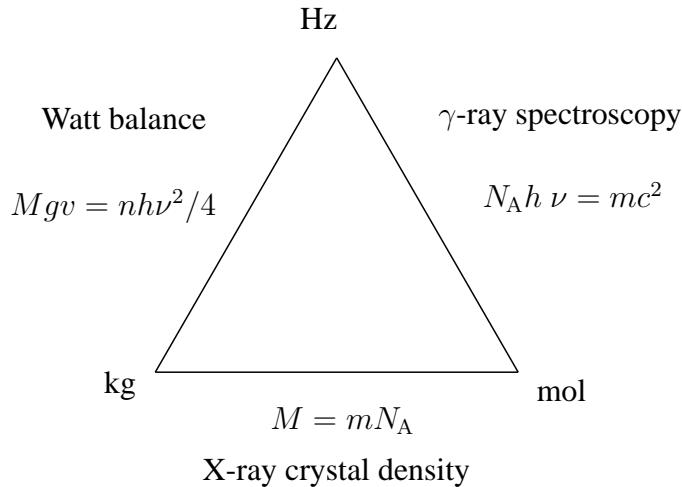
Figure 1.5: Metrological triangle of the mass-related units. The SI-units are placed in the corners, along the sides those experiments relating two of the units.

1.1.4 The metrological triangle of energy and mass

It is obvious that for a redefinition of the kilogram, all measurements of the involved quantities should be consistent with each other. At the time of the start of this work in 2005 this was clearly not the case. While in 1998 the recommended values by CODATA for h and N_{A} had relative uncertainties of 7.8×10^{-8} and 7.9×10^{-8}, respectively. These uncertainties had to be increased to 1.7×10^{-7} due to a newly published value by the Avogadro collaboration [CoData06]. Their value mismatched the values for h obtained by the watt balance by one part in a million. In the global adjustment of fundamental constants, the uncertainties had to be raised to account for the discrepancy of the experimental results of the watt balance (1.1.5) and Avogadro project (1.1.6). Both measurements are linked together through the indirect determination of the molar Planck constant via the fine structure constant as shown in subsection 1.1.1. Obviously, in the presence of such a contradiction none of the values can be used for a definition of the kilogram. Hence there was a strong demand to resolve this mismatch [CIP06].

Independent from that, it must be noted that any definition of the kilogram via fixing the Planck constant relies on the correctness of the mass-energy-equivalence, expressed in Einstein's equation $E = mc^2$. So far it has been verified experimentally only with an accuracy of 4×10^{-7} [Rai+05; JKM09].

Figure 1.5 illustrates the relation between the quantities involved. As the unit hertz is very well established and easily reproducible, any two of the experiments mentioned are necessary and sufficient to define the mole *and* the kilogram. A third experiment can then serve as an additional cross check.
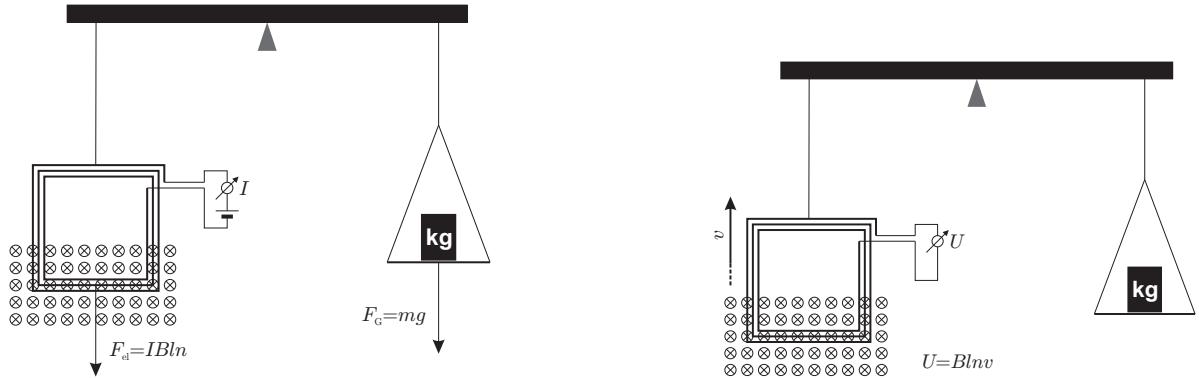
(a) Static mode: on the right side of the balance a mass m is attracted by the Earth's gravity g. On the left side a coil of width l with n wires is placed in a static external magnetic field B. A current I is applied to the coil such that the electromagnetic force F_el compensates the gravitational force F_G.

(b) Moving mode: to avoid a difficult determination of the magnetic field and coil geometry, the balance is moved by an auxiliary motor with constant speed v. The voltage U induced in the coil is measured. It is necessary that the magnetic field is not changed compared to the static mode.

Figure 1.6: Watt balance: combining moving and static mode, allows to eliminate the magnetic field and coil geometry Bln. Hence the force-equivalence transfers to a power-equivalence $UI = mgv$.

1.1.5 Determination of the Planck constant h

The currently most precise method to determine the Planck constant h is the watt balance. Its measurement principle is described in Figure 1.6. In this experiment, the mechanical force of local gravity g on a test mass m is compared to the electromagnetic force of a current I through a coil in a magnetic flux gradient $\frac{\mathrm{d}\Phi_\mathrm{m}}{\mathrm{d}z}$ along the direction of gravity z:

$$mg = -I\frac{\mathrm{d}\Phi_\mathrm{m}}{\mathrm{d}z} \ . \tag{1.16}$$

Moving the coil in a second step with a constant speed $v = \mathrm{d}z/\mathrm{d}t$ through the flux gradient will induce a voltage U in the coil. This can be used to measure the field gradient as the induced voltage is:

$$U = -\frac{\mathrm{d}\Phi_\mathrm{m}}{\mathrm{d}t} = -\frac{\mathrm{d}z}{\mathrm{d}t}\frac{\mathrm{d}\Phi_\mathrm{m}}{\mathrm{d}z} = -v\frac{\mathrm{d}\Phi_\mathrm{m}}{\mathrm{d}z} \ . \tag{1.17}$$

So the field gradient in equation (1.16) can be eliminated and one obtains the power equation

$$mgv = UI \ . \tag{1.18}$$

The gravity acceleration g can be determined by a commercial gravimeter, which records the trajectory of a test mass dropped in vacuum. These devices are specified for $u_\mathrm{r}(g) = 2 \times 10^{-9}$ [LaCoste]. Hence all variables can be measured. And indeed, this method is

conversely suggested by the CIPM as the practical realization of the unit definition of the electrical SI-units (i.e. the watt *or* the ampere) [BIP06, Appendix 2].

It should be noted that so far there is no link to the Planck constant. In 1975 the watt balance was not designed to have such a link [Kib75]. However, as soon as the Josephson effect and the quantum Hall effect were found, the situation changed. The Josephson effect was found to provide an exact voltage U to frequency ν ratio:

$$U = \frac{1}{K_{\mathrm{J}}}\nu \ . \tag{1.19}$$

Frequencies can be measured very accurately. Consequently, when defining the Josephson constant K_{J}, the Josephson effect can serve as a voltage standard and voltages can be measured in units of $\mathrm{Hz}/K_{\mathrm{J}}$.

The (integer) quantum Hall effect can be used for creating a unit for the electrical resistance R. The Hall conductivity $1/R$ has exactly quantized steps at integer multiples of the inverse of the von Klitzing constant R_{K}:

$$\frac{1}{R} = n\frac{1}{R_{\mathrm{K}}} \ . \tag{1.20}$$

Hence any resistance can be measured in units of R_{K}.

Following Ohm's law $I = U/R$, one can derive also units for the current and the electrical power from both constants. This would read like:

$$U = Y_{\mathrm{U}} \times \frac{\mathrm{Hz}}{K_{\mathrm{J}}} \tag{1.21}$$

$$R = Y_{\mathrm{R}} \times R_{\mathrm{K}} \tag{1.22}$$

$$\Rightarrow I = Y_{\mathrm{I}} \times \frac{\mathrm{Hz}}{K_{\mathrm{J}} \ R_{\mathrm{K}}} \tag{1.23}$$

$$\Rightarrow W = Y_{\mathrm{W}} \times \frac{\mathrm{Hz}^2}{K_{\mathrm{J}}^2 \ R_{\mathrm{K}}} \ , \tag{1.24}$$

where each Y would be a dimensionless number and the remaining terms would define the corresponding unit.

If one measures the current and voltage in the way expressed in (1.21) and (1.23), the watt balance allows to determine $K_J^2 R_K$:

$$K_{\mathrm{J}}^2 R_{\mathrm{K}} = \frac{mgv}{Y_{\mathrm{U}}Y_{\mathrm{I}}} \ . \tag{1.25}$$

Both constants are linked to the charge of the electron e and the Planck constant h:

$$K_J = \frac{2e}{h} \tag{1.26}$$

$$R_K = \frac{h}{e^2} \tag{1.27}$$

$$\Rightarrow \quad h = \frac{4}{K_J^2 R_K} \ . \tag{1.28}$$

While K_J is the inverse of the magnetic flux quantum, there is yet no consistent theory which describes the quantum Hall effect fully. Consequently, equations (1.27) and (1.28) must be verified experimentally.

However, if one assumes (1.28) to be correct, the watt balance allows the determination of the Planck constant since K_J and R_K are known more accurately than h.

SI-90 units

In 1989 the CIPM adapted exact conventional values for the Josephson and von Klitzing constants: $K_{J\text{-}90} = 483\,597.9$ GHz V^{-1} and $R_{K\text{-}90} = 25\,812.807\,\Omega$ [Qui89]. This was done to profit from the high precision of experiments using these effects. Consequently, all measuring devices for electrical quantities can be calibrated using the exact values of these constants. It should be noted that although these values have no uncertainty, they are not compatible with the SI. Indeed, both constants have a value within the SI − $K_J = 483\,597.891(12)$ GHz V^{-1} and $R_K = 25\,812.807\,557(18)\,\Omega$ [CoData06] − which differ from the conventional values $K_{J\text{-}90}$ and $R_{K\text{-}90}$ by up to 3 standard deviations. Both SI-90 constants are not integrated in the SI in the sense of a definition of a base unit. To do so would change the status of the magnetic constant μ_0 from that of a constant having an exactly defined value (and would therefore abrogate the definition of the ampere) and would also produce electrical units which would be incompatible with the definition of the kilogram and units derived from it. However, there are ambitions to revise large parts of the SI and include these constants as bases [Mil+06].

Using the electrical SI units to measure h

Electrical measurements are now more precise when measured and expressed in SI-90 units. Consequently, one will measure the UI term of the watt balance with devices calibrated in SI-90 units and one can derive h as

$$h = \frac{mgv}{U_{90} \cdot I_{90}} \frac{4}{K_{J\text{-}90}^2 R_{K\text{-}90}} \ . \tag{1.29}$$

While mgv is measured in SI units, U and I are measured with devices calibrated to SI-90 units. As $K_{\text{J-90}}^2 R_{\text{K-90}}$ is based on the very same SI-90 units plus the dimension $\left[\text{Hz}^2\right]$ (which is identical for SI and SI-90), the SI-90 units cancel out and the Planck constant is obtained in SI units [SNW05].

At present there are different implementations of the watt balance around the world. They all use slightly different geometry but the principle is the same. The major projects are at the National Institute of Standards and Technology (NIST), Gaithersburg, Md, USA, the National Physical Laboratory (NPL) Teddington, Middlesex, UK, the Swiss Federal Office of Metrology and Accreditation (METAS), Bern-Wabern, the French Laboratoire National d'Essais (LNE), Paris and the Bureau International des Poids et Mesures (BIPM), Sèvres, France. Only two of them have provided competitive results so far. In 2007, the NIST balance obtained $h = 6.626\,068\,91(24) \times 10^{-34}$ J s, with a relative uncertainty of 3.6×10^{-8} [Ste+07]. Also in 2007 the NPL obtained an initial value of $h = 6.626\,070\,95(44) \times 10^{-34}$ J s with a relative uncertainty of 6.6×10^{-8} [RK07]. The two values mismatch by 4 standard deviations. For a more complete listing of values of the Planck constant see Table 1.2 and Figure 1.7.

1.1.6   Determination of the Avogadro constant N_{A}

The Avogadro constant is the number of particles per mole of the corresponding substance. Consequently, it has the dimension [mole^{-1}]. The value suggested by [CoData06] is $6.022\,141\,79(30) \times 10^{23}$ mol^{-1}. The relative uncertainty is 5.0×10^{-8}.

The current interpretation of N_{A} is directly inferred from the definition of the SI-unit mole, which is:

1. The mole is the amount of substance of a system which contains as many elementary entities as there are atoms in 0.012 kilogram of carbon-12.

2. When the mole is used, the elementary entities must be specified and may be atoms, molecules, ions, electrons, other particles, or specified groups of such particles.

A re-definition of the kilogram by fixing the value of N_{A} would at the same time change the definition of the mole into something much more understandable, e.g. [Mil+06]:

The mole is the amount of substance of a system that contains exactly $6.022\,141\,5 \times 10^{23}$ specified elementary entities, which may be atoms, molecules, ions, electrons, other particles or specified groups of such particles.

Measured quantity	Institute and year	$h/(10^{-34}\,\mathrm{J\,s})$	Relative standard uncertainty u_r
$\Gamma'_{\mathrm{p}-90}(\mathrm{hi})$	NPL-79	6.626 0729(67)	1.0×10^{-6}
$\mathcal{F}_{90}$	NIST-80	6.626 0657(88)	1.3×10^{-6}
K_J	NMI-89	6.626 0684(36)	5.4×10^{-7}
$K_\mathrm{J}^2 R_\mathrm{K}$	NPL-90	6.626 0682(13)	2.0×10^{-7}
K_J	PTB-91	6.626 0670(42)	6.3×10^{-7}
$\Gamma'_{\mathrm{p}-90}(\mathrm{hi})$	NIM-95	6.626 071(11)	1.7×10^{-6}
$K_\mathrm{J}^2 R_\mathrm{K}$	NIST-98	6.626 068 91(58)	8.8×10^{-8}
	CODATA-02	6.626 0693(11)	1.7×10^{-7}
$V_\mathrm{m}(\mathrm{Si})$	N/P/I-05	6.626 0745(19)	2.9×10^{-7}
$K_\mathrm{J}^2 R_\mathrm{K}$	NIST-07	6.626 068 91(24)	3.6×10^{-8}
	CODATA-06	6.626 068 96(33)	5.0×10^{-8}
$K_\mathrm{J}^2 R_\mathrm{K}$	NPL-07	6.626 070 95(44)	6.6×10^{-8}

Table 1.2: Most competitive measurements of the Planck constant h in chronological order. The CODATA values take into account the adjustment of other constants. The value "$V_\mathrm{m}(\mathrm{Si})$ N/P/I-05" is derived from the XRCD method (see section 1.1.6) and converted to h using equation (1.6). Values are from [CoData06; RK07].
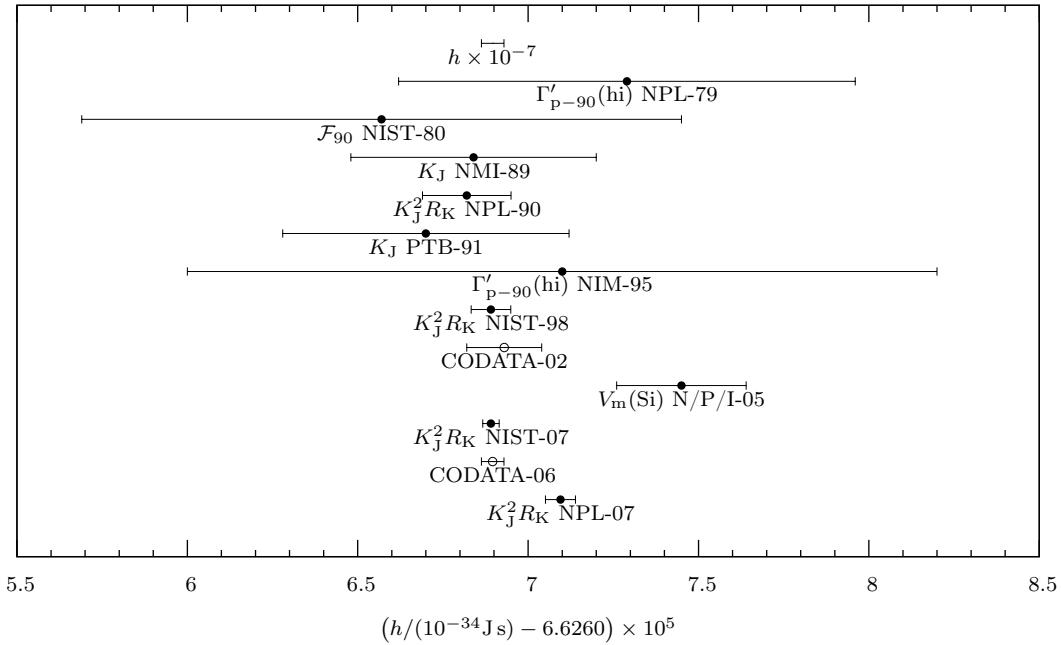
Figure 1.7: The most competitive measurements of the Planck constant h in chronological order. See Table 1.2.

28

For any redefinition of either the kilogram and/or the mole it is necessary to provide an according practical realization or in other words, a measurement of the Avogadro constant in current SI-units with sufficiently low uncertainty. Otherwise, measured quantities based on the future definition might contradict to measurements performed with the actual definitions.

Two direct approaches to the Avogadro constant have been used so far: ion accumulation and X-ray crystal density comparison. In the ion accumulation method, single ions are counted and accumulated until they sum up to a measurable macroscopic mass that can be compared to one kilogram with reasonable accuracy. A project at the Physikalisch-Technische Bundesanstalt (PTB) in Braunschweig, Germany accumulated about 10 g of bismuth-209 within a week with a 10 mA ion beam. It reached a relative accuracy of several parts in 10^4 [BG06]. In the meantime the project has been stopped, as there were no competitive results to be expected until 2010.

XRCD

In the **X-r**ay **c**rystal **d**ensity method, a macroscopic density $\rho_\odot$ of a large sphere of mono-crystalline silicon is compared with the microscopic density $\rho_\bullet$ of a primitive cell of the same crystal.

$$\rho_\odot = \rho_\bullet \ . \tag{1.30}$$

The macroscopic density is derived from a volume $V_\odot$ and a mass $m_\odot$ measurement of a solid silicon sphere of about 1 kg:

$$\rho_\odot = \frac{m_\odot}{V_\odot} \ . \tag{1.31}$$

The microscopic density can be derived from the size of a primitive cell a^3 of the crystal, the number of atoms n in each cell and the average mass $m_\bullet$ of each silicon atom:

$$\rho_\bullet = \frac{m_\bullet \cdot n}{a^3} \ , \tag{1.32}$$

where the binding energy of about 5 eV per atom is neglected. With equation (1.3) the microscopic mass $m_\bullet$ of silicon can be expressed by its relative atomic mass $A_r(\text{Si})$. Hence we can write (1.32) and (1.30) as

$$\frac{m_\odot}{V_\odot} = \frac{\frac{A_r(\text{Si})M_u}{N_A}n}{a^3} \tag{1.33}$$

$$\Updownarrow$$

$$N_A = \frac{n}{a^3} A_r(\text{Si}) M_u \frac{m_\odot}{V_\odot} \ . \tag{1.34}$$

Usually the volume of the silicon unit cell a^3 is expressed by the lattice constant derived from the lattice spacing in the [220] orientation of the crystal. Hence N_{A} is expressed in this d_{220} lattice constant as:

$$N_{\mathrm{A}} = \frac{A_{\mathrm{r}}(\mathrm{Si})M_{\mathrm{u}}}{\sqrt{8}d_{220}^3} \frac{V_{\odot}}{m_{\odot}} \ . \tag{1.35}$$

Therefore the Avogadro constant can be derived from the measurement of two microscopic and two macroscopic quantities from the same material:

The relative atomic mass, also called molar mass, is measured in Penning traps relative to the mass of carbon-12. The relative atomic mass of silicon-28 has been determined with a relative uncertainty of 6.8×10^{-11} by [DiF+94] and [Aud+03]. The silicon used until 2007 had a natural isotopic composition, i.e. roughly 4.7% and 3.1% of $^{29}\mathrm{Si}$ and $^{30}\mathrm{Si}$, respectively. Therefore, these molar masses and, more difficultly, their abundances, must be known accurately. Furthermore, any residual impurities of the material must also be measured and corrected for. The relative uncertainty is 1.5×10^{-7} and thus the dominating contribution to the total uncertainty of N_{A}.

The macroscopic volume of the sphere is measured by its diameter. This is done with a Fizeau interferometer (see Figure 1.8). As the diameter is measured over the whole surface of the sphere the roundness is also verified. The diameter of the spheres is about 93.6 mm where deviations of up to 57 nm from an ideal sphere were found on the surface. The relative uncertainty for the volume is 8×10^{-8} in [NB05].

Pure silicon will form immediately an oxide layer on its surface. Silicon oxide is transparent, so the Fizeau interferometer will measure the diameter of the silicon sphere, changed by a little phase shift due to the index of refraction of silicon oxide. This can be corrected for. However, more crucial, a typical oxide layer has 10 nm thickness. On a 1 kg sphere, this sums up to about 600 µg. Hence, the layer thickness must be known with a relative accuracy of 2%. This can be achieved by spectroscopic ellipsometry which is then calibrated by X-ray reflectometry. See [Bus+05] for details.

The macroscopic mass of the sphere is obviously rather easy to measure as it is very close to 1 kg and thus the usual comparison techniques can be applied. They are well established by serving already now for comparisons with the prototype and thus provide the necessary accuracy. However, there is an important difference to the comparison of the platinum-iridium blocks and to compare one of them to a silicon sphere. The latter comparison involves two bodies with a different density and hence different buoyancy forces. This must be corrected for [BGM07]. For future comparisons it is desirable to avoid buoyancy effects by comparing two masses inside vacuum. However, at least once a
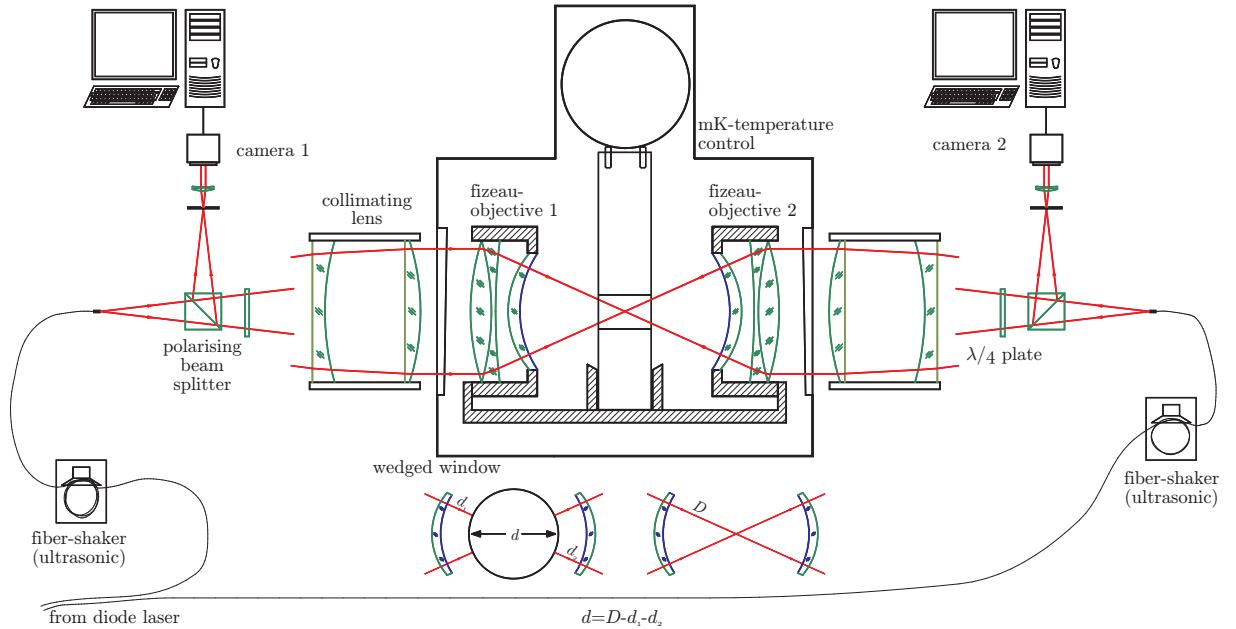
Figure 1.8: Principle of the Fizeau interferometer to determine the diameter of the SI sphere. Drawing from [Nic09].

mass in air must be compared with a mass in vacuum. Meanwhile, this can be done with a relative uncertainty of 4×10^{-9} [Pic06].

Absolute determination of the Si-lattice constant d_{220}

As the lattice constant of silicon enters with the third power into the volume of a crystal cell, it needs to be measured with a three times better relative uncertainty than the macroscopic volume. Additionally, this quantity is an input parameter to the direct determination of the molar Planck constant presented in this work.

Challenges in the determination of d_{220} are the required high relative accuracy and the need of an absolute measurement in SI-units, while its value is rather small in these units, namely $1.920\,155\,762(50) \times 10^{-10}$ m. Within the SI the metre is defined via the speed of light and the definition of the second. Thus, a laser stabilized to a known frequency provides in vacuum a representation of the metre conform to the SI. It was suggested by [DH73] to compare the lattice spacing of crystals to this length. As shown in Figure 1.9, a well orientated X-ray beam is split by a nearly perfect single crystal into two beams via Bragg diffraction. Both beams hit a second lamella of the same crystal, hence the same perfectness and orientation. Consequently, both beams match again the Bragg condition and are diffracted. If a third crystal lamella of a different crystal – but of the same type and in a sufficiently parallel orientation – is placed in the crossing point of these
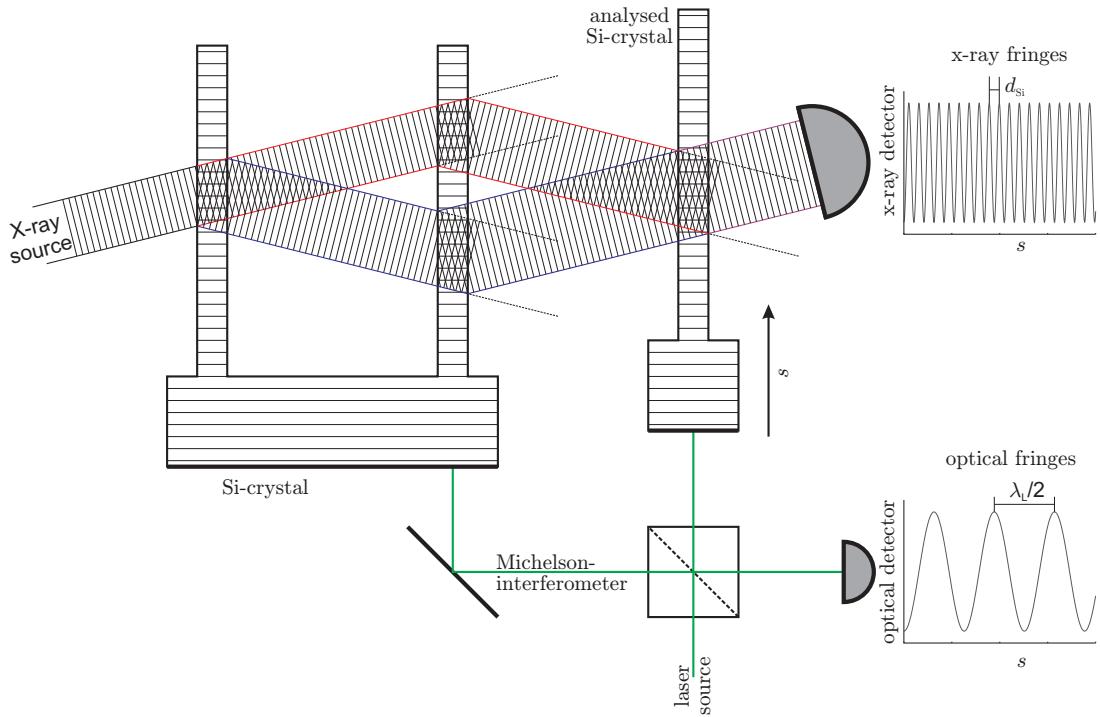
Figure 1.9: Simultaneous X-ray and optical interferometer for an absolute determination of the silicon lattice constant. An X-ray beam is split and refocused by a nearly perfect single crystal of silicon. A second silicon crystal of the very same material is slid through the focal point. The X-ray detector will detect as many fringes as silicon lattice planes are passing by. At the same time the crystal displacement is measured with a Michelson interferometer which represents the SI-definition of the metre.

beams, both beams will match again the Bragg conditions. Consequently two pairs of overlapping, parallel beams will be present, and interference effects will occur. The part belonging to the beam not being diffracted by the third lamella is naturally independent of the translation of this third lamella. Contrary, the path length, and thus the phase, of the reflected beam depend linearly on the displacement of the crystal vertical to the diffracting lattice planes. If all along the set-up a Bragg diffraction in first order has been chosen, the phase difference will be 2π, or one fringe, a soon as the crystal has been moved by the distance between two lattice planes. Thus the experimental challenge is to move the crystal by a certain amount of optical fringes and count the (much larger) number of X-ray fringes occurring at the same time. The ratio of these numbers multiplied by the wavelength of the laser is the lattice constant. First measurements following this method have been done at NIST (1973–1990) with a relative precision down to $u_r = 1.5 \times 10^{-7}$ [CoData98]. Measurements at the National Metrology Institute of Japan have been quite competitive until 2004, but then experiments were stopped as there was no sufficient

Quantity	Value	Relative standard uncertainty u_r
d_{220}(W4.2a)	$192\,015.563(12)$ fm	6.2×10^{-8}
d_{220}	$192\,015.565(13)$ fm	6.5×10^{-8}
d_{220}(NR3)	$192\,015.5919(76)$ fm	4.0×10^{-8}
d_{220}	$192\,015.5973(84)$ fm	4.4×10^{-8}
d_{220}(W4.2a)	$192\,015.5715(33)$ fm	1.7×10^{-8}
d_{220}	$192\,015.5732(53)$ fm	2.8×10^{-8}
d_{220}(MO*)	$192\,015.5498(51)$ fm	2.6×10^{-8}
d_{220}	$192\,015.5685(67)$ fm	3.5×10^{-8}
$h/m_n d_{220}$(W04)	$2060.267\,004(84)$ m s^{-1}	4.1×10^{-8}
d_{220}	$192\,015.5982(79)$ fm	4.1×10^{-8}

Table 1.3: Summary of measurements of the absolute {220} lattice spacing of various silicon crystals. Every second line indicates the lattice spacing d_{220} of a hypothetical, ideal and perfect crystal without impurities and defects inferred from the real crystal mentioned the line above. The last value is a fine structure constant measurement, see page 19. Table from [CoData06].
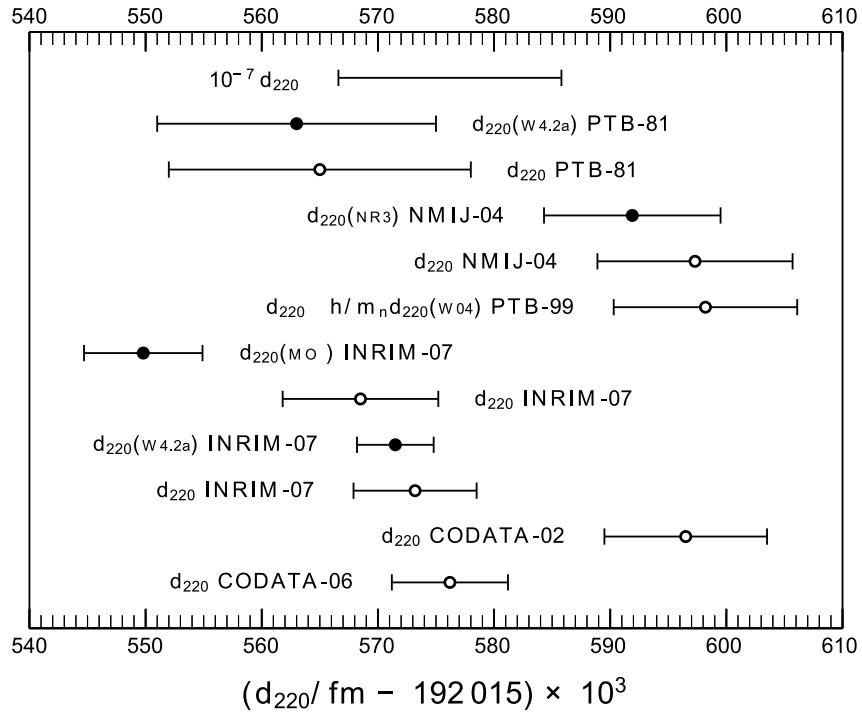
Figure 1.10: Inferred values (open circles) of d_{220} from various measurements (solid circles) of $d_{220}(X)$. For comparison, the 2002 and 2006 CODATA recommended values of d_{220} are also shown. The topmost bar illustrates the scale. Values are listed in Table 1.3. Graph taken from [CoData06].

increase in accuracy expected until 2010. Currently ongoing projects exist at PTB and at the Istituto Nazionale di Ricerca Metrologica (INRIM) in Turin, Italy.

The most competitive values are given in Table 1.3 and Figure 1.10. These measurements use different crystals coming from the ingots named (abbreviation in parentheses) as WASO 4.2a (W4.2a), NRLM3 (NR3), WASO 04 (W04) and NR4 (NRLM4). No distinction is made between different crystals taken from the same ingot. Note that all these crystals are of a natural isotopic composition. This composition may vary between different ingots. However the variation of d_{220} due to this is lower than the current experimental uncertainty. Impurities – mainly carbon, oxygen, and nitrogen – have a much larger effect. Consequently, the directly measured value $d_{220}(X)$ of a real crystal X must be converted to the {220} lattice spacing d_{220} of a "pure" crystal. There are a few lattice constant measurements performed in air. Recent and future measurements are carried out in vacuum. When comparing those measurements, the compression of the crystal lattice by the atmospheric pressure must be taken into account.

X-ray interferometry on silicon crystals requires a fine lamella (≈ 0.5 mm). The production of this lamella causes strains in the crystal lattice. These strains cause a bad crystallographic resolution and need to be removed. Usually a chemical "etching" of the crystal surface is applied. This etching introduces microscopic deformations to the surface, which influence the X-ray patterns and thus the determination of the lattice spacing. This effect is particularly important if the lamella is thin, and if rather low X-ray energies (<100 keV) are used. The actual size of this effect is not known and is currently under experimental and theoretical investigation [Man09].

International Avogadro Coordination

So far, measurements have been performed with natural silicon. However, the accurate determination of the isotopic composition is becoming the limiting factor in the aim to improve on the uncertainty. Hence, one tries now to use an enriched silicon-28 sample. However, this approach is too expensive to be handled by a single national metrology institute. Thus in the International Avogadro Coordination the efforts of seven national metrology institutes plus the BIPM are combined. An amount of 5 kg of ^{28}Si was enriched to $99.9938\% \pm 0.0024\%$, using centrifuges and a gaseous phase of SiF. Then the fluorine was removed and amorphous silicon was obtained. Contamination by carbon and oxygen are below 10^{16} particles per cm^3. From this material a nearly perfect single crystal was grown. Two 1 kg-spheres, two X-ray interferometers and several smaller pieces were cut. A summary of the recent state of the individual measurements is presented in [Fuj+05]. Final results from these experiments were scheduled for 2010. The result obtained is $N_\mathrm{A} = 6.022\,140\,84(18) \times 10^{23}$ mol^{-1}. This is "the most accurate input datum for a new definition of the kilogram" [And+10].

In principle, any material could be used for the determination of the Avogadro constant. Silicon, however, provides a high hardness which allows precise machining and polishing. Due to technical advancements of the semiconductor industry, it is possible to grow large crystals that are very pure and of very high quality. Those crystals fit the requirements for crystallographic measurements.

Systematic problems of the lattice determination

Currently, all lattice parameter measurements use an X-ray source of low energy (about 17 keV). Due to the strong absorption only thin crystal pieces can be measured. It is thus unknown if these pieces have the same lattice constant as bulk silicon, or if their lattices are different, e.g. due to machining. Additionally, the diffraction of these thin pieces is more sensitive to unavoidable surface roughness.

A further technological disadvantage of this method is the restriction to a single material and a single lattice orientation. For the measurement of a different lattice spacing a completely new triple Laue interferometer (see Figure 1.9) needs to be built.

It would be desirable to have a measurement method that can be applied to any thickness of the specimen, lattice orientation and material.

1.1.7 Importance of direct $N_\mathrm{A} h$ determination

The redefinition of the kilogram, which is aspired for 2011, requires the quantities involved – the Avogadro and Planck constants – to be known to a few parts in 10^8. And all measurements must be consistent with related quantities, like the fine structure constant, to provide a trustworthy basement for the new SI units.

When this thesis project was started in the year 2005, the accepted value of the silicon lattice constant d_{220} was subject to a significant change due to a revealed systematic error in the instrument set-up. Thus the faith in any of these lattice constant measurements was distressed. At the same time the value for the molar volume of silicon provided by the Working Group on the Avogadro Constant (WGAC) consisted of intrinsically slightly inconsistent data. Combined with the actual d_{220} value the yielded Avogadro constant differed 1.2 parts in 10^6 from those values inferred through the watt balance measurements. This is illustrated in Figure 1.11. Therefore a new measurement was desired, which would establish a different relation between the the lattice constant and another involved quantity. *Gams* offers such a possibility by linking the molar Planck constant to the silicon lattice constant.

Recent results in 2009 resolved this discrepancy on the ppm level. Shortly after, the NPL watt balance result infers a Planck constant which differs from the NIST value by 3 parts

relative accuracy		possible application of the measurement
$<$	1.4×10^{-9}	dominate value of $N_A h$ and α
2×10^{-9} –	2×10^{-8}	verification of QED-calculations
1×10^{-8} –	2×10^{-8}	possible mise-en-pratique for kg or mole redefinition
2×10^{-8} –	4×10^{-7}	improve trust in $E = mc^2$
$>$	4×10^{-7}	no gain in information

Table 1.4: Required relative uncertainty for future $N_A h$ determinations and application of such a measurement. Better uncertainties imply the applications given for larger uncertainties, of course.

in 10^7. But now with a better accuracy making this discrepancy more than four standard deviations. Thus in terms of probability the inconsistency is larger than ever before.

As the molar Planck constant can be inferred from the fine structure constant with a relative uncertainty of 1.4×10^{-9} (see equation (1.7) and subsection 1.1.2), a measurement delivering only a value of $N_A h$ would be rather pointless if it was not more accurate. However, depending on which relation the measurement is based, even a less accurate
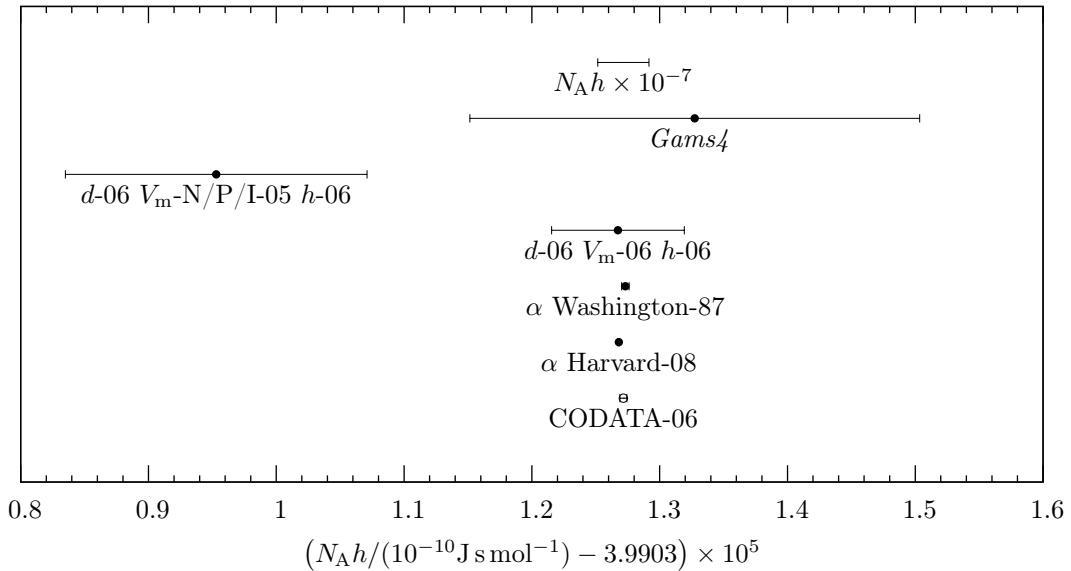
Figure 1.11: Values for $N_A h$. All "-06" values are the recommended values by CODATA-06, where d indicates the {220} lattice parameter, V_m the molar volume of natural silicon and h the Planck constant. Values derived from α are converted using (1.6) and the CODATA values for R_∞ and $A_r(e)$. The value *Gams4* is extracted from [Rai+05], assuming the correctness of $E = mc^2$. V_m-N/P/I-05 is the value coming from the XRCD methode [Fuj+05]. Its weight for the CODATA adjustment was obviously negligible.

36

measurement can be valuable.

Any definition of the kilogram by fixing the value of the Planck constant implies the validity of $E = mc^2$. So far, this relation has been verified with an uncertainty of 4×10^{-7}. A more accurate measurement would be appreciated to have a trustworthy basis for the SI. The method to measure $N_{\mathrm{A}} h$ proposed in this work provides such a test [Bec08].

The most precise measurement of the Planck constant is provided by the watt balance. However, this experiment implies the validity of equation (1.28), for which so far no consistent theory is available. Hence this must be approved at least experimentally before using it as a base of the SI.

The method to determine the molar Planck constant described in this work is based on the absolute lattice spacing of a silicon crystal. The latter is measured using the same instruments which actually are used in the XRCD-method of the Avogadro project. Therefore this puts a new constraint to the metrological triangle of mass related quantities.

The molar Planck constant links directly two measurable quantities: the molar mass of a particle and its de-Broglie frequency. Hence a measurement of this ratio is the most direct measurement of the molar Planck constant.

The recent relative uncertainty of such a measurement is 4×10^{-7}. Any better result would provide more information. However, only at a relative uncertainty of 2×10^{-8} will the measurement be really valuable and become an important contribution to the redefinition of the kilogram as summarized in table 1.4. Values of better than 1×10^{-8} would open the field of testing QED. However, this is of the range of this project as discussed later on.

1.2 The energy-mass equivalence principle

The special relativity published by Einstein [Ein05b] bases on two assumptions only. First, in any non-accelerated reference system all physical laws have the same form. And second, there is a universal speed (of signal transmission) which is, following the first assumption, the same in all non-accelerated reference systems. It follows intrinsically that this speed is the maximum speed for transmitting energy or information. Einstein identifies this maximum speed with the speed of light in vacuum c. A priori this is not necessary. However, this equivalence is generally accepted and experimentally well approved [Luo+03].

Using only these principles one can infer that a particle with the rest mass m has at rest the energy E [Ein05a], with

$$E = mc^2 \ . \tag{1.36}$$

This is known as the mass-energy equivalence principle. It applies to all processes where a massive particle undergoes an energetic change. This process may be as different as the solving of two chemicals, the lift of a body in the gravitational field, the change of orientation of a magnet within an external magnetic field, the decay of a neutron or many more. In most systems the energy involved – and hence the change in mass – is small compared to the total mass. Therefore, this effect is important in nuclear and particle physics only.

1.2.1   From $E = mc^2$ to $N_\mathrm{A}h$

The decay of a particle or a nucleus is a process where mass is converted into energy. In some cases this energy is electromagnetic radiation and kinetic energy only. In many of these cases, the quantities of both, radiation energy and mass (differences) are experimentally well accessible. This allows high precision measurements as the kinetic energy can be calculated in most cases. The energy of the electromagnetic radiation can be expressed by

$$E = h\nu, \tag{1.37}$$

where h is the Planck constant and ν the frequency of the radiation. This frequency can be expressed by the wavelength λ using:

$$\nu = c/\lambda \ . \tag{1.38}$$

If the mass is measured in multiples A_r of the atomic mass constant M_u, or technically in multiples of a ^{12}C atom, we can use equation (1.3) to express the energy mass equivalence (1.36) as:

$$h\frac{c}{\lambda} = \frac{A_\mathrm{r}\, M_\mathrm{u}}{N_\mathrm{A}}c^2 \tag{1.39}$$

$$\Updownarrow$$

$$N_\mathrm{A}h = A_\mathrm{r}\, \lambda\, M_\mathrm{u}\, c \ . \tag{1.40}$$

1.3   Choice of the investigated system

Annihilation

To obtain the energy equivalent of a kilogram in the SI, it would be preferable to convert 1 kg of mass fully into energy or more precisely into electromagnetic radiation, for example by annihilation with anti-matter. This would be a direct way to measure the Planck

constant. However, the energy equivalent of $1\,\text{kg}$ is $9 \times 10^{16}\,\text{J}$. This is about the energy which was released by the largest nuclear weapon that has ever exploded (Tsar Bomba in 1961, about 50 megatons of TNT). For obvious reasons this is not suitable for a high precision experiment.

Generally, annihilation is not very suitable for high precision measurements. For the production of the necessary anti-matter high energies are unavoidable. Consequently the created anti particle has a large and unknown energy. Cooling down these anti-particles (so that the kinetic energy scattering is smaller than 10^{-8} parts of their rest energy) is not possible for a sufficiently large number of particles. An accurate measurement of the $511\,\text{keV}$ annihilation radiation of positronium would require 10^{14} photons/s as explained in section 6.2.

Nuclear reactions

Nuclear reactions on the other hand provide a total mass difference on the order of some MeV. The corresponding electromagnetic radiation is measurable. These reactions can be induced by thermal neutron capture in massive numbers, so that the measurement of the radiation energy can be very precise. The inducing neutron has a kinetic energy on the order of $0.03\,\text{eV}$ and thus does not perturb an accurate measurement down to a relative uncertainty of 5×10^{-9}. At the same time the masses of the nuclei can be compared accurately to the atomic mass standard.

Following equation (1.40) the measurement splits into two different experiments: one determining the relative atomic masses of the nuclei involved and a second to determine the wavelength of the emitted radiation in the nuclear reaction. Both experiments can be performed independently at completely different times and places.

Detector

Typical nuclear neutron capture reactions release their energy in quanta of $100\,\text{keV}$ to $7\,\text{MeV}$. Hence, a detector has to cover this range. Additionally, it has to provide a relative accuracy of 10^{-8} over the full range. Neither this accuracy nor an absolute calibration is available for absorption-based detectors over this energy range. These detectors are not even sufficiently linear.
However, single-crystal scattering provides a mean to access this wide energy range. It can be analysed by rotating a single-crystal in different diffraction orders and measuring the Bragg angle. Only the lattice constant of the crystal needs to be known. It can be measured accurately by comparison to the optical length standard as shown in section 1.1.6 on page 31. The absolute calibration of the Bragg angle can be done by comparison with

the well-defined angle 360° of a full rotation. This goniometer is explained in detail in chapter 2.

The Bragg angle must be obtained from a rocking curve. At typical count rates, the peak position can be determined with a precision of about 1/1000 of the width of the rocking curve. This width is determined by the acceptance angle of the crystal which is described by the dynamical theory of diffraction. [BC64]. At high energies the Bragg angle becomes small. To provide a relative precision of 10^{-8} of the peak position, a crystal with an acceptance angle of only 10^{-7} is necessary. Perfect silicon crystals provide such a low acceptance angle. Together with the acceptance angle in the perpendicular plane of only a few mrad[†], this leads to a solid angle of 10^{-11} sr. To provide a reasonable count rate (i.e. more than $1\,\mathrm{s}^{-1}$) the initial photon rate must be larger than $10^{12}\,\mathrm{s}^{-1}$. This number is not even accounting for the reflectivity of crystals and the efficiency of the γ-detector, which will account for another two orders of magnitude of loss.

The only way to provide this event rate is a reactor based on nuclear fission. Close to the reactor core thermal neutron fluxes of $5 \times 10^{14}\,\mathrm{n/cm^2/s}$ are obtainable. If a target material is placed there, neutron capture reactions will happen and the resulting nucleus will initially be in an excited state. It will then decay rapidly into its ground state by γ-emission:

$$^{A}X + \mathrm{n} \ \rightarrow \ ^{A+1}X^* \ \rightarrow \ ^{A+1}X + \gamma \ . \tag{1.41}$$
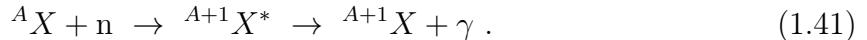
For isotopes relevant to this work, the decay process can be considered to start promptly after the neutron capture reaction. The lifetime of all states including the capture state is yet long enough (femto- to pico-seconds) that the natural energy uncertainty is below the instrument resolution. Usually the de-excitation happens not in a single transition, but in a cascade of several γ-emissions. These γ-events have to be identified to belong to the same cascade by prior measurements. This information is available from databases, e.g., `http://www.nndc.bnl.gov/`.

Due to mass conservation, the sum of the masses of products and educts must be the same. When using the energy-mass equivalence principle (1.36) for the emitted radiation, the mass conservation reads:

$$m\left(^{A}X\right) + m\left(\mathrm{n}\right) = m\left(^{A+1}X\right) + \frac{1}{c^2}\sum E_\gamma \ . \tag{1.42}$$

It is important to sum only over those γ-energies belonging to one cascade connecting capture state and ground state. Measuring different cascades provides an intrinsic consistency test.

In equation (1.42) the masses $m\left(^{A}X\right)$ and $m\left(^{A+1}X\right)$ can be determined by measurements on ionised atoms in Penning traps. This provides a precise mass ratio. This measurement

---

[†]See vertical alignment in subsection 3.3.4

and the conversion into mass differences is described in subsection 1.3.2. The wavelength λ of the γ-radiation can be measured with *Gams* as described in chapter 2. The energy of the cascade is then $\sum E_\gamma = \sum hc/\lambda$. However, the mass of the neutron $m\,(\text{n})$ is not directly accessible with Penning traps as it is a neutral particle and cannot be ionised.

Therefore the experiment is conducted for an additional pair of isotopes $^{A'}Y$ and $^{A'+1}Y$. Subtracting equation (1.42) of both experiments yields:

$$m\left(^AX\right) - m\left(^{A'}Y\right) = m\left(^{A+1}X\right) - m\left(^{A'+1}Y\right) + \frac{hc}{c^2}\left(\sum \frac{1}{\lambda_X} - \sum \frac{1}{\lambda_Y}\right) \,, \quad (1.43)$$

and the neutron mass cancels out. Hence, the equation contains only measurable quantities.

Penning traps yield mass ratios and therefore provide only accurate values for relative atomic masses. They do not provide a value in kilogram. A conversion to such a value requires a multiplication with the Avogadro constant, which is known only with a relative accuracy of 10^{-8}. This determines the uncertainty of atomic or molecular masses when specified in kilogram.

To determine the molar Planck constant from this experiment, one has to adapt equation (1.40) with the relative atomic mass differences for both isotope pairs:

$$N_A h = \left\{A_r\left(^AX\right) - A_r\left(^{A'}Y\right) - \left[A_r\left(^{A+1}X\right) - A_r\left(^{A'+1}Y\right)\right]\right\} M_u \, \frac{1}{\sum \frac{1}{\lambda_X} - \sum \frac{1}{\lambda_Y}} \cdot$$
$$(1.44)$$

Consequently for a determination of the molar Planck constant, two isotope pairs are necessary. With more pairs consistency checks are possible.

1.3.1 Mass of the neutron

At the same time equation (1.42) can be used to determine the neutron mass when measured with two isotope pairs:

$$m\,(\text{n}) = \frac{m\left(^{A+1}X\right) + m\left(^{A'+1}Y\right) - m\left(^AX\right) - m\left(^{A'}Y\right) + \frac{hc}{c^2}\left(\sum \frac{1}{\lambda_X} + \sum \frac{1}{\lambda_Y}\right)}{2} \,. \quad (1.45)$$

This experiment would not require any prior knowledge of $N_A h$ as this can be determined in the same experiment from equation (1.44). However, microscopic masses can only be measured in multiples of the atomic mass unit, hence the individual masses involve the Avogadro constant to be converted into kilogram, as the relative uncertainty of N_A given

by [CoData06] is 5×10^{-8}, this would dominate the total uncertainty. Measuring the neutron mass relative to the atomic mass unit is more accurate:

$$A_{\mathrm{r}}\left(\mathrm{n}\right) = \frac{A_{\mathrm{r}}\left(^{A+1}X\right) + A_{\mathrm{r}}\left(^{A'+1}Y\right) - A_{\mathrm{r}}\left(^{A}X\right) - A_{\mathrm{r}}\left(^{A'}Y\right) + \frac{N_{\mathrm{A}}h}{c\,M_{\mathrm{u}}}\left(\sum \frac{1}{\lambda_{X}} + \sum \frac{1}{\lambda_{Y}}\right)}{2} \,.$$
$$(1.46)$$

The accuracy can be increased when including the value of $N_{\mathrm{A}}h$ deduced from the fine-structure constant as described in subsection 1.1.1. Then it is sufficient to measure one isotope pair. For best accuracy one uses the combination of deuterium and hydrogen. The relative neutron mass can then be determined as:

$$A_{\mathrm{r}}\left(\mathrm{n}\right) = A_{\mathrm{r}}\left(^{2}\mathrm{D}\right) - A_{\mathrm{r}}\left(^{1}\mathrm{H}\right) + \sum \frac{1}{\lambda_{\mathrm{H}}} \frac{N_{\mathrm{A}}h}{c\,M_{\mathrm{u}}} \,. \tag{1.47}$$

In fact, the currently most accurate value of the neutron mass $A_{\mathrm{r}}(\mathrm{n}) = 1.008\,664\,916\,37(82)$ is deduced by this method [Kes+99]. [CoData06] suggests a different value with a reduced uncertainty $A_{\mathrm{r}}(\mathrm{n}) = 1.008\,664\,915\,97(43)$. This value is also based on the same deuteron binding energy measurement, but the underlying values and uncertainties for $N_{\mathrm{A}}h$ and d_{220} have changed.

In the adjustment of fundamental constants it is preferred to express the result of the measurement above as a ratio to the lattice parameter $d_{220}(\mathrm{ILL})$ of the silicon crystal used for the measurement: $\frac{\lambda_{\mathrm{H}}}{d_{220}(\mathrm{ILL})} = 0.002\,904\,302\,46(50)$. This indicates a problem of measurements done previously at *Gams*: if at a later time the value for the silicon lattice parameter has to be changed, this will also affect the results from *Gams*. It is thus strongly desired to become perform measurements which are independent from the recommended lattice parameter of silicon.

1.3.2 Penning trap

Charged particles follow a helical motion when moving inside a constant and homogeneous magnetic field. If the motion parallel to the magnetic field is confined by a supplementary electrical quadrupole field, the helical motion is compressed to a circular motion, as illustrated in Figure 1.12. The circulation frequency f_{c} is determined by the charge over mass ratio q/m of the particles and the magnetic flux density B as

$$2\pi\, f_{\mathrm{c}} = qB/m \,. \tag{1.48}$$

As the charge is quantized, f_{c} can take only discrete values. Hence, a comparison of masses of different ions is possible by comparing their cyclotron frequencies. As absolute measurements of the magnetic flux density are difficult, accurate mass measurements are only possible when comparing to the atomic mass standard. This is given by the mass

of a carbon-12 atom. Also, only charged ions can be trapped. To conclude the mass of the uncharged atom, a small correction (the ionisation energy) has to be applied. For a detailed survey of various traps see [Bla06].

The limiting factors of current ion mass measurements are instability and inhomogeneity of the magnetic field. In the currently most accurate experiment this problem is solved by measuring the reference ion and the test ion at the same time inside the trap [RTP04; DiF+94]. In this way a relative accuracy of 10^{-11} for the ion masses was achieved. The two ions are trapped within a volume of only 1 mm^3. At such a small separation the ion-ion interaction starts to become the limiting factor, even more so for high atomic numbers.

The determination of the molar Planck constant requires the knowledge of the mass difference of two neighbouring isotopes with a relative uncertainty of 10^{-8}. This mass difference $|m(X) - m(X')|$ is always approximately 1 GeV/c^2, while the isotope masses $m(X)$ are usually around 30 GeV/c^2. The uncertainty of the mass difference is thus:

$$u_{\mathrm{r}}\left(m(X) - m(X')\right) \approx u_{\mathrm{r}}\left(m(X)\right)\sqrt{2}\frac{m(X)}{|m(X) - m(X')|} \; , \qquad (1.49)$$

where $u_{\mathrm{r}}\left(m(X)\right) = u_{\mathrm{r}}\left(m(X')\right)$ and $|m(X) - m(X')| \ll m(X)$ are assumed. To satisfy the accuracy for a determination of the molar Planck constant with 10^{-8} uncertainty, the masses of the isotopes involved must be measured with a relative uncertainty of better than 3×10^{-10}.

An exception are hydrogen and deuterium. The approximation above is not valid in this case, as they have a relatively light mass of 1 GeV/c^2 and 2 GeV/c^2, respectively. In this case, the relative uncertainty of the mass difference is only a bit more than the double of the single mass uncertainties.

There is some legal limitation to the choice of isotopes used in the experiment: According to legal restrictions in some countries a Penning trap cannot be operated with (even slightly) radioactive ions with reasonable effort. Thus neighbouring pairs of stable isotopes are most suitable.

1.3.3 Isotope selection

In principle any isotope could be used as target for a γ-energy measurement. However, only few are really suitable since they must be used for two totally different experiments: first, the mass determination in the Penning trap which requires:

- A long lifetime of each isotope on the order of at least several weeks to provide precise mass values.
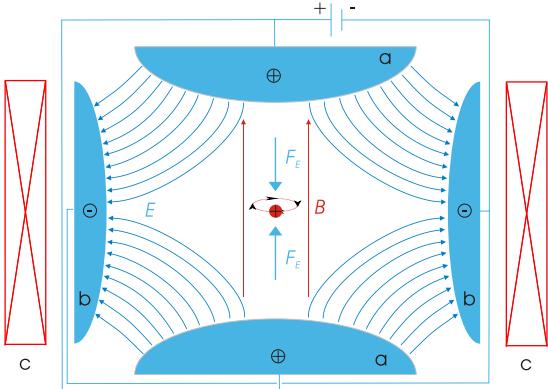
Figure 1.12: Field configuration of a Penning trap. A static homogeneous magnetic field (created by a solenoid marked in red) confines the charged particle on a helix. The static electric quadrupole field (created by two pole and one ring electrode marked in blue) compresses this helix to a circle. Drawing from [Kri09].
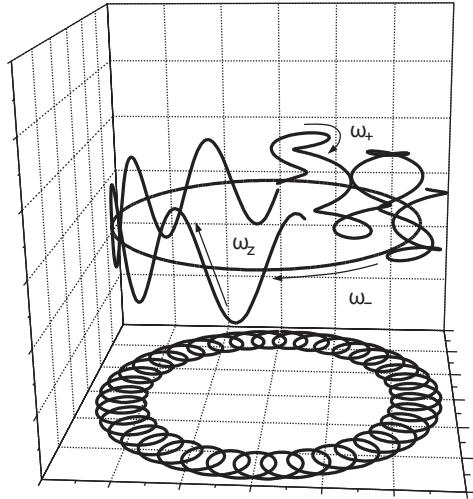
**Figure 1.13:** Schematic trajectory (three-dimensional and projection onto the xy-plane) with ideally three independent eigenmotions of an ion in a Penning trap. Reprinted from [Bla06], copyright (2006), with permission from Elsevier.

- Preferably a low mass, as according to equation (1.49) the relative accuracy for the mass difference is better.

Second, the lighter isotope of each pair must serve as neutron target. This requires:

- A large neutron capture cross section, for a sufficiently high event rate.

- The availability of a mechanical form or chemical compound which can resist the temperatures inside the reactor of 400 °C–800 °C.

- In the case of a compound, the other atoms should have relatively small neutron capture cross sections in order not to produce background. This is particularly important for high γ-energies.

- The branching rate of a single cascade must be sufficiently high. This is typically better for lighter isotopes.

- A high abundance of the isotope in the target material for high event rate and low background.

According to theses conditions, four isotope pairs are most promising for the experiment: $^1\text{H} \to {}^2\text{D}$, $^{28}\text{Si} \to {}^{29}\text{Si}$, $^{32}\text{S} \to {}^{33}\text{S}$ and $^{35}\text{Cl} \to {}^{36}\text{Cl}$. Their interesting transitions are shown
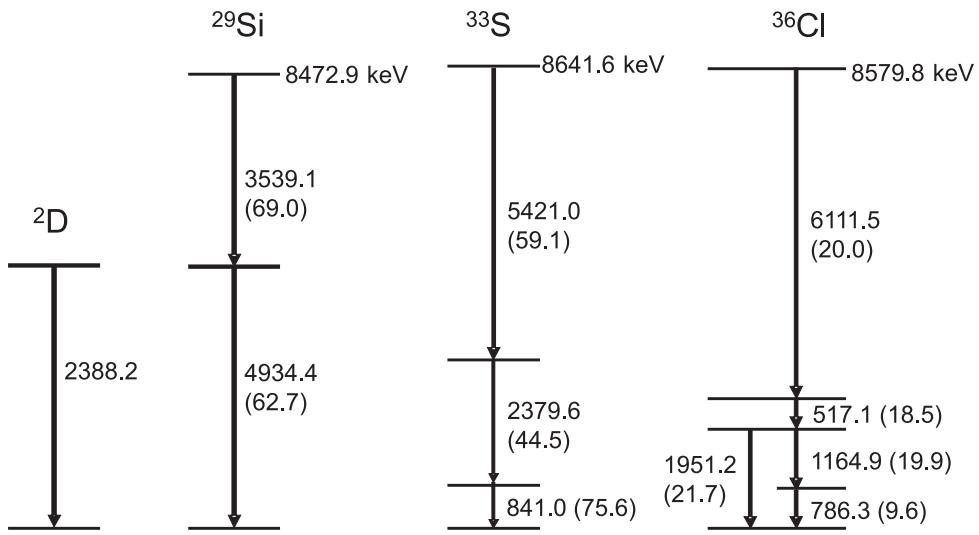
Figure 1.14: Partial level schemes. Only the strongest transitions are shown. The numbers along the arrows indicate the respective transition energy. The numbers in parentheses indicate the probability of these γ-emissions per 100 neutron captures.

in Figure 1.14. The γ-energies range from $517\,\mathrm{keV}$ to $6.1\,\mathrm{MeV}$. It should be mentioned that chlorine may already not be suitable due to the limitations of the Penning trap mentioned in subsection 1.3.2.

1.4 Instrumentation to measure the neutron binding energy

The sum over the γ energies of one cascade in equation (1.42) is called neutron binding energy. This parameter is determined directly by a measurement of all γ-wavelengths of a cascade and it is cited in literature as such [Dew+06].

1.4.1 Two single-crystal spectrometer

The highly monochromatic γ-radiation is diffracted only when impinging under the Bragg angle Θ on a crystal with lattice spacing d. The wavelength λ of the radiation has to match the Bragg condition in any diffraction order n:

$$n\lambda = 2d\sin\Theta \; . \tag{1.50}$$

As mentioned previously, the Bragg angle must be obtained from a rocking curve. For the desired precision of the position this curve must be sufficiently small. This is equivalent to a small acceptance angle of the crystal, typically 10^{-7} rad. The nearly perfect silicon crystal provides this. But it is also necessary to have an incoming beam divergence of about the same angle.

There are no lenses for γ-rays available which could reduce the beam divergence efficiently. Thus larger divergence has to be cut away. This could be done by a very small beam diaphragm or a very large distance between two diaphragms. Both would result in a very low count rate. Additionally this is technically almost impossible, and furthermore, the direction of this beam has to be stable with respect to the diffraction goniometer unit. All these problems can be solved by using another crystal as collimator. Having the same angular acceptance it delivers the perfect beam divergence for the analyser crystal. In the direction perpendicular to the dispersion plane, the divergence can be large and adapted to the particular experiment, typically some mrad, see subsection 3.3.4 for details. This crystal can easily have the width of several millimetres and provides a beam which is almost parallel over the full width, i.e. its divergence is as low as the acceptance angle of the crystal. Both effects allow a much higher count rate than with diaphragms. Furthermore, both crystals can be mounted in a convenient distance of several decimetres, such that the relative angle between the crystals can be measured accurately by an optical interferometer. Hence the direction of the beam which is given by the first crystal serves as the coordinate system for the analyser crystal.

The Bragg angles are acquired by rotating the analyser crystal in different diffraction orders and recording a rocking curve at each. The Bragg angles must be obtained by finding the centre of these curves. It should be stressed that only the lattice constant of the second crystal needs to be known as input parameter for equation (1.50). It can be measured accurately by comparison to the optical length standard as shown in section 1.1.6 on page 31.

It should be noted that the improvement of this spectrometer including its absolute angle calibration is the main subject of this work. All other input parameters are side products of other experiments.

1.4.2 γ-detection

Even though the Bragg angle is defined by the crystal position, it still has to be measured how many γ's were diffracted at each angle. In principle a simple Geiger-Müller counter or a scintillator combined with a photo multiplier would be sufficient. However, only a high-purity germanium detector provides a sufficiently high energy resolution to discriminate against the background radiation. At high energies for example, annihilation escape peaks can be resolved and used to increase the signal-to-noise ratio.

It should be stressed that neither the energy resolution of those detectors is high enough nor do they provide the necessary accuracy for the energy determination; this information must be deduced from the crystal spectrometer.

1.4.3 Single-crystal lattice spacing

The absolute determination of the γ-wavelength requires the knowledge of the absolute lattice constant of the crystal. This lattice parameter is measured by comparing the lattice spacing to the definition of the meter which is given by an optical interferometer. This is done by our collaboration partner at INRIM in Turin [Mas+09]. The method is briefly described in section 1.1.6.

For previous measurements the lattice spacing of the silicon crystals used at *Gams* were never measured directly in absolute terms, that is in a triple Laue interferometer (see section 1.1.6) with respect to the optical length standard of the metre. Only silicon pieces originating from the same ingot where compared to pieces from another silicon ingot. The lattice constant was then measured with respect to the optical length standard on again different pieces coming from that second silicon ingot. As comparison chains over different crystals resulted in contradicting values, the uncertainty for the lattice spacing of the *Gams* crystals had to be increased. To obtain the best value the *Gams* crystal lattice constant was linked to an "ideal" crystal without any chemical impurities. Any later discovery of a correction of the results in this comparison chain, e.g., due to a discovery of chemical impurity of one of the crystals, causes a change in the generally adopted lattice parameter of silicon. And thus it influences the lattice constant of the *Gams* crystal, too.

This lengthy comparison chain was necessary for a technical reason: the absolute lattice parameter determination requires a thin silicon lamella of medium length. γ-diffraction with *Gams* requires a thick lamella which was produced in a short version, only. The relative lattice comparator requires a thin and long lamella. And of course, all apparatuses require a different and incompatible mounting of the lamella. Within this work a new crystal design was incorporated and tested. It allows the direct measurement of the absolute lattice parameter with respect to the optical length standard, and the very same crystal can be used as analyser crystal on *Gams6*. As the lattice parameter of this individual crystal is now measured in absolute terms, no later adjustment is necessary.

1.4.4 Further impact of this work

Despite the main purpose of this project being to provide a direct measurement of the molar Planck constant with direct correlation to the Avogadro project by using the same lattice constant measurement, many other measurements will improve or become feasible.

Already mentioned was the mass of the neutron.

But all high accuracy nuclear spectroscopy data will profit. There is so far no model describing consistently all transitions or energy levels of nuclei consisting of more than a few nucleons. New measurements with higher accuracy may push or disprove new theories like tetrahedral symmetry [Dud+02; Jen+10].

The instrument is the only one providing measurement of large angles with high accuracy. Using the new crystal mounting mechanism, measurements like testing the orthogonality of the silicon unit cell become possible.

Furthermore the Bragg law itself is in doubt. Specifically for low energies and thin crystals, surface effects may shift the effective lattice constant for diffraction. *Gams* provides a unique opportunity to compare diffraction with different energies on different crystal thicknesses, particularly with the new crystals.

1.5 Constraints to the γ-spectrometer

In order to be fulfil all the demands, the instrument has to provide certain properties:

- a large angular range,

- an absolute calibration over the full range and

- a high angular resolution.

From these demands an interferometric measurement of the angle is indispensable.

- Perfect crystals with a small acceptance angle

are necessary to provide the resolution of the γ-wavelength. At the same time this limits the solid angle enormously and requires

- a high initial event rate which is given only inside a nuclear reactor.

The desired high accuracy at the low count rate induces a long measurement time. Consequently the instrument must provide

- an excellent long time stability.

This involves compensating environmental influences, as well as avoiding any of such influences as much as possible.

1.6 History of *Gams*

All of the conceptional ideas presented so far in this work are not new. Particularly the *Gams*-instrument itself has a long history. It started in the 1970's at ILL as single crystal spectrometer used for nuclear structure measurements. With *Gams4* – constructed at NIST – the first time a metrology device became operational at ILL, leading to the latest high impact result, the verification of $E = mc^2$ with the uncertainty of 4×10^{-7} [Dew+06]. Old versions of *Gams* were replaced by *Gams4* and *Gams5*. The latter is an improved version of the spectrometer of *Gams4* but equipped with bent crystals.

The latest direct determination of $N_\mathrm{A}h$ at *Gams4*, basing on data from 2001, was published in 2005 and has an uncertainty of 4×10^{-7}. To fulfil the current demands the experiment has to be improved by a factor of 20. *Gams6* is designed to achieve this accuracy. It will replace *Gams4*, while *Gams5* will stays in parallel operation for use with bent crystals.

1.7 Summary

The current definition of the kilogram as an artefact is generally deprecated and due to drifts of mass of the copies of the prototype a redefinition is required. Two possible candidates for the re-definition are either the Planck constant or the Avogadro constant. Experiments all over the world try to determine these constants, but so far deliver contradicting results. A determination of the molar Planck constant using the crystal lattice constant from the Avogadro project as input parameter is an important cross check for these measurements and can help to trace down the inconsistencies.

The CIPM suggested in 2005 to achieve a consistent relative uncertainty of a few parts in 10^8 before any re-definition as the International Prototype of the kilogram is suspected to drift by this amount per century. In consequence, to contribute to a re-definition a measurement of the molar Planck constant must be at this level of accuracy.

This experiment is done by observing the mass to radiation energy conversion in a nuclear neutron caption reaction. As the molar masses of the particles involved can be measured in a Penning trap relative to the atomic mass standard, the molar Planck constant can be determined by measuring the wavelength of the emitted radiation. A dedicated two single-crystal spectrometer can provide the necessary accuracy. The accuracy from the existing *Gams4* spectrometer must be improved by a factor of 20 to do so. The present work describes the upgrade process towards *Gams6*.

Chapter 2

γ-spectrometer

When I heard Scott Dewey saying: "Gams is such a complicated instrument", I thought he was exaggerating.
*Meanwhile I know he was understating.*

This chapter splits up into three parts. Section 2.1 gives an overview of the instrument. Its nomenclature and standard acquisition procedures will be introduced, and some new effects are analysed for the first time. Section 2.2 describes the total process of the data evaluation: how the γ-wavelength is obtained from the raw data. This includes the mathematical properties of all components in detail and precision of a new quality. Section 2.3 describes the instrument calibration which relates the interferometer read-out to an absolute angle. The procedure will be described as well as theory and predicted uncertainties.
Measured data are presented in chapter 3.

All explanations in this chapter base on *Gams4*, which is almost identical to *Gams5*. Some problems described here will be overcome in *Gams6* which is currently in its final construction phase and eventually will replace *Gams4*. The advantages of the new instrument are described in chapter 4.

2.1   Instrument Components

A high resolution double crystal spectrometer measures the wavelength λ of the γ-radiation emitted by a intense source. This radiation is roughly collimated by lead diaphragms before it hits the actual spectrometer which consists of two single crystals. Both
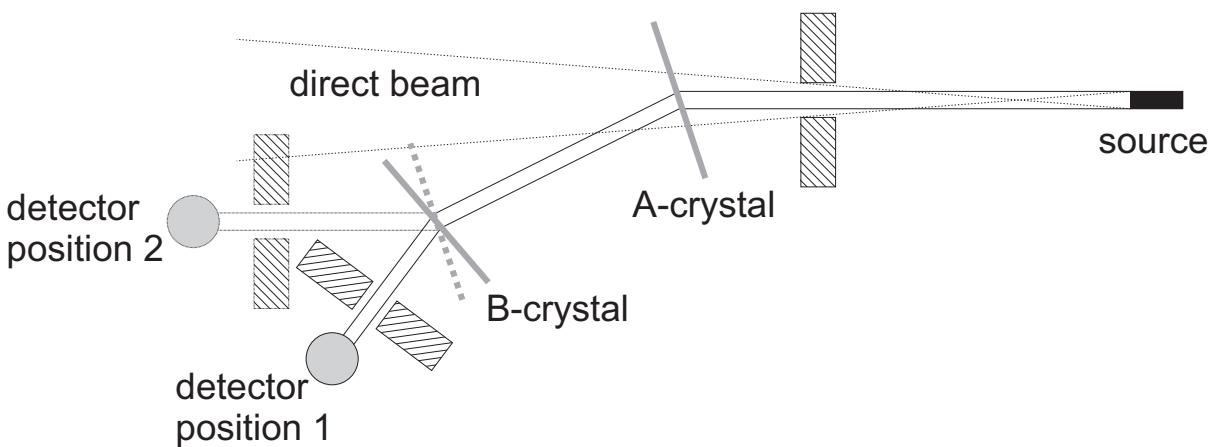
Figure 2.1: Sketch of a double crystal spectrometer. The Radiation is emitted by the source (black). The pre-spectrometer lead collimation shapes the beam roughly (hatched). The first crystal "A" (grey) diffracts the desired energy and gives fine collimation and orientation. The second crystal "B" analyses the energy, as it diffracts only if put in the correct angle. After a further collimation, the radiation reaches the detector (circle). A second diffraction order (dotted) is required as nothing else could serve as an accurate angle reference. The direct or non-diffracted beam (dashed) must be shielded carefully.

crystals can be rotated around their vertical axis. Their angle is measured with a highly accurate goniometer. The beam is diffracted if the incoming angle θ_{X,m_X} of the radiation on a crystal meets the Bragg condition:

$$m_X \lambda = 2d_X \sin \theta_{X,m_X} \qquad X \in \{\mathrm{A}, \mathrm{B}\} \qquad (2.1)$$

in an arbitrary order m_X where d_X is the lattice spacing of the crystal. The first crystal is referred to as "A" and the second as "B", The observables of each crystal are indexed correspondingly. If the original radiation is diffracted by the "A"-crystal and then this diffracted beam meets also the Bragg condition of the "B"-crystal, it will finally hit the detector and be counted. A further lead diaphragm in front of the detector shields the non-diffracted (direct) and single-diffracted beam. The experiment could be done with one single crystal only. However, the incoming radiation would be very divergent, consequently the resolution very low. Additionally it would be technically very difficult to determine its accurate direction. This is the purpose of the "A"-crystal: Out of the divergent primary beam, it diffracts only a small fraction. This secondary beam has a divergence as small as the little acceptance angle of the first crystal. Additionally the "A"-crystal fixes also very well the orientation of the secondary beam. Now the "B"-crystal is rotated – together with the detector and its diaphragm – such that the angle between two Bragg orders is measured while the "A" crystal is not moved. Now the wavelength can be calculated. The only parameter that is required from external experiments is the lattice spacing of the "B"-crystal.
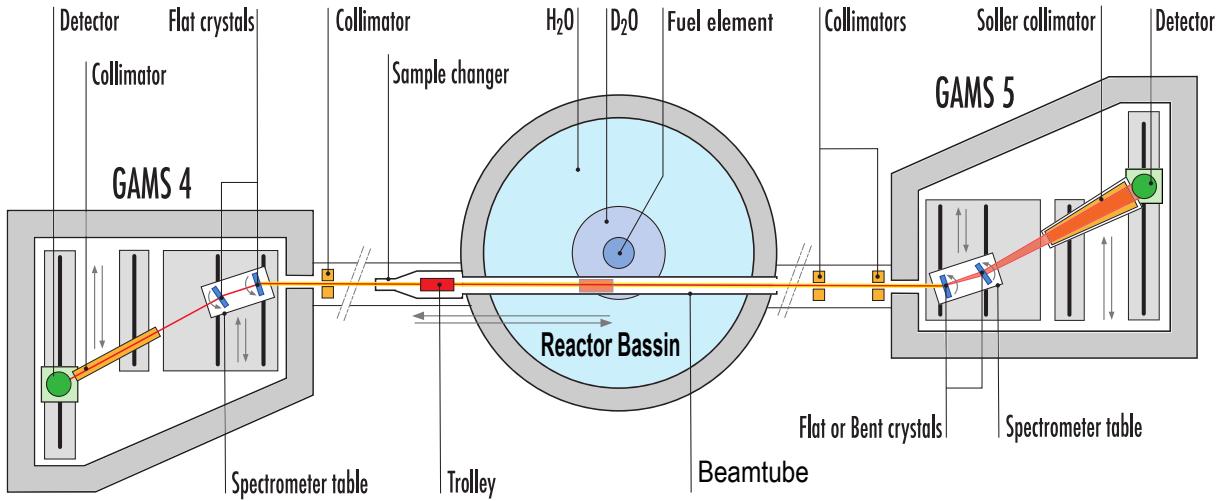
**Figure 2.2:** PN3-instrument – *Gams4* and *Gams5* besides the reactor basin. Sketch received from [ILL09].

2.1.1 In-pile γ-source

As explained in section 1.3, the desired resolution requires a low angular acceptance, and hence a high initial count rate. To provide the necessary neutron flux, the entire *Gams* facility is placed at the high flux neutron source of the *Institut Laue-Langevin* (ILL) in Grenoble, France. It is officially named "instrument PN3". A sketch can be seen in Figure 2.2. The instrument bases on a beam tube passing through the moderator tank (D_2O) of the reactor. At each end is an individual spectrometer: *Gams4* and *Gams5*. They are still inside the reactor building. Inside the tube a small sample can be placed close to the fuel element. This target is usually 2 or 4 mm wide. The neutron capture reaction causes γ-radiation which is emitted isotropically. The reactor basin (H_2O) and some lead diaphragms absorb the bulk majority of the radiation. Only a small fraction passing parallel along the beam tube is used. This γ-beam leaves beam tube and enters the spectrometers in about 20 m distance from the target.

Any material analysed on *Gams* is exposed to a high neutron flux. This material is synonymously called sample, source or target. It is placed in 50 cm distance to the fuel element. Due to the high radiation level the source heats up. Only thermal radiation and heat dissipation by the Helium atmosphere of 800 mbar can serve for cooling. The preceding security calculations neglect the atmospheric dissipation. As the source may – depending on the mass – achieve up to 1000 °C the choice of materials is limited. While some metals can be used as bulk material, most elements are used as oxide in the form of a powder. They are put in graphite containers as shown in Figure 2.3. Up to three of these containers can be brought close to the fuel element. They are aligned such that the

holder bridge (graphite)

holder rod (metal)

container (graphite)

target material

40

4

17
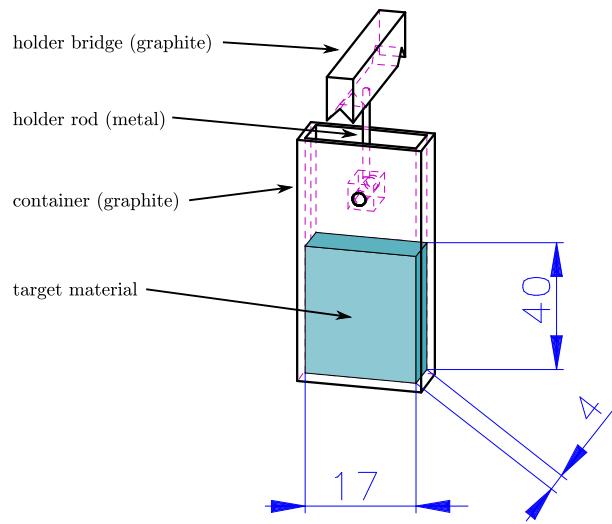
Figure 2.3: The target containers are made out of graphite. The maximum inner dimensions are given in mm. The wall thickness may vary between 0.5 mm and 1 mm.

Figure 2.4: Top view of the trolley. The three mounting positions for target containers are visible. The diameter of the trolley is about 15 cm.

Figure 2.5: Face view of the trolley with a target container mounted. The mechanism for rotating the target containers while being in the beam tube is visible at the sides.

surfaces facing along the beam tube are congruent. The typical width of this surface is 2 or 4 mm. This defines the width of the γ-beam seen by the instrument. The height of the beam depends on the filling level, the containers can take up to 40 mm. The γ-radiation

54

emerges isotropically. As the spectrometer is placed 20 m away the beam size corresponds to a solid angle of 5×10^{-9} sr. Hence only a small fraction of the initial capture events will be used.

The nuclear rector at ILL produces neutron by fission inside the fuel element. These fast neutrons are moderated to thermal neutrons in a heavy water tank. Therefore the flux of thermal neutrons has its maximum of 1.5×10^{15} n cm^{-2}s^{-1} outside the fuel element. The flux at the target position is referred with 5×10^{14} n cm^{-2}s^{-1}. It is assumed to be homogeneous over the sample size. However, there are no measurements about isotropy available. Only thermal neutrons are considered as the capture cross section decreases with increasing neutron energy and hence neutrons of higher energy are hardly captured, while colder neutrons which would interact more likely, are negligible due to the thermal equilibrium with the surrounding water. In the case of resonances also high energetic neutrons can have a large capture cross section. This is not the case for nuclides used in this work.

2.1.2 Beam line

After the γ-ray has left the beam tube through a thin metal window, it passes through air before it reaches the interferometer which is in 20 m distance from the source. Lead diaphragms limit the divergence of the isotropic radiation. They shape only the height of the beam. They *do not* define the width of the used beam. The horizontal fine collimation is done by the A-crystal. All horizontal diaphragms serve either as background suppression or as beam dump for the non-diffracted radiation. The latter is necessary as, at the detector, the distance between the diffracted beam and the direct beam may be as little as 4 mm. In order not to produce any additional background, no diaphragm surface that is hit by the beam should face to the detector. And if possible, it should not even face to other surfaces with direct view to the detector. Consequently all diaphragms should provide a sawtooth shape where the opening angle should be larger than the geometrical divergence of the beam at this position. The length of the teeth should be adapted to the absorption length of the γ-wavelength one wants to measure. At *Gams4* only the pre-crystal collimator provides a sawtooth shape. The other collimation lead bricks are flat and parallel to the beam. Providing them with a sawtooth shape may further reduce the background. However, the effort is high, and the size of the effect should be studied carefully before any larger investment. See Figure 2.8 for a sketch of the beam line. Additional information is given in the item beam diaphragm in subsection 2.1.6.

2.1.3 Spectrometer

The spectrometer consists of the two crystals whose horizontal relative angle is measured with high precision by a Michelson interferometer. Due to its small angular acceptance for γ-rays, the A-Crystal serves as collimator. At the same time it defines the reference angle for the B-Crystal. Only the relative angle between the two crystal is important for the wavelength measurement. The absolute angle and position of the A-Crystal versus the target must only be maintained within the geometrical divergence of the beam defined by the collimation which is about 15 mrad. This can be done easily. Note that this collimation works only in the case of a line spectrum, i.e. a source providing not a white beam, but a mix of individual very sharp γ-lines.

The distance between A- and B-crystal is 53 cm at *Gams4* and 70 cm at *Gams5* and *Gams6*. As desired Bragg angles can vary from 0.2°–3° the once diffracted beam may be displaced at the level of the B-crystal by up to 70 mm which makes it necessary to move the B-crystal in the beam reflected by the A-crystal.

Each crystal is mounted rigidly to an axis that is equipped with a lever arm so that the angular position can be recorded precisely with an Michelson interferometer. Both axes including their interferometers sit on a common solid block of Invar™ which is called interferometer table. This ensures that the relative position of the crystals can be maintained. Even if the whole table is rotated to bring the B-crystal into the diffracted beam, the relative position can be maintained without rotating the crystal axes versus the table.

2.1.4 Crystals

Both crystals are perfect single crystals. At *Gams5* bent Crystals can be mounted to increase luminosity [Dol+00]. However their lattice spacing is not known well enough for the purpose of this work. Therefore this work refers only to flat crystals. Some of the properties of a double flat crystal spectrometer described here are not valid in the bent crystal case.

The crystals are used in Laue geometry and have a thickness of a few millimetres. The usual material for the crystals is natural silicon, but crystals of germanium are also available. The crystals are nearly perfect. Their diffraction properties match very well with the predictions of the dynamical theory of diffraction. Consequently the acceptance angle of one crystal for a monochromatic γ-beam is as small as 10^{-7} rad. Therefore the horizontal collimation is made best by selecting the γ-rays with the crystal and just dump the non-refracted beam.

The crystals have to be mounted rigidly to the axis, as only the angle of the axes, i.e., the goniometer arm, is measured. One has to rely on the fix connection between arm
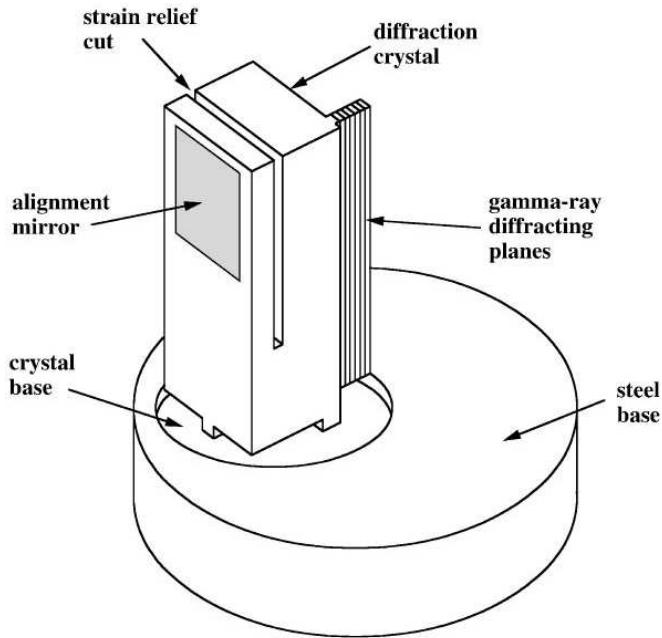
Figure 2.6: Sketch of a crystal used at *Gams4*, including adapter socket for mounting on axis. The actual diffraction lamella (containing the diffraction planes) is 8 mm wide and 50 mm high. Different crystals with lamella thicknesses of 1.1 mm to 6.9 mm exist. The mirror is parallel to the diffraction planes within some arcseconds. Drawing taken from [Kes+01].
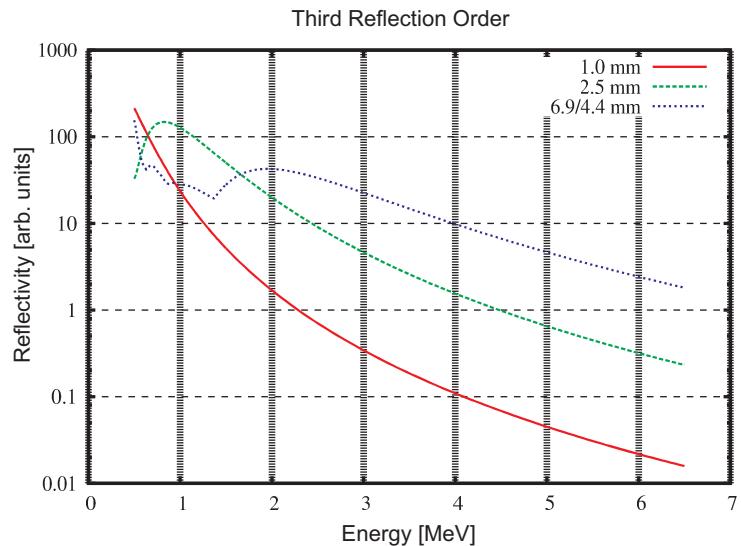
**Figure 2.7:** Reflectivity of a pair of silicon crystals in (220) direction. For 1.0 mm and 2.5 mm two crystals of the same thickness are available. Only one crystal of 4.4 mm and one of 6.9 mm are available; for high energies they must be used in combination. The plot ignores absorption and detector efficiency.

and crystal. However, it is also necessary to change the crystals. Due to absorption and dynamical theory of diffraction [Lis94] the optimal crystal thickness varies for different energies from 1 mm to 6 mm as shown in Figure 2.7. For a decent count rate, several crystals with different lamella thicknesses exist. They must be changed according to the γ-energy that is supposed to be measured. For a good resolution the crystals must be aligned better than an arcsecond. Each crystal has an optically polished surface which is almost parallel with respect to the diffraction lattice planes. The deviation angle is within a few arcseconds and known for each crystal. As optical polishing introduces strains to the lattice, the crystal provides a cut such that these strains do not affect the diffraction lamella. This is sketched in Figure 2.6. The silicon is glued on three legs to a steel base. This base can be fixed with three screws to the axis. The symmetric positions of the screws ensure a sufficiently rigid connection. A rough alignment to about 2 arcseconds can be achieved by the use of shims and verification by the polished surface with an autocollimator. For further fine-adjustment the head of the axis can be tilted up to 8″. All crystals are pre-aligned to be measured in the (220) direction, as this is the standard orientation used in silicon lattice spacing metrology due to the high reflectivity.

2.1.5   HPGe-detector

The acquisition of the γ-rays is done with a high-purity germanium detector ($\approx$ 32% relative effciency [Kes+01]). Operated at a tension of 3 kV, every γ-photon dissipating its energy in the depletion zone causes a voltage drop proportional to the energy of the photon. After amplification and reshaping with 2 µs shaping time the signal has an amplitude of up to 4 V. Usual count rates at *Gams* are below 1 kHz and can be handled without worrying about dead time corrections. The energy resolution is a few keV. This helps to distinguish from γ-events with different energies originating from a different Bragg order or from a different crystal lattice layer.

The detector must be shielded from undesired radiation to obtain an acceptable signal-to-background ratio and to avoid saturation and thus dead-time effects. For general background radiation the detector is protected by a 10 cm thick lead shielding covering the full solid angle (see Figure 2.8). As the diameter of the detector front is 10 cm, and the diffracted beam is sometimes only a few mm displaced from the non diffracted beam, a dedicated collimation line of two times 50 cm length is placed in front of the detector. The position of this collimation line must be adapted for each Bragg order and wavelength as well as the detector position itself. As all other horizontal diaphragms, the collimation line should not touch the actual diffracted beam.
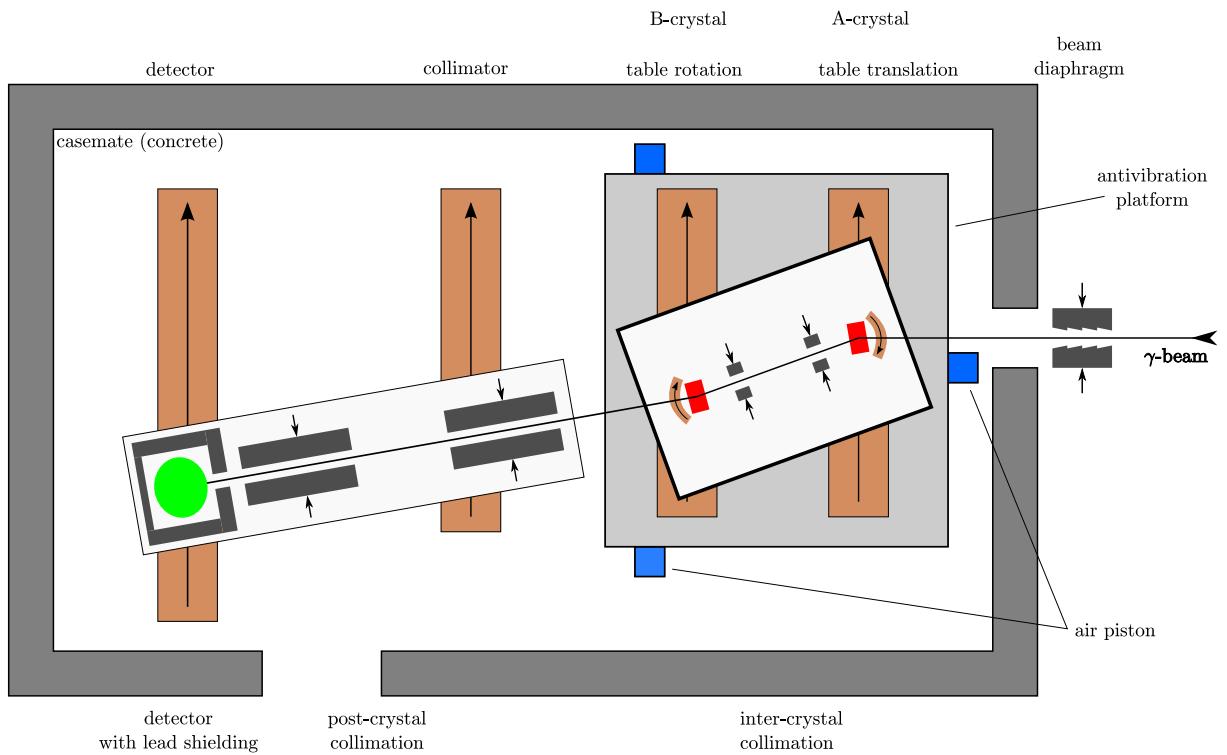
Figure 2.8: *Gams4*-axes. The scheme is not true to scale and shows the spectrometer in a sort of (+2,+1) Bragg order for a low energy. Axes which are motor controlled are marked with arrows on brown background. Lead shielding and diaphragms are drawn in dark grey. They are manually actuated (indicated by a small arrow without background). The crystals are drawn in red.

2.1.6   Axes & coordinate system

Apart from the Ge-detector that provides a quantitative value of the energy per event, all other observables of the instrument are displacements in space, to be more precise: in most cases rotations. A consequence is a large number of rotation and translation axes, which are listed here:

A-axis The rotation of the crystal is coarse positioned via a step-motor with a resolution of 0.8 µrad and fine positioned with a piezo actuator with a range of 2 µrad. Position read out is done by an Michelson interferometer with a resolution of better than 2×10^{-10} rad.

B-axis The B-crystal is controlled as described for the A-crystal, with independent mechanics and interferometer.

Table translation Both crystal axes and the interferometers sit on a common solid unit called "interferometer table". This entire table can be translated laterally. However this operation is required only to position the A-crystal relative to the target. Apart from the initial alignment this is rarely used.

Table rotation Additionally, the table can be rotated around the A-axis. This is necessary to place the B-crystal in the centre of the beam diffracted by the A-crystal. This frequent movement is done by a step-motor. The readout is taken from a *Heidenhain* ruler. The linear movement is transferred by a trolley and a pivot point to a rotation. A reproducibility of 20 µrad is reached.

Detector The opening slit of the shielding of the Ge-detector has to be placed in the centre of the twofold diffracted beam. Therefore the detector with the entire lead shielding can be lifted by some air pads and translated over 4 m with a resolution of 10 µm.

Collimator The collimation line in front of the detector has to be placed properly including a slight rotation of the detector collimator unit to follow the diffracted beam. The collimation translation places the front end of the collimator at the proper positions and profits from the air pads of the detector to rotate the back end. The resolution is better than 10 µm over a range of 1 m.

Beam diaphragm The actual beam must be shaped only in height. This is done by some lead bricks which are placed by the skilled hands of the experimenter. The horizontal shaping is done by the A-crystal. However it is crucial for a low background to block all unused radiation as early as possible. For this a pair of lead bricks is placed half way in front of the spectrometer. As the target may have different widths the bricks can be moved individually by step motors with 10 µm resolution.

Inter-crystal collimator Two pairs of diaphragms are placed between the two crystals. Their use for initial alignment is priceless. Their use for background reduction depends strongly on the measured γ-energy. Each lead brick can be driven manually by micrometre screws.

Crystal tilt The crystals have to be aligned vertically parallel to each other (lateral inclination). Otherwise the rocking curve will widen largely. The coarse inclining is done by shims. A piezo actuator can incline the A-crystal in a range of $10''$.

Polygon motor For the calibration of the angle interferometer it is necessary to couple a polygon to the B-axis. This is done by two precision gears with 360 teeth. The polygon – fixed to one of the gears – can be lifted (in order to decouple the gears) by a motor and after that it can be lowered at another gear position.

Note that for historical reasons all angles at *Gams* are counted clock wise (inverse mathematical rotation sense) if seen from the top. Translations are oriented the same way provided they are seen as approximative circles around the reactor core.

If a coordinate system is necessary for construction designs it originates from the centre of the γ-beam at the level of the A-axis rotation centre. The Z-axis points against gravity. The X-axis points along the γ-beam. The Y-axis completes the orthogonal right handed system. Attention: the coordinate system is only defined if the interferometer table is aligned parallel to the γ-beam (meaning source, A-crystal and B-crystal in line).

The notation of double crystal Bragg orders is different from the usual literature nomenclature used in X-ray diffraction. At *Gams* the non-dispersive configuration is named (m,m) – as usual both orders have the same absolute value, but at *Gams* they have the same sign, contrary to most low energy nomenclatures. This has the advantages that the Bragg order of a crystal has the same sign as the angle in which this Bragg condition occurs and both crystal rotations have the same sign of rotation. Note that the crystal rotations are measured always relative to the interferometer table which must be rotated itself. For a (1,4)-reflex one would rotate the table by $-2\,\Theta_A|_{m=1}$, the A-crystal by $+1\,\Theta_A|_{m=1}$ and the B-crystal by $+\,\Theta_B|_{m=4}$.

2.1.7 Goniometer

The angles of the crystals have to be measured very precisely over a large range. For this purpose optical interferometers are best suited. At *Gams* heterodyne Michaelson
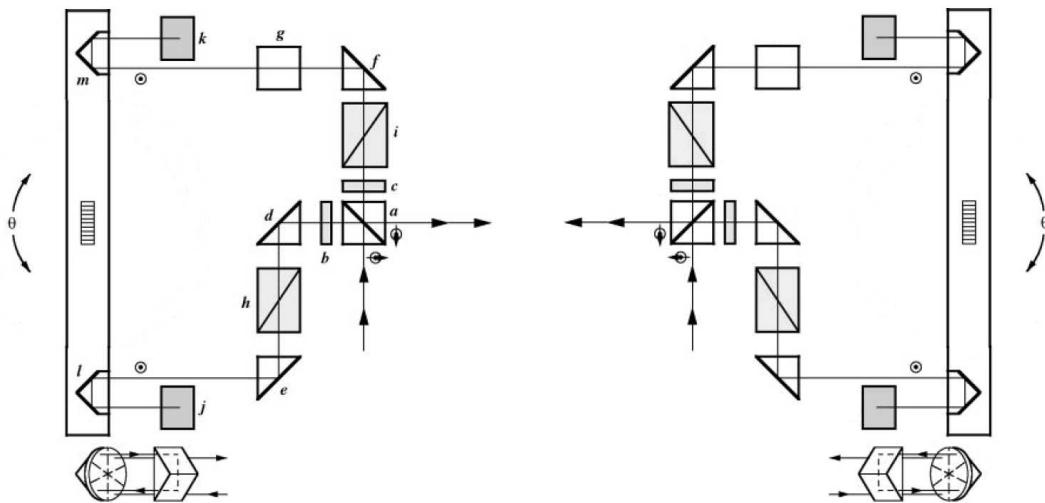
Figure 2.9: *Gams4* interferometer layout. The goniometer arms with crystals are at the very left and very right. An explanation of the optics is given in subsection 4.1.2.

interferometers are used. A lever arm is fixed symmetrically and rigidly to the axis with the crystal. At both ends a triple mirror is fixed. These triple mirrors, also referred as corner cubes, reflects back light parallel to its incident direction. So the interferometer will detect the sine of the rotation of the axis as linear displacement of the two triple mirrors. The absolute axis angle Φ can be calculated from the interferometer readout F from the equation:

$$F = K \sin(\Phi) + F_0 \; , \tag{2.2}$$

when the calibration constant K and the interferometer zero F_0 are known. This equation is discussed extensively in section 2.2. The lever arm together with the corner cube is called goniometer arm. K is a measure for its length.

The Michelson interferometer splits a laser beam into two and guides these to the triple mirrors. It recombines the reflected beams and measures the path length difference by analysing the phase via the interferences. *Gams* uses a heterodyne interferometer where the beams for each triple mirror have a slightly different wavelength. The difference is a radio frequency (RF). In the recombined beam this RF-frequency shows up as a beating frequency that has the same phase as the optical waves. This simplifies the electronic acquisition a lot, provides always information about the sense of any displacement and is hardly sensitive to fluctuations in the light intensity.

Any interferometer provides only the displacement information within a distance of one wavelength (632 nm) of the laser light in use. This is the phase of the electronic signal. Any longer range distance information must be obtained by continuously surveying the phase signal and counting full phase revolutions, or in optical language: fringes. In this work, the combined information is called interferometer read-out. It comprises the number of integer fringes and the fractional phase information. It is formally a dimensionless number. However, its conversion factor K is different for the instruments *Gams4*, *Gams5* and *Gams6*. To indicate which K applies, the readout is given with the unit f_4, f_5 or f_6. The interferometer read-out is of the dimension of length, but for a rough estimation it can be converted to angles by dividing through K.

To simplify this acquisition with an analogue electronic system the number of fringes was multiplied electronically by four. Consequently also K is four times bigger. Also some non-linearity effects are stretched. These "quarter-fringes" were used in *Gams4*. They were in use at *Gams5* as well. However, since the installation of a new data acquisition system in 2006, *Gams5* uses unmodified fringes. *Gams6* will use unmodified fringes from the very beginning. Details of the interferometer and the phase acquisition are given in chapter 4.

2.1.8   Angle calibration

For deducing the γ-wavelength via the Bragg equation (2.1) it is required to know the angles with absolute accuracy. However the transformation from interferometer readout

into angles requires the knowledge of the calibration constant K, see equation (2.2). This is the distance between the two corner cubes of an axis measured in laser wavelengths. However, this length is not accessible by mechanical means in the required accuracy (i.e. 10^{-8} for *Gams6*). Hence a calibration is necessary. A full rotation is the well defined angle of 360°. As the range of the interferometer covers only 30° the full rotation must be folded somehow into this range. This is done by a 24-sided regular polygon. Its sum of exterior angles is 360°. The interferometer can perfectly measure the angle between two adjacent sides. After such a measurement is made, the polygon is decoupled, rotated by 15° versus the axis and then re-coupled. The angle of the next adjacent sides can be measured at the same interferometer positions as before. After doing this for all 24 corners, the sum of the angle differences obtained from the interferometer read out corresponds to 360°. The interferometer read out is hence calibrated to absolute angle units now. The procedure requires a mean to rigidly couple the polygon to the axis in various positions. This is done by a pair of high precision gears with 360 teeth. The lower gear is attached to the goniometer arm, while the upper gear is attached to the polygon. So the polygon can be coupled to the axis in any multiple of a 1° step. Normally steps of 15° are used. The coupling is done by gravitation, thus in all positions occurs the same force. The reproducibility of this coupling is better than 2×10^{-7} rad. The precision of each re-coupling is verified by an autocollimator which can measure the orientation of one polygon surface with a precision of about one nanoradian, however, only within a small acceptance range. The procedure, its theory and uncertainty analysis are described in section 2.3. The performance of the *Gams4* calibration and the corresponding data evaluation is presented in section 3.2.

2.1.9 Environmental isolation

The entire instrument is placed in the reactor hall. This is not an environment which is desirable for metrology instruments: The floor is vibrating due to the heavy water pumps of the reactor and the temperature varies up to 0.5° within a day. Additionally, the Ge-detector needs to be filled with liquid nitrogen regularly, causing a huge temperature drop. Luckily the main radiation protection, a casemate of 30 cm concrete walls all around the spectrometer, can be used to improve temperature stability and also to shield against acoustic vibrations. The temperature inside the casemate is already stable to 0.3° due to the air conditioning of the reactor hall and the thermal mass of the casemate. Though this stability is disturbed by the daily or weekly re-filling of the nitrogen dewar of the γ-detector. Several lamps of 100 W that are controlled by a thermometer stabilize the temperature additionally. A housing out of multi layered aluminium foil and isolation material separates the central part of the spectrometer from the Ge-detector and the lamps. A further Mylar cover reduces convection around the interferometer and crystals. To isolate the instrument from the vibrations transmitted by the ground, the whole central
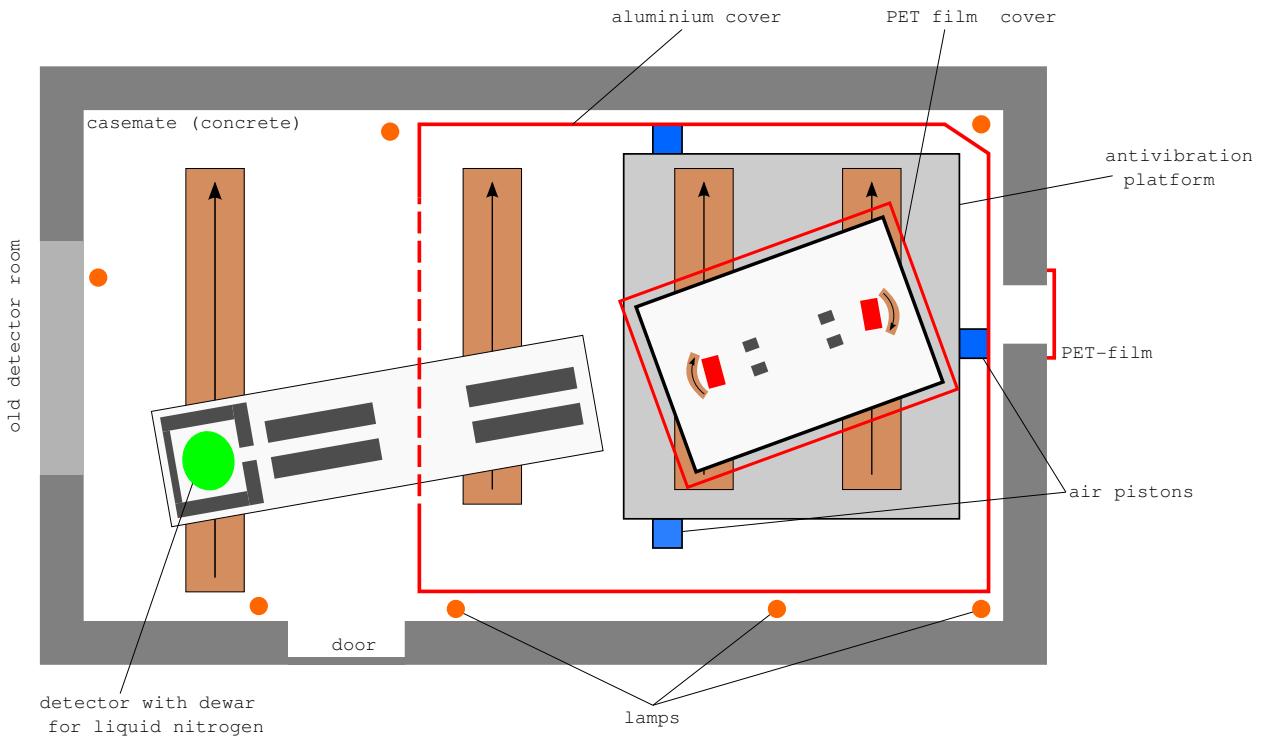
Figure 2.10: *Gams4* thermal shielding. The aluminium cover consists of a multilayer of aluminium foil and mineral wool. In the region of the detector collimation line it is not that close to allow the detector moving. The casemate has even more thermal leaks, the most important in the rear wall towards the old detector room. The lead diaphragms are marked dark grey. For elements not named here see Figure 2.8.

part of the spectrometer is placed on a solid and massive platform (about 3 t and out of iron or granite respectively). This plate is hold by air pistons. Their pressure is controlled actively to keep the platform in place with 1 µm translational and 1 µrad angular precision relative to the ground. The set-up is sketched in Figure 2.10.

2.1.10 Acquisition sequence

Even though the crystals are quite perfect, they still have a finite line width which can be resolved by the instrument. Therefore one of the crystals is rotated around the expected angle of Bragg condition while an intensity profile is taken. The result is called rocking curve. The real Bragg angle is obtained by parameter estimation – typically a most-likelihood fit. As for the angle measurements there is no absolute zero orientation given, one has to measure the Bragg angle in two different orders and deduce the wavelength from the difference of these angles. Typically one leaves the A-crystal fix and changes the

orders of the B-crystal. This has the advantage that throughout the whole measurement most of the instrument can stay at one position, only the B-crystal and the detector with its collimation need to be moved. If one would change the A-crystal order the beam diffracted by it would displace and one would have to displace the B-crystal. Such a displacement would require a rotation of the whole spectrometer table and certainly would disturb environmental stabilization. For convenience one leaves the A-crystal at a fixed position and performs also the rocking with the B-crystal.

As the acquisition is sequential, throughout the measurement of both Bragg orders the environmental condition should stay stable. To compensate at least for linear drifts the acquisition sequence consists of 4 rocking curves:

$\theta_{\mathrm{B},(c,i)+}$ at order (c,i); positive scan direction,
$\theta_{\mathrm{B},(c,j)-}$ at order (c,j); negative scan direction,
$\theta_{\mathrm{B},(c,j)+}$ at order (c,j); positive scan direction,
$\theta_{\mathrm{B},(c,i)-}$ at order (c,i); negative scan direction.

During such a 4-pack the A-crystal is always kept at $m_{\mathrm{A}} = c$. The B-crystal is alternated between $m_{\mathrm{B}} = i$ and $m_{\mathrm{B}} = j$. The orders c, i, and j may be chosen freely. However the case $c = i = -j$ provides symmetry effects that simplify the evaluation and increase the accuracy. The acquisition time for such a 4-pack can vary between a few minutes and several hours, depending on the intensity of the γ-line.

2.2   Spectrometer mathematics

As the principle of the spectrometer interferometer is quite simple, it can be explained by only two equations, namely Bragg's law (2.1) and the interferometer equation (2.2) which reduces to a simple sine function if one assumes $F_0 = 0$:

$$n\lambda = 2d\sin\Theta \ ,$$
$$F = K\sin\Phi \ .$$

A γ-detection of a Bragg-reflex means $\Theta = \Phi$, hence λ can be calculated easily:

$$\lambda = \frac{2d}{n}\frac{F}{K} \ . \tag{2.3}$$

This approximation can be used for uncertainty estimation and very rough wavelength estimations. However, the detailed data analysis is not that trivial, mainly due to the non-linearity of the sine combined with various fringe and angular offsets.

In the past many of these offsets were ignored, partly because some parameters were assumed to be stable between two measurements and therefore would cancel out in the differential measurement, or because the spectrometer was used only in symmetric mode

and therefore offsets cancel out in differential measurements as well. However, the accuracy aimed for does not permit the assumption of a stable environment any longer. And ,due to the sine, even small offsets lead to an unacceptable error in asymmetric measurements. As the crystal lattice spacing comparison (see section 5.4) requires strong asymmetric measurements, a detailed understanding of the system is indispensable.

To describe the system in full detail without the need for too many indices in simple or general cases, a dynamic index structure is appropriate. Any variable Y can have the following combination of indices:

Y Without index the variable is used for general theory and may apply to any axis at any time.

Y_X One lower index X is the name of the axis, "A" or "B" (see section 2.1).

$Y^{(H)}$ A high index in brackets may be combined with any of the options above. If H is a number or a running index (italic letter), it indicates at which time a quantity was acquired or valid. If H is a naming index (upright letter), it indicates the data processing that has already applied to this quantity, i.e., "M" for a measured value, or "S" for a value already corrected to standard conditions in terms of temperature, pressure and humidity.

The variables are:

Φ_X The angle between interferometer lever arm and interferometer virtual zero ($\Phi_X = 0°$ when the arm is perpendicular to the laser). This zero can be different for each interferometer as long as it is stable. It will be part of the offset ϑ in (2.9). The actual instrument the zeros of both axes agree within $2''$.

ϑ_X The angle between the normal of the crystal diffraction planes and the interferometer lever arm. After mounting once, this angle must stay stable throughout the experiment (at least there must not be any non-linear drift during a four-pack). The value of this angle is not known.

φ_X The angle between crystal diffraction planes and interferometer virtual zero. This is the relevant angle as it permits to calculate the angle between the two crystals.

θ_X The Bragg angle between crystal diffraction planes and γ-beam. Incident and reflected beam are considered to be symmetric.

F_X The interferometer readout of the axis X at the reflex in m-th Bragg order.

$F_{X,0}$ The interferometer readout where $\Phi_X = 0$.
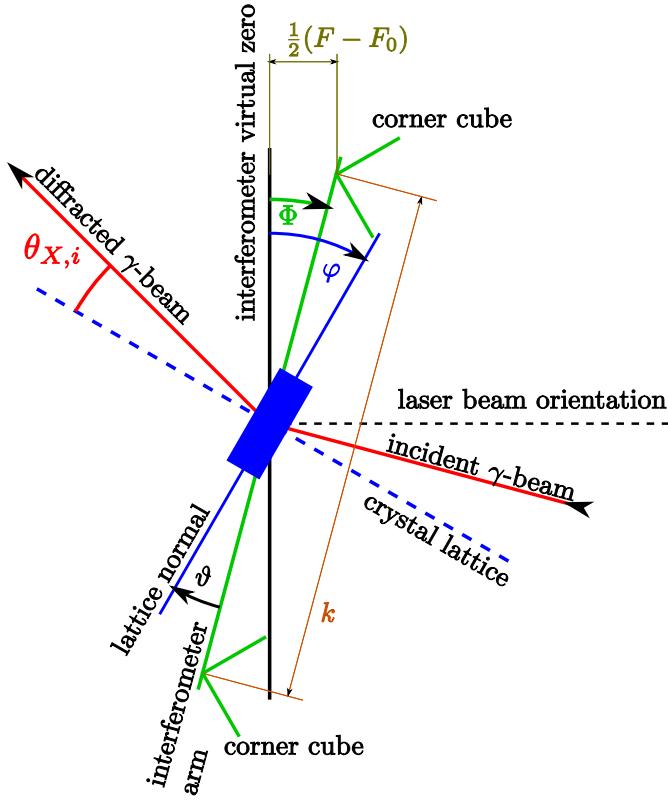
Figure 2.11: Variables used to describe the spectrometer. Each variable exists for A- and B-axis. Note that angles are measured clockwise. For the orientation of the Bragg angle θ_X see Figure 2.12. Both interferometers may have their individual orientation as long as these stay stable. They are accounted within ϑ_X.

K_X The calibration constant; it is the interferometer lever arm length in units of the laser wavelength.

From these definitions the relations:

$$\Phi_A = \varphi_A - \vartheta_A$$
$$\Phi_B = \varphi_B - \vartheta_B \tag{2.4}$$

follow directly.

As the acquisition is taken on varying the B-crystal angle and λ needs to be deduced from the difference of Bragg angles, it is best to resolve the equations in the form $\lambda(F_B)$. As the difference has to be calculated of angles and not of fringes, equations (2.2) and (2.4) are combined; solving to φ yields:

$$\varphi_X = \arcsin\left(\frac{F_X - F_{X,0}}{K_X}\right) + \vartheta_X \ . \tag{2.5}$$

The γ-beam arriving at the B-crystal has already been diffracted by the A-crystal. Therefore the Bragg condition at the A-crystal and its orientation define the orientation of the
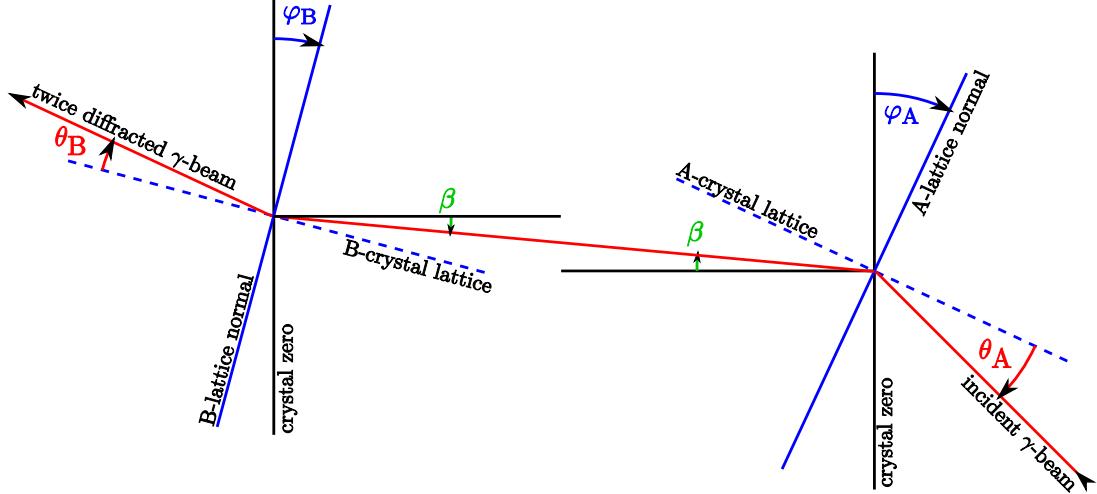
Figure 2.12: Angle relation between A- and B-axis. The first Bragg angle θ_A is assumed to be known. For its absolute value this is only roughly true, but its variations within a 4-pack are small and can be calculated precisely. The interferometers deliver the angles Φ_X. The angles φ_X can be deduced from (2.4). Hence the angle β between once diffracted γ-beam and the spectrometer symmetry line calculates as $\beta = \varphi_A - \theta_A$. This is furthermore the incident angle for the B-axis. The Bragg angle θ_B for the B-crystal can be calculated as $\theta_B = \varphi_B - \beta$. Note that the equations and the sign of the angles remain valid with a negative Bragg angle in a hence negative Bragg order. Note as well, that β has for the evaluation no meaning and was introduced for easier understanding only. The crystal zero needs to the same for both axes. But as it is an arbitrary orientation, this is without loss of generality.

γ-beam incident on the B-crystal. Together with the angle φ_B of the B-crystal at which the Bragg peak is be observed one can calculate the Bragg angle θ_B as seen in Figure 2.12:

$$\theta_B^{(i)} = \varphi_B^{(i)} - \varphi_A^{(i)} + \theta_A^{(i)} \ . \tag{2.6}$$

If this knowledge is added to the Bragg condition at the B-crystal, one obtains after solving to λ:

$$\lambda^{(i)} = \frac{2d_B^{(i)} \sin(\theta_B^{(i)})}{m_B^{(i)}} \tag{2.7}$$

$$= \frac{2d_B^{(i)} \sin((\Phi_B^{(i)} + \vartheta_B) - (\Phi_A^{(i)} + \vartheta_A) + \theta_A^{(i)})}{m_B^{(i)}} \ . \tag{2.8}$$

The expression contains the angles ϑ_B and ϑ_A between axis and crystal. These angles are not known, therefore $\lambda^{(i)}$ cannot be derived from a single diffraction order. But these angles can be assumed to be stable as shown in chapter 3. Hence a measurement of two

different Bragg orders that is done in a 4-pack provides all necessary information. But even then the individual angle offsets stay unknown, only the combination

$$\vartheta = \vartheta_{\mathrm{B}} - \vartheta_{\mathrm{A}} \tag{2.9}$$

can be obtained. This is no problem as the individual offsets are of no interest.

2.2.1 General solution

To solve the problem of the unknown crystal offset angles, one measures the Bragg angles for different diffraction orders. These measurements are numbered with i. In the following is described how to evaluate a measurement of two different orders. If data from more orders is available, they should be grouped by two and the results merged at the end. Alternatively such multi-order measurements might by used for non-linearity-test as described in section 2.3.2.The measurement variables are indexed with (1) and (2), and observed the Baragg orders (a, b_1) and (a, b_2), respectively. For each measurement, equation (2.8) is valid:

$$\lambda^{(i)} = \frac{2d_{\mathrm{B}}^{(1)} \sin(\Phi_{\mathrm{B}}^{(1)} - \Phi_{\mathrm{A}}^{(1)} + \vartheta + \theta_{\mathrm{A}}^{(1)})}{b_1} \tag{2.10}$$

$$\lambda^{(i)} = \frac{2d_{\mathrm{B}}^{(2)} \sin(\Phi_{\mathrm{B}}^{(2)} - \Phi_{\mathrm{A}}^{(2)} + \vartheta + \theta_{\mathrm{A}}^{(2)})}{b_2} \ . \tag{2.11}$$

The evaluation consists of determining ϑ such that all $\lambda^{(i)}$ become equal.

It should be mentioned here, that this section gives a general solution to obtain a wavelength value from the measurement of two arbitrary Bragg orders. However, as will be seen below, this method is not convenient for data evaluation. Hence limiting the experimental set-up to symmetric orders $b_1 = -b_2$ and doing an additional offset measurement described in Section 2.2.2 on page 76 is the recommended method. The simplified data treatment is described in the next section. For the rare cases were such measurements are not possible the general solution is given here.

After solving both equations to ϑ they can be equalised.

$$\arcsin \frac{\lambda \cdot b_1}{2d_{\mathrm{B}}^{(1)}} - \arcsin \frac{\lambda \cdot b_2}{2d_{\mathrm{B}}^{(2)}} = \Phi_{\mathrm{B}}^{(1)} - \Phi_{\mathrm{B}}^{(2)} - \Phi_{\mathrm{A}}^{(1)} + \Phi_{\mathrm{A}}^{(2)} + \theta_{\mathrm{A}}^{(1)} - \theta_{\mathrm{A}}^{(2)} \ . \tag{2.12}$$

Note that all variables hardly change between the two measurements, only Φ_{B} and the B-Bragg order change largely.

With the substitutions

$$U = \frac{\lambda \cdot b_1}{2d_{\mathrm{B}}^{(1)}} \ , \tag{2.13}$$

$$v = -\frac{b_2}{b_1} \frac{d_{\mathrm{B}}^{(1)}}{d_{\mathrm{B}}^{(2)}} \ , \tag{2.14}$$

$$W = \sin\left(\Phi_{\mathrm{B}}^{(1)} - \Phi_{\mathrm{B}}^{(2)} - \Phi_{\mathrm{A}}^{(1)} + \Phi_{\mathrm{A}}^{(2)} + \theta_{\mathrm{A}}^{(1)} - \theta_{\mathrm{A}}^{(2)}\right) \ ,$$

the equation is of the form:

$$\arcsin U + \arcsin(v \cdot U) = \arcsin W \ . \tag{2.15}$$

As all variables are well within the interval $\left]-\frac{\pi}{2}, +\frac{\pi}{2}\right[$ this has the same solutions as:

$$U\sqrt{1 - V^2} + V\sqrt{1 - U^2} = W \ . \tag{2.16}$$

The equation has four solutions for U, where only the following solves the physical problem:

$$U = W\sqrt{\frac{1 + v^2 - (2\sqrt{v^2 + v^2 W^2})}{1 - 2v^2 + v^4 - 4v^2 W^2}} \ . \tag{2.17}$$

Thus equation (2.12) seems to be solvable to λ. However, the term $\theta_{\mathrm{A}}^{(1)} - \theta_{\mathrm{A}}^{(2)}$ depends on λ:

$$\delta\theta_{\mathrm{A}} = \theta_{\mathrm{A}}^{(1)} - \theta_{\mathrm{A}}^{(2)} = \arcsin\frac{a \cdot \lambda}{2d_{\mathrm{A}}^{(1)}} - \arcsin\frac{a \cdot \lambda}{2d_{\mathrm{A}}^{(2)}} \ . \tag{2.18}$$

The changes of the lattice constant of the A-crystal are small during a 4-pack. The coefficient of thermal expansion (CTE) of silicon is $\alpha = 2.6 \times 10^{-6}$ /K and changes in temperature are usually smaller than $\delta T \lesssim 0.01$ K. With $d_{\mathrm{A}}^{(2)} = d_{\mathrm{A}}^{(1)} \cdot \alpha \cdot \delta T$ follows that $\delta\theta_{\mathrm{A}} \approx \theta_{\mathrm{A}} \cdot \alpha \cdot \delta T$. Its influence on the relative change δ_{r} of λ can be roughly estimated by linearising the arcsine in (2.12):

$$\delta_{\mathrm{r}}(\lambda) \approx \frac{1}{\Phi_B^{(1)} - \Phi_B^{(2)}} \cdot \theta_{\mathrm{A}} \cdot \alpha \cdot \delta T \ . \tag{2.19}$$

As $\frac{\theta_{\mathrm{A}}}{\Phi_B^{(1)} - \Phi_B^{(2)}}$ is in the order of one this means that even when using $\delta\theta_{\mathrm{A}} = 0$ for the evaluation of λ despite having a huge temperature change of 1 K, the relative error will be smaller than $2.6 \cdot 10^{-6}$. Fortunately $\delta\theta_{\mathrm{A}}$ is depending on λ only very weakly for all possible configurations at *Gams*. This rough value obtained for λ is then used to calculate $\delta\theta_{\mathrm{A}}$, then λ is calculated again. After one iteration the obtained relative error is below 10^{-11}.

2.2.2 Environmental corrections

Neither the recursive calculation with $\delta\theta_{\mathrm{A}}$, nor the complicated equation (2.17) is convenient for data evaluation. Furthermore a fundamental problem is not solved. In subsection 2.2.1 it is assumed that all angle information is given as single values. However, the interferometer output describes only a rocking curve, from which a fringe or angle value must be obtained by parameter estimation i.e. a fit. If there was some change in the environmental parameters within the rocking curve acquisition the theoretical rocking curve will not describe the data any more. This leads in the best case to a larger uncertainty of the fit, but it can also result in a biased fit.

Hence it is much better to correct the data to standard conditions *before* the fitting is performed. Additionally the angle information obtained by the fit correspond all to the same standard conditions. Therefore the lattice parameters d_{B} and d_{A} in equations (2.12) and (2.18) do not vary any more and simplify the data evaluation a lot.

It should be mentioned that it is not necessary to correct to general standard condition (like vacuum and $0\,°\mathrm{C}$) immediately, but preferably to some average condition at *Gams* during the measurement. Hence the correction will be as small as possible and uncertainties in the correction coefficients do not harm the data. In this work a temperature of $T = 22.5\,°\mathrm{C}$, a pressure of $p = 760\,\mathrm{Torr} = 1023.5\,\mathrm{hPa}^{\dagger}$ and a relative humidity of $h = 40\%$ are used as reference conditions. The transfer to general standard conditions (in silicon lattice spacing metrology: $22.5\,°\mathrm{C}$ and vacuum) should be done after the fusion of all data measured at *Gams*.

In this section the corrections for each parameter will be explained individually, as if in a thought experiment where only this single parameter is affected by changes of environmental conditions. This is valid, as all corrections are independent if applied in correct order.

Laser wavelength

The laser measuring the axis-angle runs through air and is therefore sensitive to the index of refraction η. The refractive index changes the speed of light c, and as the laser has a

---

†*Gams4* uses Torr as unit for air pressure from the measurement process to the data evaluation. This is followed in this work for compatibility with old data evaluation algorithms. The upcoming *Gams6* will operate in vacuum, hence a different pressure gauge will be used and the problem will not persist. 1 Torr $= (101\,325/760)\,\mathrm{Pa}$.

stabilized frequency ν it changes the wavelength of the laser λ_{L}.

$$c^{(\mathrm{M})} = c^{(\mathrm{S})} \frac{\eta^{(S)}}{\eta^{(M)}} \tag{2.20}$$

$$\nu \cdot \lambda_{\mathrm{L}} = c \tag{2.21}$$

$$\Rightarrow \lambda_{\mathrm{L}}^{(\mathrm{M})} = \lambda_{\mathrm{L}}^{(\mathrm{S})} \frac{\eta^{(S)}}{\eta^{(M)}} \ . \tag{2.22}$$

The interferometer readout measures the distance of the laser path in units of the wavelength. The entire interferometer is exposed to air. However all laser paths are affected the same way by atmospheric changes. Hence only the asymmetric path must be considered for corrections. The interferometer is build such that the laser path have equal length in the 0° position which is when the connection line of the corner-cube centres is perpendicular to the laser beam. The path length difference l which is measured by the interferometer does not change in function of the refractive index, hence the transformation from wavelength to absolute fringes is valid in both situations, "S" standard conditions and "M" measurement conditions:

$$F^{(\mathrm{S})} - F_0 = \frac{l}{\lambda_{\mathrm{L}}^{(\mathrm{S})}} \quad , \quad F^{(\mathrm{M})} - F_0 = \frac{l}{\lambda_{\mathrm{L}}^{(\mathrm{M})}} \ . \tag{2.23}$$

The combination of equations (2.22) and (2.23) yields:

$$F^{(\mathrm{S})} = \frac{\eta^{(\mathrm{S})}}{\eta^{(\mathrm{M})}} \left(F^{(\mathrm{M})} - F_0 \right) + F_0 \ . \tag{2.24}$$

This means if the interferometer read outs which are obtained from measurement $F^{(\mathrm{M})}$, are replaced by the one corrected to standard condition $F^{(\mathrm{S})}$, these data can be evaluated as if the measurement had been conducted at standard conditions.

Refractive index of air   The index of refraction η which is needed for the correction depends on temperature, pressure, and gas composition. Apart from the humidity, the air composition is regarded as stable on *Gams*. The index of refraction can be calculated by the updated Edlén equation [BD93; BD94]:

$$\eta(T, p, h) = 1 + A \cdot B - C \ , \tag{2.25}$$

with

$$A = \frac{1 + p/\mathrm{Torr} \times (0.801\,27 - 0.012\,959 \cdot T/°\mathrm{C}) \times 10^{-6}}{1 + 0.003\,6610 \cdot T/°\mathrm{C}} \ , \tag{2.26}$$

$$B = \frac{p/\mathrm{Torr} \times \left(\eta^{(\mathrm{R})} - 1 \right)}{720.7770} \ , \tag{2.27}$$

$$C = h_{\mathrm{abs}}/\mathrm{Torr} \times \left(4.9789 - 0.0535 \left(\sigma/\mathrm{\mu m}^{-1} \right)^2 \right) \times 10^{-8} \ . \tag{2.28}$$

T denotes the temperature, p the pressure and h_{abs} the partial pressure of water vapour. The index of refraction of standard air on which these equations are based is measured at the reference conditions "R" , which are $15\,°\mathrm{C}$ and $1013.25\,\mathrm{hPa} = 760\,\mathrm{Torr}$. It can be calculated as:

$$
\begin{aligned}
\left(\eta^{(\mathrm{R})} - 1\right) \times 10^8 = & \, 8342.54 \\
& + 2\,406\,147 \left(130 - \left(\sigma/\mu\mathrm{m}^{-1}\right)^2\right)^{-1} \\
& + 15\,998 \left(38.9 - \left(\sigma/\mu\mathrm{m}^{-1}\right)^2\right)^{-1} .
\end{aligned}
$$

where $\sigma = 1/\lambda_{\mathrm{L}}$ is the inverse laser wavelength in vacuum. At *Gams* lasers with $\lambda_{\mathrm{L}} = 0.632\,99\,\mu\mathrm{m}$ are in use.

As the humidity sensor delivers the relative humidity h it must be converted to the partial pressure. In former *Gams* data evaluations this was done by:

$$ h_{\mathrm{abs}} = h \cdot 20.1072\,\mathrm{Torr} , \tag{2.29} $$

which is correct for a temperature of $22.5\,°\mathrm{C}$. To adapt this for the actual temperature a second degree polynomial was fitted to some data of equilibrium vapour pressure of water from [Wea71] in the range of 14–$24\,°\mathrm{C}$. That yielded the expression

$$ h_{\mathrm{abs}} = h \left(10.33 - 0.372 \cdot T/°\mathrm{C} + 0.0363 \times (T/°\mathrm{C})^2\right)\,\mathrm{Torr} . \tag{2.30} $$

Calibration constant

The interferometer measures the rotation of the axis by measuring a projection of the corner-cube movement, and calculating the angle using the arcsine function. However, if the distance between the two corner cubes changes the interferometer read out will change as well, unless $\Phi = 0°$. The expansion of the goniometer arm, that is supporting the two corner cubes and thus is responsible for the distance of those, is linearly depending on the temperature. And so is the calibration constant:

$$ K^{(\mathrm{M})} = (1 + \alpha \cdot T)K^{(\mathrm{S})} . \tag{2.31} $$

The material has a low CTE of $\alpha \approx 10^{-7}/\mathrm{K}$. Assuming that between two measurements only K has changed, then the angle of the axis at which the Bragg reflex has been observed must be the same:

$$ \Phi^{(\mathrm{S})} = \Phi^{(\mathrm{M})} \tag{2.32} $$

$$ \arcsin \frac{F^{(\mathrm{S})} - F_0}{K^{(\mathrm{S})}} = \arcsin \frac{F^{(\mathrm{M})} - F_0}{K^{(\mathrm{M})}} \tag{2.33} $$

$$ \Rightarrow F^{(\mathrm{S})} = (F^{(\mathrm{M})} - F_0) \cdot \frac{K^{(\mathrm{S})}}{K^{(\mathrm{M})}} + F_0 . \tag{2.34} $$

This correction has to be applied to both axes and after the corresponding fringe number has been corrected for the refractive index of air.

A-axis mispositioning

The data evaluation implies that a theoretical rocking curve is fitted to the experimental data. This requires that one crystal ("B") is scanned while the other ("A") stays at a fixed position. If within a scan the A-crystal moves the fit would not work any more, so the position data of the B-crystal must be corrected. This means if the A-crystal is misplaced by an angle $\delta\varphi$, the position data of the B-crystal must be modified by this angle. It is important to note that this correction applies linear in angles, but not linear in fringes.

If the corrections to interferometer read out and calibration constant that were explained in the previous two sections are applied to the A-axis, the following situation arises: the corrected A-axis position $F_A^{(S)}$ is not fix throughout a scan. But also mispositioning due to a failure of the electronics may require such a correction.
In any case we obtain different (pre-corrected) interferometer read outs $F_A^{(M)}$ for the scan points, while we want them all to be a fixed value $F_A^{(S)}$. The B-axis readout should be adapted to compensate for these variations.

This can be done, as an experiment at any conditions should always lead to the same value of the γ-wavelength λ. So one can write following (2.8):

$$\lambda^{(S)} = \lambda^{(M)} \tag{2.35}$$

$$\frac{2d_B \sin(\Phi_B^{(S)} - \Phi_A^{(S)} + \vartheta + \theta_A)}{m_B} = \frac{2d_B \sin(\Phi_B^{(M)} - \Phi_A^{(M)} + \vartheta + \theta_A)}{m_B} \tag{2.36}$$

$$\Phi_B^{(S)} - \Phi_A^{(S)} = \Phi_B^{(M)} - \Phi_A^{(M)} \tag{2.37}$$

and thus together with (2.5):

$$\frac{F_B^{(S)} - F_{B,0}}{K_B} = \sin\left(\arcsin\frac{F_B^{(M)} - F_{B,0}}{K_B} + \arcsin\frac{F_A^{(S)} - F_{A,0}}{K_A} - \arcsin\frac{F_A^{(M)} - F_{A,0}}{K_A}\right) . \tag{2.38}$$

For K_A and K_B one should use standard condition values, as also $F_A^{(M)}$ and $F_B^{(M)}$ are corrected to standard conditions for calibration constant and index of refraction. $F_A^{(S)}$ can be chosen freely, as long as it is the same for all data within a 4-pack. In practice, one will use the set-point value. If this is not available, an average value of $F_A^{(M)}$ can be used.

A-crystal lattice spacing

Due to a temperature variation the crystal lattice spacing may change and consequently the Bragg angle. If this happens within a 4-pack the data must be corrected for this. Fortunately the lattice changes of A- and B-crystal can be treated independently. First the A-crystal is analysed. Similar to the A-axis mispositioning in the previous subsection, one can assume that two experiments at different conditions must deliver the same γ-wavelength, thus:

$$\frac{2d_B \sin(\Phi_B^{(S)} + \vartheta - \Phi_A + \theta_A^{(S)})}{m_B} = \frac{2d_B \sin(\Phi_B^{(M)} + \vartheta - \Phi_A + \theta_A^{(M)})}{m_B} \tag{2.39}$$

$$\Phi_B^{(S)} + \theta_A^{(S)} = \Phi_B^{(M)} + \theta_A^{(M)} \tag{2.40}$$

$$F_B^{(S)} = F_{B,0} + K_B \cdot \sin\left(\arcsin\frac{F_B^{(M)} - F_{B,0}}{K_B} + \arcsin\frac{m_A\lambda}{2d_A^{(M)}} - \arcsin\frac{m_A\lambda}{2d_A^{(S)}}\right) , \tag{2.41}$$

where the lattice constant changes with temperature $T^{(M)}$ as:

$$d^{(M)} = d^{(S)} \cdot (1 + \alpha \cdot \delta T) \tag{2.42}$$

$$\text{with } \delta T = T^{(M)} - T^{(S)} \tag{2.43}$$

The lattice spacing is also influenced by the atmospheric pressure. However this influence is so small that any changes during the measurement (due to weather) are not significant. Only for comparison with measurements performed in vacuum a correction has to be applied. See equation (3.1) for details.

B-crystal lattice spacing

The B-lattice spacing may change because of temperature variations. Due to the algebraic structure the correction is a bit more laborious. Starting from equation (2.8):

$$\frac{2d_B^{(S)} \sin(\Phi_B^{(S)} + \vartheta - \Phi_A + \theta_A)}{m_B} = \frac{2d_B^{(M)} \sin(\Phi_B^{(M)} + \vartheta - \Phi_A + \theta_A)}{m_B} \tag{2.44}$$

and using the abbreviation

$$\xi = -\Phi_A + \theta_A + \vartheta \tag{2.45}$$

we find

$$\arcsin\frac{F_B^{(S)} - F_{B,0}}{K_B} = \arcsin\left(\frac{d_B^{(M)}}{d_B^{(S)}} \sin\left(\arcsin\frac{F_B^{(M)} - F_{B,0}}{K_B} + \xi\right)\right) - \xi , \tag{2.46}$$

where $d_{\mathrm{B}}^{(\mathrm{M})}/d_{\mathrm{B}}^{(\mathrm{S})}$ is calculated from (2.42). ξ contains ϑ, the difference of the angle offsets of the crystals towards the goniometer arm. This is a priori unknown, but can be determined in a separate measurement. Without dismounting the crystals one has to acquire an extra 4-pack – preferably of a high intense γ-line with a low energy and thus a high reflectivity and large Bragg angles which means high sensitivity. Consequently this 4-pack can be measured very quickly. Therefore the environmental conditions will not change during the measurement – no correction is necessary and $\Phi_{\mathrm{A}}^{(1)} \cong \Phi_{\mathrm{A}}^{(2)}$ as well as $\theta_{\mathrm{A}}^{(1)} \cong \theta_{\mathrm{A}}^{(2)}$. If one chooses additionally $b_1 = -b_2$, (2.10) and (2.11) can be solved easily to ϑ:

$$\vartheta = -\frac{\Phi_{\mathrm{B}}^{(1)} + \Phi_{\mathrm{B}}^{(2)}}{2} + \Phi_{\mathrm{A}}^{(1)} - \theta_{\mathrm{A}}^{(1)} \;. \tag{2.47}$$

γ-wavelength calculation

The raw data obtained from γ-wavelength measurement must be corrected stepwise as was described in this section:

1. First the interferometer readout $F^{(\mathrm{M})}$ must be corrected for changes in the refractive index of air for both axes independently.

2. Then these modified values are uses as input data for the corrections for changes of the calibration constant. This has to be done for both axes independently, too.

3. Then the corrections of both axes are combined, so that the mispositioning of the A-axis is compensated by modifying the B-axis readout.

4. Now the A-crystal lattice spacing corrections are applied.

5. The B-crystal lattice spacing correction results in the final data.

It should be emphasized that all these corrections must be applied to each data point of all scans. The reference weather parameters, referenced as standard conditions can be chosen freely, but at least for an entire 4-pack they must be the same. For convenience they stay fixed for a whole measurement campaign. Practically they were never changed during the lifetime of the instrument. It is valid to apply this stepwise procedure, as none of the steps uses any observables which was not corrected previously. Accordingly any observable that appears in a expression and is not subject of the actual correction must be used in standard conditions.

Now the corrected B-axis interferometer readout can be fitted to the theoretical rocking curve. It should be noted that the line shape calculations bases on the linearised equation (2.3). This can be used without modification if there are no offsets. However, the fit

should account for any non-negligible offset in F_0 or ϑ (see crystal lattice comparison in section 5.4). At an offset of $\vartheta = 0.14\,\text{rad}$ the peak width will change by 1%. Any higher order like quadratic a distortion of the peak shape is below 10^{-8} and thus not important for any known applications at *Gams*.

With the estimated peak positions a simple evaluation following subsection 2.2.1 can be done while using all parameters at standard conditions. If the 4-pack is measured symmetric on the B-crystal (i.e. $b_1 = -b_2$), equation (2.12) simplifies to

$$2\arcsin\frac{\lambda b_1}{2d_{\text{B}}} = \Phi_{\text{B},b_1} - \Phi_{\text{B},b_2} \ , \tag{2.48}$$

as $\Phi_{\text{A},b_1} = \Phi_{\text{A},b_2}$ and $\theta_{\text{A},b_1} = \theta_{\text{A},b_2}$ at standard conditions.

2.3   Instrument calibration

The *Gams* facility can deliver absolute gamma ray wavelength measurements. It requires only one input parameter: the crystal lattice spacing. All other parameters (e.g. laser wavelength, corner-cube distance) can be derived from a self-calibration. This only requires the stability of these parameters throughout the whole measurement and calibration process. This calibration is crucial as some parameters cannot be accessed with the required relative accuracy of 10^{-8} by any other means. For example, the corner-cube distance can be measured with a coordinate measurement machine with a relative accuracy of 10^{-6} only. In the past, a lot of effort has been made to analyse the change of the calibration constant and to relate it to external conditions (temperature, humidity, and pressure) [Dew+06]. Despite the fact that this calibration procedure has existed for already 30 years and has been described in several publications [Kes+01; Kes+94; Dew+06], no information about the uncertainty of this procedure is published, and more seriously, there are wrong rumours about the theoretically possible accuracy. Therefore, a detailed description and mathematical analysis of the calibration is given in this section. Furthermore, new results about the systematic uncertainty of the experimental set-up are revealed. The experimental results of an actual calibration are presented in section 3.2.

2.3.1   Description of the procedure

Due to the transformation from angle position Φ to linear displacement, the interferometer readout F (measured in fringes: f_4, f_5, or f_6 depending on the instrument) needs to be calibrated to a reference angle using equation (2.2) which is after simplification:

$$F = K\sin\Phi \ . \tag{2.49}$$

The calibration constant K can be deduced roughly from the interferometer lever arm length, but on the desired level of precision it is a priori unknown.

A 24-sided polygon folds the well defined angle of 360° to the reachable 15°-range of the interferometer. Following the procedure explained in Figure 2.13 one obtains 24 pairs of readouts (F_i^+, F_i^-). Each pair corresponds to an angle difference. Knowing that these angle differences must sum up to 360°:

$$\sum_{i=1}^{24} \left(\Phi_i^+ - \Phi_i^- \right) = 2\pi, \qquad (2.50)$$

one can obtain K by solving the equation:

$$\sum_{i=1}^{24} \left(\arcsin \frac{F_i^+}{K} - \arcsin \frac{F_i^-}{K} \right) = 2\pi. \qquad (2.51)$$

This procedure is called a full symmetric calibration. Additionally, by calibrating asymmetrically information about non-linearity can be obtained (see subsection 2.3.3).

Polygon stability

In the measurement campaign 1997-2000 [Dew+06], a big effort had been made to do multiple instrument calibrations over a large time interval. The idea was to investigate the dependence of the calibration function on environmental parameters. However, one single full calibration takes about 12 hours. This does not only consume a lot of time, which is then not available for γ-wavelength measurements any more, but also has the disadvantage that fluctuations on shorter time scales will be hidden or even disturb the measurement significantly.

However, it is not necessary to do a full calibration (360° turn of the polygon, including the measurement of all 24 angles between all adjacent mirrors). The measurement of only one angle between two adjacent mirrors provides the same stability information. On *Gams4* such a measurement takes 21 minutes plus a lead time of 12 minutes, resulting in a possible repetition rate of about 33 minutes. Such a short measurement can be performed much more often. However, now the stability of one polygon angle has to be assumed. When comparing full calibrations this is theoretically not required, as the sum of the angles will always be 360°. But even here the polygon angles must not change during each full calibration process.

The polygon is made out of Zerodur® providing a CTE of $|\alpha| \leq 10^{-8}/$K. The material is a mixture of amorphous and crystalline glass. There is no information about the anisotropy of the thermal expansion. Therefore, the worst case is assumed. Following
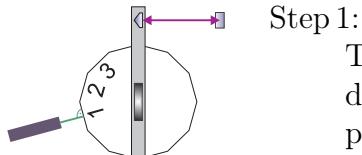
Step 1:

> The autocollimator verifies that polygon surface 1 is perpendicular to it. At this time the interferometer measures the position of the arm.
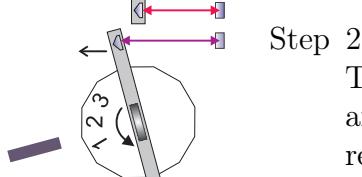
Step 2:

> The polygon rotates to the next surface with the goniometer arm is rigidly fixed. The passing fringes of the interferometer read-out must be counted.
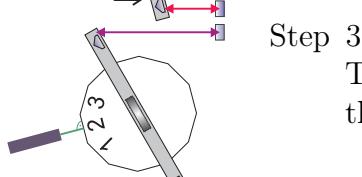
Step 3:

> The autocollimator verifies surface 2 to be perpendicular after the polygon rotation. Interferometer measures position again.
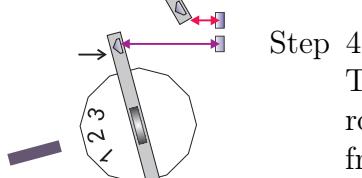
Step 4:

> The Connection between arm and polygon is loose. The arm rotates back while the polygon stays in position. The passing fringes are uninteresting for the symmetric calibration. Yet, they are counted in order not to lose the interferometer offset F_0.
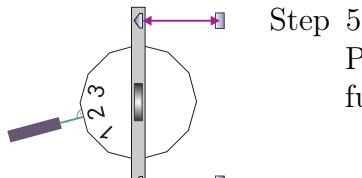
Step 5 (=Step 1):

> Polygon and arm are coupled again. Repeat from step 1 for a full revolution until surface 1 is reached again.

Figure 2.13: Full symmetric calibration of the goniometer, using polygon and autocollimator.
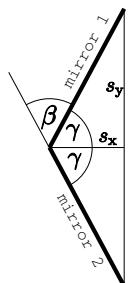
Figure 2.14: Polygon – thermal deformation: the angle β between two mirror surfaces is given by $\beta = 180° - 2\gamma$ and $\tan\gamma = \frac{s_y}{s_x}$. In the case of a 24-sided regular polygon one finds the initial length ratio $\frac{s_{y,0}}{s_{x,0}} = \frac{1}{\tan(360°/24/2)}$. Considering the worst case anisotropy of the CTE α: $s_x = s_{x,0} \times (1 - \alpha\,\Delta T)$, $s_y = s_{y,0} \times (1 + \alpha\,\Delta T)$, one obtains for a temperature change ΔT the change of the angle between the mirrors $\Delta\beta \approx -0.52\,\alpha\,\Delta T + 0.5\,(\alpha\,\Delta T)^2 + O\,[\alpha\,\Delta T]^3$.

the equations of Figure 2.14 the temperature must be stable to $|\Delta T| \leq \frac{|\Delta_r\beta|}{0.52\alpha}$ where $\Delta_r\beta$ is the desired relative uncertainty. The temperature ranges given in table 2.1 show that this effect currently does not affect the experiment. However it must be considered in a measurement of the disintegration energy of positronium (see section 6.2).

Desired rel. uncertainty	necessary temperature stability	comment
$4 \cdot 10^{-7}$	70 K	*Gams4* accuracy
$2 \cdot 10^{-8}$	3.6 K	target accuracy for $N_A h$ with *Gams6*
$4 \cdot 10^{-9}$	0.7 K	desired accuracy with positronium

Table 2.1: Necessary temperature stabilities to avoid polygon deformation. Down to a relative uncertainty of $2 \cdot 10^{-8}$, a single polygon angle can be used to compare calibration values over a range of several Kelvin.

Autocollimator response function

A description of the autocollimator which is used to measure the polygon position is given in [LDT84]. This publication states a resolution of some 100 microarcseconds or better. Measurements on *Gams4* confirmed a resolution of about 200 microarcseconds. However, some previously unknown systematic effects influencing stability and accuracy were found. They are described in subsection 3.2.1 and section A.3.

2.3.2   Calibration theory

Determination of the calibration constant K   The 24 angles of the polygon are measured with the interferometer in symmetric mode. Symmetric means that one surface is measured at roughly $+7.5°$, the other surface at -7.5°, resulting in F^+ and F^- respectively. So the 24 symmetric angle measurements result in 24 pairs of interferometer read-outs $\left(F_{S,i}^+; F_{S,i}^-\right)$. Hence, now all the external angles of the polygon are known in units of the interferometer. As the sum of these angles is 360° the conversion from interferometer fringes to absolute angles can be deduced.

When replacing (2.49) with the full interferometer equation (2.2):

$$F = F_0 + K \sin \Phi$$

then equation (2.51) changes to:

$$\sum_{i=1}^{24} \left(\arcsin \frac{F_{S,i}^+ - F_0}{K} - \arcsin \frac{F_{S,i}^- - F_0}{K} \right) = 2\pi \ . \tag{2.52}$$

This equation must be solved for K. For all possibly occurring values there is only one physically reasonable solution. Due to the arcsine the equation can be solved numerically only, but, using the corner-cube distance as a starting value, this is not a problem.

However, F_0 is unknown at this time and should be assumed to be 0 in this first iteration.

Error estimation   The fringe numbers indicating the polygon surfaces are error-prone: the autocollimator has a limited resolution ($0.0025\,\mathrm{f_4}$), which is surpassed by instability of *Gams4* ($0.07\,\mathrm{f_4}$). The individual uncertainties are known. Their contribution to K can be estimated by linearising equation (2.52) with

$$\arcsin x = x \ . \tag{2.53}$$

When resolved for K this yields:

$$K = \frac{\sum_{i=1}^{24} \left(F_{\mathrm{S},i}^+ - F_{\mathrm{S},i}^- \right)}{2\pi} \ , \tag{2.54}$$

and thus:

$$\Delta K = \frac{1}{2\pi} \sqrt{ \sum_{i=1}^{24} \left(\Delta F_{\mathrm{S},i}^+ \right)^2 + \sum_{i=1}^{24} \left(\Delta F_{\mathrm{S},i}^- \right)^2 } \ , \tag{2.55}$$

or, if one assumes all fringe errors to be the same ΔF_{S}:

$$\Delta K = \frac{1}{2\pi} \sqrt{48} \Delta F_{\mathrm{S}} \ . \tag{2.56}$$

A similar analysis is done in [Est98], where the uncertainty is described to be smaller. However, this applies only to one angle of the polygon, thus in the present case an angle of 15°. However, in the present case the calibration constant K must refer to the full rotation of 360°. Hence, both analyses are in agreement.

Determine interferometer offset F_0   One of the polygon angles is measured several times at different offset angles. The polygon mechanics allows steps of 1° and a maximal shift of ±6°. Thus a single polygon angle can be measured in 13 different interferometer positions. Roughly $(13.5°; -1.5°)$, $(12.5°; -2.5°)$, $(11.5°; -3.5°)$, ..., $(1.5°; -13.5°)$. This results in 13 pairs of interferometer readouts $\left(F_{\mathrm{A},j}^+; F_{\mathrm{A},j}^- \right)$. All of these pairs represent the same, but unknown angle. The calculation of this angle from each pair is:

$$\Psi_j = \arcsin \frac{F_{\mathrm{A},j}^+ - F_0}{K} - \arcsin \frac{F_{\mathrm{A},j}^- - F_0}{K} \ . \tag{2.57}$$

The values Ψ_j depend strongly on F_0.

An average $\overline{\Psi}$ can be defined as:

$$\overline{\Psi} = 1/13 \cdot \sum_{j=1}^{13} \Psi_j \ . \tag{2.58}$$

Then, similar to a least squares fit, one varies F_0 until the sum of the squares of the residuals reaches a minimum:

$$\chi^2(F_0) = \sum_{j=1}^{13} \frac{\left(\overline{\Psi} - \Psi_j\right)^2}{\left(\Delta\Psi_j\right)^2} \ . \tag{2.59}$$

The value of K which has been obtained by the previous calculation from the symmetric mode should be used in this calculation.

Error estimation   The uncertainty ΔF_0 is determined by:

$$\chi^2(F_0) + 1 = \chi^2(F_0 + \Delta F_0) \ , \tag{2.60}$$

where $\chi^2(F_0)$ is the minimal χ^2 obtained above. There are two solutions, but their absolute value is the same, due to the parabolic shape of χ^2. To cope with the instability of the instrument, the errors of the individual interferometer read outs must be increased so that $\chi^2/(N-1) = 1$. This is done by multiplying ΔF_0 with $\sqrt{\chi^2(F_0)}$

Alternatively or additionally to this asymmetric polygon method, multiple Bragg-angles can be measured. When an appropriate γ-energy is chosen, the higher orders cover a wide range of the goniometer. As the angular distance between the Bragg-orders is always the same, a similar analysis as described above is possible. It has the advantage that finer steps than 1° can be chosen. Though the angular precision of a γ-peak at the appropriate energies is not as good as an autocollimator.

Iterative calculation   The calculation of K and F_0 should be done alternating and iteratively unless the values do not change significantly any more. This is usually the case after two iterations.

2.3.3   Higher non-linearities

So far only alignment asymmetries and instabilities were considered. The interferometer itself was considered to have a response function following perfectly a sine as described in equation (2.2):

$$F = K\sin\left(\Phi\right) + F_0 \ .$$

However, this is too much simplified. All optical elements used to build the interferometer are specified (and at least in the case of *Gams6* verified) to be homogeneous and flat to 60 nm. But below this level the surfaces can have a structure. Within the main part of the interferometer (laser source, beam splitter and detector), these structures are of no

important influence as the laser is affected always by the same surface. However, when the goniometer arm is rotated by an angle Φ, the corner cube is displaced by $\frac{L}{2}(1 - \cos\Phi)$. Hence the laser scans different spots of the corner cube and of the main mirror – the latter because the beam reflected from the corner cube is displaced by $2\frac{L}{2}(1 - \cos\Phi)$. Consequently the laser experiences a change $V(x)$ of the path length additional to the expected F. As the laser is reflected by the surface the maximal amplitude of $V(x)$ is twice the non-flatness of the surface, in our case 120 nm or $\lambda_L/5$. Notably $V(x)$ depends only on the displacement x of the laser and hence on $\cos(\Phi)$, i.e. V is symmetric around $\Phi = 0°$. The dependence on x is illustrated in Figure 2.15.

The interferometer equation has to be modified to:

$$F' = K\sin(\Phi) + F_0 + V(\cos(\Phi)) \ . \tag{2.61}$$

Misalignment

Another deviation from the perfect behaviour may arise from a bad alignment of the interferometer. Especially if the two laser beams towards the corner cubes of one axis are not parallel, or if the corner cube surfaces do not form exactly 90°, deviations from the expected interferometer response function will be unavoidable.

Despite of the careful alignment, a better accuracy than 2 arcseconds cannot be achieved or verified. Hence the additional path length change is small but a priori unknown. Due to the small amount of misalignment any dependence on Φ higher than second order can be ignored. Thus the effect can be described by coefficients v_1 and v_2. section A.2 gives more details about the influence of misalignment. v_1 and v_2 can be determined experimentally by fitting equation (2.62) to the data of an asymmetric calibration.

As shown in section 4.1.4 on page 130, the contribution of these parameters to F' is smaller than 10^{-8} and can be neglected.

Finally the interferometer equation has to be completed to:

$$F' = K\sin(\Phi) + F_0 + V(\cos(\Phi)) + v_1\Phi + v_2\Phi^2 \ . \tag{2.62}$$

Surface-step effects

Effects from surface-steps and misalignment should be analysed separately. Hence $v_1 = v_2 = 0$ is assumed from here on within this chapter.

In the worst case the mirror is a flat surface with one single step of the maximum amount of the specified flatness. A case like this is illustrated in Figure 2.15. In general this may lead to a non-continuous interferometer function, and in bad cases the function would even not be injective, which means that two different goniometer angles would result
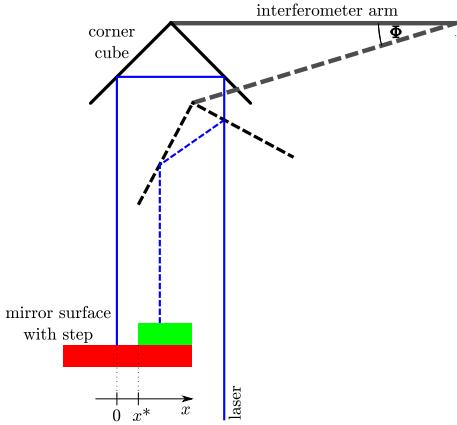
Figure 2.15: Surface-step illustration. One corner cube is sketched in symmetric position and at a large angle. The laser beam gets displaced. Hence during an axis rotation the laser scans the surface of the mirror. If the latter is not perfectly flat the interferometer readout will depend on the surface, and not only on the rotation.

in the same interferometer read-out. However, the laser has a finite diameter. In good approximation the interferometer readout is an average over this width. Diffraction effects can be neglected. Using a coordinate system where the centre of the Gaussian laser profile is at $x = 0$ when the axis is at $\Phi = 0°$, a surface with a single step of the height $\lambda_{\mathrm{L}}/10$ at the position x^* will result in:

$$V(cos(\Phi)) = \int\limits_{-\infty}^{\infty} \frac{1}{w\sqrt{2\pi}}\, e^{-\frac{(x - L(1 - \cos\Phi))^2}{2w^2}}\, \frac{2}{10}\frac{\lambda_{\mathrm{L}}}{10}\Theta(x - x^*)\,\mathrm{d}x \ , \qquad (2.63)$$

where $\Theta(x)$ is the Heaviside step function.

When using the given instrument parameters

$$\begin{aligned}
&L = 0.2\,\mathrm{m} \ (\text{for } \textit{Gams4}, \ 0.3\,\mathrm{m} \ \text{in the case of } \textit{Gams6}), \\
&K = 4L \ (\text{due to 4-fold usage of the corner cube displacement}), \\
&\lambda_{\mathrm{L}} = 632.8\,\mathrm{nm} \ (\text{for } \textit{Gams4}, \ 633\,\mathrm{nm} \ \text{in the case of } \textit{Gams6}), \\
&w = 2.2\,\mathrm{mm} \ \text{in the case of } \textit{Gams6},
\end{aligned} \qquad (2.64)$$

it can be shown easily that F' is always continuous and strictly monotonic for all $\Phi < 89°$ and thus always true in the goniometer range. Therefore the effective interferometer function is injective and allows proper angle measurements.

The relative accuracy of an angle separation measurement with the instrument is:

$$U_{\mathrm{r}\angle}(\Phi_1, \Phi_2) = \frac{\overline{\Phi}(\Phi_1) - \overline{\Phi}(\Phi_2) - (\Phi_1 - \Phi_2)}{\Phi_1 - \Phi_2} \ , \qquad (2.65)$$

where $\overline{\Phi}(\Phi) = \arcsin\frac{F'(\Phi) - F_0}{K}$ denotes the conversion from the interferometer readout into an angle. $U_{\mathrm{r}\angle}$ is targeted for *Gams6* to be better than 2×10^{-8}. On *Gams4* the interferometer instability is not better than 4×10^{-7}. Thus $U_{\mathrm{r}\angle}$ does not need to be better in this case.
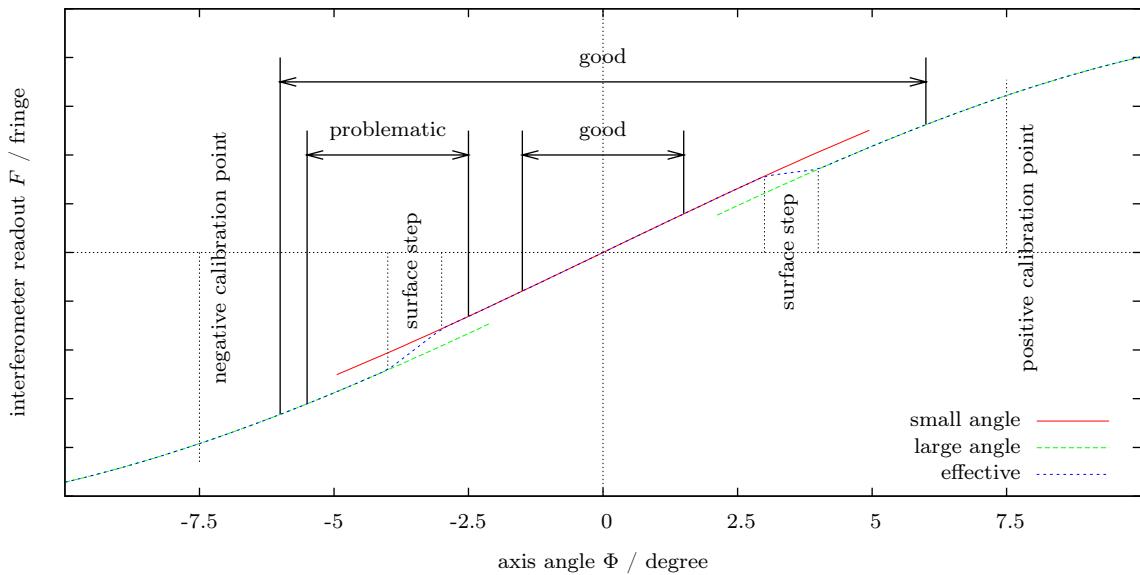
Figure 2.16: Higher order non-linearities. The interferometer may be perfectly sinusoidal for small angles. However a step on the surface of one mirror (as indicated in Figure 2.15) may cause a reduced path length at larger angles. The laser averages over its diameter when walking over the mirror. Consequently the step is smeared out in the effective interferometer readout.

Any deformation will infer on the signal symmetrically at positive and negative angles. Thus angle measurements symmetric to $\Phi = 0°$ will deliver a correct result. Even the calibration constant for measurements on different sides of the step is the same, as the step introduces a constant shift in the interferometer readout.

However, asymmetric measurements are problematic. They do not benefit from this compensation. Their start point may be subject to a different shift then the end point. Thus the deduced angle difference will yield a wrong value when using the uncorrected interferometer read out.

(a) *Gams4* $\Phi_1 - \Phi_2 = 15°$

(b) *Gams4* $\Phi_1 - \Phi_2 = 0.2°$

(c) *Gams6* $\Phi_1 - \Phi_2 = 15°$

(d) *Gams6* $\Phi_1 - \Phi_2 = 0.2°$
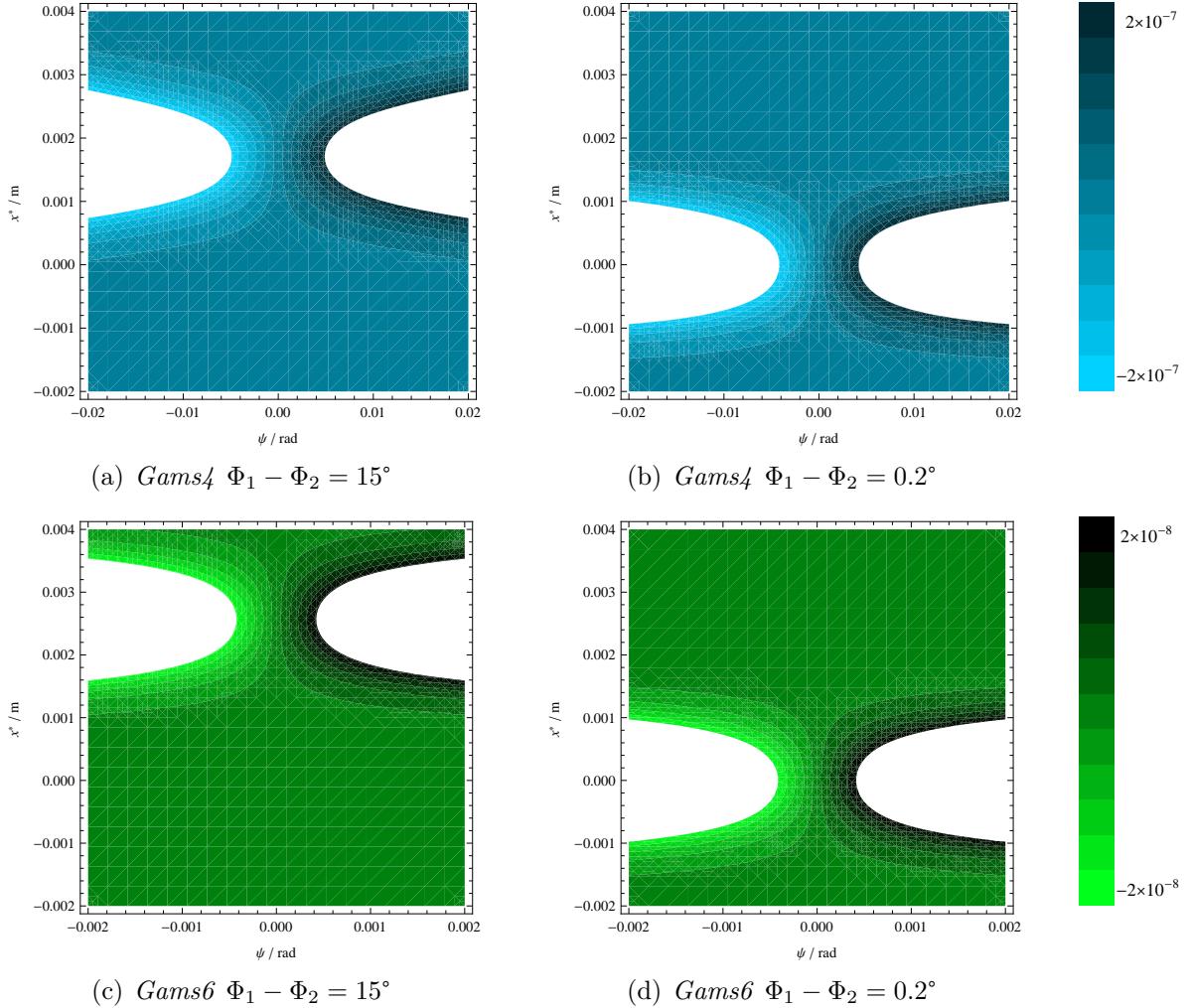
Figure 2.17: Maximum acceptable asymmetry in symmetric measurements. The plots show the relative measurement error $E_r(\psi)$ when an angle Φ is measured between the slightly asymmetric positions $\frac{-\Phi}{2} + \psi$ and $\frac{+\Phi}{2} + \psi$, with a worst case situation of a mirror surface step of $60\,\mathrm{nm}$ at the position x^*. The parameter space where the error is unacceptably large is drawn white.

The parameters of these graphs were chosen to illustrate the most extreme cases for intended measurements: The calibration with large angles of $\Phi = 15°$ and the smallest angle $\Phi = 0.2°$ in a ^{36}Cl-binding energy measurement. The accuracy limits are adapted to the overall instrument accuracy: 2×10^{-7} on *Gams4*, and 2×10^{-8} on *Gams6*.

The lever arm length is different for *Gams4* and *Gams6*, thus the worst-case influencing position is slightly different for both instruments.
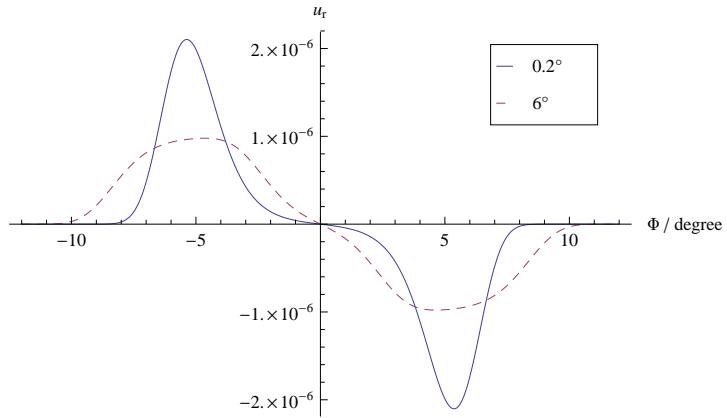
Figure 2.18: Asymmetric measurement: effect of a step on the mirror surface of $60\,\text{nm}$ at $x^* = 1.2\,\text{mm}$. Drawn is the relative offset when measuring a 0.2° and a 6° angle, at different asymmetric positions. A symmetric measurement ($\Phi = 0$) has no offset, as expected.

Symmetric measurements

A measurement which is symmetric to $\Phi = 0°$ is not affected by surface imperfection as shown in Figure 2.16. However no measurement can be perfectly symmetric, a threshold must be found from where a measurement cannot be considered as symmetric. The respective function $E_\text{r}(\psi) = U_{\text{r}\angle}(\frac{-\Phi}{2}+\psi, \frac{+\Phi}{2}+\psi)$ is not trivial and hence an error estimation cannot be calculated analytically. Even if the function looks locally very regular, it is not, neither on a local scale and high resolution, nor is it fairly symmetric on large scales. However a numerical analysis as shown in Figure 2.17 reveals that this error is smaller than 2×10^{-8} for any configuration as long as the misalignment ψ is less than 0.9 mrad (200″). This restriction has to be considered when mounting crystals or the polygon on *Gams6*. The polygon of *Gams4* has been mounted symmetrically within 0.2 µrad and is hence symmetric enough. The total instrument performance of 2×10^{-7} requires the crystal mounting to be symmetric within 9 mrad ($\approx 4\times 10^4\,\text{f}_4$) which is easy to achieve. The consideration of this effect is very important, as usual measurements consist of a Bragg angle measurement of small angles ($\approx 0.2°$–2° resulting in $x^* \lesssim 0.03\,\text{mm}$). These are calibrated with the polygon angles of 15° (corresponding to $x^* \approx 2\,\text{mm}$). If one or several of them would be made asymmetric (even when using the same asymmetry) a wrong calibration constant would be used for the conversion from interferometer readout to angles.

Asymmetric measurements

The *Gams* interferometer concept had been designed for symmetric measurements. Consequently asymmetric measurements are only possible when done with care. A naive approach where an angle is measured asymmetrically just-like-this may fail. Figure 2.18 shows that a possible step in one of the mirror surfaces will cause mistakes in the measurement in the order of 10^{-6}. However, with some extra calibration work one can reach for certain cases also asymmetrically a relative accuracy of 10^{-8}.

As asymmetric measurements are that delicate and usually not necessary, this section will restrict to those cases where they are vital. This is particularly the lattice comparison at different crystal positions, as described in chapter 5.4 on page 168. These measurements are done at a γ-energy of 184keV in third Bragg order, resulting in a Bragg angle of $\approx 3.0°$. Additionally the B-crystal will be shifted by up to 25 mm by turning the interferometer table (base length 700 mm), resulting in another 2°. Altogether the measurement covers a goniometer range from +5° to -5° and measures angle differences of $\phi_{\rm t} = 6°$ with a desired relative accuracy of 2×10^{-8}.

Assuming there is given a grid of points ϕ_i with spacing $\triangle\phi$ which are known to be at the real position. Hence the corresponding interferometer readout $F(\phi_i)$ can be measured. Consequently the higher non-linearity at these points are known and the goniometer can be fine-calibrated. One has only to assure that the non-linearity between these points is sufficiently small. This is fulfilled if:

$$\left| \left(\overline{\phi}(\phi_i) - \phi_i \right) \; - \; \left(\overline{\phi}(\phi_i + \beta \triangle \phi) - (\phi_i + \beta \triangle \phi) \right) \right| < u_{\rm r} \cdot \phi_{\rm t} \;\; \forall \beta \in [0,1] \; , \qquad (2.66)$$

where $u_{\rm r}$ is the desired relative accuracy and $\phi_{\rm t}$ the angle which will be measured. The expression is difficult to calculate, but can be estimated by:

$$\frac{\partial \left(\overline{\phi}(\phi) - \phi \right)}{\partial \phi} \triangle \phi < u_{\rm r} \cdot \phi_{\rm t} \; . \qquad (2.67)$$

One finds $\frac{\partial \left(\overline{\phi}(\phi) - \phi \right)}{\partial \phi}$ smaller than 2×10^{-6} for a 60 nm surface step at any position in the angle range $\phi \in [-5.1°, 5.1°]$. Consequently, the linear grid spacing must be as small as $\triangle\phi \leq 1 \times 10^{-3}$ rad $\approx 0.06°$.

This calculation is based on the effect of a single surface step. However any surface structure finer than 12 µm will cause absolute non-linearity effects $\overline{\phi}(\phi) - \phi$ smaller than the target accuracy of 6° $\times$ 2×10^{-8} within the required interferometer range. As a rotation of the goniometer of 5×10^{-4} is smaller than 12 µm any significant structure will be accounted by the linear grid. Hence, any surface effect is either too small to be important, or can be corrected for by the non-linearity map.
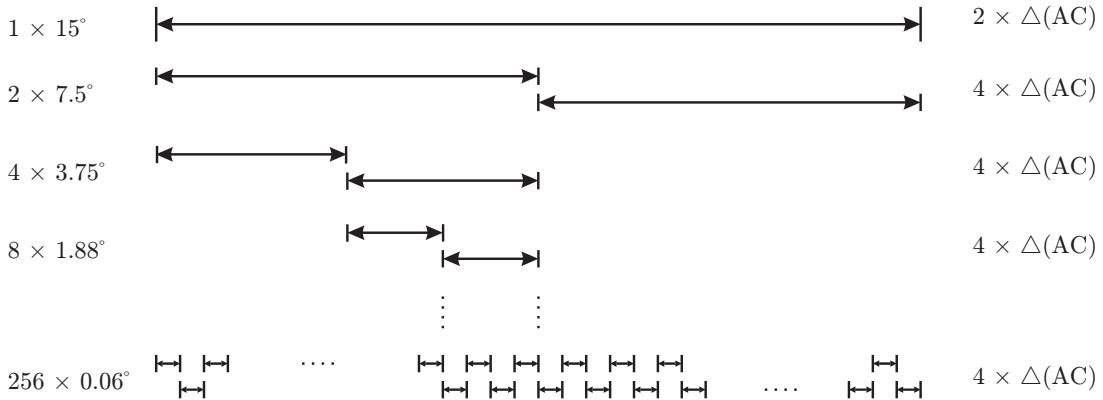
Figure 2.19: Non-linearity mapping: An angle of 15° is continuously subdivided into $15°/2^8$. Any subdivision introduces the autocollimator uncertainty $U(\mathrm{AC})$ as many times as it has to be measured. Hence every range of 0.06° can be linked to the full 15° range with $2 + 4 \times 8$ autocollimator measurements.

.

Non-linearity mapping

The non-linearities described above are given by material and alignment of the interferometer. Therefore they remain constant during the interferometer lifetime. Hence one can correct for them if they are known. Obtaining this knowledge is rather easy: A small and stable angle must be measured at many different positions of the interferometer, equal to the method to determine the interferometer offset F_0 (see section 2.3.2 on page 81).

A Zerodur plate with two mirrors bonded to it such that these mirror from an angle of 0.06° is placed on the axis. The interferometer readout is recorded when each of the surfaces is perpendicular to the autocollimator. Then the ensemble of the two mirrors is rotated by a small angle (ideally by the difference angle). This is repeated until the ensemble has been rotated over the full goniometer range. To cover the 15° of one polygon angle 512 readouts are necessary. As the autocollimator accuracy is 9.7×10^{-10} rad the total relative accuracy is

$$\frac{\sqrt{512} \ \times \ 9.7 \times 10^{-10} \ \mathrm{rad}}{15°} = 8 \times 10^{-8} \ , \tag{2.68}$$

which is above our target accuracy. However, if one uses a set of $n + 1 = 9$ mirrors of the angles $\{15°, 7.5°, 3.75°, \ldots, 0.06° \ (= 15°/2^n) \ \}$ each angle of 0.06° can be directly linked to the calibration points at 15° with only $32 \ (= 2 + n \times 4)$ readouts. Hence the relative error is only 2×10^{-8}.

From this measurements a map can be drawn which has to be applied to each interferometer readout to correct for the non-linearity effect.

This map has to be determined only once after the final set-up of the spectrometer (interferometer, axes and corner cubes). It can be used as long as the alignment of the interferometer stays unchanged. It should be noted that this map can be produced without the use of γ-radiation and thus without the reactor running. In these periods the environment is much less vibrating and will allow a better accuracy. Additionally there is no time pressure from the ILL instrument scheduling procedure. However, the required thermal stability is more difficult to achieve.

2.4 Summary

In this chapter the instrument was described in detail and a mathematical model was set up to describe the instrument and show how a physical result can be obtained from the experimental raw data. It should be noted that these information have never been published in a single work. Some parts even have never been published before and have been heavily discussed within the group [Jen07].
Besides this recapitulative part, also completely new facts were presented such as the proper way of the horizontal collimation.
The way how to convert the raw data into a physical result was completely redone, now respecting much more corrections (environmental conditions) and offsets (angular in crystal mounting, and fringe offset in weather corrections) and using less assumptions that were valid in the past but can not hold for the accuracy newly aimed for.
A possibility and the limitations for making asymmetric measurements was shown. This allows the comparison of crystal lattice spacing over different spots of the crystal without re-mounting it. These results will be essential for section 5.4.

The investigated physical system as well as the technical installations make *Gams* to a unique tool which allow this particular experiment. The main characteristics are: A very high initial event rate, given by the high neutron flux, is necessary as only a few γ-rays pass the small angular acceptance of the diffraction crystals. Due to this small acceptance no collimation is needed apart from shielding the detector from the direct view to the target and to reduce background. For the wavelength determination only the relative angle between the two crystals is required to be measured accurately. The angle relative to the target is much less sensitive. The instrument is self-calibrating. Only the lattice spacing of the diffraction crystal is required as external parameter. In non-dispersive Bragg order (both crystals parallel) the rocking curve delivers the instrument resolution, which allows an optimal vertical alignment of the crystals.

Chapter 3

Binding energy measurements

The work for this thesis was started with the intention to measure a more precise value for $N_A h$. It turned out quickly that the available instrument *Gams4* was doing well with a relative uncertainty above 10^{-7}, but it would be impossible to improve this significantly. Therefore it was decided to build a new instrument, merging the knowledge of the old *Gams4* and the advancement in technology of the last 20 years. To confirm the feasibility and to justify the need for certain pieces, some measurements from the past were repeated with a partially upgraded instrument. All data analysis is done with the intention to compare with old values, to verify that the theoretical description is also valid for the new instrument, to estimate the limits of the future instrument and to find issues where future studies are necessary. Obtaining a better accuracy was not the highest priority, although it would be useful to trigger high accuracy mass measurements of chlorine.

The last precise neutron binding energy measurements of ^{29}Si, ^{33}S, and ^{2}H were published in 2006 [Dew+06]. The data were taken from 1997 to 2000. Since then the instrument *Gams4* has undergone some changes which are assumed to lead to a better signal-to-background ratio. Therefore, a shorter acquisition time is possible and the measurement should be less disturbed by drifts.
Between the last high precision measurement in 2000 and the start of the present campaign in 2007, the instrument has been in heavy use for low-precision measurements. During this time less care was taken for high stability. Little modifications and wearing have accumulated and may have changed the vibration-level of the instrument as well as its stability.

Consequently, the relative accuracy of the data in this chapter will be compared with two thresholds: 4×10^{-7}, the most accurate measurement achieved so far with *Gams4*, and 2×10^{-8}, the accuracy aimed for with *Gams6* which will go into operation in 2011.

3.1 Changes since the last measurement

The major change was that the full instrument was moved by about 10 m away from the reactor core. This has the advantage that exchanges of the beam tube, which occur every ten years, do not require to dismount the instrument any longer. Furthermore, the radiation background from the reactor decreases with the inverse of the square of the distance. As the horizontal acceptance angle of the diffraction crystals is much smaller than the beam divergence, the beam intensity decreases only with the inverse of the distance. This leads to an improved signal-to-background ratio.

At the same time, the thermal isolation was rebuilt. The concept stayed the same, but the details of the implementation vary and it was unclear if the construction can compete with the previous. Additionally, the motors that control the crystal axis were changed and are now much closer to the instrument, causing thermal gradients and instabilities. During the present campaign a new cooling system for these motors was installed.

In measurements before 2001 the A-crystal was brought into position. It was kept there while the B-crystal was scanning. However, the position of the A-crystal was not measured. A second data acquisition system has been installed to monitor the A-axis permanently as well.

The data treatment requires a parameter estimation from the recorded rocking curves. In the past this was done by a least-squares-fit. Meanwhile, studies at *Gams* have shown that a maximum-likelihood fit is more appropriate [HJ01].

The algorithm for the calibration procedure was optimized. A full calibration can now be done in 12 hours, as compared to 24 hours previously.

3.2 Calibration

The *Gams* goniometer delivers its read-out in fringes. The conversion into absolute angles requires to calibrate the instrument. The procedure and data evaluation theory is described in detail in section 2.3.

The results of some previous calibrations are documented in [Kes+01]. However, material ageing and strong temperature influences make it necessary to have a calibration shortly before and after the measurement campaign. It would be desirable to obtain more calibrations during the γ-acquisition, but as the procedure lasts about 12 hours, this has to be weighed carefully.

Throughout the years 2007 and 2008 twenty full "symmetric" and seven "asymmetric" calibrations were done. Additionally, the angle of one polygon corner was monitored frequently as a quick stability check with low cost in beam time. The following subsections
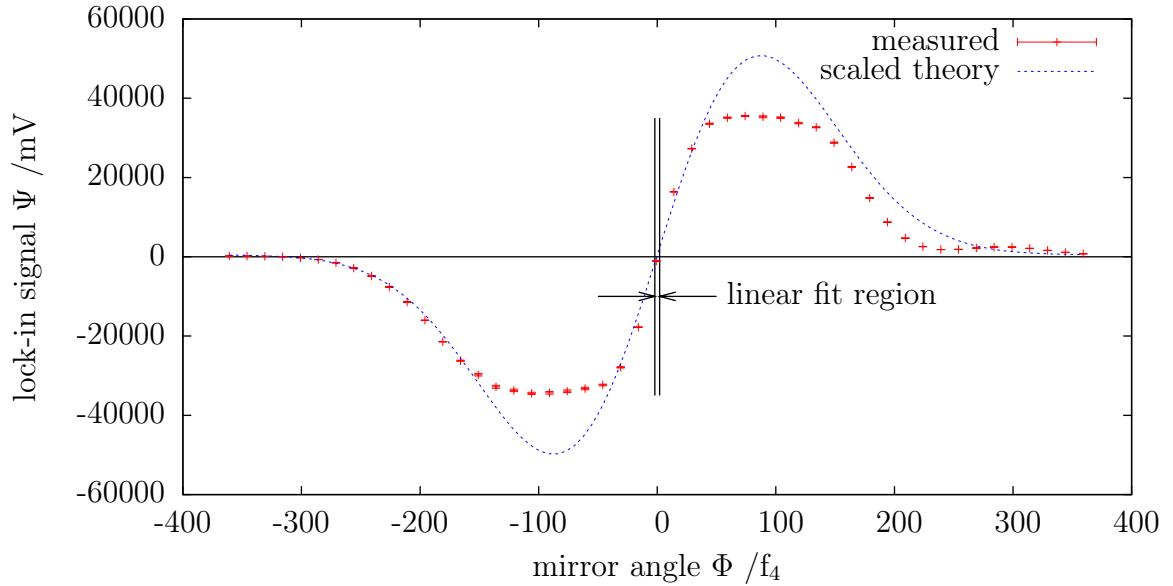
Figure 3.1: Theoretical and measured autocollimator response function. For this graph the voltage was attenuated by ten and then scaled back to avoid saturation of the lock-in amplifier. For details see section A.3. For the calibration only a small region is recorded and used for the linear fit.

describe the observed irregularity in the autocollimator and its consequences on the quick stability check. Finally the result of the full calibrations and the determination of the interferometer offset is presented.

3.2.1 Autocollimator function

The autocollimator verifies the precise positioning of the polygon. Details on its internal design and a mathematical description are given in section A.3. The autocollimator returns voltage Ψ which depends highly on the angel of the facing mirror, and thus, on the goniometer angle Φ. In a small range ($< 10\,\mu$rad) when a polygon mirror is almost perpendicular to the optical axis of the autocollimator this response function is very linear (see Figure 3.1). The zero-crossing angle ($\Phi_0|_{\Psi(\Phi_0)=0}$) of the goniometer and the slope of this function are obtained by weighted linear regression. After comparing the zero-crossing positions of two polygon mirrors, the angle between those mirrors can be expressed in interferometer units.

This simple method has also been used in previous experiments. However, at the end of this campaign an offset voltage was found. When any polygon mirror is far from being perpendicular, the voltage should be $0\,$mV, but a voltage of about $250\,$mV was observed. This becomes a problem if either this offset or the slope changes between two
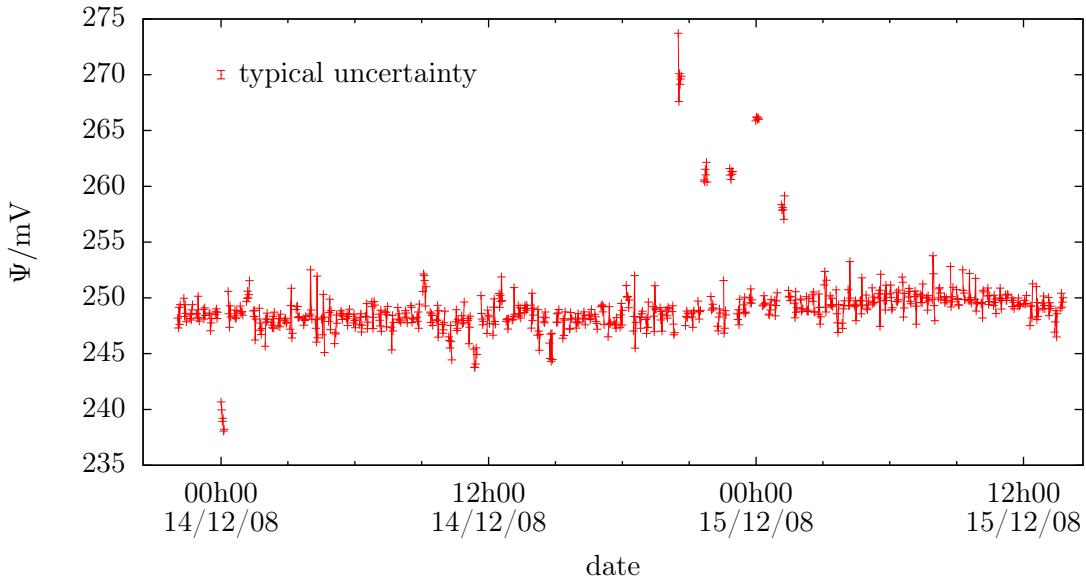
Figure 3.2: The autocollimator offset monitored during a full calibration. If any mirror was in the range of the autocollimator, the sample was excluded and the line in the graph interrupted. The voltage was sampled with 10 Hz. Each data point is the average over 500 samples.

measurements. Unfortunately, the existence of this offset was discovered only after the campaign. Furthermore, the offset had not been written into the data files. In a posterior measurement the typical changes of the offset were characterized over 40 hours. To this end, the voltage was sampled every 0.1 s with a resolution of 0.3 mV during a calibration procedure. If any polygon mirror was out of range, 500 consecutive samples were averaged. Hence they represent the autocollimator offset. These averages are shown in Figure 3.2. Their mean is 248.8 mV, and their mean error is 0.4 mV. The mean did not show any drift larger than 1 mV over three days. However, several consecutive outliers could be observed. If such an outlier was observed, it was not an isolated group of 500 samples, but it lasted for the full time where no mirror was in the autocollimator range which lasts about 9 minutes. The origin of these outliers is unclear, they may come from the autocollimator itself or from the analogue electronic signal processing. Fortunately, the size of this effect is negligible for any measurement with *Gams4*, as even with a low slope of $300\,\mathrm{mV/f_4}$ the extreme outliers of 20 mV cause an error of the angle determination of $0.07\,\mathrm{f_4}$, which corresponds to a relative uncertainty of 5×10^{-8} and is hence for the present measurement of no significance. Nevertheless, for calibrations of *Gams6* the offset must be monitored permanently. If necessary adjacent measurements have to be repeated.

All slopes measured on the surfaces "150°" and "165°" during the years 2007 and 2008 are shown in Figure 3.3. The systematic difference between slopes measured on the positive
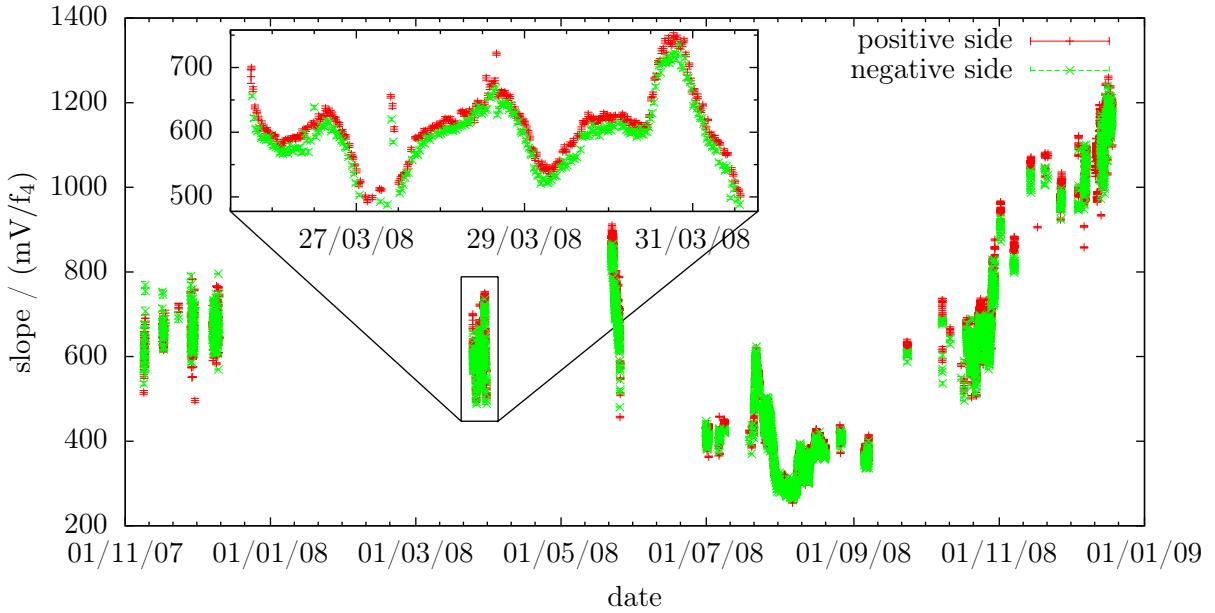
Figure 3.3: Autocollimator response function slope–variation over time. Notable is the systematically steeper slope on the positive side (positive interferometer fringe readout) of about 4%.

side ("165°") and on the negative side ("150°") is unexplained. The variation of the slope over on long term may be due to drifts in the autocollimator construction or the electronic equipment (see section A.3). The reason for both effects were not further investigated. For *Gams6* new autocollimators of the same type are used. Due to the fact that the operation speed if much faster and that two autocollimators are used, a detailed study on these effects will be easier to do.

The consequences of these effects are described within the following sections.

3.2.2 Single polygon-corner stability

A full calibration is very time consuming. A quick way to verify the stability of the instrument is desirable. According to Figure 2.14 on page 79, this can be done by measuring only the angle of one corner of the polygon. This measurement takes only about 35 minutes. Additionally, no operations that could disturb the thermal stability, e.g. lifting the polygon, are necessary. During 18 months the angle between the polygon mirrors "165°" and "150°" was measured 1344 times.

The environmental corrections are described in subsection 2.2.2. Only those for goniometer arm length† and refractive index were applied to the data, as only they apply to a

---

†The correction for the arm length is called calibration constant correction for the γ-type data.
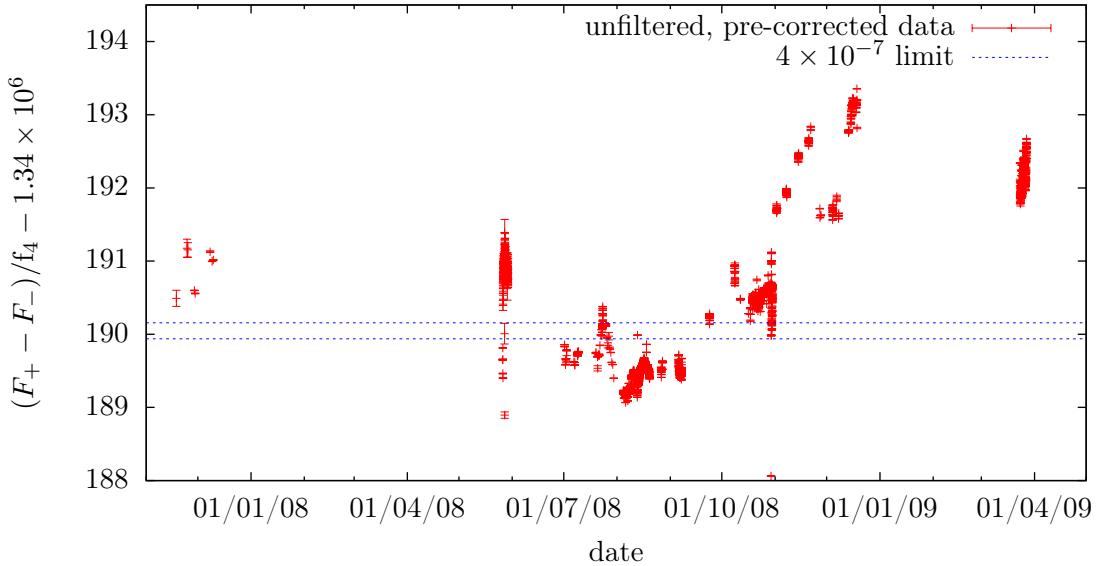
Figure 3.4: Stability test with the calibration unit. The angle of one corner was monitored over 1.5 years. All known environmental corrections have been applied to the interferometer readout. The scattering exceeds largely the range that would permit a full calibration with a relative uncertainty of 4×10^{-7}.

calibration-type data. This is called "pre-correction" because an additional correction will appear later on. Throughout this section all data were pre-corrected to the reference usual *Gams* reference conditions: temperature 22.5 °C, pressure 760 Torr, relative humidity 40%. The corrections applied by the built-in algorithms of the acquisition software were withdrawn.

As shown in Figure 3.4, the stability measurement of the "150°/165°" polygon corner shows a large instability with a standard deviation of $0.86 f_4$. This corresponds to a relative uncertainty of 6.4×10^{-7}. In a full calibration, all 24 sides of the polygon are summed up. Therefore the expected uncertainty of a full calibration is $\sqrt{24}$ times bigger. Hence it would be 3.1×10^{-6} – too large. Therefore, the pre-corrected data were searched for correlations with environmental parameters. A linear correlation of $(0.0003372 \pm 5 \times 10^{-6}) \, f_4/(\mathrm{mV}/f_4)$ with the autocollimator slope was found (See Figure 3.5). This slope itself is already surprisingly unstable, as mentioned in the previous subsection. It is unexpected that any correlation between slope and measured angle exists and moreover that this correlation is linear. The reason for this correlation is unclear. However, it describes the data very well. Therefore it was tried to correct the data using this correlation. This correction is done after and on top of the environmental pre-correction. It is applied even after the zero-crossing determination. Therefore, it is called "post-correction".
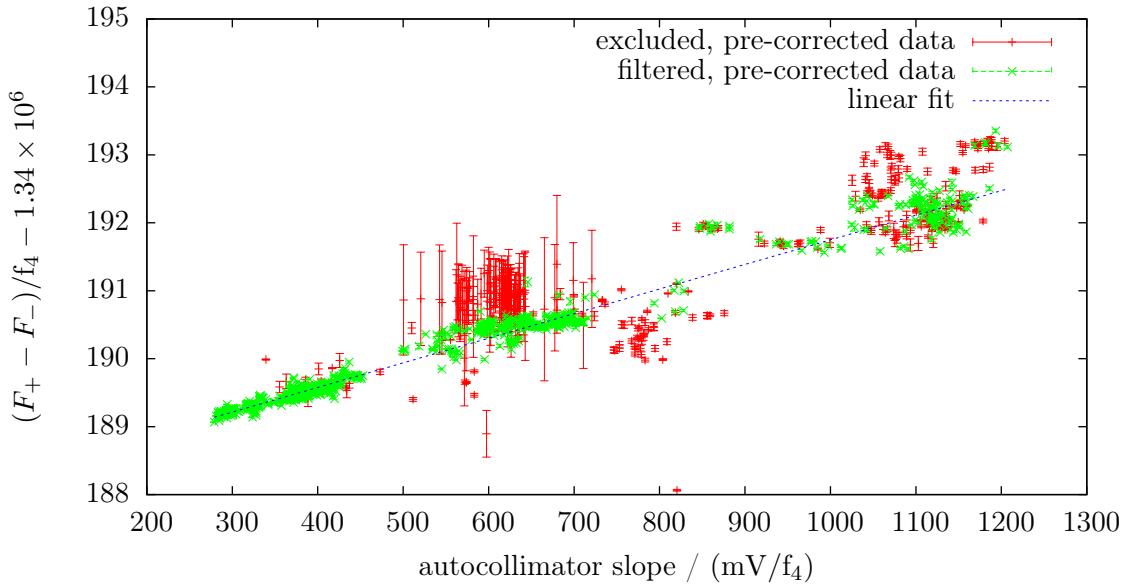
Figure 3.5: Correlation of single corner angle with slope. The data are filtered for temperature change between positive and negative zero-crossing to be less than 4 mK and a slope determination with $\chi^2 < 10$.

Additionally the data for which the temperature changed more than 4 mK between the measurement of the two mirrors were cut away. This is justified as such a rapid change is always accompanied with temperature gradients that cannot be mapped appropriately with the five sensors. Hence, a proper correction is not possible.

Furthermore, the data where the fit of the zero-crossing resulted in a $\chi^2 > 10$ were dropped. Details on this fit problems are given in the next subsection, particularly in Figure 3.9.

The post-corrected data are plotted in Figure 3.6. They have a mean of 1340189.566 f_4 and a standard deviation of 0.072 f_4. For a full calibration, where 24 of this uncertainties sum up, a total relative uncertainty of 2.6×10^{-7} can be expected.

The subset of data with a slope of more than 900 mV/f_4 have a standard deviation of 0.22 f_4, thus high slope values lead to a larger scattering of the data. This is contrary to the intuitive assumption that a steeper slope should lead to a more precise determination of the zero-crossing point. It may be caused by the presence of the autocollimator offset. The persistence of this effect on *Gams6* must be examined; if yes, an optimal slope must be found by adjusting the autocollimator parameters (see section A.3).

There is an additional problem arising from the slope correction. It leads to a systematic change of the calibration constant. To reduce this effect, a mean slope of 400 mV/f_4[†] can

---

[†]Obtained by averaging only the data that pass all filters.
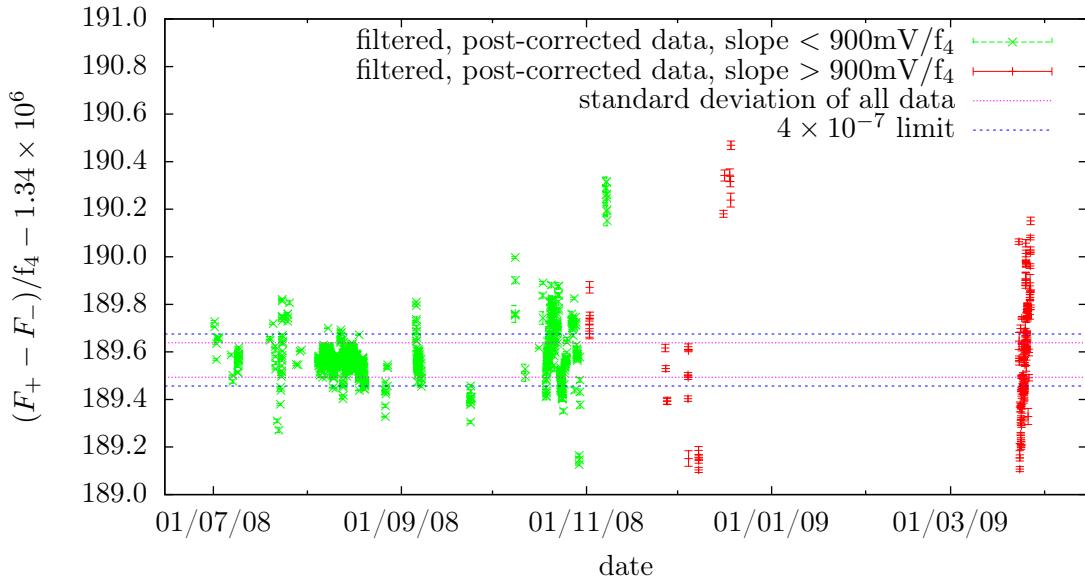
Figure 3.6: Stability test with the calibration unit. The same data are shown as in Figure 3.4, but now filtered and post-corrected. Data points with a large slope show a bad stability. The dotted line indicates the limit of scattering that would lead to a full calibration with a relative uncertainty of 4×10^{-7}.

be deducted from each measured slope before using it for the correction. Consequently the correction is fine on the 4×10^{-7} level. However, this will not work for more accurate measurements. Therefore the slope correction is not applied in the further data evaluation.

3.2.3 Full symmetric calibration

For a good calibration a high stability – and thus low scattering – is as important, as the absence of systematic effects. As mentioned in subsection 3.2.1 an offset in the autocollimator function was observed. Such an offset would not be important if it was stable and if the autocollimator slope was stable. The long time stability of the offset is unknown, the short time stability seems to be fine with some exceptions (see Figure 3.2). However, the slope does not only vary over time, it is also typically larger by 4% on the positive side, as shown in Figure 3.3. Considering a slope of $400 \, \mathrm{mV/f_4}$ and an offset of $250 \, \mathrm{mV}$, the measured calibration constant would be $(1 + 2 \times 10^{-8})$ times too big. For *Gams6* this effect has to be either eliminated or measured so well that it can be corrected for. For the present measurement there will be no correction as the effect is far smaller than other uncertainties.
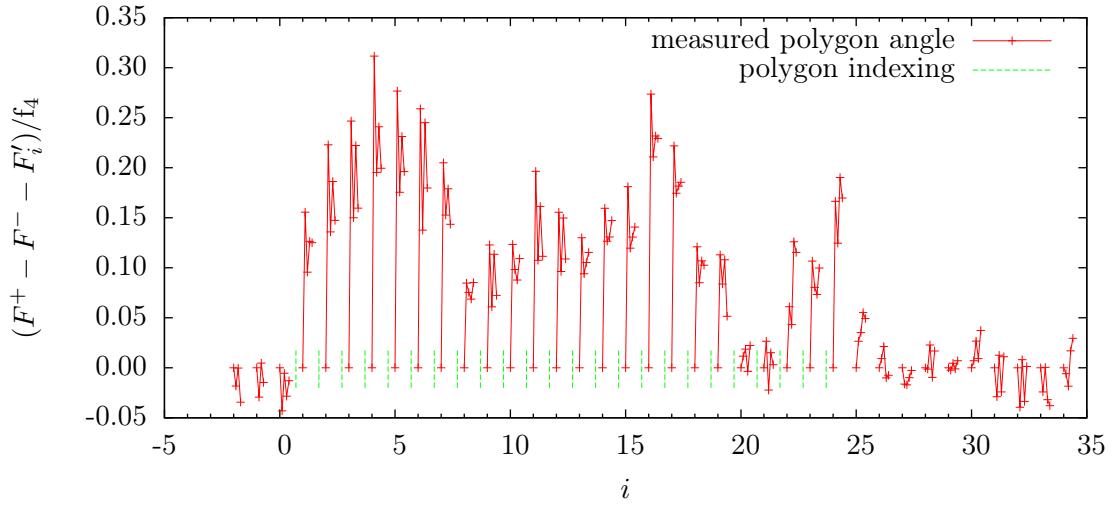
Figure 3.7: Calibration instability after polygon indexing. Drawn is a full symmetric calibration with some heading and tailing non-indexed stability measurements. Each integer i represents 6 zero-crossings, alternating of two adjacent mirrors. Hence 5 angle differences can be plotted. For better comparison, each point on a continuous part i of the line has the same reduction F_i'. All F_i' are chosen such that the first point of each continuous part is 0. The deviations from 0 show the drift of the instrument after each polygon lifting.
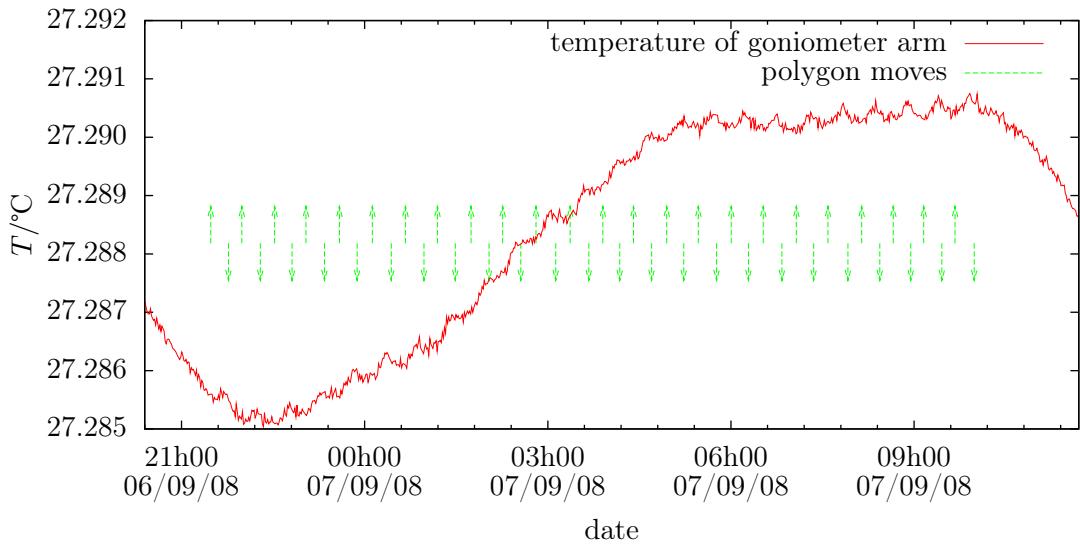
Figure 3.8: Temperature instability induced by polygon indexing. The temperature oscillates with the same period as the polygon is lifted. It seems also that the the polygon lifting heats the system, as the general cooling trend is stopped for the same period the polygon is lifted. Though, the reaction time seems too short to be causal.

To perform the full calibration, the polygon must be indexed. The set-up is described in subsection 2.1.8 and the procedure in Figure 2.13 on page 79. The polygon and the upper gear are lifted by 5 mm during de-coupling. The re-coupling of the two gears is forced by the weight of the polygon only (~ 2 kg), though its reproducibility is better than 2×10^{-7} rad $\hat{=} 1$ f_4.

However it turned out, that either the coupling takes a certain amount of time to slide to its final position, or – more probable – the vertical movement of the polygon disturbs the stability of the goniometer. This was discovered in a special run of the calibration procedure. Between each indexing of the polygon, the angle of the mirror pair was measured three consecutive times, instead of only once. More precisely, six mirror-position measurements were taken per indexing, resulting in 5 values for the corner angle. The total time of one calibration increases from 12 to 36 hours.

As shown in Figure 3.7 the first angle measured after an indexing is 0.1–0.3 f_4 smaller than the succeeding measurements which themselves vary by ≈ 0.05 f_4 and seem to converge alternating towards a central value. This alternating may be explained by the fact that the measurement direction of these angle-differences is alternating. If there is a drift in one direction, all measurements along this direction will yield larger values. If the drift decreases with time, a pattern like the one obtained is the result. However, it is not clear whether this drift is caused by a bad coupling of the gears or a thermal distortion of the goniometer.

Figure 3.8 shows the temperature of the goniometer arm during a calibration. An oscillation of the temperature with the same periodicity as that of the lifting of the polygon is observed. There are two possible reasons for such a temperature change. It is either the heat dissipated from the lifting motor, or it is caused by the change of the convection. This may happen as the lifting structure is rather large and can block air currents. The periodicity of the temperature favours the second possibility. However, one might argue that an upward movement generates more heat than a downward movement.

Nevertheless, the magnitude of the observed effect may result in a relative shift of 8×10^{-8} and does not threaten the present campaign. At *Gams6* the situation is different, as it operates in vacuum and hence no convection can occur. Also, a thermal decoupling of the motor has been established. Furthermore, the mechanical friction in vacuum is much different. This is a very different situation with respect to the gear coupling.

It should be noted that at the beginning of the present campaign the algorithm for the full calibration was optimized so that it lasts only 12 hours instead of 24 hours. It is unclear if the coupling instability was known in the year 2001 and before. It is certain that the calibration procedure lasted 24 hours. However, the instrument control software, as found in 2007, registered only three zero-crossings per indexing, instead of four (the maximum in 24 hours). With this behaviour a slight compensation of this effect by averaging is possible.
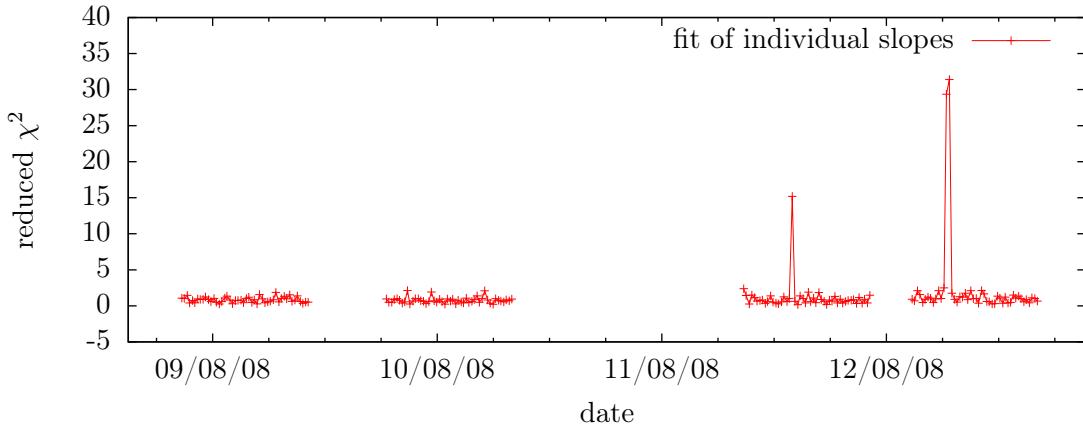
Figure 3.9: Reduced χ^2 values of the individual slope fits from four arbitrary calibration procedures. Two of them follow a χ^2-distribution (number of degrees of freedom is 18). The last two have unexplained outliers, and thus will be disregarded.
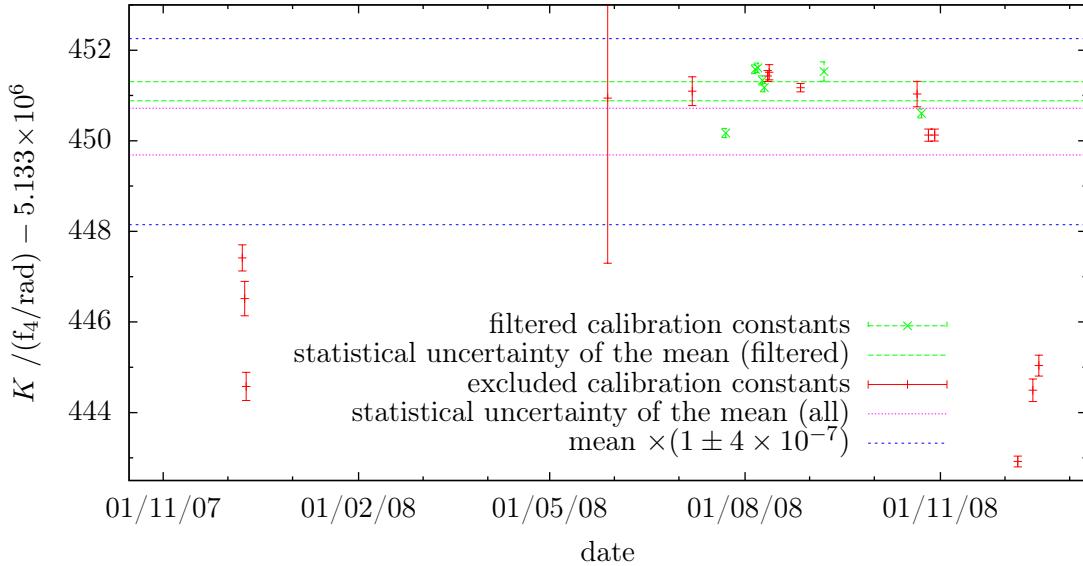
Figure 3.10: Calibration constants. The error bars of the data points are deduced from the slope determination. For visibility they are increased by a factor 5. The uncertainty of the mean is dominated by the scattering of the data and thus the remaining instability of the instrument. Shown is the mean and uncertainty of all (unfiltered) data, and the same after filtering for $\chi^2 < 10$ and temperature more stable than 0.1 K. One data point from 25/11/07 is out of scale (see Figure 3.11). It is included in the unfiltered mean, though its weight is very small.

101
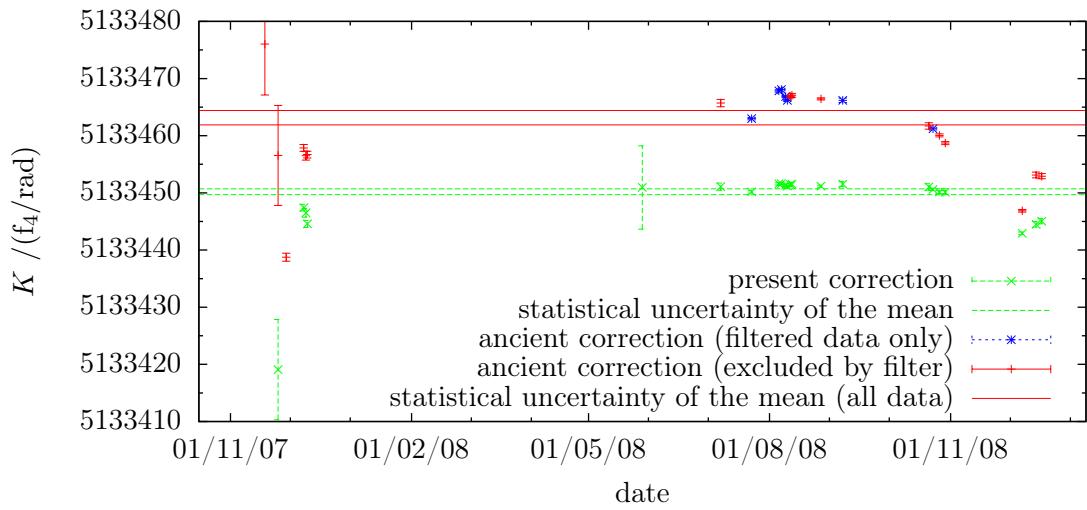
Figure 3.11: Comparison of environmental correction algorithms. The present algorithm results in a 60% smaller error than the algorithm used prior to 2005. The uncertainty of data with old correction can be reduced by excluding data with a bad χ^2 and an unstable temperature. However, this reduces the statistics so much that the total uncertainty does not get smaller. The difference between the mean of the two correction algorithms results from the missing correction to thermal expansion of the Invar interferometer arm. Leaving out this correction is acceptable if it is done consistently in calibration and γ-data, and if all data sets are measured at similar temperatures.

After filtering for thermal stability of $0.1\,\mathrm{K}$ throughout a full calibration, the data show still a large scattering. It was found that most of the zero-crossing determinations worked fine with respect to the χ^2-distribution of the fits. However, a few fits provide strong outliers, as shown in Figure 3.9. The error accumulated by this fit does not explain the scattering of the resulting calibration constants. However, these outlier seem to coincide with a change in the thermal drift which means a change from warming to cooling or vice versa. This makes a thermal correction very unreliable. Therefore, these data were disregarded. From the twenty full calibrations performed, only seven fulfil these criteria, as shown in Figure 3.10. But the scattering of even only those data points is that large that the uncertainty of the mean is dominated by it. This shows that the total uncertainty is determined by the instrument stability, not by the zero-crossing determination.

The weighted mean of the filtered data is $5133451.00\ \mathrm{f_4/rad}$ with an uncertainty of $0.21\,\mathrm{f_4/rad}$ which is a relative uncertainty of 4.1×10^{-8}. The standard deviation of those filtered data is $0.55\,\mathrm{f_4/rad}$ or relative 1.0×10^{-7}. This is the uncertainty we have to assign to a single calibration, if it is not combined with others, but used solitarily for calibration γ-type data.

When using the unfiltered data, the weighted mean would be $(5133450.11\pm0.52)\ \mathrm{f_4/rad}$ which is a relative uncertainty of 1.0×10^{-7}. The scattering is $2.7\,\mathrm{f_4/rad}$ which is 5.2×10^{-7}.

However, both values will be corrected for the interferometer offset as described in the next subsection.

To illustrate the importance of a proper correction for environmental influences, the same data is shown again in Figure 3.11. This time only the old corrections from the year 2001 was applied. That algorithm accounts for the change of the refractive index of air only. It uses the original Edlén equation from 1966. The new algorithms uses the updated Edlén equation from 1994 and additionally it corrects for the thermal expansion of the interferometer arm which is made out of Invar and has a CTE of $0.61\times10^{-6}/\text{\textcelsius}$ [Jen10; BJN76]. The offset between both methods comes mainly from the fact that the old methods ignores the expansion of Invar. If this correction is also left out in the correction of the γ-type data the total result will be the same, but only if the temperature is sufficiently stable between calibration and γ-type measurement.

3.2.4 Asymmetric calibration

In order to determine the goniometer offset F_0, seven asymmetric calibrations were performed. The same corrections and filtering as previously discussed have been applied. All data pass the filter. However, a different problem affects asymmetric measurements: the autocollimator slope is theoretically constant when measured in voltage per angle. In contrast, the fringe to angle ratio is not constant, and consequently increases the slope
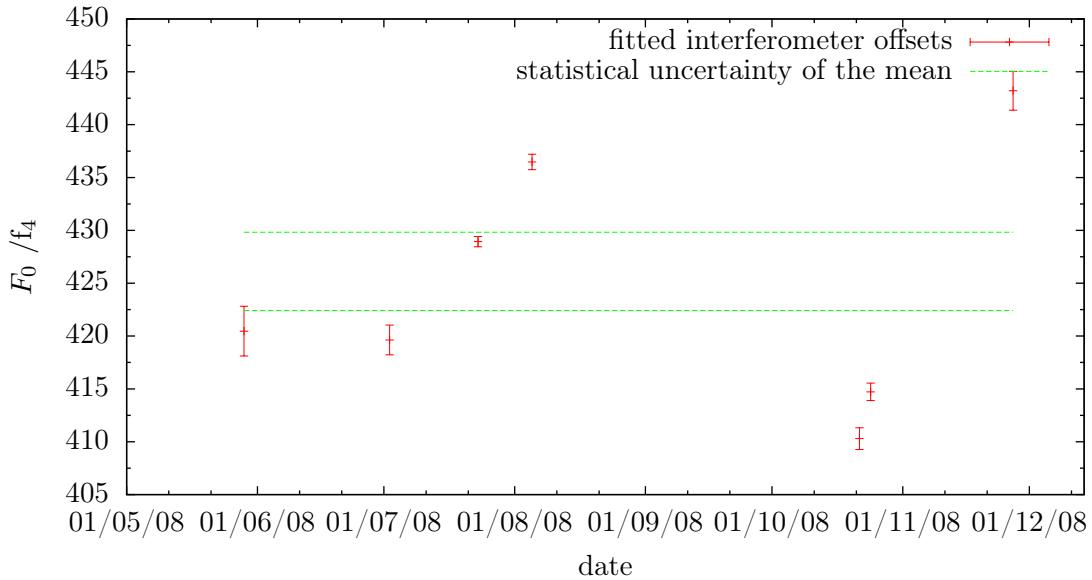
Figure 3.12: The interferometer offset F_0 is obtained from seven asymmetric calibrations.

$F_0 = 0$	$F_0 = 1000$
$\hookrightarrow K = 5133450.10841$	$\hookrightarrow K = 5133450.38540$
$\hookrightarrow F_0 = 425.067$	$\hookrightarrow F_0 = 425.084$
$\hookrightarrow K = 5133450.20193$	$\hookrightarrow K = 5133450.20194$
$\hookrightarrow F_0 = 425.073$	

Table 3.1: The iterative determination of K and F_0 converges quickly. One step is sufficient as the individual uncertainties are $u_{\mathrm{a}}(K) = 0.21\,\mathrm{f_4/rad}$ and $u_{\mathrm{a}}(F_0) = 3.7\,\mathrm{f_4}$

with the cosine of the goniometer angle, when measured in voltage per fringes. In the presence of an offset this leads to an asymmetric error. The maximal change of the slope within the goniometer range is 2%, as can be concluded from simple geometric considerations. Assuming a stable offset of 250 mV and a slope of 300 mV/$\mathrm{f_4}$, an error of 0.02 $\mathrm{f_4}$ occurs. This is far below the stability of *Gams4*, but it may be significant for *Gams6*.

To calculate F_0, all data were fitted according to equation (2.58) on page 81, using the calibration constant value from the previous section. The data are shown in Figure 3.12. Then the weighted mean of the resulting F_0 was taken for a new evaluation of the calibration constant as described in the previous subsection. This procedure was repeated once to be sure that the changes are smaller than the uncertainty given by the scattering. To verify that the arbitrary starting value of $F_0 = 0$ did not give a bias, the calculation was repeated with a starting value higher than the result. And as table 3.1 shows, one iteration is sufficient and the result is unbiased.

The final result for the goniometer offset is is $F_0 = (425.1 \pm 3.7)$ f$_4$. The calibration constant for the unfiltered data is $K = (5133450.20 \pm 0.52)$ f$_4$/rad which is a relative uncertainty of 1.0×10^{-7}. For the filtered data the result is $K = (5133451.09 \pm 0.21)$ f$_4$/rad which is a relative uncertainty of 4.1×10^{-8}.

The residuals of the asymmetric calibrations are shown in Figure 3.13. The high values at $\phi \approx 6°$ indicate a higher order non-linearity. However the data is not detailed enough to create a model which would be suitable for a correction. The reason for this behaviour may be a laser beam which is touching the border of a mirror and is thus slightly diffracted. However, the effect is small enough to be ignored on *Gams4*. If a similar effect is found on the new instrument *Gams6*, measuring several Bragg orders in asymmetric goniometer position (see section 5.4) may be used to create such a correction model.

3.2.5 Comparison with old calibrations

[Dew+06] calculates a calibration constant for each set of uncorrected data. Then they perform a global parameter adjustment for environmental conditions. For the present data this seems inappropriate, as the environmental conditions changed too much throughout a single calibration procedure. Thus the individual interferometer readouts must be corrected for these influences before evaluating the calibration constant. After compensating the different calculation models, both results should agree as the apparatus is the same and was not changed in this respect. [Dew+06] specifies $K_0 = 5133462.12 \pm 0.59$ f$_4$/rad which is valid for 26 °C. The present value $K = (5133451.09 \pm 0.21)$ f$_4$/rad is specified for 22.5 °C. The $K_\theta = (7.5 \pm 1.3)$/°C obtained by [Dew+06] does not explain the difference. However, using the CTE of Invar of 0.61×10^{-6}/°C explains the difference perfectly. [Dew+06] obtains a relative standard deviation of the residuals of 0.33×10^{-6}. The relative standard deviation obtained here is 0.52×10^{-6} for unfiltered and 0.10×10^{-7}. Hence by carefully selecting the data a factor 3 was gained with respect to earlier data. For [Dew+06] the total statistical uncertainty of the calibration constant is given by the uncertainty of K_0 plus the uncertainty of the various coefficients which have to be multiplied by the corresponding parameter. The dominant term is K_{laser}. The sum of these uncertainties will always be larger then 0.8 f$_4$/rad which is a relative uncertainty of 1.6×10^{-7}, compared to 4.1×10^{-8} in the present data.

3.2.6 Summary

A calibration constant of $K = 5133451.09$ f$_4$/rad was determined. Its statistical uncertainty is 0.21 f$_4$/rad, this comprises the uncertainty in the zero-crossing determination as well as the instability of the instrument between different calibrations. This uncertainty is a factor three more precise than any other measurement before. There are additional
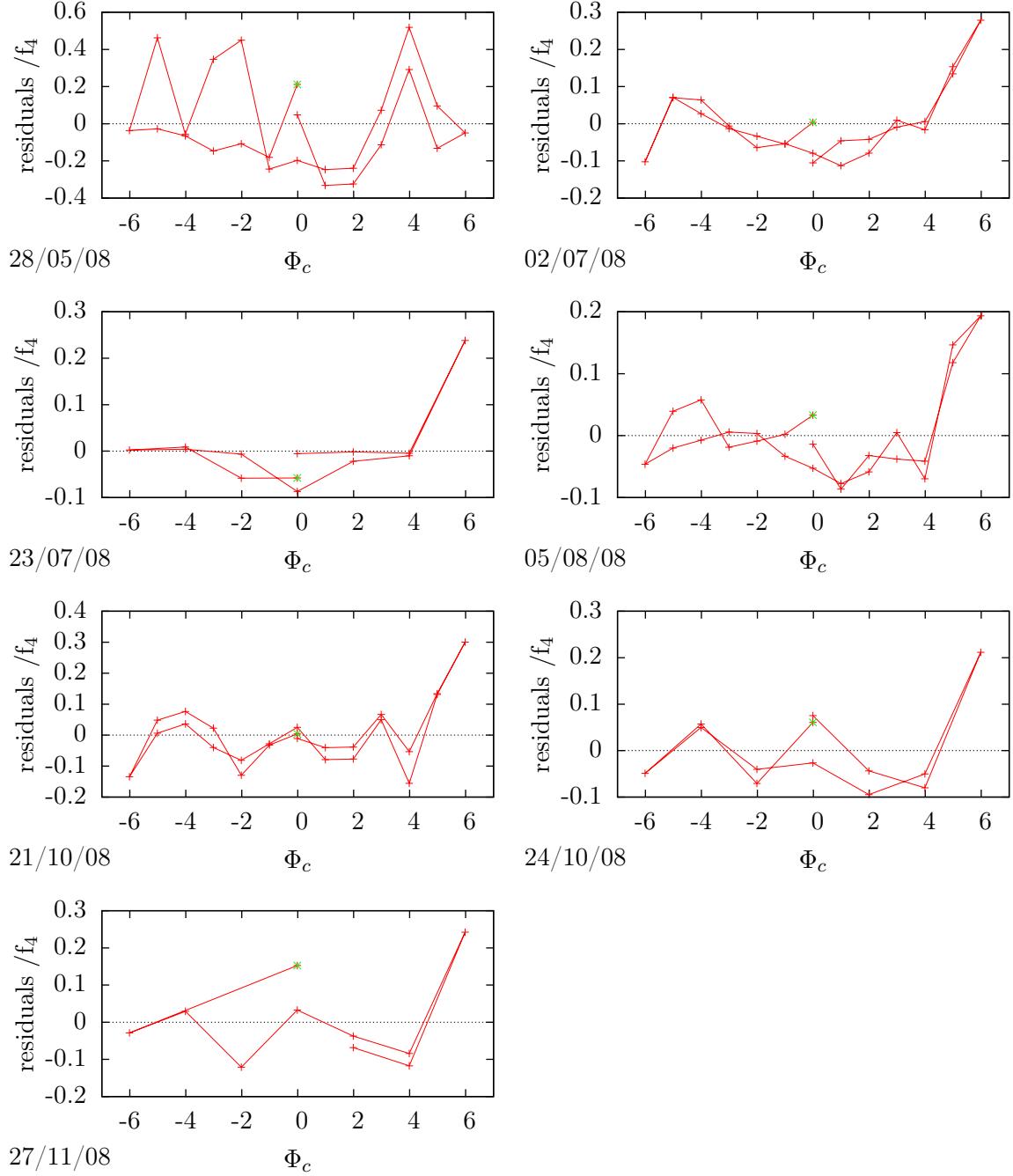
Figure 3.13: Residuals of the F_0 fit for the asymmetric calibrations. These residuals are calculated as $(\arcsin \frac{F_{A,j}^+ - F_0}{K} - \arcsin \frac{F_{A,j}^- - F_0}{K} - \overline{\Psi}) \times K$ as described in (see (2.57) and (2.58)) on page 81. The asymmetry $\Phi_c = \arcsin \frac{F_{A,j}^+}{K} - \arcsin \frac{F_{A,j}^-}{K}$ is illustrative; it does not enter the calculation. The lines mark the order of acquisition, the first point is marked differently.

systematic uncertainties as discussed in the preceding subsections. These are:
- 5×10^{-8} sporadic variations of the offset voltage;
- 2×10^{-8} different slope for positive and negative sides, while an offset voltage is present;
- 8×10^{-8} instability after gear re-coupling.

In total this is a systematic uncertainty of 9×10^{-8}. The systematic uncertainty has never been investigated systematically before, thus a comparison is not possible. The goniometer offset was determined to $F_0 = (425.1 \pm 3.7) \, f_4$

The obtained result is accurate enough to serve for a good calibration of the γ-data of the chlorine binding energy described in section 3.3.

The calibration was studied extensively. It was found, that in principle the calibration is accurate enough to reach the intended accuracy of *Gams6*. Several systematic effects were found which would currently perturb at this level of accuracy. These effects can either be eliminated or measured so precisely that a correction is possible: A permanent monitoring of the voltage neutralizes any offset. A vacuum chamber avoids convection and reduces heat flow, so that the polygon coupling should not disturb the thermal stability any more. A complete redesign of mechanic, bearings, motors, data acquisition system and operation algorithms make the procedure much faster. Hence it will be less opposed to drifts and systematic studies of any effects are much easier.

3.3 Binding energy of chlorine-36

The best $N_A h$ measurement on *Gams4* so far was based on deuterium, silicon-29 and sulfur-33 [Dew+06]. However, chlorine-36 has the potential to reduce the uncertainty significantly. The measurement was performed on the old *Gams4*-instrument with enhancements in the γ-beam collimation. The measurement started with the intention to prove the feasibility of the measurement of a chlorine binding energy with a relative statistical uncertainty of 2×10^{-8}. This was necessary to justify the budget for the further instrument development, and also to motivate the high accuracy penning-trap community to go on with mass measurements of chlorine. Furthermore the best strategy for data acquisition and source materials was searched. Before this campaign, it was believed, that the instabilities of *Gams6* would limit any chlorine binding energy to a relative uncertainty of 4×10^{-7} at best.

3.3.1 Acquisition schedule

In 1997 NaCl was used as source material [Dew+06]. This time three targets with $2 \, \text{g} \, BaCl_2$ each were used. $BaCl_2$ provides more Cl-atoms per foreign atoms. Thus it may lead to a better signal to background ratio. However, it has the disadvantage of a lower number of

γ-energy	date	duration of 4-pack	number of 4-packs	crystal	Bragg order
keV		minutes			
6112	24–27 Nov 2007	170	23	ILL4/7	(1;3)–(1;-3)
6112	29 Nov–2 Dec 2007	90	47	ILL4/7	(1;3)–(1;-3)
6112	7–14 Oct 2008	126	58	ILL4/7	(1;3)–(1;-3)
1165	10–11 Nov 2007	77	16	ILL2.5	(3;3)–(3;-3)
786	11–13 Nov 2007	90	21	ILL2.5	(3;3)–(3;-3)
517	10 Nov 2007	48	15	ILL2.5	(2;2)–(2;-2)

Table 3.2: Data sets used for chlorine binding energy. The Bragg order is given for (A;B) crystal in multiples of (220). Information on the crystals are given in table 3.4.

γ-energy	Bragg order	count rate	background	acquisition time
6112 keV (2008)	(1,3)	30	8	60 s
6112 keV (2008)	(1,-3)	22	7	60 s
6112 keV (2007)	(1,3)	120	70	60 s
6112 keV (2007)	(1,-3)	120	40	60 s
1165 keV	(3,3)	20	0	20 s
1165 keV	(3,-3)	20	0	30 s
786 keV	(3,3)	30	0	20 s
786 keV	(3,-3)	13	0	40 s
517 keV	(2,2)	60	0	10 s
517 keV	(2,-2)	60	0	10 s

Table 3.3: Count rate in the maximum position. The peak count number includes the background. In 2008 the collimation system was aligned with a new strategy. The numbers come from the VB-algorithm and may contain spurious energies.

Cl-atoms per target mass, which may limit the intensity. Four different transition energies were recorded to have a complete cascade (see Figure 1.14 on 45). The measurement started in November 2007 with the lower energies that were quickly done due to the high count rates and large Bragg angles. Table 3.2 list the scheduling of the various measurements. Table 3.3 gives the corresponding count rates.

3.3.2 Problematic high energy

As expected, the 6112 keV line was the most difficult to measure. Due to the low reflectivity of the crystals and the low efficiency of the Germanium detector the acquisition
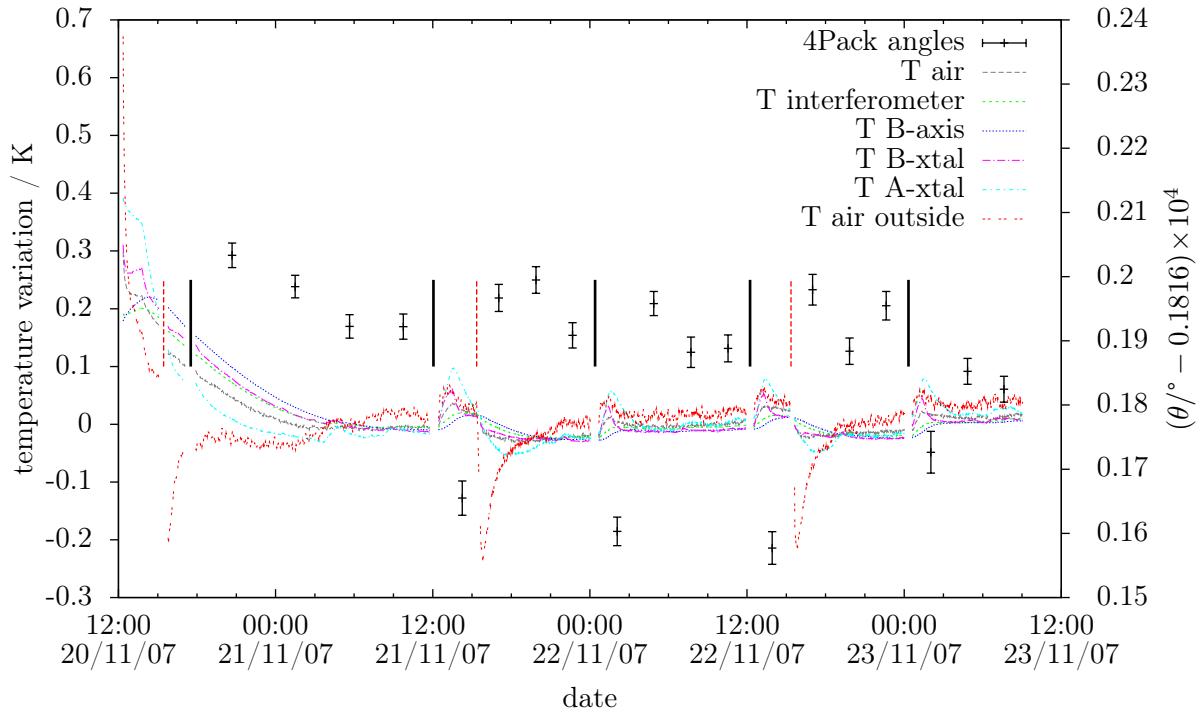
Figure 3.14: Influence of thermal variations on instrument instability. The temperature is perturbed by the filling of the Germanium-detector (vertical line, red dashed), and – more important for the instrument stability – by reference scans (vertical line, solid black). Therefore, this whole data set has been disregarded.

times are rather long, hence the measurement is strongly affected by instabilities. Additionally the Bragg angles are small, thus the same amount of instability causes a large relative effect. Moreover the small Bragg angle forces the detector to be close to the direct (non-diffracted) beam which causes a large background.

The instrument control software is provided with an algorithm that allows to follow a drift of the instrument, such that the observed angle range remains well centred around the Bragg-peak. However for large energies and low signal-to-background ratios this algorithm did not work well. To compensate this, after four 4-packs a reference scan was performed. This is a 2-pack of a 1165 keV in the Bragg order $(3, \pm 3)$. At this configuration, the peak can be tracked easily.

However, as shown in Figure 3.14, these reference scans perturbed the temperature stability massively. The introduced goniometer instability is larger than the one caused by the filling of the Germanium detector with liquid nitrogen which was necessary every 24 hours. The reason for the large impact is the different Bragg angle of the A crystal during the reference scan. This requires to rotate the whole spectrometer table. Consequently the convection changes completely. Additionally, the spectrometer rotation implies a
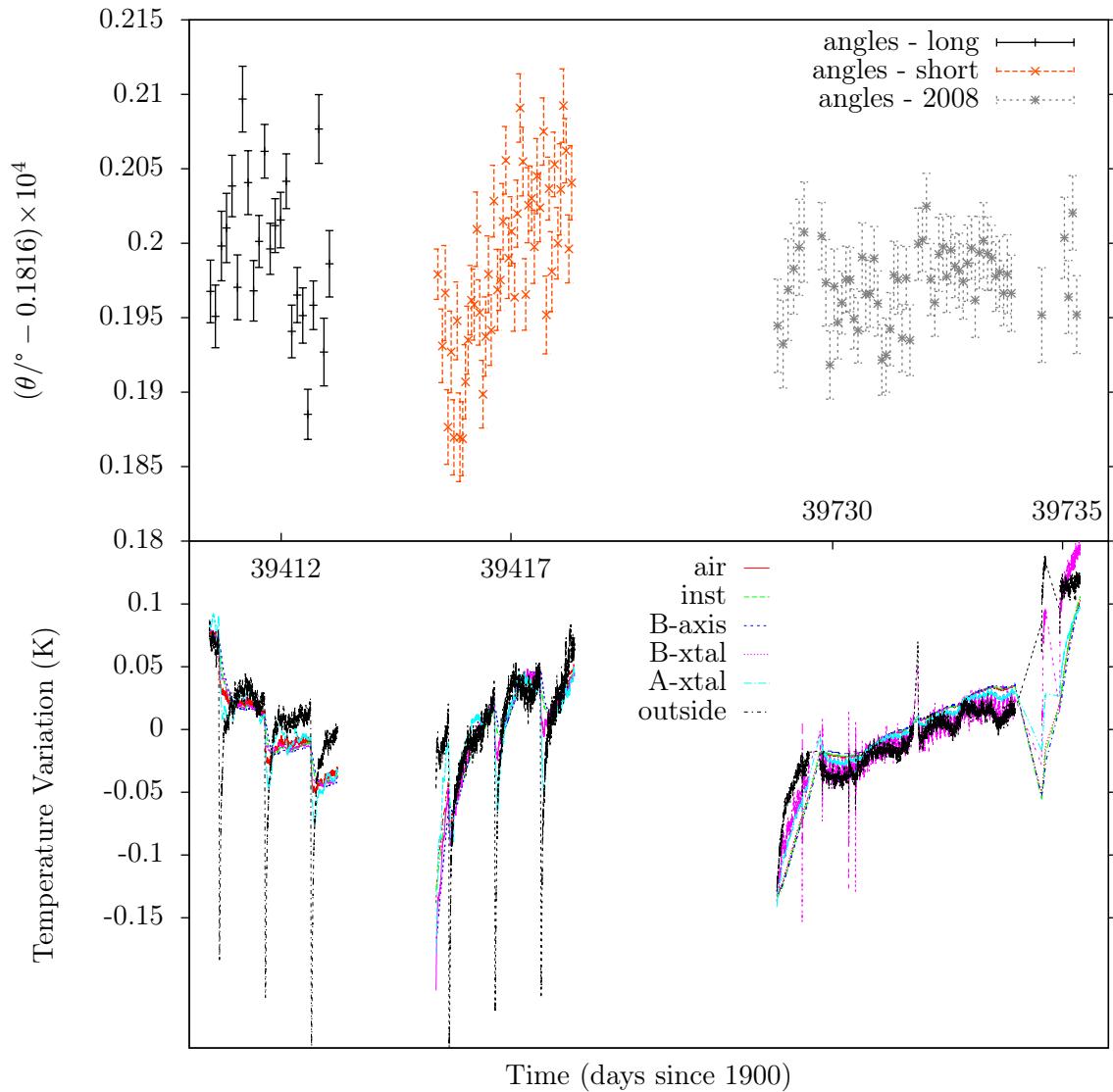
Figure 3.15: Bragg angles of the different 6112 keV data sets, and temperature during the measurement. The temperatures are plotted with a different offset for each data set such that they fit into a common graph. The large temperature peaks in 2007 are caused by the nitrogen filling of the detector. In 2008 the thermal insulation was carefully optimized.

hover cushion, hence thermally unconditioned compressed air is inserted inside the thermal aluminium shield. And the motor heat is much higher than during standard 4-packs. Furthermore the crystal positioning motors are step motors operated in micro-stepping mode. This results in a different heating for different A-crystal positions. It is unclear how much the four effect contribute to the stability. But non of them was avoidable with *Gams4*. All of them will be reduced strongly at *Gams6*.

To succeed with the campaign, the peak-tracking algorithm was improved. Consequently the reference scans could be omitted. After that two data sets with different strategies were recorded: one with a long acquisition time, collecting a good statistic per scan. The second used rather short scans. The necessary counts should be accumulated over many repetitive scans. The second method has the advantage to be less sensitive to instabilities, but there is some limitation imposed by the instrument hardware of *Gams4*: the motors (crystal-axis, collimator and detector) cannot drive at the same time and their speed is rather slow. Therefore changes from the positive to the negative Bragg-order and vice versa take several minutes in which no data can be recorded. It turned out that the short scans resulted in a larger scattering. The standard deviation is 1.2 times as high as for long scans. However, as the number of scans is higher, the resulting statistical uncertainty of the mean is 15% smaller than those of the long scans when comparing a data set of the same total duration. It should be emphasized that these numbers will be different for every other degree of instrument instabilities and motor speed.

The first evaluation of the data was very disappointing, due to large thermal variations the results were still very unsatisfying. Therefore the experiment was repeated one year later, after improving the thermal insulation and installing a temperature-controlled water-cooling for the crystal-axis motors. This was successful: the temperature became much more stable. Though the obtained Bragg angles still showed a large scattering on the 10^{-6} level only after carefully studying and improving the algorithm for the correction on environmental influences the scatter diminished. The successful algorithm was presented in subsection 2.2.2.

3.3.3 Data evaluation

Each recorded angle in each γ-profile was corrected for environmental influences according to section 2.2.2. To each profile a line shape, obtained from dynamical theory of diffraction [Zac45], was fitted via a Maximum-likelihood method [HJ01]. Prior to the fit, the theoretical line shapes were convoluted with a Gaussian, where each Bragg order and energy has a global sigma. This resulted in one goniometer position per profile. These goniometer positions were converted into angles via (2.2) and using the common calibration constant $K = 5133451.09\,\mathrm{f_4/rad}$ which is given in subsection 3.2.6. It may surprise that not the calibration constant measured right after each γ-acquisition is used; but all

crystal name	$d_{(220)}$
ILL2.5	$1.920155822(96) \times 10^{-10}$ m
(ILL2.5 - ILL4/7)/ILL2.5	$4.0(1.0) \times 10^{-8}$
ILL4/7	$1.920155745(96) \times 10^{-10}$ m

Table 3.4: Lattice constants of the silicon crystals. ILL4/7 refers to one 4.4mm thick crystal and one 6.9mm thick crystal made out of the same ingot. ILL2.5 refers to two crystals of 2.5mm thickness made out of the same ingot. The lattice constants are given for 22.5 °C and vacuum. Values from [Dew+06].

calibration performed in 2007 have quite large error bars. And all of them disqualify by either containing bad zero-crossing fits or large thermal perturbations. This unbiased criterion has been explained in subsection 3.2.3. Additionally, when using those individual constants, the 6112 keV angles obtained in 2007 would mismatch with those in 2008. In contrast, using the global calibration constant for all data, they match within one standard deviation.

Four of those angles (belonging to one so-called 4-pack) were combined by making twice a weighted average and then taking the difference of them. The resulting angle differences are then converted into γ-wavelengths by (2.48). The corresponding Bragg order and lattice parameter noted in table 3.2 are used. These values have to be corrected for the atmospheric pressure [McS53; Nye57; Bas+89]:

$$d_{220}(p) = d_{220,\text{vac}} \times (1 - \epsilon p/(760\,\text{Torr})) , \qquad (3.1)$$

where $\epsilon = 0.3452 \times 10^{-6}$. $p = 760$ Torr is used for all data. The relative error induced by this simplification is smaller than 10^{-8}. It should be noted that this correction is based on elasticity-measurements, the actual deformation over 1 bar has never been measured on that level of accuracy. This may be a task for *Gams6*.

Finally, the measured wavelengths λ_{meas} and hence energies E_{meas} have to be corrected for recoil during the γ-emission.

$$\frac{hc}{\lambda_{\text{trans}}} = \frac{hc}{\lambda_{\text{meas}}} + \frac{1}{2Mc^2} \left(\frac{hc}{\lambda_{\text{meas}}} \right)^2 . \qquad (3.2)$$

The obtained values $E_{\text{trans}} = hc/\lambda_{\text{trans}}$ may be summed up and result in the binding energy. The value of $h = 4.135\,667\,33(10) \times 10^{-15}$ eVs has a relative uncertainty of 2.5×10^{-8} [CoData06]. $M \approx 36$ u is the mass of the decaying nucleus.

3.3.4 Vertical angular alignment correction

All measured Bragg-angles given in this section, have undergone a prior correction to the vertical divergence and alignment of the γ-beam. According to [Sch65] the correction is
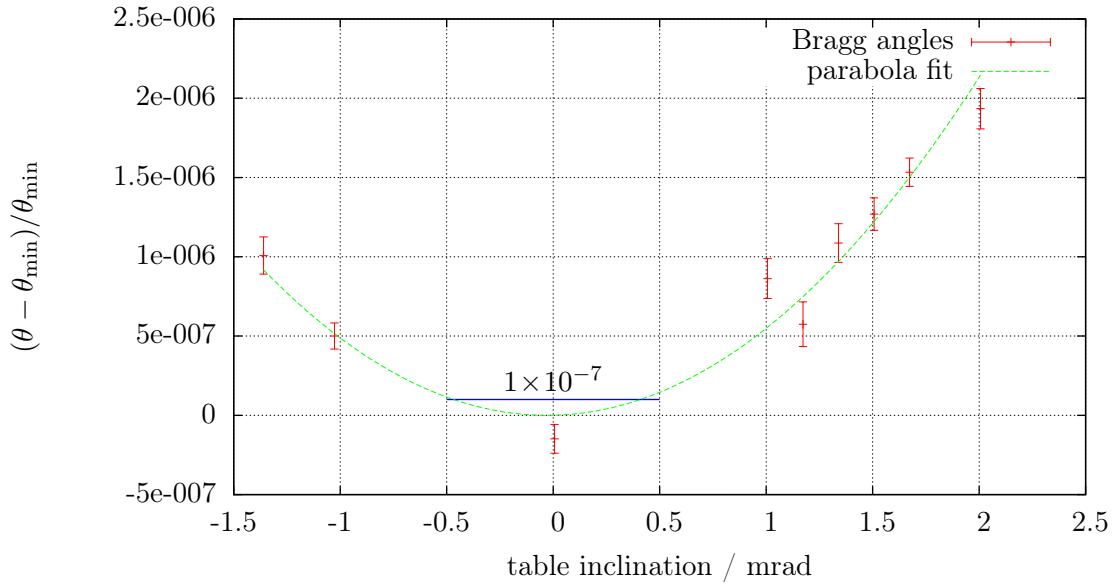
Figure 3.16: Scan of the inclination of the spectrometer table. Positive inclination means that the side pointing towards the rector is pulled up. Shown is the Bragg angle difference θ between the orders (2,2) and (2,-2) of the 517 keV line. The vertical axis is scaled to the minimum $\theta_{\min}$ of a parabola which was fitted to the data.

based on three terms:

a) the divergence of the beam which results from the 40 mm source- and collimation-height divided by the distance of 23 m from target to detector,

b) the orientation of the diffraction plane versus the γ-beam and

c) the orientation of the goniometer rotation axes versus the diffraction plane.

The latter is negligible as the alignment is far better than 60 arc seconds. The correction for (a) can be calculated for each Bragg angle. They are between 8×10^{-8} and 3×10^{-7} in relative size.

The contribution of (b) was measured by tilting the spectrometer platform as shown in Figure 3.16. For the binding energy measurement, the tilt was assured to be in the minimum position. Hence the effect on the data is less than 2×10^{-8}.

3.3.5 Binding energy result

The results of the individual transition energies are listed in table 3.5. Summing up all E_{trans} yields to the binding energy $S_n = 8579797.4$ eV with statistical uncertainty of 1.3 eV which is in relative terms 1.5×10^{-7}. This statistical uncertainty comprises the instrument instability during the γ-acquisition. Several uncertainties have to be added, all

| γ-energy | angle θ | λ_{meas} | λ_{trans} |
keV	degree	fm	fm
6112	0.181619943(38)	0.202887478(42)	0.202887486(42)
1165	0.95284201(21)	1.06437168(23)	1.06437182(23)
786	1.41166425(15)	1.57681199(17)	1.57681219(17)
517	1.43112681(12)	2.39782042(20)	2.39782072(20)

| γ-energy | E_{meas} | E_{trans} | u_{r} |
keV	eV	eV	
6112	6110982.5(1.3)	6111539.3(1.3)	2.1×10^{-7}
1165	1164857.86(25)	1164878.09(25)	2.2×10^{-7}
786	786296.482(86)	786305.700(86)	1.1×10^{-7}
517	517070.298(42)	517074.284(42)	8.2×10^{-8}

Table 3.5: Results for the different Chlorine γ-transitions. The transition energies E_{trans} differ from the measured energies E_{meas} by a correction for recoil.

listed in relative terms: The calibration contribute with 4.1×10^{-8} statistical and 9×10^{-8} systematic uncertainty. The absolute calibration of the temperature sensor is good to $0.05 \, \mathrm{K}$, considering the CTE of silicon this gives an uncertainty of 1×10^{-7}. The absolute determination of the lattice constant accounts for 5×10^{-8}.

This results in total to a relative statistical uncertainty of 1.6×10^{-7} and a relative systematic uncertainty of 1.4×10^{-7}. The combined uncertainty yields to:

$$S_n = (8579797.4 \pm 1.8) \, \mathrm{eV} \qquad u_{\mathrm{r}} = 2.1 \times 10^{-7} \ . \tag{3.3}$$

3.3.6 Predictions for future measurements

Under the assumption that *Gams6* has negligible instability but otherwise performs as *Gams4*, one can estimate the reachable statistical uncertainty by ignoring the scatter between the different 4-packs. Combining the individual uncertainties of the 6112 keV measurements in 2008 yields to a relative uncertainty of 2.2×10^{-8} within 6.5 days. Hence, in three weeks a relative precision of 1×10^{-8} is reachable.

Consequently the systematic uncertainty has to reduced as well. With state of the art thermometer equipment an absolute accuracy of $1 \, \mathrm{mK}$ is feasible. This will reduce the corresponding uncertainty to 3×10^{-9}. The corresponding equipment will be provided by collaboration partners from INRIM.

The uncertainties of the calibration could be reduced sufficiently maybe even with *Gams4*, though this would require very time consuming studies of the gear-coupling delay. With

Gams6 there is a very good chance that this problem is gone, if not, it can be studied sufficiently within a day.

3.3.7 Comparison with literature

The results can be compared to [Dew+06] and [Kes+85] which describe the same measurement with the very same apparatus. The values of the individual γ-transitions are listed in table 3.6. The uncertainties for the binding energy obtained here are a factor of 2.7 smaller than in [Dew+06]. The values match within the uncertainties.

A comparison to the molar Planck constant is not possible at this point, as the uncertainties in the mass determination of the chlorine ions are huge. However, the equipment for those measurements exists, as it has been proven with the measurement of the sulfur and silicon masses. Yet community needed the motivation to conduct the measurement [Mye07].

3.3.8 Summary

The Chlorine-36 binding energy was measured in 2007–2008. While the low transition energies were unproblematic, the 6112keV line required improvements on the experiment. Any rotations of the spectrometer table must be strictly avoided; this makes reference scans impossible. They could be omitted after optimizing the instrument software. Furthermore, the thermal stability could be improved by better insulation and installing a controlled and active motor-cooling. The residual thermal instabilities could be compensated by developing a better correction algorithm. A new test for the vertical alignment of the spectrometer was performed for the first time. All this improvements resulted in a reduction of the uncertainty of the chlorine-36 binding energy by a factor of 2.7. It could be shown, that after an improvement of the instrument stability and thermometer calibration it will be possible to achieve a relative uncertainty of 10^{-8} within a few weeks.

| reference	year	$E_{\text{trans}}/$ eV	$E_{\text{trans}}/$ eV	$E_{\text{trans}}/$ eV
[Kes+85][a]	1984	517070.10(23)	786297.02(39)	
[Dew+06]	1997	517069.62(22)	786296.43(53)	6110980.2(4.0)
This work	2007	517070.298(42)	786296.482(86)	6110982.5(1.3)

Table 3.6: Comparison of transition energies ^{36}Cl with literature values.

[a]values are adjusted for changes in h and d_{220}, following [Dew+06].

3.4   Further limitations of *Gams4*

To trace down the reasons for the instability of the instrument, a γ-transition was measured over several days. The measured energies were compared with all available parameters. A correlation was found with the humidity of the air as shown in Figure 3.17. However the goniometer readout follows the humidity with a delay of about 10 hours. This fact would be explained by a humidity sensitivity of the glue f used for bonding the interferometer optics. This behaviour is known since 2002 and is sort of the origin for the idea of a major upgrade of the instrument.

Figure 3.18 shows a remarkable effect of the environmental conditions at the experimental site. The ILL reactor is hermetically enclosed and for security reasons kept at roughly 5 mbar below the external atmospheric pressure. The pressure curve reveals that the pressure inside the reactor oscillates with an amplitude of about 1 mbar and a rough period of 23 minutes. A closer analysis shows that the amplitude is more stable than the period. This leads to the assumption that the pressure control has a resolution or set-pint of 1 mbar. And the time constant of the pressure leaks is about 23 minutes. It was verified that this oscillation is not a local effect at *Gams4*. It appears as well at *Gams5* which is situated 30 m away at the opposite end of the reactor hall. As the compression is small and happens rather quickly it can be considered as adiabatic. This means that the air cannot exchange heat with the walls or any other material, and hence will change temperature. The effect is too small to affect *Gams4* at the current level, but it would perturb *Gams6*.
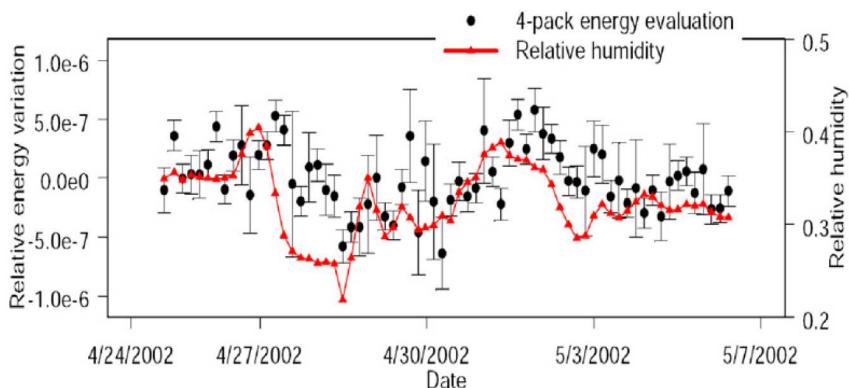
Figure 3.17: Instability of *Gams4* due to humidity. The measured energy is correlated to the humidity with a delay of about half a day. Graph from [JKM09]
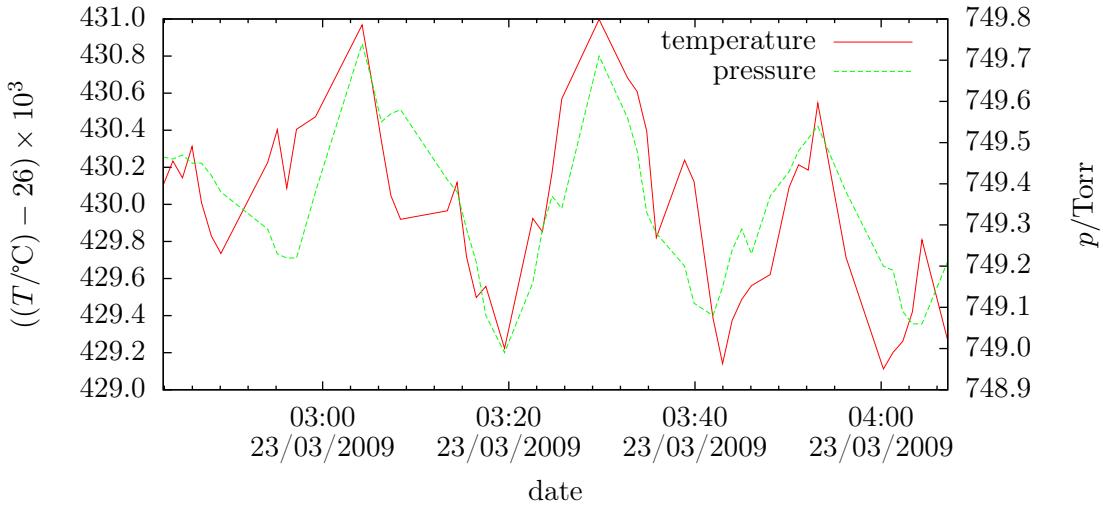
Figure 3.18: Adiabatic pressure oscillation inside the reactor building cause temperature oscillation. The temperature T oscillates with an amplitude of 1 mK, the pressure p with 0.7 Torr which is 1 mbar. The oscillation period is about 1500 s.

3.5   Summary

The instrument has been calibrated over 14 month, leading to a calibration constant whose uncertainty is a factor 2 better than ever before. The chlorine-36 neutron binding energy has been measured with an uncertainty being a factor 2.6 better than ever before. At the same time the relative accuracy of this binding energy is a factor 1.8 better than any other element that have a binding energy above 8 MeV – in other words everything except deuterium.

The key to these improvements was, besides the thermal stabilization, the new algorithm for correcting the goniometer read out for environmental parameters.

Furthermore, it was shown, that a relative precision of 2×10^{-8} will be reachable with *Gams6* in four weeks of beam time.

For the γ-acquisition a new systematic test has been introduced with measuring the vertical angular alignment.

Several problems in the calibration procedure were revealed. They were analysed carefully, such that the level of accuracy could be increased sufficiently for the present measurement. Strategies were developed how to successfully overcome those issues with *Gams6*.

Chapter 4

New instrument

The new instrument called *Gams6* bases on many concepts of *Gams4*. In this chapter only the improvements will be explained. The spectrometer theory is explained in chapter 2.

For a better understanding, the description of the improvements is split into individual independent parts: the target inside the reactor, the front collimation, the spectrometer table with two crystals and the interferometer, back collimation and detector. The critical part for the instrument stability – which needs a major increase – is the spectrometer. Thus most research was invested here. The other parts have undergone a slight development to improve the signal-to-background ratio or to increase the ratio between acquisition time and maintenance time by e.g. faster motor movements.

4.1 Interferometer

Many high resolution angle measurements are realized via a transfer towards a displacement measurement. A review of displacement measurement techniques and involved problems can be found in [Bob93]. A particular role in displacement measurement techniques is played by displacement interferometry [Law04; MNH79; DG70]. It combines several advantages, as it yields a very good accuracy down to 10 pm and it provides an extraordinary high dynamic range of more than eleven orders of magnitude. Two types of displacement interferometers are realized nowadays: homodyne and heterodyne. In the first case only one laser wavelength is used in all branches of the interferometer. The displacement dependence of the interference pattern is intensity encoded. These interferometers require a high intensity- and frequency-stability of the light source. In the case of heterodyne interferometers, different branches of the interferometer use an individual laser wavelength. Consequently the interference pattern has a time dependent intensity modulation and

the displacement information is phase encoded in the modulation. In this type of interferometer only frequency stabilisation is required for the price of an additional reference signal because phase measurements are always relative. A particular advantage of the heterodyne type is its capability to detect the direction of a displacement without further effort.

A contrary example is the use of accurate homodyne interferometry for the determination of the lattice parameter of silicon as described in [BCM93] and [FMM08].

4.1.1 Heterodyne interferometry

Heterodyne interferometry uses two beams with slightly different wavelengths. In a simple model, a beam can be described fully at each point by its amplitude A_1, frequency ω_1 and phase ϕ_1; A_2, ω_2 and ϕ_2 describe the second beam, correspondingly. A wave propagating in a medium with the speed of light c' is described by:

$$S_1(t, x) = A_1 \times \sin\left(\omega_1 t - c' s - \phi_1'\right) \ , \tag{4.1}$$

The phase $\phi_1 = c' s_1 + \phi_1'$ contains all information about the geometrical path length s_1 a beam has travelled up to that point. Though, it requires the original phase offset ϕ_1' to stay constant. If the path length difference $s_1 - s_2$ is of interest, only $\phi_1' - \phi_2'$ has to stay constant. This is the case when both beams emerge of the same laser.

It should be noted that the optical path length $s' = s\frac{c}{c'} = s\eta$ is a more descriptive quantity, as the refractive index η of passed materials can change, while the vacuum speed of light c is constant.

When two beams overlap at a certain point, a detector observes a beating signal which oscillates with the frequency difference of the beams. If both beams are of the same amplitude A, the detection intensity D can be calculated as:

$$D(t) = A^2 \times \left(\sin(\omega_1 t - \phi_1) + \sin(\omega_2 t - \phi_2)\right)^2 \tag{4.2}$$

$$= A^2 \times \left(\cos\left(\frac{\omega_1 + \omega_2}{2} t - \frac{\phi_1 + \phi_2}{2}\right) \times \sin\left(\frac{\omega_1 - \omega_2}{2} t - \frac{\phi_1 - \phi_2}{2}\right)\right)^2 \tag{4.3}$$

$$= A^2 \times \cos\left(\frac{\omega_1 + \omega_2}{2} t - \frac{\phi_1 + \phi_2}{2}\right)^2 \times \frac{1}{2}\left(1 - \cos\left[(\omega_1 - \omega_2)t - (\phi_1 - \phi_2)\right]\right) \ . \tag{4.4}$$

The left part oscillates with the average frequency $\frac{\omega_1 + \omega_2}{2} \approx 4.7 \times 10^{14}$ Hz. This frequency is in the optical domain and therefore assures that the signal can be detected by a photo diode. The photo diode will convert this component to a DC current. The right part acts as a time modulation of the current. Notably this modulation inherits the phase properties of the beams.

Previously, heterodyne laser sources generated the two frequencies using the Zeeman effect. The most common model, which is also used in *Gams4*, was the HP-5501B laser providing a beating frequency of 1.8 MHz. Modern concepts base on acousto-optic modulators (AOM). In these devices a frequency shift of laser light is obtained as a result of inelastic Bragg scattering of the light on a travelling density wave in a transparent medium. This technique gives a free choice of the beating frequency in the range of 0–400 MHz to the experimenter. For *Gams6* 100 kHz are used as a compromise of electronic accuracy and available bandwidth.

The interferometer signal (measurement signal) is detected according to (4.4) as a oscillating sine signal. In order to retrieve the phase of this signal, it needs to be compared to a second signal of the same frequency. This so-called reference signal is typically generated by an additional superposition of the laser beam branches before the impact of the path length variation. In the case of a beating generated by AOMs, the reference can be deduced from the signals that drive the AOMs.

The comparison of the reference and the measurement signals can be realized by electronic devices like a time-interval counter or a lock-in amplifier.

So far, the considerations or heterodyne interferometry are based on the assumption that in each branch of the interferometer exactly one frequency is present. However, in practice this condition is fulfilled only approximately. In particular, the lasers based on the Zeeman effect provide a laser beam which is contaminated with a so-called frequency mixing. In each branch a slight component of the wrong frequency is contained. This generates a beating modulation which does not depend on the displacement to be measured by the interferometer. The general signatures of this effect are well-studied [WD98; Sut87; AD90] and pronounce themselves as a periodic non-linearity in the measured signal of the interferometer as a function of displacement.

Any interferometer layout aiming for high accuracy has to be designed such that this mixing is suppressed as much as possible. This is particularly important for *Gams*, as there are only few calibration points and these are at large distances. Hence a correction of periodic non-linearities is very difficult.

4.1.2   Old interferometer layout

Gams4 used a simple Michelson layout to measure the axis angles as illustrated in Figure 4.1. The HP5501B laser provides the two frequencies within the same beam, separated by perpendicular linear polarization. In the interferometer, the laser beam is split at the central polarising beam splitter cube *a*. This provides the frequency splitting for each interferometer branch. Both beams are guided by mirror prisms *d,e,f* to two retro reflectors *l,m* sitting on each end of the goniometer arm. Each beam path continues

to a roof prism *j,k* which reflects the beam by 180° but displaced in height. The beams return their way through the retro reflectors back to the splitter cube *a* which now serves as beam combiner. From there the beam goes on to the detector. Some $\frac{\lambda}{2}$-retarder plates *b,c*, which are passed only once, rotate the beam polarization, and thus the beam is deviated to the detector instead of going back to the laser. Two Glan-Thompson prisms *i,h* are used to clean for components of the wrong polarization and thus the wrong frequency. A compensating element *g* ensures that both beams pass through the same amount of glass. This is important as optical path length is heavily influenced by the refractive index of the material. This changes with temperature. For usual materials it influences the optical path length stronger than the thermal expansion.

An exact copy of this is used to measure the angle of the second goniometer arm.

Weak points

The central beam splitter which provides the frequency separation is cube-type. The separation power is far from being sufficient. Additionally the frequency separation, provided by the HP5501B-laser, is hardly better than -50 dB. This leads to frequency mixing and thus to periodic non-linearity in the interferometer response function on the nanometre level [LK00].

The layout of each interferometer was chosen such that the optical path length in the zero position as well as all paths in glass are the same for both branches. Hence they will compensate for global temperature changes and consequent changes of the refractive index. However, this layout is not able to compensate movements of the optical elements themselves. Any of such a drift would falsify the measurement without a possibility for the experimenter to notice.

This is probably the dominating effect of the *Gams4* instrument instability. The optics were mounted on asymmetric alignment elements and bonded with a humidity sensitive glue. A stability test showed a correlation with humidity. See section 3.4 for details.

Furthermore, the old set-up consisted of two separate interferometers mounted on individual support plates. If these plates drift with respect to each other, the angle measurement will be wrong, again without any mean to notice.

The reference signal was taken right at the laser, which is some optical elements and distance away from the interferometer. Any change of the birefringence in the optics may introduce a phase shift and hence a wrong measurement.

The laser was placed under the interferometer, and hence introduces thermal gradients and probably also thermal instability.

Each of these points is faced with the new interferometer layout.
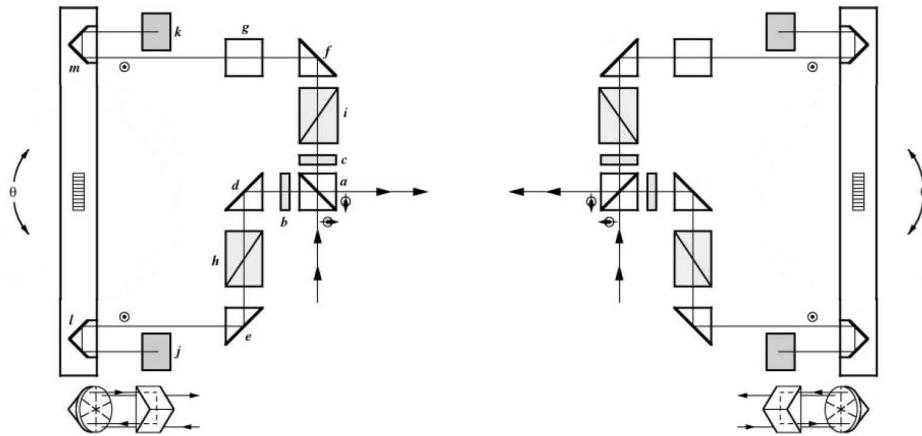
Figure 4.1: *Gams4* interferometer layout. The goniometer arms with the diffraction crystals are on the very left and very right. See text for an explanation. Graph taken from [Kes+01]
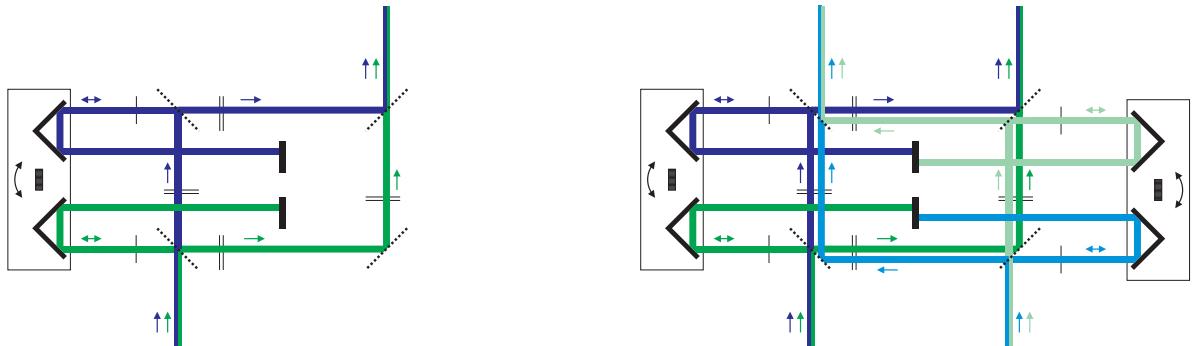

(a) Interferometer layout for one side or axis only. It is a combination of Michelson and Mach-Zehnder interferometer. The laser is injected at one spot; the two frequencies must be separated by perpendicular polarization.

(b) Layout for two sides or axes. The same polarizing mirrors are used for both sides. A second laser also providing two frequencies – again separated by polarization – is injected at a different spot. It may be a copy of the first one, created by a non-polarizing beam splitter. Beams for left and right axis may overlay.

Figure 4.2: Scheme of heterodyne interferometer. The moving mirrors (solid black lines) on the sides can be replaced by corner cubes to obtain a goniometer. Only four polarizing mirrors (dashed black lines) are necessary for both interferometers. Retarder plates ($\lambda/4-$thin black lines, $\lambda/2-$thin black double-lines) are used to guide the different frequencies to the correct path. The laser source must provide two frequencies, separated by perpendicular polarization. For simplicity, the retro-reflectors are illustrated by two flat mirrors (thick black lines).
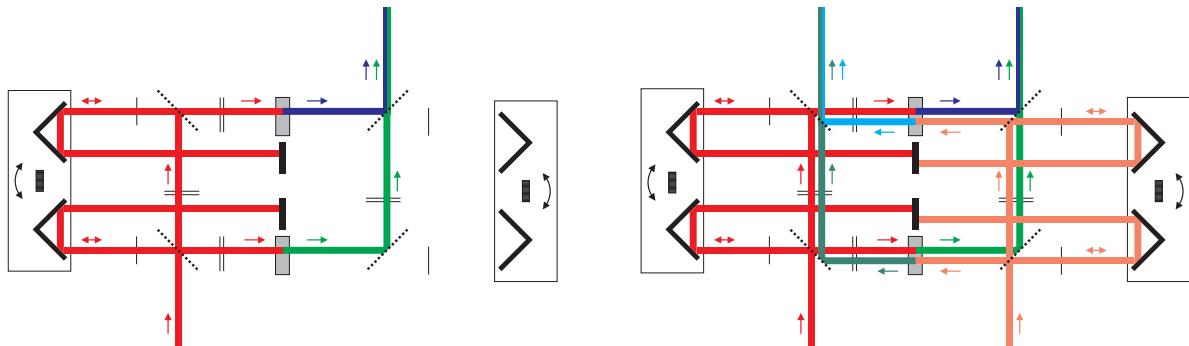
(a) Layout for one side or axis only. Monochromatic laser light is injected at one spot. After passing the measuring path, it is frequency shifted by AOMs (grey boxes) to two different frequencies. They overlap in the detector and induce a beating signal.

(b) Two sides or axes. A second laser is injected at a different spot. The AOMs are used from both sides. The beams for left and right axis may overlay.

Figure 4.3: Interferometer layout using AOMs inside the interferometer. The monochromatic laser source provides a single frequency. The light is still homodyne when passing through displacement mirrors. It is shifted by AOMs into two different frequencies before recombination.
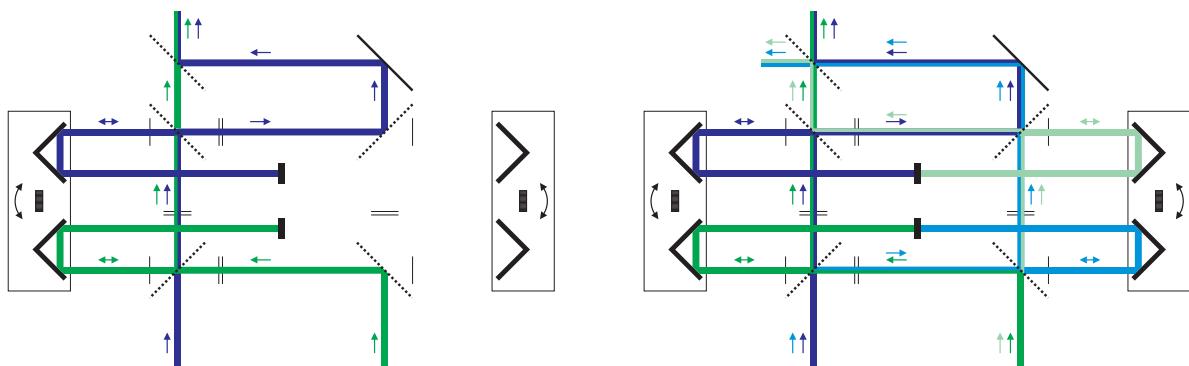
(a) Layout for one side or axis only.

(b) Layout for two sides or axes. The beams for left and right axis *must* overlay. Frequency separation is done by polarization.

Figure 4.4: Interferometer layout with no AOM inside. Two lasers with slightly different frequencies are injected at two different spots.

4.1.3 New interferometer layout

In order to explain the functionality of the new interferometer it appears useful, to follow a stepwise description which recalls the design process. Each step provides a fully functional interferometer which may find its niche application.

In the first step the fixed part of the interferometer is reduced to only four polarizing beam splitters. Some additional retarder plates are necessary, but very thin and do not influence the optical path length. As illustrated in Figure 4.2(a), the layout is not fully Michelson-like. Beam splitting and recombination occur at different spots. It resembles much more a Mach-Zehnder interferometer. However, the measure device is still a displaced mirror which is hit under 90°, and the optical path to this mirror is travelled twice by the laser beam.

The big advantage of this layout is the extendibility to two sides without any new optics. As illustrated in Figure 4.2(b), a second laser is injected at a different spot. Then, the same optics is used to measure another axis on the opposite side.

The intention of the second step was to get rid of the Zeeman-stabilized helium-neon laser and its frequency mixing [KJM06]. The layout was modified such that a monochromatic laser is used to supply the interferometer (see Figure 4.3(a) and 4.3(b)). The light runs like in a homodyne interferometer, but before recombination each beam is frequency-shifted by an AOM. Both beams are shifted to provide a symmetric dependence on possible drifts of the AOM. Though, each beam has a slightly different frequency, typically 40.05 MHz and 39.95 MHz, resulting in a 100 kHz beating.

In the third step, see Figure 4.4(a) and 4.4(b), the AOMs were brought out of the interferometer to avoid the heating of typically 50 mW. The laser beam is split outside the interferometer and both parts are shifted by different frequencies. These two beams enter the interferometer at different spots. To provide a working interferometer two additional optical elements are necessary to make the corresponding beams overlapping. In this layout the beams for the two axes cannot be separated spatially. All separation has to be done by polarization.

In the fourth step this spatial separation is re-established as illustrated in Figure 4.5. At the same time the practical realization of the layout is faced. So far all mirrors and polarizing beam splitters were assumed to be (infinitely) thin surfaces. However real beam splitters require a substrate. A common splitter is a cube that consists of two right angled prisms that are in contact on their hypotenuse-surfaces. The contact got a special coating which defines the reflection, transmission and polarization properties. These cubes match the theoretical thin surfaces quite well. However the perpendicularly passed entry and exit surfaces cause unavoidable reflections. This causes periodic non-linearities [Wu03]. Consequently, surfaces perpendicular to the beam should be avoided. Additionally those cubes deviate the transmitted beam due to imperfect manufacturing.
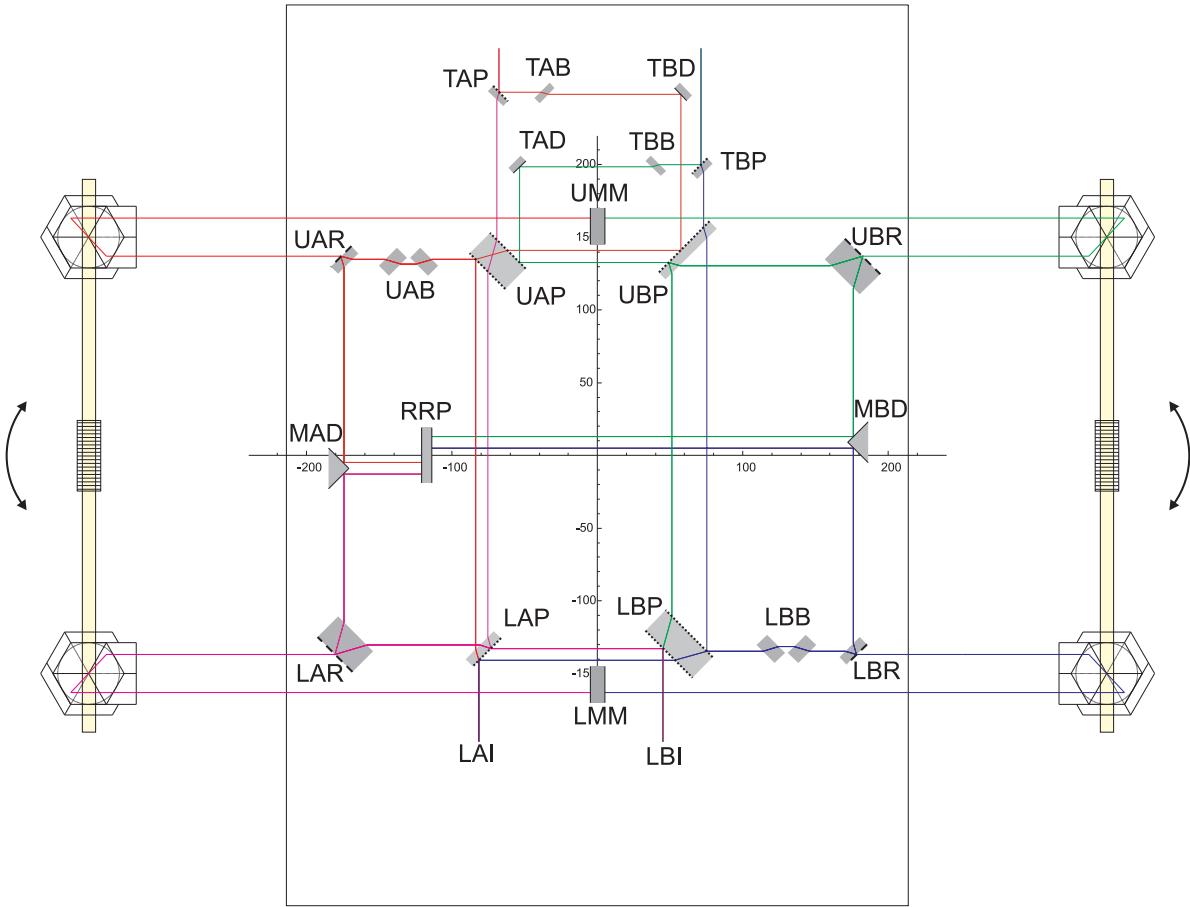
Naming conventions:

First letter – position on z-axis:
L – lower side of the map and close to the laser;
M – middle part, used for reference beams;
U – upper side of the map;
T – top, close to the detector and serves for recombination of the beams.

Second letter – position on x-axis:
A – A-axis of spectrometer, the γ-beam arrives here first. on the left side of the layout-map.
B – B-axis of spectrometer,

Third letter – function:
P – polarizing beam splitter,
R – reference beam splitter (non-polarizing),
D – deviation of the beam,
B – balancing, to provide same path length inside material,
I – injection of the laser beam.

Exceptions are LMM and UMM – main mirrors and RRP – reference roof prism.

Figure 4.5: The final interferometer Layout in a true to scale scheme. The optics is realized by substrates (grey boxes) with parallel and flat surfaces that got different coatings: full mirror (solid black lines), polarization dependant mirror (dotted line), non-polarizing semi-mirror (dashed line) or anti-reflection (no line). Retarder plates are not drawn. All beams lie within a plane, except the second half of the reference beams, that are shifted through the roof prism RRP by 7 mm to a parallel plane. See Figure 4.4(b) for the direction of the light. The coordinate system is described in subsection 2.1.6.

With these deviations the proposed layout is difficult to build, as each optics is used for several beams. Hence, there are more alignment constraints than free parameters, and no deviation can be compensated. Possible substrates for the reflection surfaces are flat cuboid substrates. They can be produced sufficiently flat, such that the beam is not deviated. If placed in a 45°-angle they displace the beam and can provide all necessary reflective properties by different coatings (none, polarization dependent and full reflection). Furthermore a stable mounting (see section 4.1.8) is easier with this solid cuboid-shaped substrates. The layout provides the possibility to be upgraded with an additional beam to monitor the effective length of the goniometer arm. However, at the current stage this does not seem to be necessary, and is not scheduled so far.

Further variations of the basic layout were studied. The one described in step four and Figure 4.5 was chosen as best compromise. It was found to be the only one providing all of the following advantages.

- The beams towards the retro reflectors are symmetric. If all four beams to the retro-reflectors have the same distance to the goniometer axis, systematic effects can be studied much easier, and some drift effects are even compensated by this symmetry.

- Frequencies are separated spatially throughout the interferometer. The alternative separation by polarization can never be perfect and would hence cause periodic non-linearities.

- A more stable laser than those based on the Zeeman-effect can be used.

- No heat sources inside the interferometer. Any AOM inside the interferometer would cause thermal gradients and eventually interferometer instability.

- The layout can easily be equipped with reference beams.

- There are no surfaces perpendicular to the beam. Consequently there are no residual reflection which would cause periodic non-linearities.

However, it implies also some negative aspects.

- There are additional optics necessary to make all paths to be of the same length. Even though the total path length difference $(B_{\mathrm{sig}} - B_{\mathrm{ref}}) - (A_{\mathrm{sig}} - A_{\mathrm{ref}})$ would be balanced, small asymmetries introduced during the mounting process would cause asymmetric drifts. This would reduce the auto-compensation feature.

- The optical paths are not of the same length. As the interferometer is operated in vacuum only, this is less critical. Only small residual effects caused by the beam divergence remain. To monitor these effects over time, the length of the reference beams was chosen to be asymmetric as well.

- Parallel flat optics can shift the optical path length when rotated around an axis which is not parallel to the beam. This effect is much stronger when the substrates are passed in an 45° angle than passing them perpendicular. Consequently the substrates must be fixated rigidly concerning rotation. However, the reference beams compensate most of this effect.

- The retarder plates can not be fixed onto the main optics – as it would be possible with beam splitter cubes. Consequently the retarder plates require individual mountings. Fortunately they are very thin, consequently any drift has no significant influence on the optical path length. And finally most retarder plates are monitored by the reference beams. A small influence on the polarization does not matter, as polarization is only used for intensity optimization.

Auto compensation

One big feature of the layout is the auto-compensation of drifts of the optics. If any of the main optics (polarizing beam splitter or main mirror) drifts, the interferometer of one goniometer axis will provide a false readout. However, exactly the same drift is also seen by the other interferometer side since it uses the same element. This will result in the same false readout. Consequently the difference is independent from any drift. As the *Gams* spectrometer depends only on the angle of the two crystals relative to each other, the total result does not depend on any drift. However this is only true, if both goniometer arms are of the same length. If they are not, any drift is suppressed by the ratio between the arm length difference and the average arm length. Considering the design of the interferometer arm and the retro reflectors, achieving the same interferometer arm length, i.e. distance of the optical centre or the corner cubes, should be feasible within 0.1 mm or better. Together with an arm length of 300 mm this results in a drift suppression of 1/3000 or better. Considering the target accuracy of 2×10^{-8} this means e.g. for the main mirror a possible drift of ~ 50 nm without consequence. Without the compensation effect a stability of ~ 20 pm would be required.

4.1.4 General goniometer theory

So far, the goniometer-interferometer relation was always reduced to equation (2.2), sometimes extended by diverse offsets of angles and interferometer readout. This relation including all the extensions assume an ideal interferometer. The real interferometer will show deviations from this behaviour due to unavoidable things like misalignment of laser beams or non-centric bearings of the goniometer axes. The size of the consequences on the accuracy of the goniometer have to be estimated. Therefore it is necessary to know which projections of which length do finally impact on the readout.

The intention of the goniometer is to measure the rotation of the crystal around a vertical axis. A goniometer arm is used to amplify the arc length of this movement. At each end of this arm a retro reflector is mounted. The interferometer monitors the displacement of these reflectors. As explained below, retro reflectors of corner-cube type reflect the beam in a way that the path length of the beam is independent from the orientation of the corner cube or the incident point of the laser.

Properties of perfect corner-cube retro-reflectors

Retro reflectors are defined from the property to reflect back light parallel to the incident direction; independent from the orientation of the beam with respect to the retro reflector. They exist as cat eye or as corner cube type. Only for the latter the total path length of the beam is independent from its position. Already [Pec48] studied the use of corner cubes within a Michelson interferometer. These corner cubes consists of three reflecting surfaces which are pairwise perpendicular. A typical former production was to cut a corner from a cube of glass and hence to form a three-sided pyramid.

The present corner cubes are hollow that means that the full light path is in vacuum, not in glass. The actual way of production is described in section 4.1.7 where the cubes are characterized. The advantages against the solid glass-type is explained there as well.

The main properties of perfect corner-cubes are:
 - A perfect corner cube reflects a beam anti parallel to its incident direction.
 - The distance between incident and reflected beam is invariant to rotations around its optical centre, which is for the new hollow corner cubes identical to the geometrical corner.
 - The total path length of a light beam is independent on its incident spot if measured along the incoming light direction. This is not trivial as the interferometer layout requires a "main mirror" which is perfectly perpendicular to the beam.
 - The total path length of the beam does not change when the corner cube is translated perpendicular to the incident light direction. Though the light spot travels on the main mirror, hence this must be very flat to not change the laser path length.

Goniometer with two perfect corner cubes

The interferometer measures the projection of the corner cube movement on the laser beam. However, several deviations from a perfect situation can occur.
- The movement of the axis may be not a plane rotation, but any irregular movement in three dimensions. The consequences of such an movement and the required perfectness are described in section A.1. A characterization of the actual axes is given in section A.1.
- The interferometer measures two corner cubes on an axis. The results of these measures
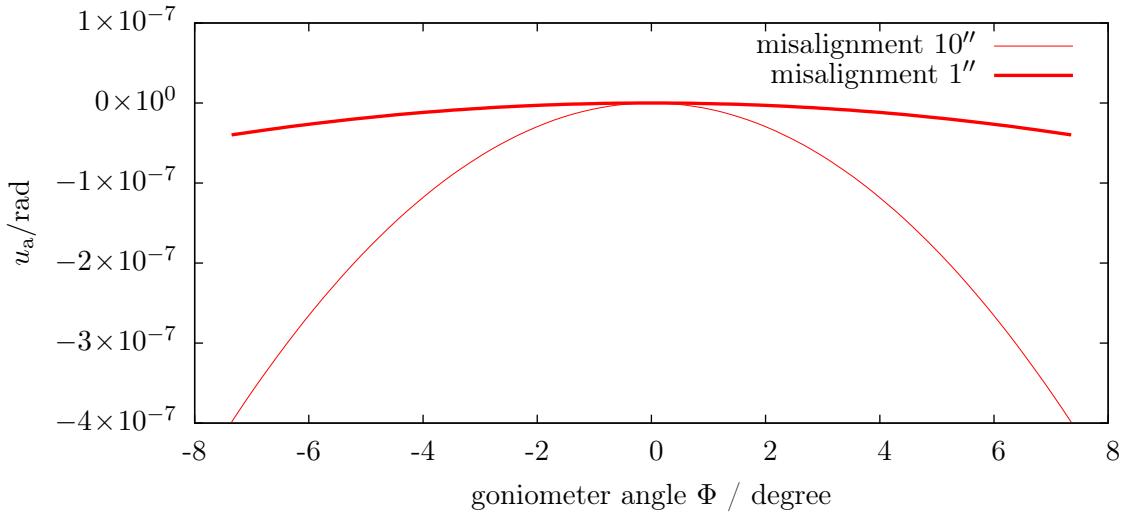
Figure 4.6: Wrong interferometer readout due to horizontal misalignment of the interferometer beams towards the corner cubes.

add linearly. However, if the laser beams towards the corner cubes are not parallel this leads to non-linearities. This is explained in the next paragraph.

If the rotation itself is perfect, and both interferometer beams are parallel, it still might be the case that the axis of rotation is not perpendicular to the plane formed by the interferometer beams. In this case only the rotation projected on this interferometer plane is measured. Consequently also a projection of the Bragg angle will be measured. it is necessary to align axis and interferometer plane within $30''$, to keep the relative uncertainty below $1 - \cos(30'') \approx 2 \times 10^{-8}$.

Horizontal alignment requirements for interferometer beams

If the two laser beams are parallel, they form a Euclidean plane. If one of the lasers is slightly misaligned by an angle ξ within this plane, its "zero" angle changes, and thus its interferometer equation (2.2) from:

$$F = K/2 \sin(\Phi)$$

to

$$F = K/2 \sin(\Phi + \xi) \ .$$

The assumption that both corner cubes contribute equally to the interferometer read out is quite good, and so the calibration constant K is "split" equally between both corner cubes. For simplicity the interferometer zero F_0 is left away.

The combined readout of both corner cubes is then:

$$F = K/2 \times \sin(\Phi) + K/2 \times \sin(\Phi + \xi) \ . \tag{4.5}$$

If one tries to deduce the original goniometer angle from this read out via equation (2.2), one obtains:

$$\Phi' = \arcsin\left(\frac{K/2 \times \sin(\Phi) + K/2 \times \sin(\Phi + \xi)}{K}\right) \tag{4.6}$$

The absolute incorrectness $\Phi' - \Phi$ of the obtained read out is illustrated in Figure 4.6. If one tries to estimate relative incorrectness of such a measurement between an arbitrary goniometer positions Φ_1 and the zero position $\Phi_2 = 0$, one retrieves large values. These values, illustrated in Figure 4.7 would indicate the necessity of either very parallel interferometer beams of far better than $1''$, which is impossible, or the need for a quadratic correction of (2.2) as suggested in (2.62) on page 83.

However, the estimation the relative incorrectness of a measurement between the goniometer positions Φ_1 and Φ_2, both arbitrary, yields:

$$\frac{\arcsin\left(\frac{\sin(\Phi_1)+\sin(\Phi_1+\xi)}{2}\right) - \arcsin\left(\frac{\sin(\Phi_2)+\sin(\Phi_2+\xi)}{2}\right) - (\Phi_1 - \Phi_2)}{\Phi_1 - \Phi_2} \ . \tag{4.7}$$

The illustration in Figure 4.8 show the high correctness with moderate alignment requirements of $80''$. It should be noted that the offset is not important, as the goniometer is calibrated afterwards. Important is that the difference between the error of a polygon angle of $15°$ and of the smallest angle in a ^{36}Cl binding energy measurement of $0.2°$ is lower than the desired relative accuracy of 2×10^{-8}.

Vertical alignment requirements for interferometer beams

If the second interferometer beam is misaligned in the vertical direction, strictly spoken the interferometer plane is not defined any more. But the original plane without misalignment can be considered as this plane to estimate the incorrectness.

In this view, the beam tilted by an angle ξ experiences a change in path length elongated by the factor $\frac{1}{\cos(\xi)}$. This results in a relative incorrectness of a measurement between the goniometer positions Φ_1 and Φ_2, both arbitrary, if:

$$\frac{\arcsin\left(\frac{\frac{\sin(\Phi_1)}{\cos(\xi)}+\sin(\Phi_1)}{2}\right) - \arcsin\left(\frac{\frac{\sin(\Phi_2)}{\cos(\xi)}+\sin(\Phi_2)}{2}\right) - (\Phi_1 - \Phi_2)}{\Phi_1 - \Phi_2} \tag{4.8}$$

As illustrated in Figure 4.9 a parallelism of $80''$ is sufficient for the desired accuracy.
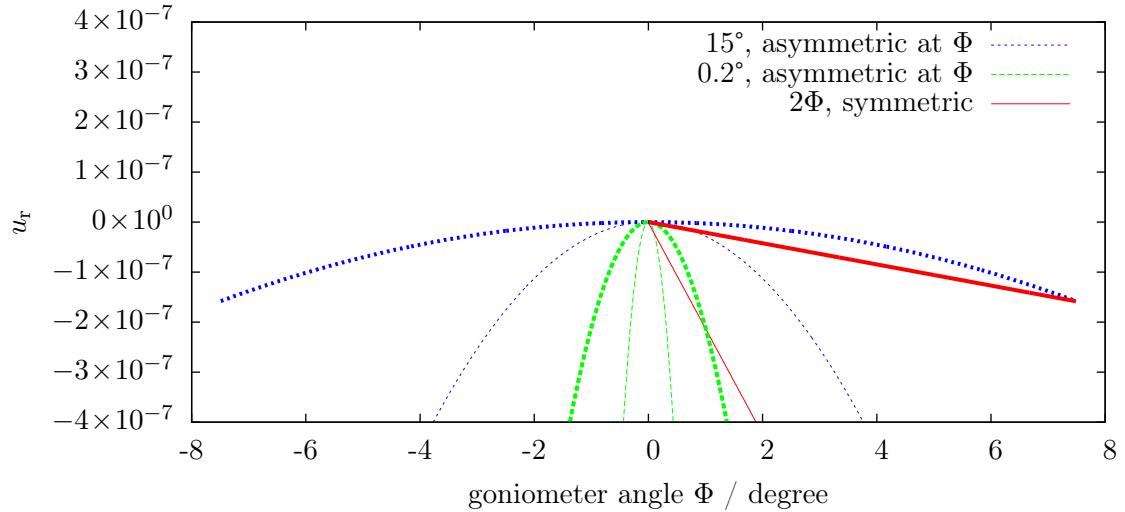
Figure 4.7: Resulting relative error in an angle measurement due to horizontal misalignment of $10''$ (thin line) and $1''$ (thick line). This would require very parallel beams to reach a relative accuracy of 10^{-8}. However, this is a result of a simple interpretation of Figure 4.6 and it is irrelevant for angle difference measurements conducted in binding energy measurements. An interpretation which is more meaningful to this is found in Figure 4.8. This graph is only presented here to allow error estimations in future if *Gams6* is used in an unintended mode.
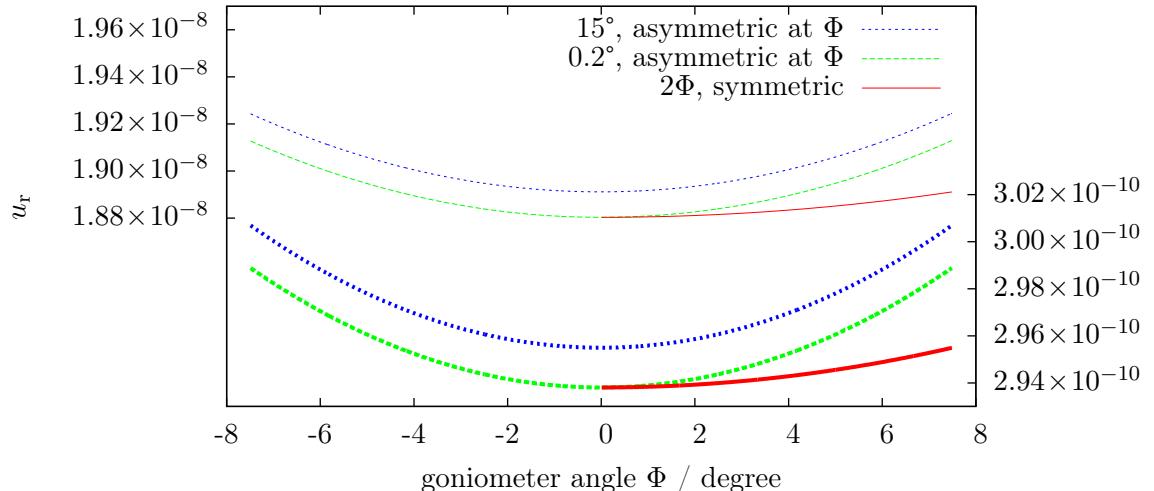
Figure 4.8: Error of an angle-difference measurement due to horizontal misalignment of the interferometer beam. Misalignments of $80''$ (thin line – left scale) and $10''$ (thick line – right scale) are drawn. For an interpretation see text.
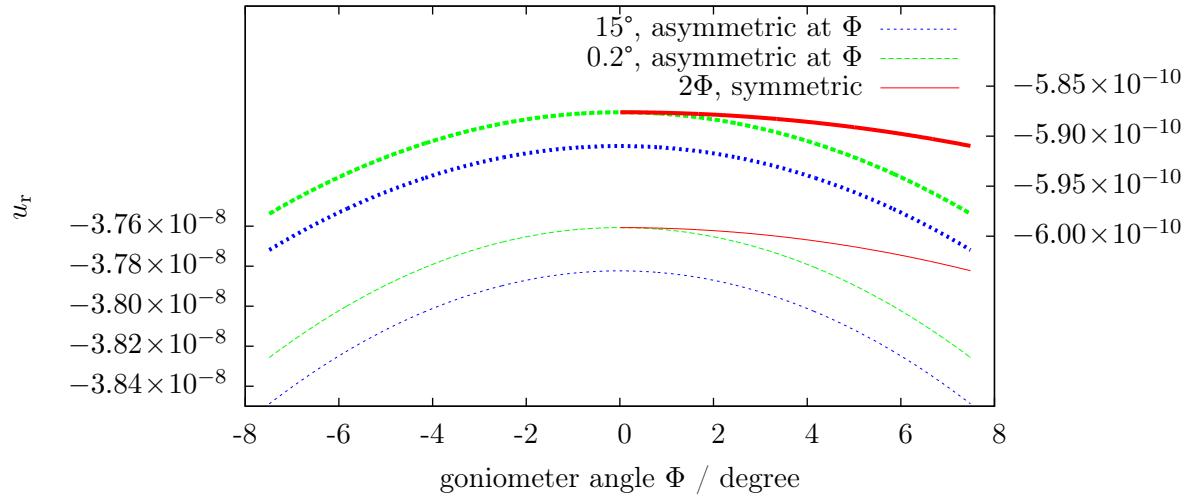
Figure 4.9: Error of an angle-difference measurement due to vertical misalignment of the interferometer beam. Misalignments of $80''$ (thin line – left scale) and $10''$ (thick line – right scale) are drawn.
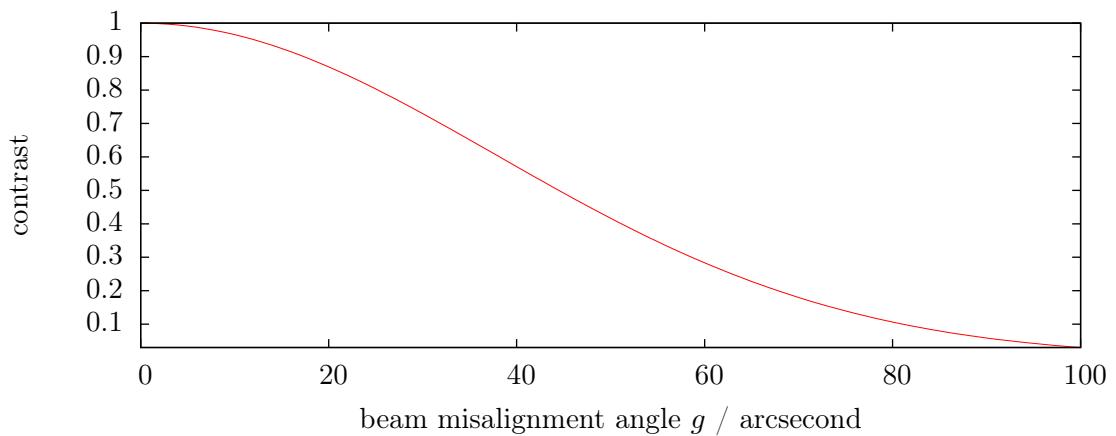
Figure 4.10: Angular misalignment of two beam components leads to loss of contrast. It should be emphasized that this is the final misalignment at the detector.

Interferometer contrast

A further restriction for the beam alignment comes from the interference principle and the finite beam width. Two overlapping beams of the same intensity produce a beating depending on the phase of the beam according to equation (4.4) at each point on the detector. If assuming nearly plane wave fronts perpendicular to each beam propagation vector and if placing the detector perpendicular to one of those beams, then the phase of the second beam has a spatial dependence on the detector surface:

$$\phi_2 = \phi_1 + x/\lambda_{\mathrm{L}} 2\pi \sin(\xi) \ , \tag{4.9}$$

where ξ is the angle between the two beams, and x the distance from both beam centres in the direction of the projection of the second beam on the detector plane. The laser has the wavelength λ_{L}, a beam diameter $w \approx 2.2\,\mathrm{mm}$ and an intensity profile of:

$$f(r) = \left(e^{\left(-\frac{r^2}{(w/2)^2}\right)} \right)^2 \ , \tag{4.10}$$

where r is the distance from the beam centre. As the detector is a photodiode with a sinlge pixel, it sums all light on the surface and converts into an electrical signal

$$D_{\mathrm{el}} = \iint f\left(\sqrt{x^2 + y^2} \right) 1/2 \left[1 - \cos(\omega t - [\phi_1 - \phi_2]) \right] \mathrm{d}x\,\mathrm{d}y \ . \tag{4.11}$$

The contrast is given by:

$$\frac{\max(D_{\mathrm{el}}) - \min(D_{\mathrm{el}})}{\max(D_{\mathrm{el}}) + \min(D_{\mathrm{el}})} \ . \tag{4.12}$$

The evaluation of this term is drawn in Figure 4.10. It turns out that a misalignment of $40''$ still deliver a contrast of 50%. It must be noted, that this misalignment angle refers to the total deviation of the beam finally arriving at the detector. This may be the sum of all previous misalignments. As the new interferometer layout uses most optical elements in multiple passes, it is hardly possible to compensate one misalignment by intentionally misaligning another element.

Therefore the laser beams from the interferometer plate towards the corner cubes have to be aligned parallel with a deviation less than $5''$. This accuracy is well possible with the help of an optical autocollimator and large transfer mirrors.

4.1.5 Performance tests

All four presented layout variants have been built and tested. This happened along the design process. Properties and problems learnt from earlier versions influenced the later ones.

Alignment feasibility The objective of the first variant was to prove the feasibility to built up such a layout. This was not clear at all, as the two sides put a lot of constraints and require some anti-parallel beams. Using the appropriate alignment procedure, it was possible to set up a working interferometer on an optical breadboard with commercial mounts for the optics.

A test of the interferometer provided a surprising result. Due to the influence of air and the missing thermal stabilisation, no perfect stability was expected. However the readout provided non-periodic oscillations with a time scale of about 25 minutes. An oscillation of the breadboard or the mounting is almost excluded. The most probable cause seems to be the commercial HP laser. It is stabilized through the Zeeman effect. The feedback is realized by measuring the polarization ratio and correspondingly heating the resonator. The laser frequency is thus stabilized by the thermal expansion of the resonator. It seems that the feed-back loop has a time constant in the order of 20 minutes. Thus the observed oscillation may have been induced by a back reflection from the interferometer into the laser. In subsequent set-ups this was avoided by Faraday-insulators, later on by the combination of an AOM and an optical single-mode fibre.

Linearity test The second variant was built to examine non-linearities. At the same time experience with the AOMs was gained. The interferometer readout was compared to the Nano-comparator at PTB [KFB05] which runs with a few nm accuracy. In this test, the interferometer performed well, there was no non-linearity detectable.

Also the third variant was set-up. It could be proven that it is mountable and works. However, due to the immanent polarization mixing (a few percent) the periodic non-linearities were unacceptable.

Prototype The fourth variant was build as a prototype of the final interferometer. It uses dedicated optics, and a granite block as base plate. The alignment of the optics is done by aluminium tables (see subsection 4.1.8) to which the optical elements are clamped down (see Figure 4.15).

This prototype was used to replace the *Gams5* interferometer. Here, it could be tested under real conditions. These tests included long time reliability and stability as well as linearity. However, *Gams5* is not equipped with a vacuum chamber, thus the interferometer was exposed to the influence of the refractive index of air and thus could not show its full stability capabilities.

With the availability of the *Gams6* vacuum chamber (see section 4.2) the prototype could be tested in the position of the final interferometer, admittedly without corner cubes and therefore only the reference path was operated. This path alone is not compensated in the prototype-version, thus the stability in vacuum could not be tested.

Even though the prototype was not designed for vacuum operation – it contains dead volumes and porous materials – a pressure below 10^{-4} mbar was reached quickly. The interference signal remained strong, even during evacuation.

4.1.6 New laser

Gams4 and the early version of *Gams5* used a two-frequency helium-neon laser as light source, i.e. the Model "5501B" from Hewlett-Packard (now Agilent). They have a laser tube inside a homogeneous magnetic field. Due to the Zeeman effect a splitting of the laser line occurs. These wavelengths have a different polarization.

Even though they are quite reliable, lasers of this type have several disadvantages. The separation by polarization is never perfect, more than -50 dB are not achievable. Further, this light can hardly be injected into an optical fibre (without destroying the frequency separation), thus the light cannot be transported, and the laser has to reside close to the interferometer. This causes thermal gradients and is hence unfavourable.

Therefore the laser is replaced with a monochromatic HeNe-laser. A nowadays standard model 117A from Spectra physics is frequency stabilized and operates in continuous wave mode with an output power of about 1.8 mW. Due to the calibration procedure of the goniometer an absolute knowledge of the wavelength is not necessary.

Optical fibres

To allow a spatial (and thus thermal) separation of laser and interferometer, the light is transported in optical fibres. Single mode fibres are necessary to provide a low divergence and a flat wave front of the resulting beam. The interferometer requires polarized beams, as the laser provides a high polarization, polarization maintaining fibres are used for maximum intensity.[†]

The fibres were operated together with the prototype successfully for 2 years at *Gams5*. Though during a test of the final copy on the *Gams6* vacuum chamber, a very strong sensitivity to vibration was discovered. The prototype fibres do not show this problem. It is unclear whether the problem arises from a bad production batch or a bad laser polarization before injecting. In case the problem persists in the final installation, a replacement of the fibres may be necessary. In the worst case, the interferometer can be operated without fibres. The light can be injected through a window into the vacuum chamber.

[†]Otherwise a full depolarization succeeded by a re-polarization would be necessary to get a stable intensity. This would result in a loss of 50% of the light intensity.
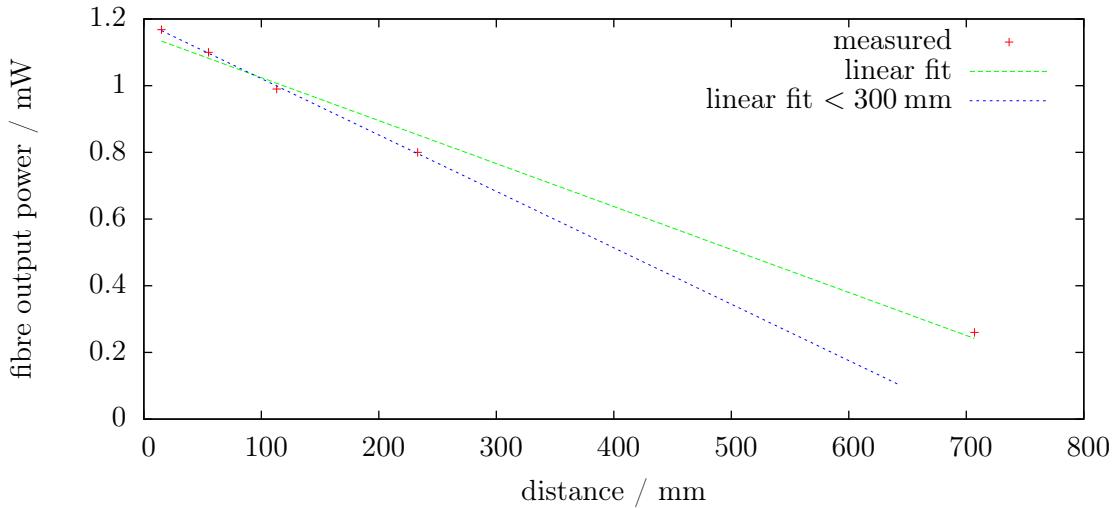
Figure 4.11: Maximal intensity coupled into the fibre at different distances from the laser. The measured laser intensity is 1.75 mW. For an interpretation see text.

AOM-box

The laser light needs to be split and shifted by two different frequencies before being injected into the interferometer in order to produce the beating. The shifting is done two AOMs, at 39.95 Mhz and 40.05 Mhz. In a first version, the laser is coupled into an optical fiber. At the end of this fibre, the light is split out-coupled and shiftd by the AOMs. Then each beam is coupled into its own fibre and guided to the interferometer. The box has been performing well on *Gams5* for the last three years. A frequency separation of more than 80 dB was reached. This value is limited by the Signal to noise ratio, a frequency mixing was not observed at all.

The second version was optimized by leaving out the first fibre. This should increase the outgoing intensity by 20%. At the same time the Fraday-isolator can be left away. In the first version it was necessary to avoid reflections from the first fibre back to the laser. This is now provided by the AOMs.

Though during the construction phase of the second box, it was discovered that the light intensity after the fibre decreases with the distance between laser and fibre as shown in Figure 4.11, much to the surprise of the manufacturer. Therefore the AOM box had to be built very compact. In its final state, the second version had an output power of 400 mW per fibre, compared to to the first version having 250 mW per fibre.

4.1.7 Optics

Former interferometers of GAMS lacked mechanical stability. Although using a low expansion ground plate, the optical elements were mounted with asymmetric flexure bindings and a glue that is supposed to be humidity sensitive. This is now avoided by fully symmetric mountings and fixation by clamping. Any symmetric material expansion does not cause any drift in the signal. Additionally "chemical bonding" is used to connect ceramics and glasses.

In the past, the optics had been a collection of polarizing beam splitter cubes, roof prisms, solid corner cubes and Glan-Thompson prisms, the latter in cylindrical housings. These irregular shapes does not permit a rigid fixation.

For *Gams6* it is assured that all optical elements can be mounted rigidly.

The beam splitter cubes were replaced by right cuboids. They provide a homogeneous flat ground surface that is ideal for a rigid fixation. Furthermore they can be produced with high parallelism. Therefore the transmitted beam is not deviated, in contrast to beam splitter cubes which create always some arc seconds deviation. Additionally a cuboid will be aligned with an angle of 45°with respect to the beam and does not have any surfaces perpendicular to the beam. This means that no reflection can cause spurious signals. Double reflection which are parallel to the beam are that much separated in space that they can be blocked by diaphragms.

The surfaces traversed by the beams are polished to $\lambda/20$ and coated according to their function: mirror, polarization sensitive or anti-reflection. These coatings are not necessary for the principal functioning of the interferometer, but without them there would be no reasonable intensity arriving at the detector. The best coating available were used, and still about 50% of the light is lost in unwanted reflections.

Hollow corner-cube retro-reflectors

Corner-cube retro-reflectors are well known in distance metrology and have been studied intensively [Pec48], also when used for a goniometer [Sch78]. However, these consideration care only the aspect of solid corner cubes. And they ignore the effect of non-perpendicular surfaces.

For *Gams6* it would be not suitable to use solid corner cubes as it is extremely difficult to assure a symmetric production and mounting; non-linearities would be unavoidable and cause too large systematic errors. The same is true for a temperature change that will move the optical centre of a solid cube. Additionally, a rigid mounting of a solid corner cube is rather difficult.

Hollow corner cubes, on the other hand, provide usually a very bad perpendicularity. Together with an optical workshop (Bernhard Halle Nachfolger GmbH, Berlin) a new
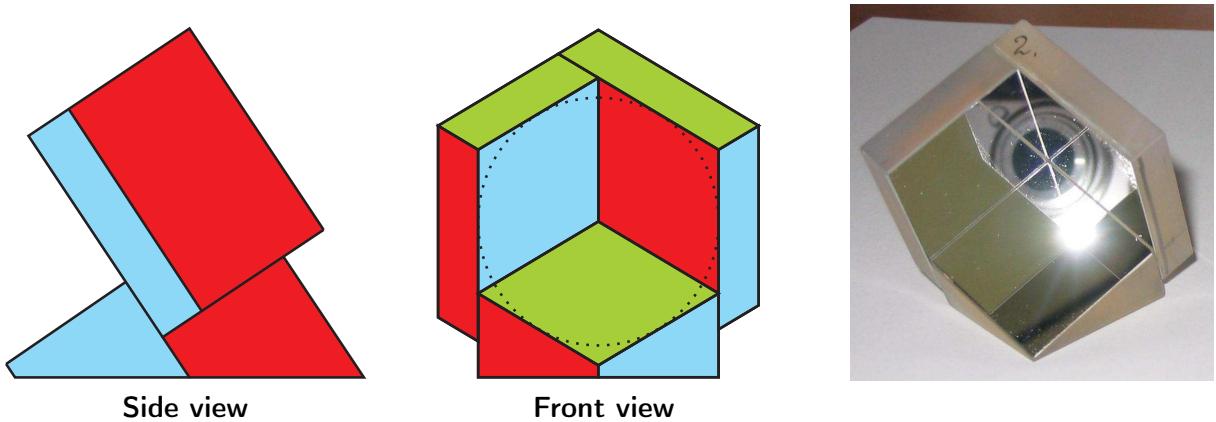
Figure 4.12: Scheme and photograph of the corner cube. Parallel surfaces are drawn in same colour. The aperture is 42 mm.

design of hollow corner cubes was developed. It provides a high perpendicularity within $1''$, a flat ground surface for good fixation and at the same time it does not require any glue which could lead to drift.

The design can be understood as a solid corner cube which stands on the surface which would normally be the entry surface. One of its side faces is coated with a mirroring layer. On the other two surfaces flat mirrors are fixed by optical bonding. This allows an excellent perpendicularity. Furthermore, the gap on the corner between two mirror surfaces can be smaller then 0.1 mm. Figure 4.12 shows a sketch of the design and one of the four pieces that have been produced.

In contrast to solid cubes that work with total reflection, the hollow cubes need a reflective coating. This reduces the final intensity a bit. During one passage of the beam it will always hit all three mirror surfaces.

The corner cubes are together with the main mirrors the only optics that experience a moving beam which means that for different goniometer angles, the laser beam probes a different spot of the optics. Consequently these surfaces need a very good flatness as explained in section 2.3.3. Therefore the surface of the four corner cubes was mapped using a WYKO 6000 fizeau interferometer. This device emits a large laser beam with a plane wave front. After being reflected from the test object this wave interferes the reflection of a flat reference plane. The interference pattern shows the total path length inhomogeneity that can appear after the three reflection in the corner cube. Figure 4.13 shows this surface flatness. A maximum wave front deformation of 30 nm was observed, up to 60 nm $(= \lambda/10)$ would be acceptable for *Gams6*.

The angles between the mirrors were measured with two different methods. First again with the WIKO 6000 fizeau interferometer. It returns a fringe pattern according to the

Figure 4.13: Surface quality of retro reflectors measured with a WIKO 6000 and a 50 nm flat reference plate. Surface deviations are given always relative to a plane fitted to each sector individually. The grey shading indicates the $\lambda/10$-range. The green line indicates the movement of the 8 mm diameter laser spot when the goniometer is rotated from 0° to 15.1°. The lower marks indicate the incoming beam from the interferometer, the upper towards the main mirror. The yellow zones apply instead, when the retro reflector is used on the right side of the goniometer arm. In other words from the interferometer always the lower side being close to the goniometer axis is used to shoot in. The image should be point symmetric. Deviations from this may indicate lens defects of the WYKO 6000. Note that goniometer can run to ±30° without loosing signal. However, it would use then different mirror sequences inside the retro reflector. As the surfaces are not perfectly rectangular this causes strong non-linearities. Additional perturbations are to be expected on the surface junctions.

140
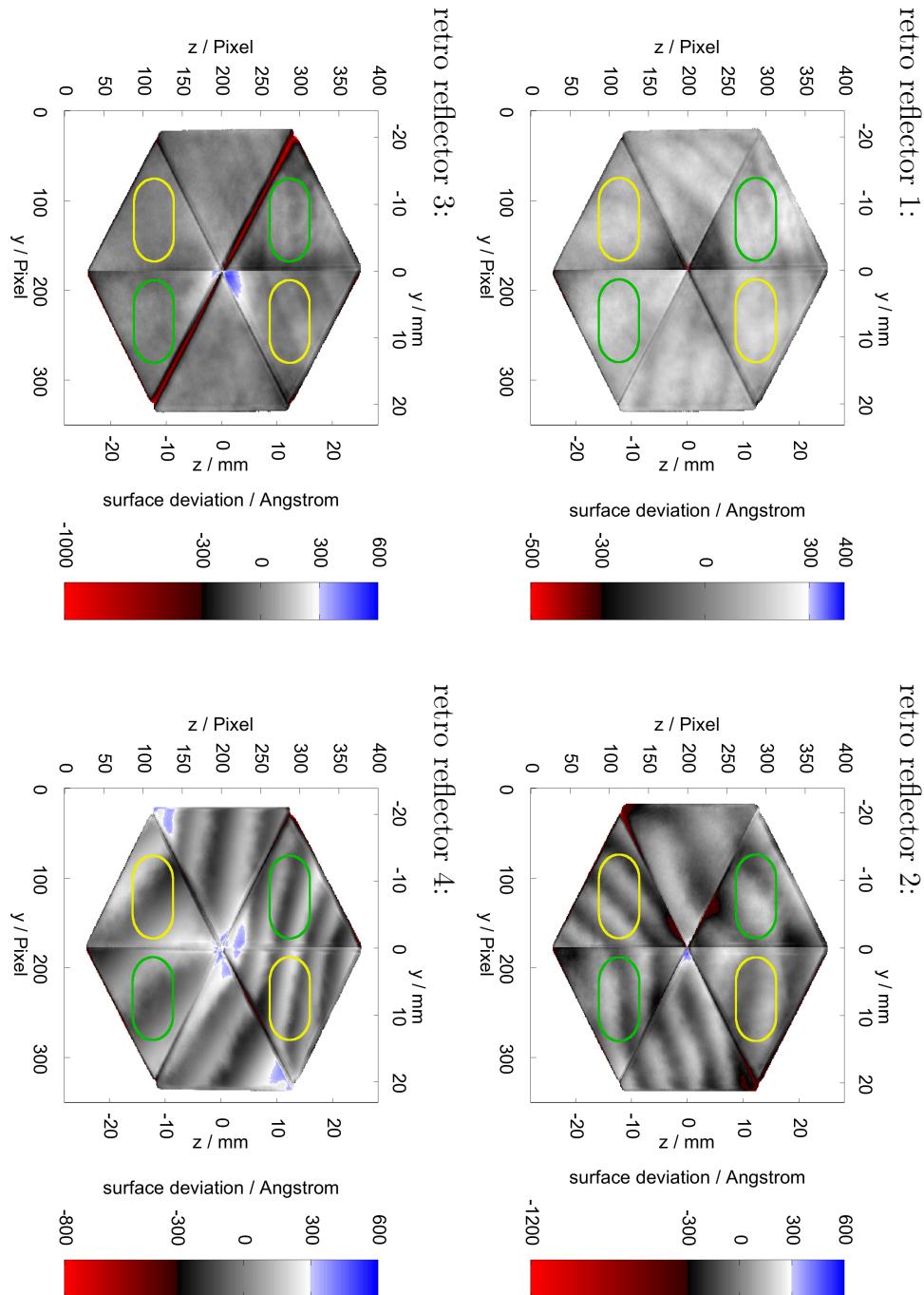
mirror sequence	direction of deviation	cc1		cc2		cc3		cc4	
		fiz.	pair	fiz.	pair	fiz.	pair	fiz.	pair
CAB	horizontal	1.60	1.06	1.98	2.04	-1.08	-1.88	-0.49	0.49
	vertical	2.29	1.56	-0.02	-1.27	2.66	2.97	1.85	1.41
	combined	2.79	1.88	1.98	2.41	2.87	3.51	1.91	1.50
ACB	horizontal	2.23	1.55	0.05	0.24	0.81	-0.24	0.64	0.98
	vertical	0.71	0.71	1.05	1.84	-0.14	0.14	-0.26	0.57
	combined	2.34	1.70	1.05	1.85	0.83	0.28	0.69	1.13
ABC	horizontal	0.57	0.24	0.79	-0.08	-1.06	-2.04	0.11	-0.16
	vertical	-2.04	-1.56	0.45	1.27	-2.65	-2.97	-1.55	-1.41
	combined	2.12	1.57	0.91	1.28	2.86	3.60	1.55	1.42

Table 4.1: Measurement of the angular imperfectness of the four corner cubes (cc1–cc4). Given is the deviation of a reflected beam versus the incoming. Two different methods have been used: "fiz." – a fizeau interferometer. "pair" – the angle between the mirrors A,B and C was measured pairwise with an accurate indexing table. The deviation of a reflected beam was then calculated. All numbers are given in arc seconds. All uncertainties are about $0.3''$.

flatness and the alignment of a surface. By fitting a plane to each of the six sections of a corner cube. The difference between two facing sections correspond to the deviation of a reflected beam. This deviation will depend on the sequence in which the the three corner cube surfaces are passed. An independent measurement was done at INRIM using an accurate indexing table. This is a calibrated table that can be rotated at discrete steps, e.g. 90°. Small deviations are measured via an electronic autocollimator [PA06]. The results of these measurements are shown in table 4.1. Two of the corner cubes where found two match the requirements of $1.5''$. The other two are at $2.5''$ and can be used on the A-axis of the goniometer as it is less sensitive to this type of misalignment.

Hollow double-sided roof-prism

Similar to the corner cubes, also solid roof prisms are problematic in fixation and optical stability with respect to temperature changes. But a similar solution is possible. A solid roof prism stands on its entrance surface and serves as a socket. A flat mirror is fixed to one of the sides. This mirror and the remaining side of the socket prism form a hollow roof prism. A second flat mirror can be added to the free side of the socket prism, then a second hollow roof prism is created.
This feature of having two opposed roof prisms on one element is used in the interferometer
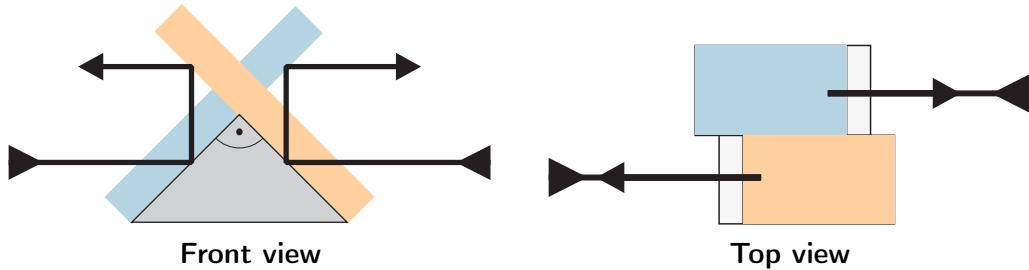
Figure 4.14: Scheme of the roof prism. The base and the orange mirror are used for the A-axis interferometer while the blue mirror and the base serve for the B-axis interferometer.

layout for compensating drifts, in case this double roof prism is drifting, the combined goniometer readout stays stable.

If using plan parallel flat mirrors, the two opposing roof prisms can be made collinear. However this would require a recess in both mirrors. As the layout requires rather small and thin pieces, the manufacturer could not guarantee their flatness.

4.1.8 Mounting method

As described in section 3.4, the stability of *Gams4* was supposed to by perturbed by a humidity sensitive glue. It is hence preferable to avoid any glue, and any material mix. Preferably only low expansion material is used and all parts should provide such a symmetry that remaining expansion do not affect the goniometer read out.

The problem is quite tough, as a complex layout of $\sim$20 individual components needs free alignment with 1 arcsecond precision. This orientation must be kept over a long time (months) and it must survive moderate mechanical shocks from rotating the spectrometer table.
The strategy to solve this problem is:
 - decouple the different alignment orientations as much as possible,
 - use symmetries,
 - use flexible springs to push objects against hard materials, thus any drift behind the spring does not matter,
 - use low expansion materials where symmetries may be broken, or where inhomogeneous expansion may cause an undesired effect,
 - do not use any glue and
 - remove all alignment actuators, once the alignment is achieved.
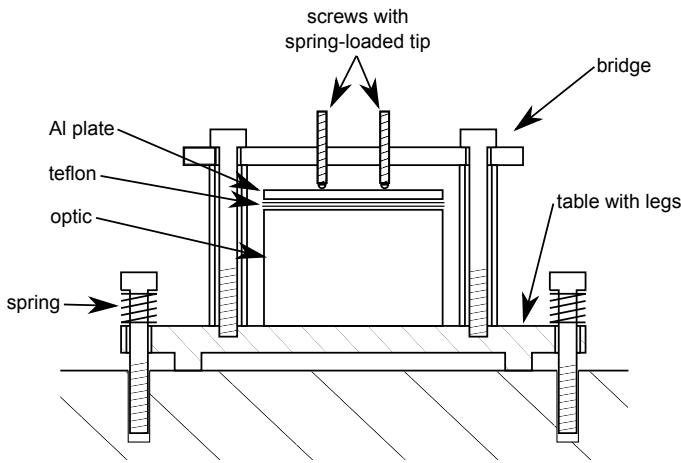
Figure 4.15: Mounting method for optics used for the prototype. The main part is a rigid bridge consisting of a horizontal bar which is supported by two vertical tubes and fixed by two screws. The latter are individually placed to avoid collisions with the laser beam. It allows to clamp down the optics by two screws with a spring loaded tip ($\sim 2\,\mathrm{N}$). An aluminium plate distributes the force on the polished bonding surface and a double layer of Teflon reduces sheer forces and avoids scratches. The vertical orientation of the table can be adjusted by polishing the legs with an accuracy of $1''$. After adjusting the horizontal orientation and position by pushing with micrometer screws, the table is fixed by clamping down via three springs ($\sim 100\,\mathrm{N}$). The micrometer screws are removed after clamping.

This led to construction principle:
  1. mount all optics to small tables with little legs that allow a fine adjustment while being rigid afterwards,
  2. clamp those tables vertically to a common base plate.

This construction principle allows to fix the optics to the little tables via chemical bonding. This rigid technique is explained in the next subsection. The little tables can be adjusted in inclination by polishing their three legs. This allows a very precise alignment. And once the alignment is done, this will neither change nor drift any more. The horizontal alignment in orientation and position is done via micrometer screws. However, these are removed after clamping the tables vertically in order to avoid drifts from expanding material. The principle is illustrated in Figure 4.15 and Figure 4.16.

For budget reasons, the same optics that was used for the prototype has to be used for the final set-up. Hence, the optics must be mounted removable on the table while still being stable enough. The final version later on can use a permanent fixation. Therefore, during the prototype phase the optics was simply clamped to the tables.
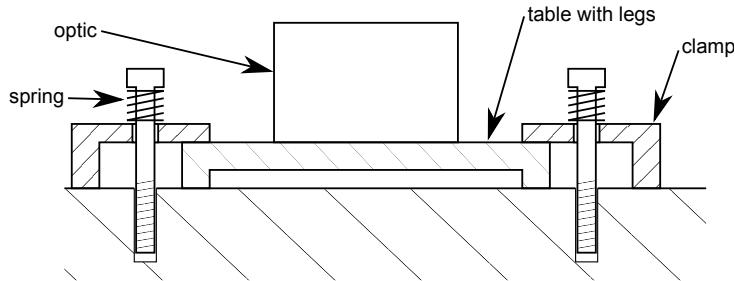
Figure 4.16: Final optics mount. The optics is bond chemically to a little Zerodur table. Its legs are polished until the desired alignment is achieved. Then this table is clamped to the interferometer plate. The metal clamps are pressed done by screws via springs ($\sim 100\,\mathrm{N}$). The clamps press on the table straight above the legs.

Chemical bonding

Constructing an interferometer requires a technique to fix an optical element rigidly that means without any drift. At *Gams4* bad experiences were mad with a glue that was particularly non-shrinking during curing, but humidity-sensitive afterwards as shown in section 3.4.

Chemical bonding is such a technique that allows to connect two surfaces of silicon oxide rigidly together [Ell+05; Bog10]. The method is patented and was improved by the university of Glasgow for interferometry in a space craft. It was tested to survive a rocket start with accelerations of $300\,\mathrm{m/s^2}$. The method was provided to ILL under non-disclosure agreement.

Chemical bonding works with two pieces of silicon-oxide such as Homosil, Zerdur and Clearceram. Both surfaces must be polished very flat. A small amount of water is applied and the two pieces are brought into contact. The water opens the Si-O bonds on each surface. After the diffusion of the water into the bulk, the bonds recombine with the other surface, forming a strong connection. Test at ILL showed that a bonding surface of $2\,\mathrm{cm^2}$ can stand shear forces of more than $800\,\mathrm{N}$. For the need of *Gams* the technique was modified, such the bonding was possible within normal laboratory conditions.

4.1.9   Summary

A new interferometer layout was presented, that includes a measurement of both crystal axis within one interferometer. Therefore it provides compensation effects against drifts. The new layout was studied in detail for systematic errors. New fixation techniques were developed that are much less susceptible to drifts, this includes new alignment and bonding techniques. A new type of retro reflecting solid were developed that allow much better

144

fixation and are much less affected by thermal changes. A prototype of the interferometer was built and tested on *Gams5* as shown in Figure 4.17. It served in regular operation for more than one year.

The final version of the interferometer has meanwhile built and installed on *Gams6*. See Figures 4.18 and 4.19, as well as Figure 4.28 on page 162.

4.2 Vacuum chamber

As any environmental change will change the index of refraction of air and therefore also the interferometer readout, the interferometer must run in vacuum to achieve the aimed accuracy. With the needs of thermal isolation and low vibration it was necessary to design a chamber such that the internal parts are completely separated from the chamber wall. Additionally the distance of the γ-beam to the floor is given by the reactor. With 94 cm it is very limited. The lack of space made many constructions very difficult.

At the same time, a vacuum chamber provides an additional thermal shield including a rather large heat capacity.

Chamber characteristics The chamber comprises a volume of 500 litres while having a mass of 550 kg. Viton joints are used for sealing. The plenty of access flanges cause a total sealing length of 12 m. The top part is removable and leaves access to the full spectrometer for manipulation and alignment. Service flanges give access to the lower parts.

To eliminate vibrations that are induced by the turbo pump, the chamber was designed such that it can hold the vacuum without pump for more than 12 hours below the critical pressure of 10^{-3} mbar. In an alternative mode, the pump can be connected with a 40 cm diameter tube of 1.5 m length for vibration insulation. This allows to keep the pressure below 10^{-4} mbar. The latter configuration was tested with the interferometer prototype inside which has very bad vacuum properties as it made out of marble and has many dead volumes.

The hole spectrometer must be rotated for different Bragg angles of the A-crystal. Therefore the chamber is mounted on a air cushion of 80 cm × 140 cm. The cushion is lifted by pressurized air only during changes of the A-crystal Bragg angle.
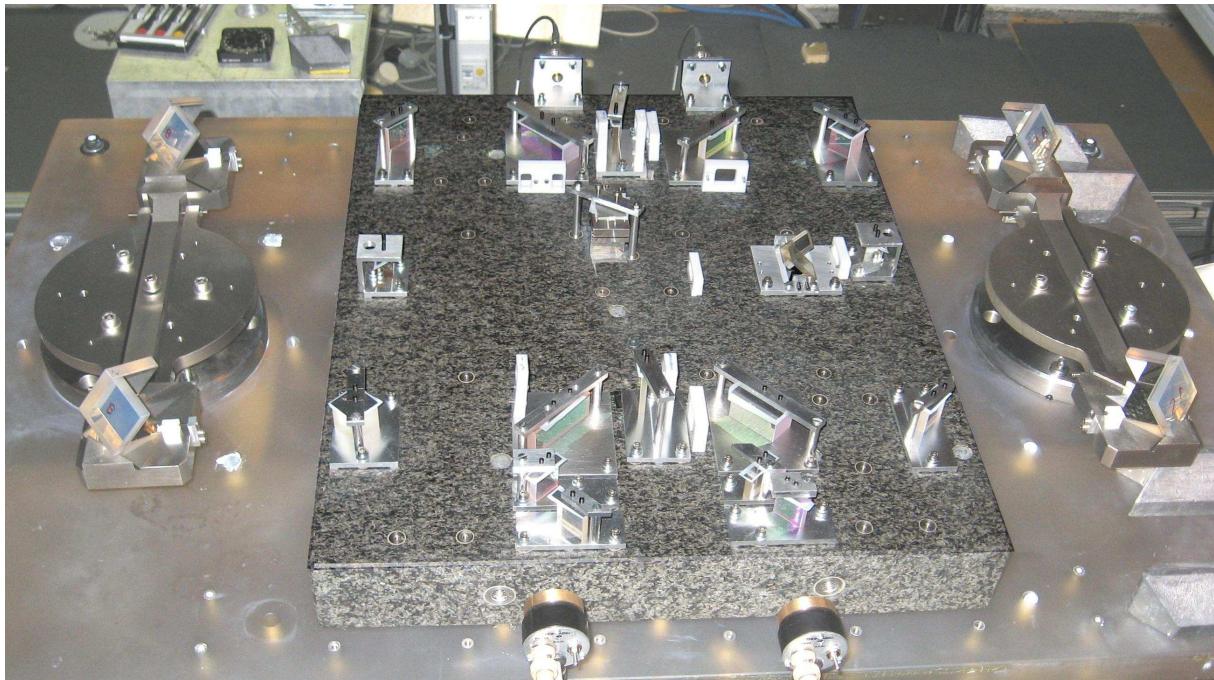
Figure 4.17: Prototype of the interferometer mounted on *Gams5*. There are no crystals mounted.
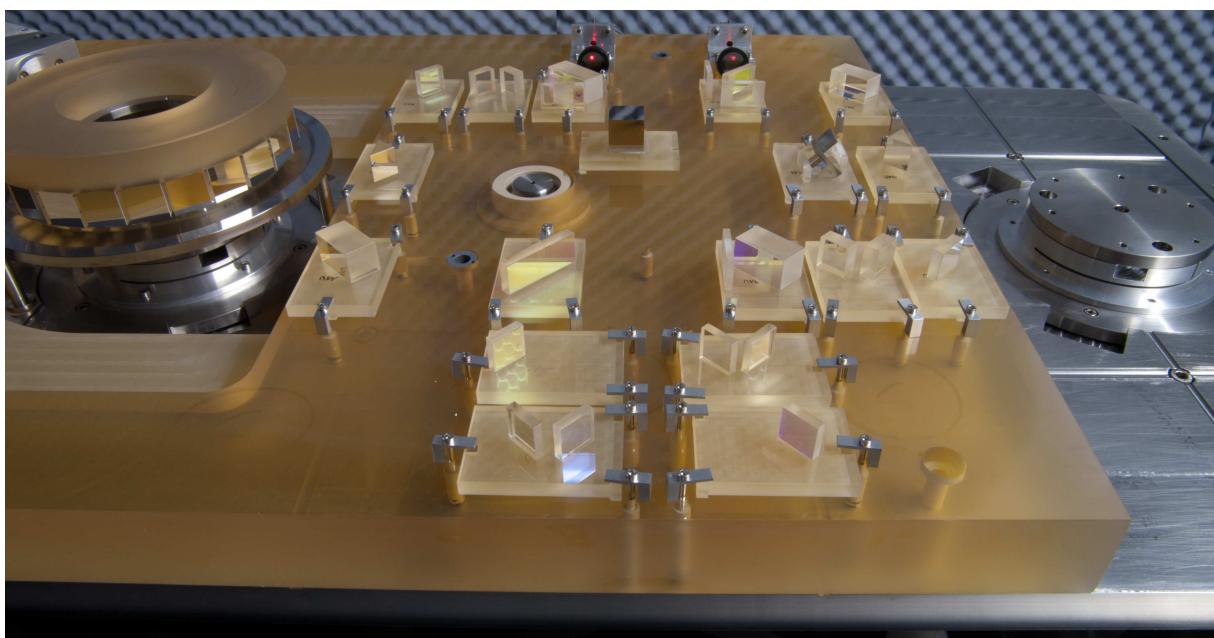
Figure 4.18: The final interferometer of *Gams6* mounted inside the vacuum chamber. Goniometer arms and crystals are not mounted.
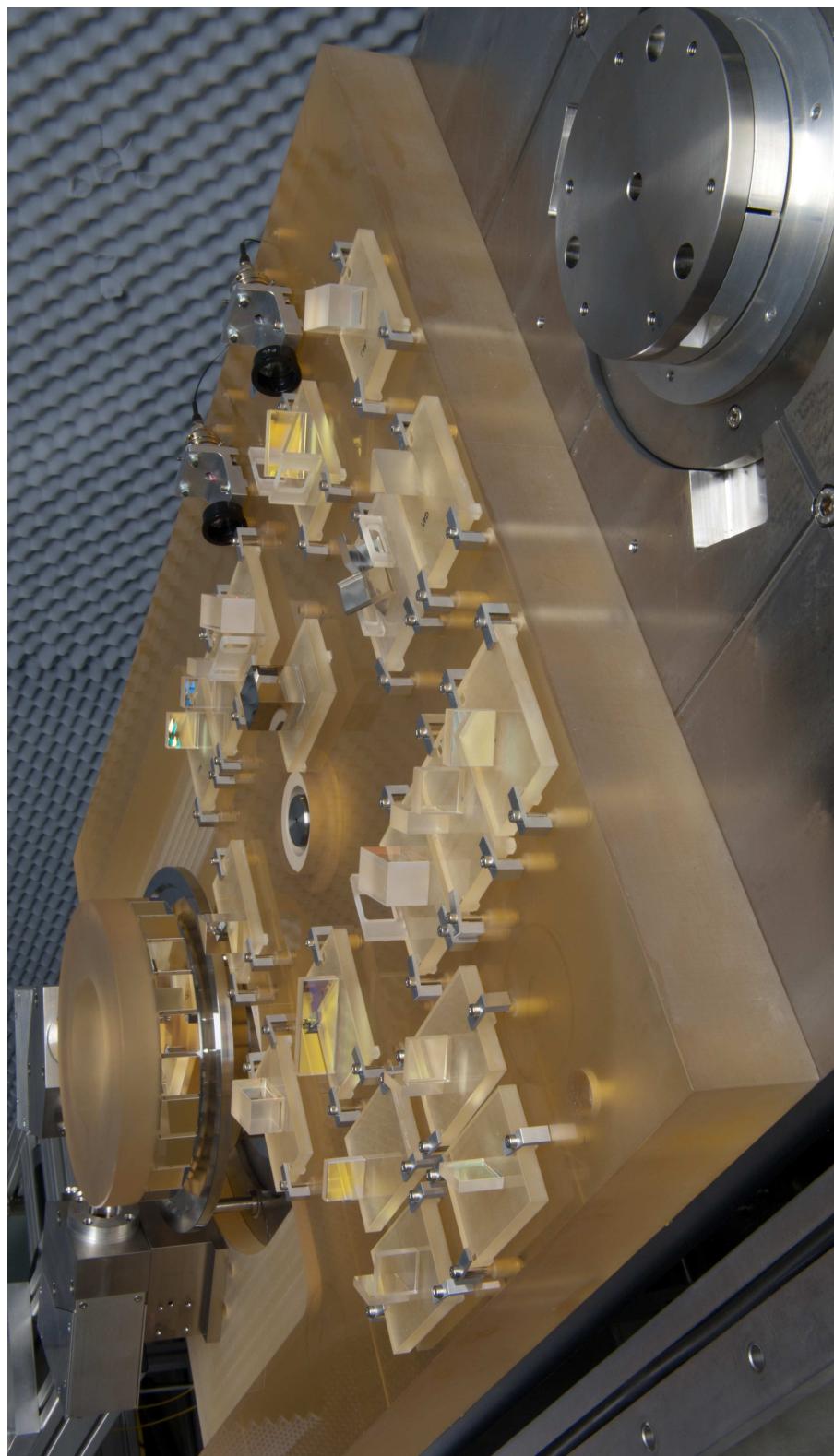
Figure 4.19: *Gams6* interferometer installed in vacuum chamber. The A-axis is visible on the right. The polygon and autocollimator are on the rear left.
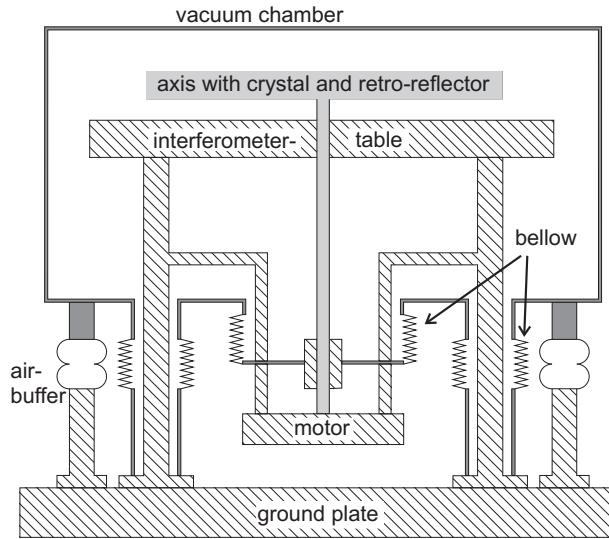
Figure 4.20: Scheme of the vacuum chamber. The internal parts are isolated against vibration of the chamber wall. The interior is rigidly fixed to the air cushion which lies on the granite block. The vacuum chamber is mounted to the air cushion via vibration damping buffers.

4.2.1   Vibration isolation

Vibrations induced by the vacuum pump and resonances from the vacuum chamber must be kept away from interferometer. Therefore the spectrometer table which holds axes and interferometer is mounted directly to the air cushion which lies on the granite block. While the vacuum chamber is mounted via damping buffers to the air cushion. The mounting points of spectrometer as well as the motor feed through of the axis are connected to the chamber via edge welded bellows. The concept is shown in Figure 4.20 and was presented in [Kre+08]. In the first stage of operation, the damping buffers have not been installed to simplify the handling, thus the chamber is mounted rigidly to the air cushion. The damping buffers can be installed at any later point.

4.2.2   Anti vibration platform

The heavy water pumps for the reactor cause a rather high level of vibration coming from the the ground. The spectrometer must be protected from these vibrations. The is done by a platform of 1.8 m × 1.4 m and a mass of 2 tons. This platform is hold on air pistons[†] which damp the vibration. The air pressure is controlled in feedback-loop by the position of the platform. A precision of better than 1 µm in position and better

---

[†]See http://www.techmfg.com/products/gimbalpiston.htm#isolationpneumatic

than $1''$ can be achieved. For *Gams4* this platform was made of iron with a honey comb structure. However the iron was too flexible and led to a deformation of the platform causing difficulties with the air cushion and a variable tilt of the spectrometer. *Gams6* uses a granite block, since this has been used successfully at *Gams5*.

4.3 Data acquisition system

In order to to achieve the desired level of systematic uncertainty it is necessary to increase acquisition speed. This task splits into a mechanical part that allows to drive the motor axis with a higher speed while not causing any vibrations that would cause the loss of fringes. Additionally the software has to be modified such that several motors can run in parallel, e.g. the crystal-axes are mechanically independent from collimator and detector. The motor control has to be optimized so that the positioning can occur much faster.
These improvements do not only reduce the necessary beam time, they also allow systematic studies of the instrument which are not possible with *Gams4* due to the low operation speed. Therefore they are crucial for the success of *Gams6*. Furthermore a γ-triggered position readout can improve the instrument performance by either reducing the necessary beam time or increasing the instrument resolution by passing a limit that was so far given by the crystal vibration.

It was not possible to modify the old acquisition system such that it would meet the requirements, neither hardware nor software. Therefore new system was developed. At ILL the instrument control group "service contrôle des instruments" (SCI) delivers most instruments at ILL with DAQ electronics and software. Traditionally the nuclear an particle groups and hence *Gams* did not profit from this service as the instruments are quite different. However *Gams* resembles a bit to neutron scattering instrument. Therefore the DAQ system was developed together with the SCI. Some parts could be easily copied from other instruments, such as all control units for motors like detector, collimator and spectrometer table. Similarly the ILL-wide instrument control software "NOMAD" could be adopted in large parts. However, the crystal-axis coarse motors, the fine positioning, the interferometer readout and γ counting have much different requirements and properties in terms of position resolution, axis speed, motor speed and axis inertia required new developments or very careful and time consuming modifications, testing and bug-fixing.

The hardware is now modularized within a common VMEbus:
The phase detection module handles the readout of the goniometer and controls the crystal-axis fine positioning with a feedback-loop. It provides the goniometer readout to other modules via the VMEbus. This module will be described in detail in the next subsection.
The motor module handles all motor movements including the coarse crystal axis. For
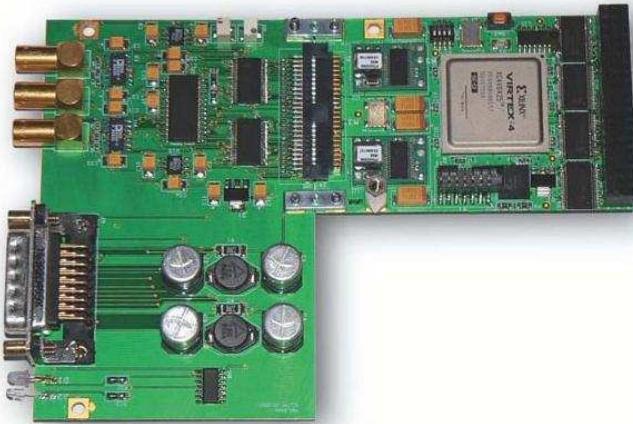
Figure 4.21: DAQ board for phase detection. The "service and control des instruments (SCI)" group of ILL developed on our demand a phase detection board. Via an interface board it is operated in a VMEbus crate. Its FPGA is running on 200 MHz and allows high accurate phase determination while at the same time it keeps track of the fringe numbers.

the latter it obtains the goniometer readout from the phase detection module.

The acquisition module can handle up to 16 channels of Germanium detector signals. They are converted into pulse height values. It is possible to obtain the data as histogram as well as a list of single events. This list comprises the goniometer position at the time of the event, obtained from the goniometer module. This Event mode data acquisition is discussed later on.

4.3.1 Phase detection module

The acquisition of an interferometer is a bit tricky as it delivers a sinusoidal signal, and all information is encoded in the phase only. This implies that only a very short range of up to one wavelength is unambiguous. This is known as the fractional part of a fringe. For any longer distance measurement the acquisition module has to count permanently the passing fringes This number as called the integer part. It is crucial that no integer fringe is "lost", for example because the acquisition device is busy. It would be impossible to recover the original position unless some kind of reference position is available.

Traditional DAQ systems split the task of fractional and integer fringe measurement in two different modules. They are recombined later on via software. However, the axis coarse-motor profits extremely if the fractional information is present. First its positioning is not limited to one fringe any more. And second the positioning speed and reliability

150

increases dramatically when targeting for a few fringe accuracy. This is crucial as the fine positioning has a range of only $\pm 8\,f_6$.

The module is consists of a FPGA which is currently running on 200 MHz, this can be changed to 800 MHz with limited effort. The goniometer signal is guided through a 1 kHz high-pass filter. Then zero-crossings of the 100 kHz beating are detected. Their delay to those of the reference signal is measured. Dividing this phase delay through the period of the signal yields the fractional part of the fringe number. This measurement is repeated continuously. Each measurement is compared with the previous one. If the difference is larger than 0.5, the internal counter of the integer fringe number is either increased or decreased by one, depending on whether the difference of the fractional numbers was positive or negative. The fractional and integer parts are then combined and provided over the VMEbus.

At the same time, the module can receive a set-position from the computer. It calculates the difference from the current position and provides a control signal to the crystal axis fine positioning. Thus the crystal position is hold by a feedback loop.

The FPGA checks for zero crossings with a frequency of 200 MHz. The goniometer beating frequency is 100 kHz. To avoid fringe loss due to a noisy signal, the maximum fringe detection rate is limited to 25 kHz. The zero-crossing measurement yields a resolution of 0.000 5 fringes with a repetition rate of 100 kHz. When averaging 100 of these values a resolution of 0.000 05 fringes can be obtained at a repetition rate of 1 kHz.

4.3.2 Event-mode data analysis

The *Gams* acquisition up to now holds the B-crystal at a certain position and counts the γ-events over a certain time. This is repeated for several positions to scan the peak profile. At each position the crystal angle is recorded and averaged over the same time interval. The γ-count rate is assigned to this averaged position. However, as the crystal underlies a certain vibration, all structural information of the rocking curve below this vibration level is lost. The idea to overcome this problem is to take the data in event-mode: For each γ-event the crystal position is recorded and stored individually.

The question arises, how to estimate the peak centre from the list of collected angle reading. Conventional fit-methods require a discrete probability distribution of the data, in other words a histogram. However, but this would require to bin the recorded angles. A coarse binning leads to the loss of information; in the extreme case of putting all angles into one single bin, no information of the peak centre is available any more. A small bin-width, which corresponds to the resolution of the detector, does not cause any loss. However most bins will be empty and consequently Least-squares fitting methods will fail[HJ01]. Maximum-Likelihood methods can deal with this. Though, even they require a uniform
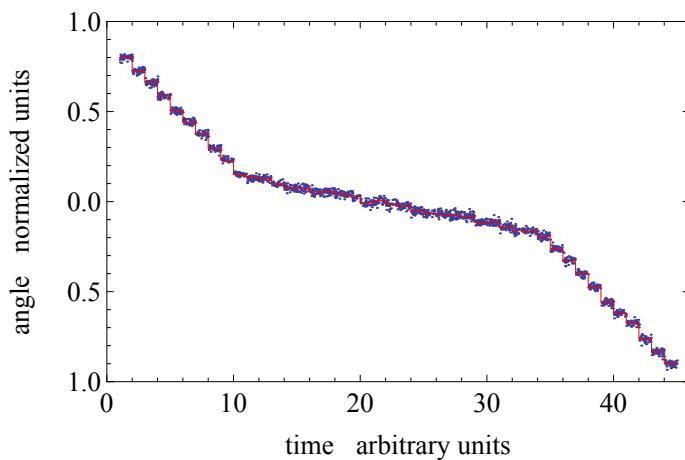
Figure 4.22: Time record of the angle values of the B-crystal axis. The red line is the measured average angle in each scan-step. The ± 1 angle range corresponds to $\pm 0.375\,\mu\mathrm{rad}$.
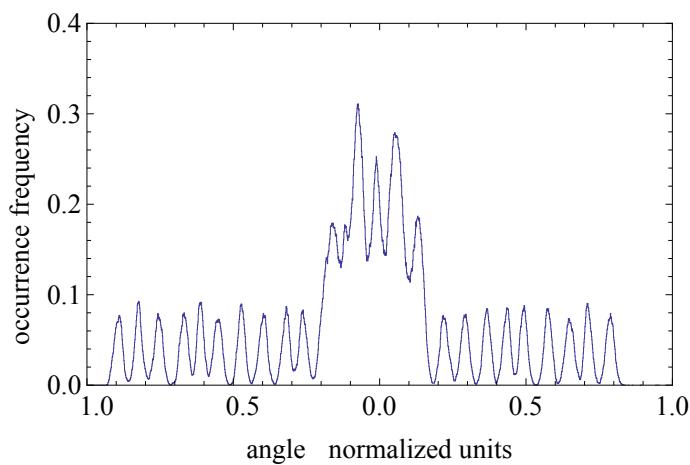
Figure 4.23: Frequencies of the angle values. The same data set as in Figure 4.22 was binned with a bin-width of $0.0001\,\mathrm{f}_5 \approx 0.623\,\mathrm{nrad}$.

probability distribution of the crystal angles prior to any γ-recording. This condition is not fulfilled at *Gams*. A typical trajectory of the crystal angle is shown in Figure 4.22. After binning, the corresponding histogram has many peaks (see Figure 4.23). These are the centres of the scan steps. They are blurred by the vibrations.

In order to cope with such irregular angle frequencies, a new data evaluation method was developed together with Giovanni Mana and Luca Ferroglio from INRIM. This theory was published and is outlined in [MKF10]. In the following paragraphs the aspects relevant to *Gams* are condensed.

The method uses the Bayes theorem [Jay03; SS06]. First, the method for peak-centre estimation in case of a general crystal angle probability distribution and a single γ-event is derived. Then, it is extended to many γ-events. Finally, it is extended to the case of measured probability distributions and it is applied to a sample data set that was recorded on *Gams5*.

In the following convention a γ-detection triggers the reading x_1 of the crystal angle x. The probability of detecting $n = n_1$ γ-events in a count interval ΔT is Poisson distributed:

$$P_n(n_1|x_1) = \frac{(I\Delta T)^{n_1}\mathrm{e}^{-I\Delta T}}{n_1!} \ , \tag{4.13}$$

where the peak profile $I(x_1)$ is assumed as known. The function $I(x_1)$ must be integrable, but it is otherwise arbitrary; for the sake of simplicity one assumes that it depends on four unknown parameters, the background level a, maximum b, centre c, and width d. The interest lies in finding the best estimator for the peak centre and its uncertainty.

In the following, the notation $P_r(r_i|s_j)$ will be used to indicate the probability that the quantity r has the particular value $r = r_i$ if the parameter s in the probability distribution P_r has the particular value $s = s_j$. Irrelevant conditionals – such as a, b, c, and d in (4.13) – are dropped.

The peak centre estimation has no answer until the prior distribution $P_x(x_1)$ is specified. It assigns the probability of reading the angle $x = x_1$ independent of any γ-detection. In case of ignorance, invariance with respect to a change of the angle origin indicates a uniform distribution [Jay68]. However, one can hardly be so ignorant: testable information restricts the probability assignment. For instance, if the goniometer scans only the angles $|x| \leq w$ or the survey frequency $p(x)$ is known, the principle of maximum entropy indicates $P_x(x_1) = \mathrm{If}(|x_1| \leq w)/(2w)$ – where If(.) is one if its argument is true and zero otherwise – or $P_x(x_1) = p(x_1)$, respectively.

$$\begin{aligned} P_x(x_1|n \geq 1) &= \frac{P_n(n \geq 1|x_1)P_x(x_1)}{Z} \\ &= \frac{\left[1 - P_n(0|x_1)\right]P_x(x_1)}{Z} \ , \end{aligned} \tag{4.14}$$

where the evidence of $n \geq 1$

$$Z = P_n(n \geq 1) = \int_{-\infty}^{+\infty} \left[1 - P_n(0|x_1)\right] P_x(x_1) \, \mathrm{d}x_1 \qquad (4.15)$$

is the probability of detecting at least one γ, independently of the goniometer angle. In the limit when the observation window tends to zero,

$$\lim_{\Delta T \to 0} P_n(0|x_1) = \lim_{\Delta T \to 0} \mathrm{e}^{-I\Delta T} = 1 - I\Delta T \qquad (4.16)$$

and the evidence is

$$Z = b\Delta T \int_{-\infty}^{+\infty} \tilde{I}(x_1; a, c, d) P_x(x_1) \, \mathrm{d}x_1 \ , \qquad (4.17)$$

where $\tilde{I} = I/b$ is the peak profile scaled to its maximum. This limit ensures that at most one γ is detected in each observation window, for all practical purposes. Eventually, (4.14) is

$$P_x(x_1|n \geq 1) = \frac{\tilde{I}(x_1; a, c, d) P_x(x_1)}{\tilde{Z}(a, c, d)} \ , \qquad (4.18)$$

where

$$\tilde{Z} = \frac{Z}{b\Delta T} = \langle \tilde{I}(a, c, d) \rangle \qquad (4.19)$$

is the expected value of the peak profile with respect to $P_x(x_1)$. It is worth noting that the peak maximum b disappears from the analysis, consistently with the fact that a single angle reading does not deliver any information about the γ-flux.

In the last step, the Bayes theorem is used again to write the probability density of the unknowns given the angle reading $x = x_1$. It is

$$\begin{aligned} P_{acd}(\hat{a}, \hat{c}, \hat{d}|x_1) &\propto P_x(x_1|n \geq 1) P_{acd}(\hat{a}, \hat{c}, \hat{d}) \\ &= \frac{\tilde{I}(x_1; \hat{a}, \hat{c}, \hat{d}) P_x(x_1) P_{acd}(\hat{a}, \hat{c}, \hat{d})}{\tilde{Z}(\hat{a}, \hat{c}, \hat{d})} \ . \end{aligned} \qquad (4.20)$$

Once the sampling distribution $P_x(x_1|n \geq 1)$ and the sorted angle are given, the only remaining input for calculating $P_{acd}(\hat{a}, \hat{c}, \hat{d}|x_1)$ is the prior probability $P_{acd}(\hat{a}, \hat{c}, \hat{d})$ – whatever the angle reading is – of the model parameters. Objective means to incorporate the available information into the prior probability are discussed in [Jay68]. It is known in advance that the background level and peak width are positive; therefore, this information must be incorporated into $P_{acd}(\hat{a}, \hat{c}, \hat{d})$.

The next step is to determine the prior probability within the parameter space. If additional testable information is available, the maximum-entropy criterion allows information

to be converted into a unique probability assignment. Otherwise, the prior probability is set by finding the parameter transformations which leave the sampling distribution unchanged – a shift of the angle origin and a change of its measurement unit – and, then, by asking for the invariance of the prior probabilities with respect to the same transformations. The result is [Jay68]:

$$P_{acd}(\hat{a}, \hat{c}, \hat{d}) \propto \frac{\text{If}(\hat{a} > 0 \ \& \ \hat{d} > 0)}{\hat{d}} \ . \tag{4.21}$$

It must be noted that (4.21) is an improper probability density. This is not a serious difficulty; while the prior norm diverges, the post-data probability density is usually integrable. If not, as in the case of a single reading, the Bayes theorem is warning that there is little information in the data and it is necessary to set at least lower and upper bounds to the prior knowledge.

If the goniometer angle is in the $[-w, w]$ interval with uniform probability, that is, $P_x(x_1) \propto \text{If}(|x_1| \leq w)$,

$$\tilde{Z} = \int_{-w}^{+w} \tilde{I}(x) \mathrm{d}x \ . \tag{4.22}$$

Contrary, if the angle is fixed, say $x = 0$, the probability of recording, irrespective of γ-detection, the angle value x_1 is $P_x(x_1) = \delta(x_1)$, where $\delta(.)$ is the Dirac's function. Therefore, $\tilde{Z} = \tilde{I}(x_1; a, c, d)$. Consequently, from (4.18) and (4.20), $P_x(x_1 | n \geq 1) = P_x(x_1)$ and $P_{acd}(\hat{a}, \hat{c}, \hat{d} | x_1, n \geq 1) = P_{acd}(\hat{a}, \hat{c}, \hat{d})$, since, in this case, proportional means equal. Hence, the post- and pre-data probability densities are equal and no information is delivered by the measurement, as expected.

The background level and peak width take part in the analysis, but they are of no interest. To obtain the probability density of the centre, irrespective of them, a and d are integrated out from $P_{acd}(\hat{a}, \hat{c}, \hat{d} | x_1, n \geq 1)$ by marginalization. Hence,

$$P_c(\hat{c} | x_1) = \int_{-\infty}^{+\infty} P_{acd}(\hat{a}, \hat{c}, \hat{d} | x_1, n \geq 1) \ \mathrm{d}\hat{a} \ \mathrm{d}\hat{d} \ . \tag{4.23}$$

Extension to many readings

The previous analysis can be extended to many readings, each one triggered by a γ-detection. In this case, the sampling distribution of N readings $\mathbf{x} = \{x_1, x_2, \ldots x_N\}$ is

$$P_x(\mathbf{x} | \forall i \ n_i \geq 1) = \frac{\prod_{i=1}^{N} \tilde{I}(x_i; a, c, d) P_x(x_i)}{\tilde{Z}^N(a, c, d)} \ . \tag{4.24}$$

The choice of independent prior-probabilities, whether γs are detected or not, reflects the absence of any time coordinate and ordering in the reading list, as well as it excludes pathological scan laws, such as a fixed goniometer position.

By leaving out all the terms independent of the model parameters, the post-data probability density is

$$P_{acd}(\hat{a}, \hat{c}, \hat{d}|\mathbf{x}) \propto \frac{P_{acd}(\hat{a}, \hat{c}, \hat{d}) \prod\limits_{i=1}^{N} \tilde{I}(x_i; \hat{a}, \hat{c}, \hat{d})}{\tilde{Z}^N(\hat{a}, \hat{c}, \hat{d})} \ . \tag{4.25}$$

The peak maximum still disappears from the analysis. This can be understood by observing that, in the absence of any time information, having the angle list collected in one second or in one hour makes no difference and there is no basis to evaluate the γ-flux.

The post-data probability density is the basic result of this analysis. To convert it into a single numerical estimate – for instance, of the peak centre – a loss associated with a wrong estimate must be specified. Hence, the optimal estimator will minimize the mean loss with respect to the relevant marginal distribution; in this case, $P_c(\hat{c}|\mathbf{x})$. If the loss function is proportional to the squared error, the optimal estimator is the mean,

$$\mathrm{E}(c) = \int_{-\infty}^{+\infty} \xi P_c(\xi|\mathbf{x}) \, \mathrm{d}\xi \ . \tag{4.26}$$

If the loss is proportional to the absolute error, or it is a constant, the optimal estimator is the median, or the most probable value. Confidence intervals are expressed by integrating $P_c(\hat{c}|\mathbf{x})$ to obtain the cumulative distribution function.

Application to *Gams* data

At *Gams*, the probability density of the angle between the A-crystal and the B-crystal deviates from a constant value. The occurrence frequencies of 35157 angle values x' were recorded by sampling the crystal rotations every 125 ms independently from γ-counting. This scan consisted of 44 angle-difference steps – each lasting 20 s. According to the detector resolution they were counted into $M = 1701$ bins resulting in a smoothed probability distribution $p(x'_j)$. It is shown in Figure 4.23. The probability-density modulation is due to the angle jitter; the increasing probability midway the angle range is due to smaller steps, because of the peak detection. A subset of the recorded angle differences is plotted versus time in Figure 4.22; a significant jitter about the mean angle-values is clearly visible. During the same scan, $N = 166$ angle values x were collected by using the Ge-detector to trigger the angle readings on γ-detection; their histogram is shown in Figure 4.24.
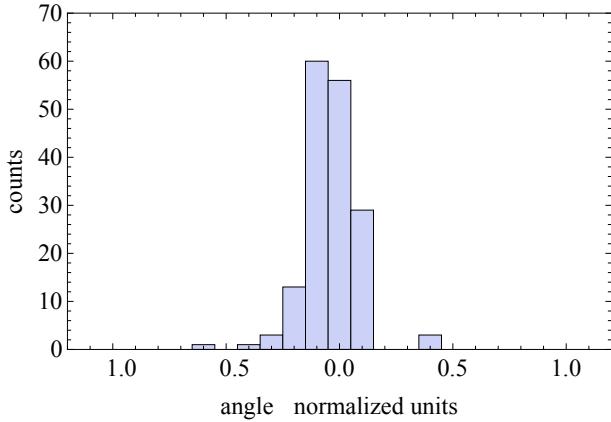
Figure 4.24: Histogram of the 166 angle readings triggered by γ-detection.

Assuming a Lorentzian intensity profile, the evidence of γ-detection is

$$\tilde{Z} \approx \sum_{j=1}^{M} p(x'_j) \left[a + \frac{1}{1 + (x'_j - c)^2/d^2} \right] , \qquad (4.27)$$

where the integral in (4.17) has been approximated by a sum, $\{x'_1, x'_2, ...x'_{M=1701}\}$ are the angle bins and $P_x(x'_j) = p(x'_j)$ the associated frequencies, as determined experimentally (see Figure 4.23). Hence,

$$P_{acd}(\hat{a}, \hat{c}, \hat{d}|\mathbf{x}) \propto \frac{\displaystyle\prod_{i=1}^{N} \left[\hat{a} + \frac{1}{1 + (x_i - \hat{c})^2/\hat{d}^2} \right]}{\left\{ \displaystyle\sum_{j=1}^{M} p(x'_j) \left[\hat{a} + \frac{1}{1 + (x'_j - \hat{c})^2/\hat{d}^2} \right] \right\}^{N} \hat{d}} , \qquad (4.28)$$

in the allowed range of the model parameters.

Apart from the $\hat{d}$ term in the denominator – which originates from the prior probability density and is irrelevant if there is a reasonable amount of data – equation (4.28) is the data likelihood. Therefore, the most probable values $a = 0.000^{+.027}_{-.000}$, $c/w = -0.045 \pm 0.011$, and $d/w = 0.104 \pm 0.016$ – where the associated uncertainty are the standard deviations of the Gaussian approximation of (4.28) – are basically the maximum likelihood estimates.

After marginalization, the probability density of the peak centre is shown in Figure 4.25; the relevant estimate is again $c/w = -0.045 \pm 0.011$ (expected value plus/minus one standard deviation). It is not so for the background level. In fact, the relevant marginal probability density is exponential, as shown in Figure 4.26. Consequently a better background estimate is $a = 0.007^{+.008}_{-.005}$ (median plus/minus quartiles).
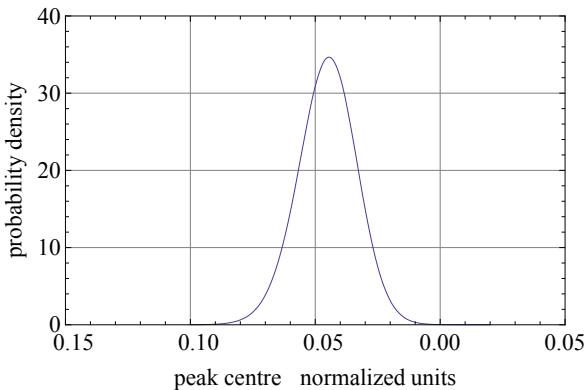
Figure 4.25: Posterior probability density of the peak centre given the angles in Figure 4.24.
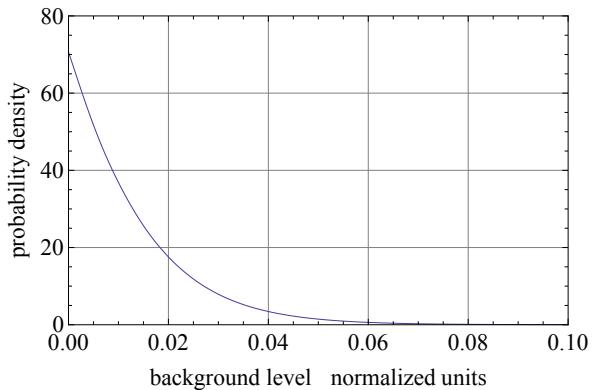
Figure 4.26: Posterior probability density of the background level given the angles in Figure 4.24.

4.3.3 Summary

The DAQ system for *Gams* was completely renewed. This comprises motors, motor-controls, interferometer readout electronics, γ-acquisition electronics and software. This system was developed and tested on *Gams5* and has been in successful operation there since 2008:

\- The motors for detector, collimator and crystal-axes can be operated in parallel.

\- A new phase detection module allows a ten times higher top-speed of the goniometer axis.

\- A better communication between this module and the motor-control reduces the time the axis needs to find its target position.

All these changes reduce the time which is necessary for changing the Bragg order, and they speed up the calibration.

\- A direct communication between phase module and γ-acquisition module allows the γ-triggered interferometer read-out.

\- A new method for evaluating such data has been developed.

\- The common instrument-control software at ILL has been adapted for *Gams*. As it is maintained by the SCI-group, it consumes less time from instrument-scientist for software issues. Additionally, it allows better scheduling of acquisition sequences and has extensive monitoring capabilities.

The system stays in operation at *Gams5*. A copy was made for *Gams6*.

4.4 Further improvements

Several small changes will further improve the performance of the instrument. These do not involve any scientific discovery, but they are crucial for the success of *Gams6*.

crystal-axis motors

The crystal axis motors used to be step motors. They were operated in micro-stepping mode to achieve the necessary precision. This mode causes a lot of heat. Even worse, this heat production is different for each crystal angle. Consequently the temperature sensitive goniometer received a systematic error. The situation was improved by installing an actively regulated water-cooling system in 2008. For *Gams6*, a further improvement will be done by changing to DC-motors with reduction gear and feedback control from the interferometer.

Thermal stability

By means of optical fibres, the laser was brought 3 m away from the goniometer. Before, it was sitting below the interferometer with the consequence of asymmetrical heating. Several holes in all layers of the thermal shielding were discovered (see Figure 2.10 on page 64). The outer concrete wall is tamped now. The aluminium foil is replaced by a polystyrene-foam housing. It is much closer to the spectrometer table. In fact, so close that the compressed air, that is used for the air-cushion for spectrometer rotations, remains outside after emerging from the cushion. It does less harm there, as the heat capacity is much higher and the active temperature regulation can heat it up quickly. The innermost thermal shielding, which has been a Mylar foil, is replaced by the vacuum chamber. Naturally, this is much more leak proof, but it also provides more heat capacity to average residual temperature fluctuations.

New diffraction crystals

To avoid crystal changes throughout a measurement, a new crystal design was developed. This includes new mounting techniques. Both is presented extensively in chapter 5.

New goniometer axes

The transfer of the spectrometer into vacuum required a new design of the goniometer axes. While the motors needed to stay outside the vacuum chamber, the axes must be inside and they must be mounted to the interferometer table only. This permits a permanent alignment relative to the interferometer and a parallelism of both axes with an accuracy of $10''$. Any play of the axes must be less than the detection limit of $1''$. Any wobble must be less than $10''$. The characterization of the axis is presented in section A.1. The fine-positioning part of the new design has a smaller moment of inertia which leads to higher resonance frequencies and thus less affection to mechanical vibrations. Special care was taken to keep the axes – including goniometer arm and corner cube – strictly symmetric. Consequently, no translational vibrations are converted into rotational vibrations

of the axes. Only the latter would perturb the performance. The coupling of the piezo-electric actuator for fine-positioning was improved by applying a pre-load from the axis, not only from the actuator housing.

Collimation

Gams4 was originally designed to be operated at NIST with an X-ray or a low-energetic γ-source. The collimation was designed accordingly. This implies an inter-crystal collimator: two pairs of little lead-bricks. They cut the non-desired beam at two positions: right after the A- and just before the B-crystal. This reduces the background very well if the non-desired beam hits the front side of these lead bricks. However, high γ-energies result in a small Bragg-angle. Consequently the parasitic beam will hit the inside of these collimator pairs. Unfortunately, the forward-scattering cross-section increases for higher energies as well. Therefore these parasitic beams are mirrored into the detector. Hence, partially removing this inter-crystal collimator can reduce the background massively. The optimal configuration depends strongly on γ-energy and Bragg order.

4.5   Summary

Gams6 bases on the same concept as *Gams4*, but all parts of the instrument have undergone improvements. The core of the instrument, the spectrometer table with the interferometer are a complete new design. The major changes are the transfer of the spectrometer into vacuum, and the redesign of the interferometer. The vacuum chamber is a rather standard engineering piece, but it has a dedicated damping concept. The interferometer is a dedicated design for *Gams*. New features are the auto-compensation effect against drifts and built-in reference beams. All optical elements were re-designed and they are mounted without glue. To improve the thermal stability the laser was separated spatially from the spectrometer and the thermal insulation was improved. A complete exchange and partial new-development of the instrument control and data acquisition system allows a much faster operation and γ-triggered position read-out. A theory for evaluating these date was developed.
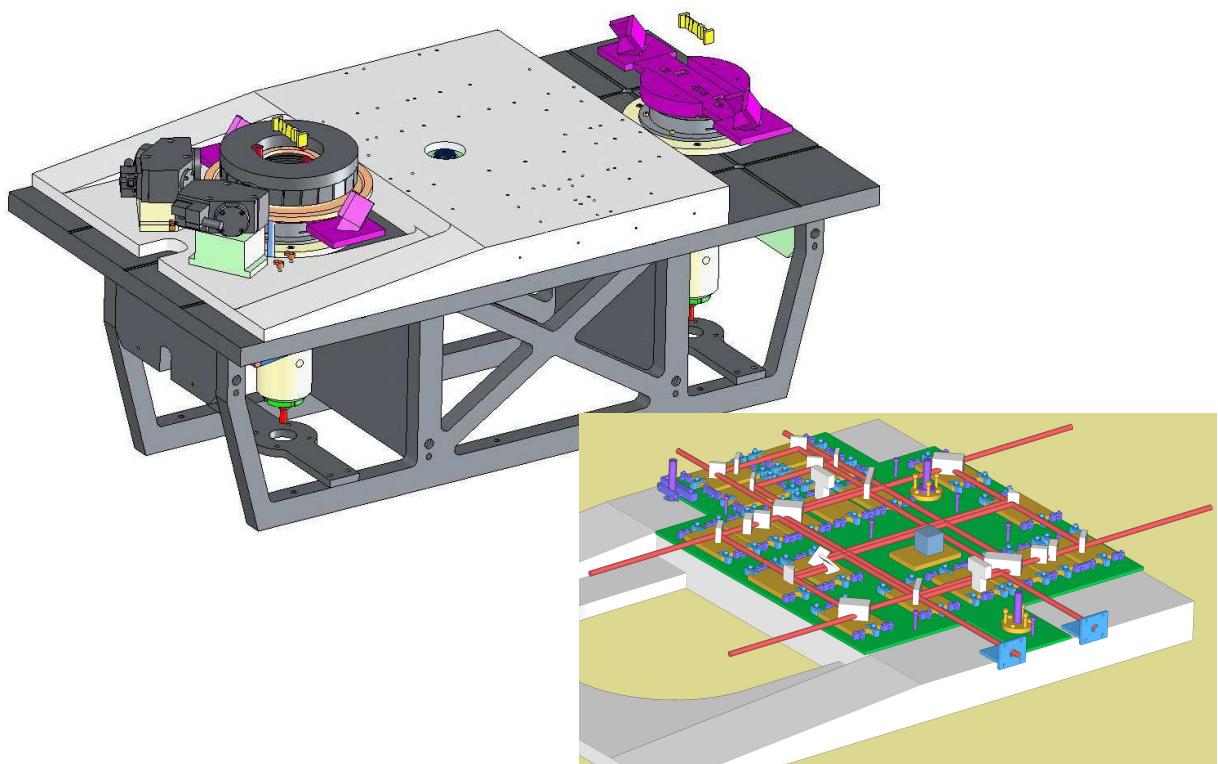
Figure 4.27: Construction plan for *Gams6*. The interior of the vacuum chamber: support structure, interferometer block, crystal axes, goniometer arms polygon and autocollimators. The vacuum chamber and the crystal holders are not drawn. The inlet shows the interferometer block equipped with alignment tables (yellow), clamping mechanism (violet), and optics (white). The mounting aid (green) is removed in normal operation. The laser paths are indicated (red).

161
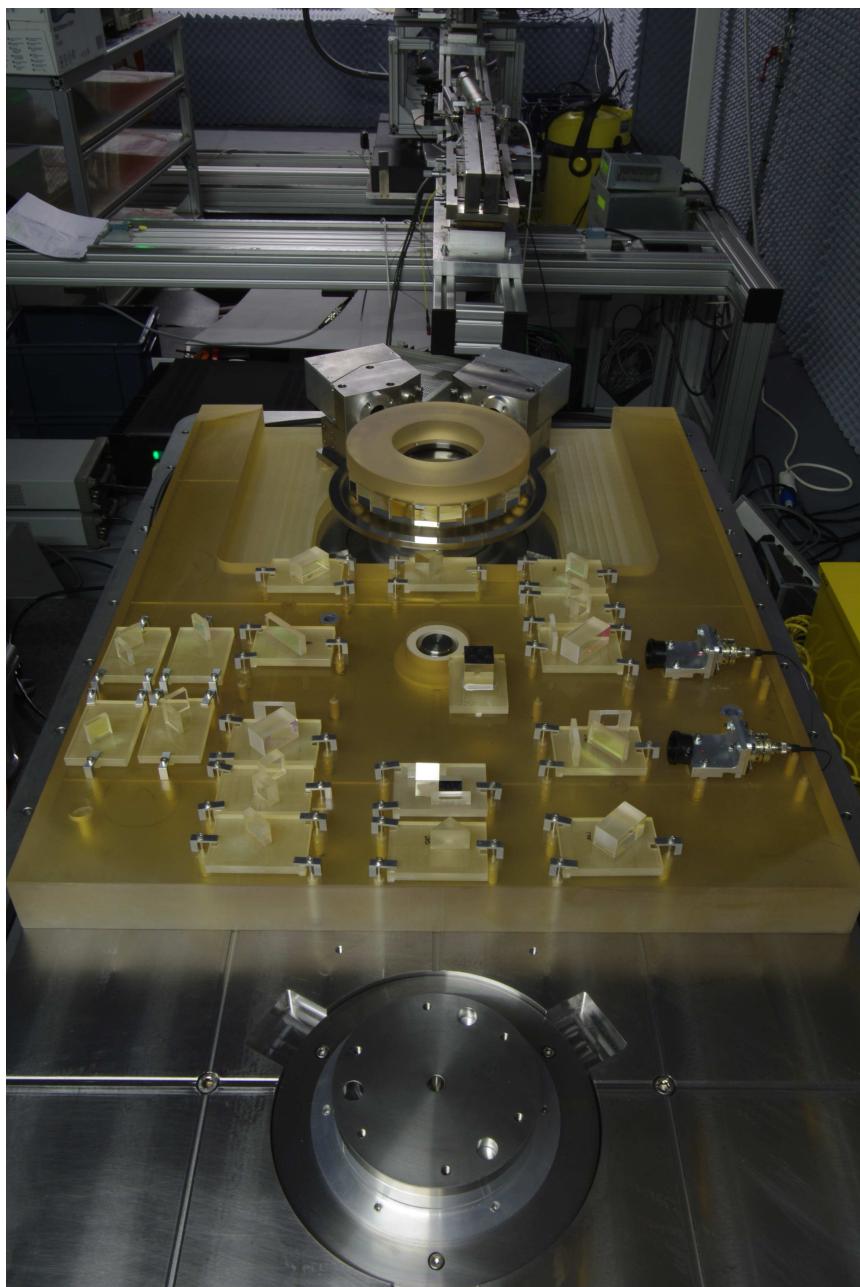
Figure 4.28: Interferometer installed inside the *Gams6* vacuum chamber. Collimator and Detector are visible in the background.

Chapter 5

New crystals

The diffraction crystals that were used for *Gams4* have two disadvantages. First, their absolute lattice spacing was never measured directly. Only pieces of the same ingot have been measured in a lattice as explained in section 1.1.6. The reason is of technical nature. The *Gams* crystals have a rather short lamella and some of them are rather thick (up to 6.9 mm). The triple Laue interferometer for the absolute lattice-constant determination requires a long lamella. Furthermore, the institutes operating such devices are equipped with a low energetic x-ray source only ($\sim$ 17 keV). A thick crystal would absorb all intensity, usually these apparatus work with a 0.5 mm thick lamella. Secondly, a binding energy measurement consists of the determination of different transition energies in a large range from 500 keV up to 6 MeV. This large range requires different crystal thicknesses. So far, a new crystal thickness required the exchange of the crystal. This means a human intervention on the spectrometer, causing a large perturbation to the thermal instability and required several days of waiting for the instrument stability. As *Gams6* operates in vacuum, a crystal change is expected to be even more inconvenient.

5.1 Design of the crystals

Both problems were solved by a new crystal design proposed by Giovanni Mana. A crystal that can be operated in a triple Laue interferometer. The lamella is over large parts sufficiently thin (1.0 mm). Two short parts of the lamella are thicker (2.5 mm and 6.0 mm) and thus optimized for binding energy measurements at *Gams*. The outer shape of the crystal, including its bounding surface is identical to that one used in the INRIM experiment for the d_{220} measurement of silicon-28 in the frame of the Avogadro-project. Therefore, the lattice constant of this crystal can be measured in absolute terms. This very same crystal can then be mounted on *Gams6*. Here the thin and the thick parts
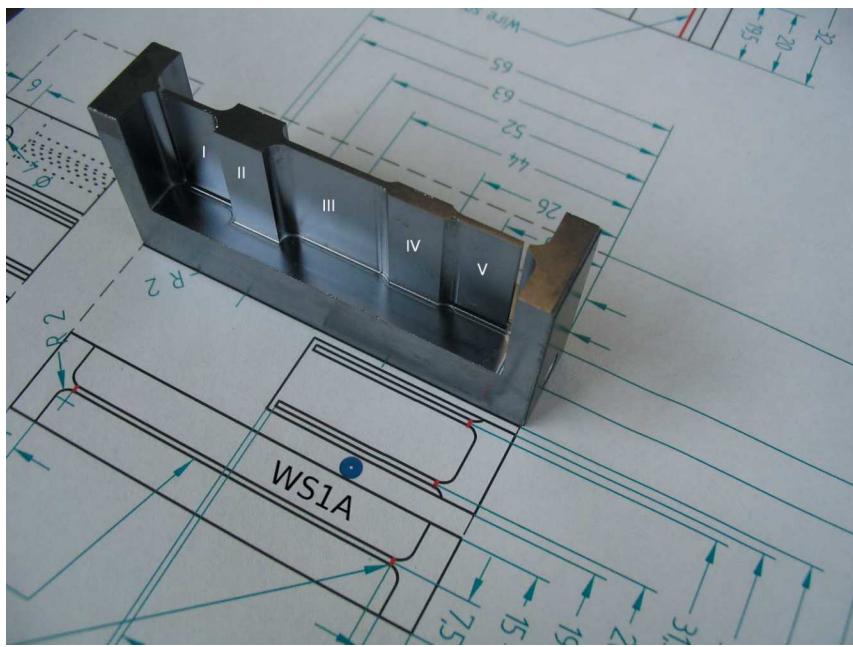
Figure 5.1: Photograph of the *Gams6* crystal. The lamella is 50 mm long. The roman numerals indicate the parts of different thickness: I,III and V are 0.980 mm IV is 2.467 mm and II is 5.963 mm thick. Photo and numbers from [Mas+10].

can be compared by measuring the same γ-energy, without changing the crystal, just by translating the spectrometer table. A photograph of the crystal is shown in Figure 5.1. Two of these crystals were produced, one for the A-axis and one for the B-axis.

The design was studied for deformation due to the own weight. After adding tiny cuts to the design, a finite element analysis yielded that the deformation of the lattice constant will be smaller than 5 parts in 10^9 in the relevant regions of the lamella. The result is shown in Figure 5.2. These studies were performed by Luca Ferroglio. The studies rely on the fact, that the crystal is mounted on three defined points of its ground surface, and that it is is hold by nothing else than its weight. Particularly no clamping at any part of the crystal is allowed.

5.2 Mounting

The deformability of the crystal lattice that has been mentioned in the last section imposes harsh restrictions to the mounting and fixation of the crystal. In a triple Laue interferometer used for the absolute lattice determination the mounting is not that critical as
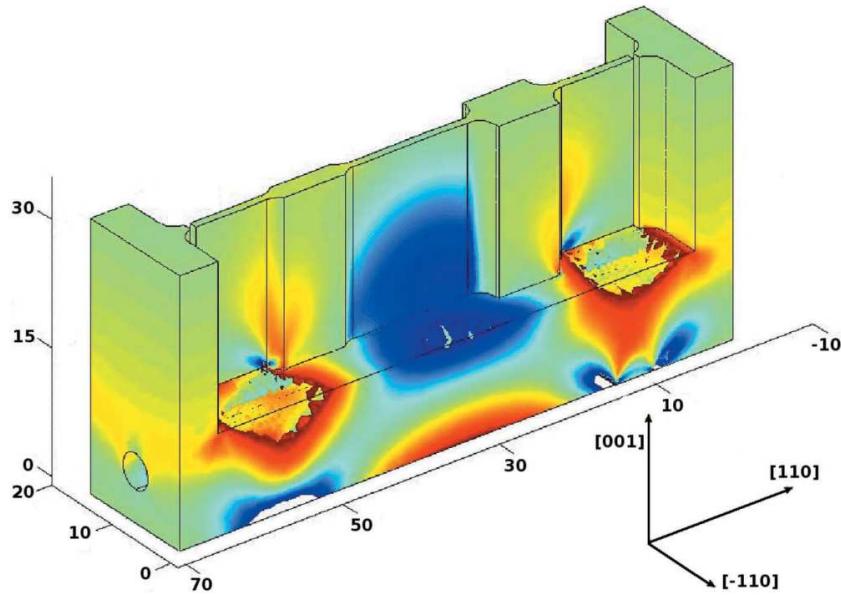
Figure 5.2: Strains in the crystal lattice, induced by its own weight. This was obtained from a finite-element analysis. Dimensions are in mm. The colour palette ranges from -5 (blue) to $+5\,\mathrm{nm/m}$ (red). Crystal parts where the strain is out of scale are blank. The graph is from [Mas+10].
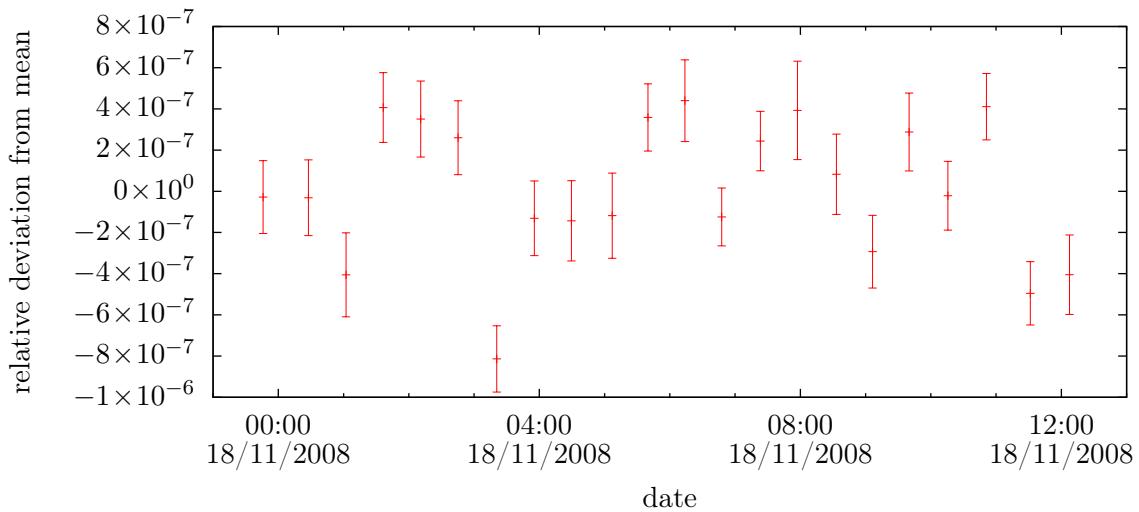

Figure 5.3: Stability of the mounting of the GAMS-I crystal on the B-axis of *Gams4*. Shown are the 4-pack values of a (3,3);(3,-3) scan of a 816 keV line.

165

the crystal itself has a polished surface which is part of the observing optical interferometer. However, *Gams* relies on the rigid mounting of the crystal to the goniometer arm, therefore a stable mounting is crucial. In a first try three balls were glued to the crystal. The goniometer was provided with an adapter that had one conical hole, one groove and one flat surface to hold the balls freely. Designs like this are used in lattice measurements [Bec+81], but it was not successful at *Gams*. Thermal changes in combination with different CTEs of different materials or little and unavoidable machining imperfections caused massive instabilities.

Another method was tested successfully. The crystal is placed on a flat silicon surface. On the three little legs a very small amount of viscous silicon oil is applied. After a setting period of some days the connection is rather fix. Even though this method has been used similarly at INRIM, the success at *Gams* was doubted. At INRIM the crystal itself is part of the optical interferometer, and hence the stability of the mount is of lower importance. Furthermore, the ongoing angular acceleration that occur during the change from one Bragg order to another are not found in other metrology experiments. However, a measurement with *Gams4* could not reveal any instabilities above the instrument instability for a sufficiently long period. The result is shown in Figure 5.3. The crucial point of this method is to use a counterpart that is thick enough so it will not deform. Its surface must be rather flat and smooth. And it must have the same CTE as the crystal. *Gams6* will use doped silicon. It provides all these properties. Additionally, it is well machinable by electric discharge machining.

5.3 Absolute lattice spacing

The lattice constant of the thin parts of the GAMS-I crystal was measured at INRIM with the same apparatus that was used to determine the lattice constant of silicon-28 in the frame of the Avogadro project [And+10]. The lattice constant was measured twice, once in March 2008 and a second time in September 2009. In between the crystal was brought to ILL and mounted on *Gams4* for a comparison of the thick parts of the lamella. The two absolute measurements differed by 1 part in 10^9, while the accuracy of the measurement was 5 parts in 10^9. This proves that the transport from Turin to Grenoble is possible without harming the crystal. The value for the (220) lattice constant for this crystal is 192.015 5702(10) pm [Mas+10]. The values for the three thin parts of the lamella are in good agreement as shown in Figure 5.4.
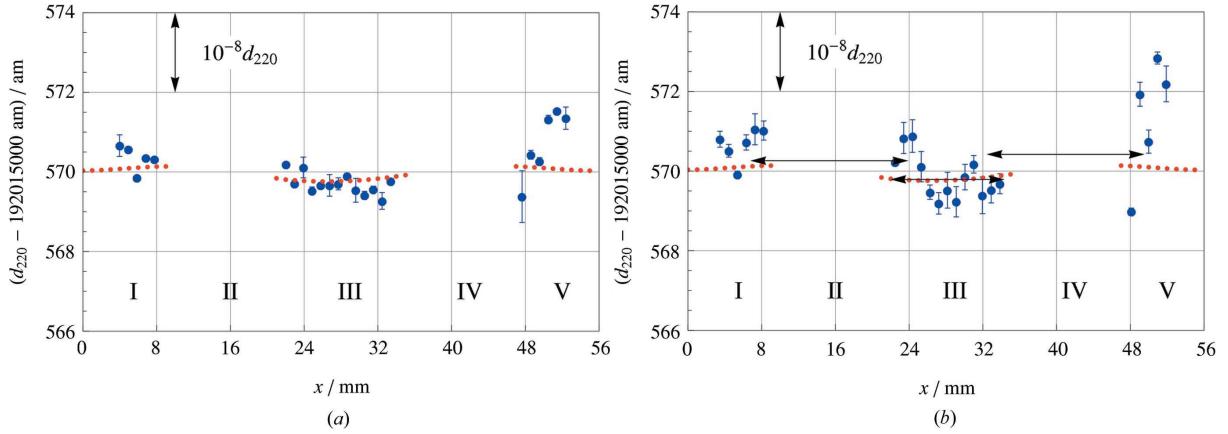
Figure 5.4: Absolute lattice constant measurement of the GAMS-I crystal. Both measurements were performed at INRIM, (a) in March 2008 and (b) in September 2009. In between the crystal was mounted on *Gams4*. Graphs from [Mas+10].
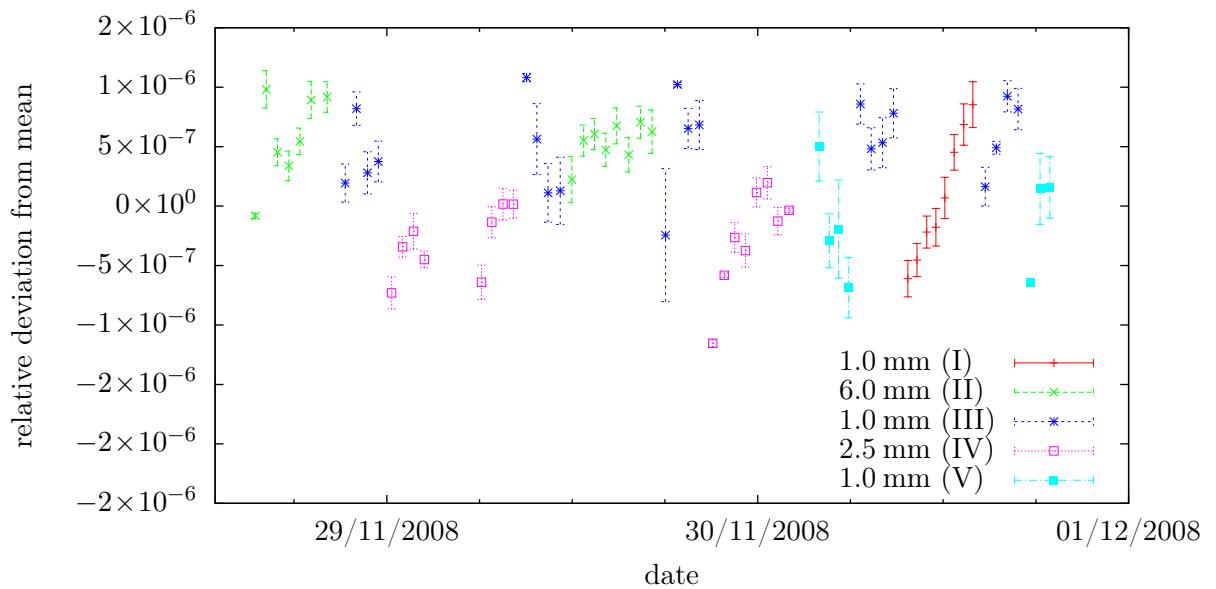
Figure 5.5: Comparison of the lattice constant of all parts of the GAMS-I crystal. The measurement was performed on *Gams4*. Thermal instabilities inhibited a better precision.

167

5.4 Lattice constant comparison

When the GAMS-I crystal was mounted on *Gams4*, it was the first time that is was possible to compare a thick lamella to a thin lamella that had been measured in absolute terms on this very same spot. Unfortunately, during the experiment only one of the new crystals was available. Consequently an unorthodox spectrometer configuration was required to measure the non-central parts of the lamella: The spectrometer table was rotated such that the once diffracted beam would hit the interesting spot. The A-crystal had to be rotated by the same angle in the opposite direction. This results in a different A-crystal position, and this perturbs the instrument stability, as already observed during the 6112 keV chlorine measurement (see Figure 3.14 on page 109). The same happened here. The instrument stability is not better than 10^{-6}. Therefore this is the upper limit that can be given on the equality of the lattice constant in all parts of the crystal. The data are shown in Figure 5.5.

On *Gams6* the thermal stability as well as the instrument stability should be much better. Additionally a second crystal of the same type will be available for the A-axis, hence by translating the spectrometer table, the measurement can be done at symmetric B-angles. Therefore a much smaller precision can be expected.

5.5 Summary

A new crystal was designed. It allowed for the first time to measure the lattice constant of the actual spot of silicon that is used for the binding energy measurement. The lattice constant was measured in absolute terms at INRIM. Then, *this* crystal was mounted on *Gams4*. The stability of the mounting could be successfully shown within the limits of the instrument. A comparison of the thick parts of the lamella (II and IV) was done. Due to the instabilities of *Gams4* this test was not better than 10^{-6}.

Chapter 6

Perspectives

Even though the *Gams* instrument was completely revised throughout this work, not all reachable improvements could be studied in detail. The issues for the near future are divers. It may be an improvement of the actual experiment by the use of new target material. It may go further by studying the molar Planck constant on another particle such as the electron. It may be also a completely different use of the instrument as accurate device for lattice constant measurements for crystals which are not accessible by other means. And it may even go so far to use the technique of *Gams6* at completely new γ-source facilities for energy-stabilization.

6.1 New target materials

The target material is brought close to the reactor core. The radiation heating is approximated with $1\,\mathrm{W/g}$. Cooling by convection or conductivity in the $800\,\mathrm{mbar}$ Helium atmosphere is little and difficult to calculate due to the complex geometry. Depending on the target material and mass, typical temperatures are between $400\,\mathrm{°C}$ and $900\,\mathrm{°C}$. Security reasons require the target to be stable at the expected temperatures. Therefore the choice of material is limited. Metals can usually stand these conditions. Other elements are typically used in the form of an ionic compound. The choice of the compound is guided by the number of interesting atoms per compound mass. But also other parameter as the neutron absorption cross section of the compound partner can be important.

With respect to the molar Planck constant determination, better target materials for sulfur and hydrogen are welcome to improve the signal to noise ratio. Al_2S_3 would be a good candidate. Though there are some open technical questions. Al_2S_3 is moisture sensitive and forms the gas hydrogen sulfide. After neutron exposure this gas will be a

169

pure beta radiation emitter. The targets are disposed in a special *poubelle*[†] after use. It is still unclear if the poubelle is and can be guaranteed to be gas tight for longer times.

For the deuterium binding energy measurements Kapton was used as target material, so far. To avoid decomposition of the material the temperature has to be kept low, hence the target mass is limited [Bö5]. A more stable material could yield a higher event rate by increasing the mass. Zirconium hydride can sustain higher temperatures. However, the compound has the chemical formula ZrH_x, where the x depends strongly on temperature and hydrogen partial pressure. At 950 °C partial pressure of 100 mbar is necessary [DB73] to keep x above 1.8, if the partial pressure drops to 1 mbar, x will become smaller than 0.1. As there is no hydrogen in the atmosphere at the target position the compound would decompose quickly. However, a thin gas tight casing can keep up the inner hydrogen partial pressure. Though the search for such a hydrogen tight housing was not successful yet.
A different solution in the future may be carbon nano-tubes. They can bind hydrogen in good atoms to mass ratios. However, the density of this material is still far to low.

6.2 Positronium

The relative accuracy of the determination of the molar Planck constant with *Gams6* is limited through the high binding energy. In particular the transitions of several MeV are difficult to measure due to their small Bragg angle and the low reflectivity. Both is leading to a very bad signal to background ratio.
Up to now no alternatives were available. However, recent developments in positron handling technology may provide a mean to produce cooled positronium in a sufficient quantity [Hug09]. Thus its decay energy can be measured with *Gams*. The γ-energy is about 511 keV. This leads to a large Bragg-angle. Hence the goniometer resolution is no longer limiting the experiment. The next limit will arise from the calibration of the goniometer. As the atomic mass of the electron is known very accurately 4×10^{-10}, a relative uncertainty of a determination of the molar Planck constant of 5×10^{-9} is conceivable.

6.3 Accurate lattice constants

So far, the only mean for absolute lattice constant measurements is a triple Laue x-ray interferometer. They require three thin lamellas of the same material that have to be be perfectly aligned. It is very laborious to build such an interferometer for every material.

[†]French: waste bin.

For some materials, it is even not possible because they are not sufficiently machinable. Copper, for example, is too soft. Any machining has a huge impact on the crystal lattice. Furthermore, it is not possible to measure the lattice constant of thick crystals, this includes objects which must not be modified or destroyed.

After *Gams6* has measured a certain transition wavelength using a silicon crystal from which the lattice constant is known, the instrument is calibrated. Subsequently, it can measure the lattice constant of any other material with sufficiently strong Bragg reflexes. High γ-energies have a large penetration depth. This allows the determination of the lattice constant of large objects. For example the 91 mm diameter silicon ball of the Avogadro-project may be measured without destruction. By this it can be measured if the lattice constant inside the bulk of this polished ball is the same as it is in the thin etched crystals (see section 1.1.6).

6.4 Intense γ-rays

Up to now *Gams* is a niche instrument. It provides unique resolution and accuracy for the spectroscopy of high-energy γ-rays. It is very specialised and can operate only at the through-going beam tube of the ILL high flux neutron source.

These days, there are new high intense γ-sources in preparation [Hab+10; Hab+08]. These sources will provide γ-beams with an energy up to 19 MeV and with a low divergence of 100 µrad and a relative energy broadness of 10^{-3}. Though, these sources lack of stability and absolute calibration. Both issues can be handled with *Gams6* or an instrument using its technologies [HK10]. It would serve as energy monitor in a feedback loop.

Also high resolution detectors are missing at this high energy. *Gams* can be used here as well. Even though the energy resolution of *Gams* is at these energies limited by the *wide* acceptance angle of the crystals of 0.1 µrad; at 10 MeV and in 3rd Bragg order this results in a resolution of 1 keV (FWHM). This relative resolution of 10^{-4} is still far better than other detectors like HPGe. When assuming a spectrum that consists of individual sharp lines the experimental resolution may be increased by about a factor 10, as the expected count rate is high and hence allows appropriate fitting methods. Despite the resolution limit an accuracy of better than 1 eV can be reached.

All limitations given in the last paragraph are based on a third Bragg order reflex. This is typically the maximum what can be measured at *Gams6* with reasonable count rates. However, the new high intense γ-sources will produce a much higher intensity. Therefore measurements at higher order become possible. For example measuring the 20th Bragg order may become feasible. This has never been done before for next neighbour atomic lattices – either the count rates were too small or the diffraction angles were larger than 180°.

It should be noted that such high intense beams have a radiation power of 2 kW. A thin silicon crystal of 1 mm would absorb only 5‰ of the radiation. This is 10 W on a quite small surface of 0.1 mm^2. This will cause thermal gradients in the crystal and destroy the knowledge of the lattice constant as well as it reduces the resolution by deforming the lattice. This problem can be faced by adding a third crystal before the spectrometer. It would yield a diffracted beam with lower intensity which can then be analysed by a double crystal spectrometer. This primarily diffracted beam would have a reduced divergence compared to the 100 μrad of the initial beam, but yet a larger divergence than the acceptance angles of the *Gams* crystals of 0.1 μrad.

6.5 Summary

Gams6 has been optimized considering the present possibilities of technology. A few little improvements concerning the γ-source can still be done. In contrast, recent developments in other technologies opened new fields where the *Gams6* technology can be applied. This implies particularly the high intensity γ-sources.

The *Gams6* instrument can certainly extend its application field to multi-purpose high-accurate lattice-constant measurements. And in case the positronium production works fine, the initial intention to determine the molar Planck constant will be boosted.

# Appendix A

Component testing

A.1   Axes

The axes for rotating the crystal and the interferometer arm have high mechanical constraints. If the effective rotation differs too much from a perfect rotation the calibration will have systematic errors, as the polygon would rotate an angle sum different from 360° during one turn. The axis-design had been chosen with care (see Figure A.2). High quality ceramic bearings ensure a precise operation even in vacuum.

While the housing of the axis is connected rigidly to the interferometer table and is therefore a good base for a coordinate system $(\hat{x}, \hat{y}, \hat{z})$, the inner shaft $\vec{A}_s$ of the axis might have any orientation. The top surface – described by its normal $\vec{A}_t$ – is rigidly connected to the inner shaft, but its orientation to the shaft is arbitrary and a priori not known. The orientation of the top surface can be identified with the orientation of crystal and interferometer arm as they are also rigidly connected, thus the option of alignment with shims and piezoelectric actuators exists. But as the Angle between $\vec{A}_t$ and $\vec{A}_s$ is arbitrary this does not limit the model.

Any rotation of the axis will result in a rotation of the entire rigid unit of shaft, top surface, crystal and interferometer arm. While the physical rotation will additionally cause a translation of this entire unit, the experiment is not sensitive to any translation. Hence we can without loss of generality limit the model to the vector $\vec{A}_t$ that will be rotated around an effective axis of rotation $\vec{r}$. Note, that all vectors indicate directions and no positions and can therefore be considered as starting from the origin. However, we have to consider that $\vec{r}$ might be different for each angle of rotation Φ. For a proper calibration it is necessary that $\vec{r} \leq 10''$ for all possible $\Phi \in [-20°, +20°]$. To determine
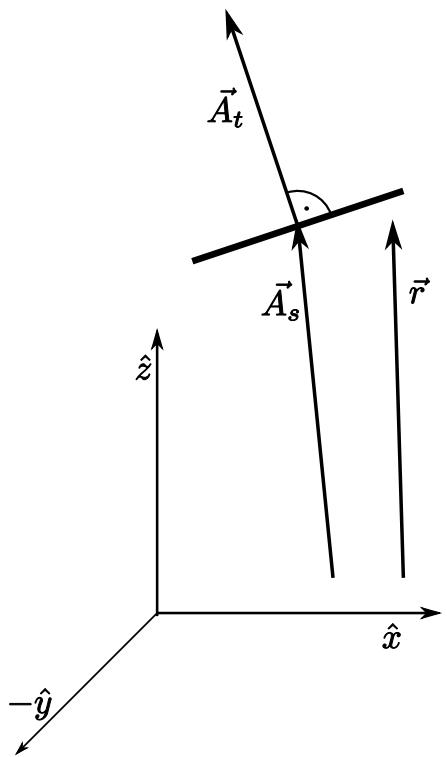
Figure A.1: Axis rotation scheme – vector model for the effective rotation of the axis which must not match any axis of a physical part. The coordinate system is chosen externally maybe from the housing of the axis. $\vec{A_s}$ directs along the inner shaft of the axis. $\vec{A_t}$ is the normal vector of the top surface of the axis. The effective rotation axis $\vec{r}$ is not necessarily collinear to any of the axis.
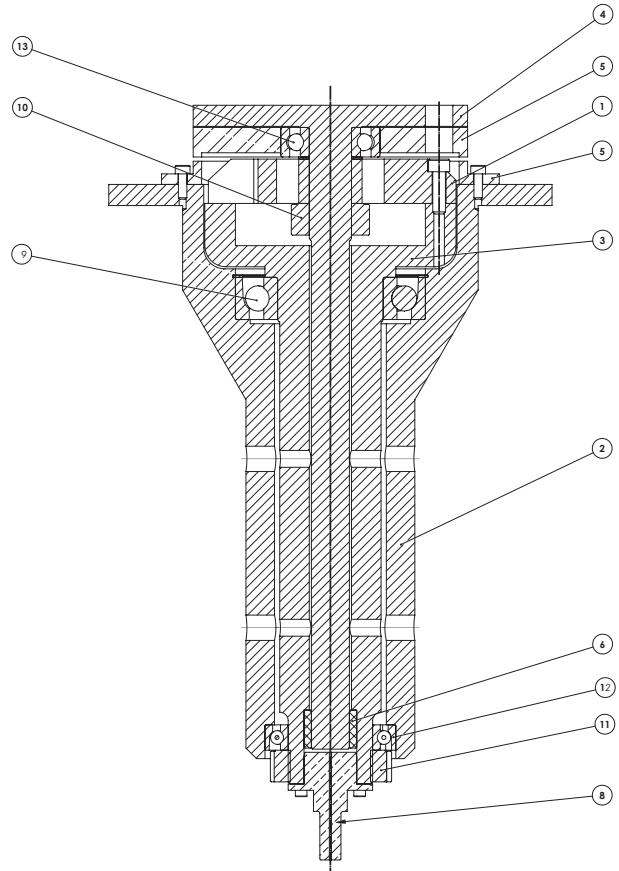
Figure A.2: Cut through the axis. 1) Flexure with piezoelectric actuator for fine movement 2) Housing 3) intermediate axis (coarse positioning) 4) top plate – fixed to crystal and interferometer arm 5) housing 6)bearing 8) connection to coarse motor 9) bearing 11) bearing 12) bearing 13) bearing.

the variation of $\vec{r}$, one measures $\vec{A}_t$, rotates the axis by Φ_1 and measures $\vec{A}_t^{(1)}$. A rotation in three dimensions around the axis $\vec{r}$ can be described:

$$\vec{A}_t^{(1)} = \vec{r}(\vec{r} \cdot \vec{A}_t) + \left(\vec{r} - \vec{r}\left(\vec{r} \cdot \vec{A}_t\right)\right) \cos \Phi + \vec{r} \times (\vec{A}_t - \vec{r}(\vec{r} \cdot \vec{A}_t)) \sin \Phi, \qquad (A.1)$$

if $|\vec{r}| = 1$. If $\vec{A}_t, \vec{A}_t^{(1)}$, and Φ are known, $\vec{r}$ can be calculated. For non-pathological cases $\sin \Phi > \sin \angle \left(\vec{A}_t, \vec{A}_t^{(1)}\right)$, there will be two solutions for $\vec{r}$. In case of the *Gams* axes the angles between all vectors are below $0.002\,\mathrm{rad}$. Hence there will be always two solutions except for those cases where Φ is $0°$, $360°$, or close to these angles and the reproducibility of the orientation measurement is not good enough. From the two solutions, one should choose that one which is not almost anti-parallel to the other vectors. If the set of obtained $\vec{r}$ is within the desired range the axis passed the test.

Both axes were tested individually after their assembly with a coordinate measuring machine (CMM). The CMM measures a number of 3D coordinates of the top surface and calculates the best fitting surface. The normal of these surfaces and the deduced $\vec{r}_\Phi$ are shown in Figure A.3.

Errors by imperfect axis bearings

The crystal and the goniometer arm are mounted on an axis shaft which is hold in positions with bearings. Two bearings per axis at *Gams4* and *Gams5*, three bearings per axis at *Gams6*. These bearings define the actual movement of the axis shaft. Depending on their mechanical properties, this movement is not necessary a pure rotation around one axis (which would be desirable). It may be any combination of rotation and translation, or even worse, this combination may change in dependence of the goniometer angle. And in the worst case the bearings have some play and the motion has some hysteresis or is not reproducible at all.

The translation induced by axis bearings   has no effect on the goniometer readout. As the optical path length of a beam reflected by a corner cube does not change when the corner cube is displaced in the perpendicular plane, any translation in $\hat{y}$ or $\hat{z}$ direction does not affect. As the interferometer measures the path length *difference* to both corner cubes, also a displacement in $\hat{x}$ direction has no effect. This is limited by the fact, that the laser beam must still hit the high quality surfaces of the corner cube.

A displacement of the silicon crystal would shift the diffracted beam, making it touching the collimation. Due to the small diffraction angles, this effect is suppressed. Further the displacement would bring a different spot of the crystal into the beam. If the crystal is not perfect this spot may have a different lattice spacing.
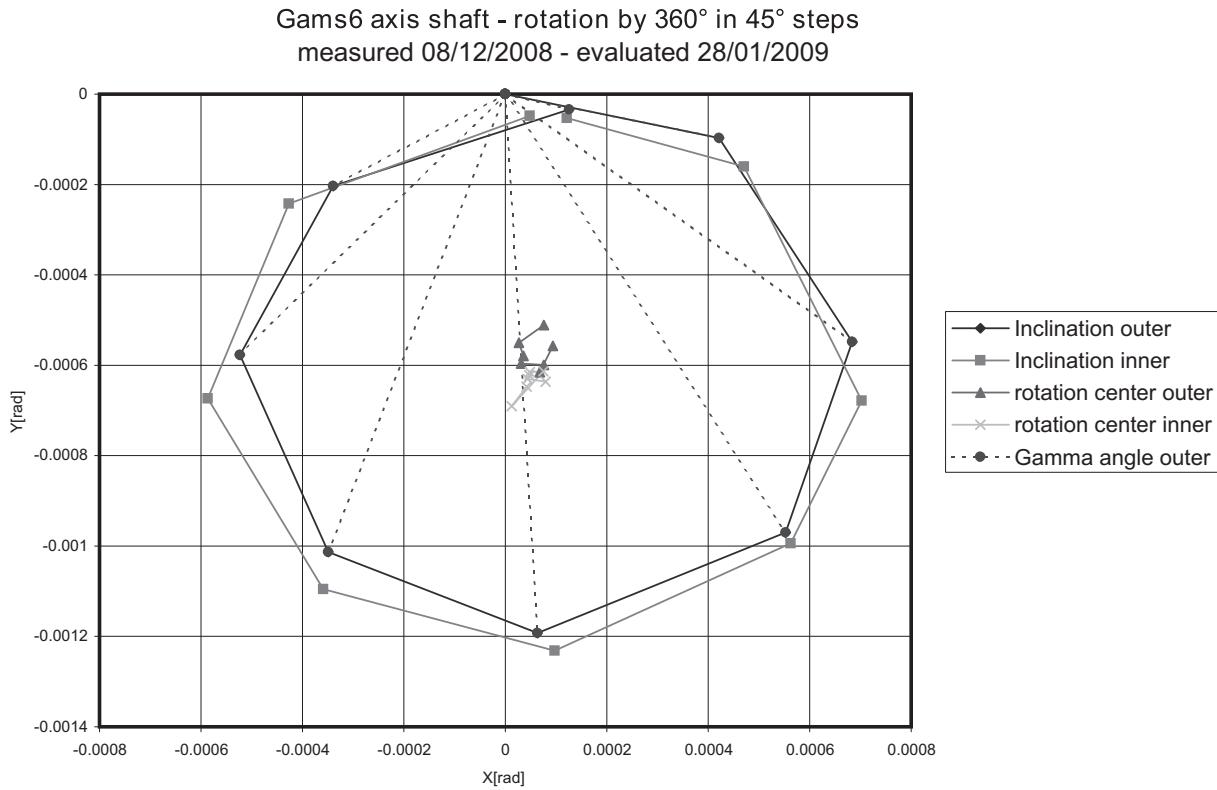
Figure A.3: Inclination of the axis during a rotation by 360°. Drawn is the actual inclination of the normal to the top surface, determined from two rings of different diameter measured by the CMM. Also shown is the centre of effective rotation which is deduced from the inclination values.
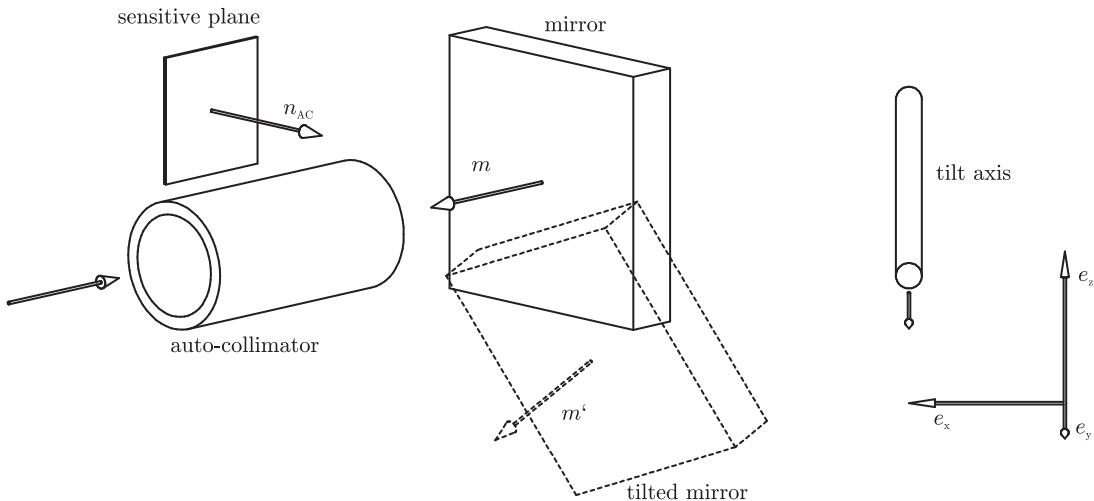
Figure A.4: Effect of axis tilt on calibration. A tilt of the axis while rotating, due to a bad bearing, would tilt the mirrors of the polygon. The autocollimator would notice such a tilt as slight projection into its measuring angle.

The calibration is not affected by translation as long as the autocollimator still sees the mirrors of the polygon.

For all these effects, a displacement of 0.5 mm would be acceptable. The new axis of *Gams6* meets these requirements as shown in the previous subsection.

A.2 Monte-Carlo simulation of interferometer properties

The approximate response function of the goniometer is given in equation (2.2). However this is only valid for a perfect system. In reality, it is influenced by the optics and the laser. The involved theory of beam propagation is well understood. Due to its linearity the calculations are easy. However, due to the numerous optical surfaces and the three-dimensional geometry (corner cubes and polarization), an analytical calculation of the interferometer response function is rather difficult. Though a Monte-Carlo simulation of the interferometer is perfectly possible.

One target of such an analysis was to estimate the induced non-linearity of the interferometer response-function. On the long range domain of several degrees such as different Bragg orders or calibration points this is induced by misalignment of the optical elements, asymmetric path length while having a divergent beam and a non-planar wave front on an expanded photo detector. On the short range domain – the distance of one wavelength or small-integer fractions of it – frequency mixing is important. In the final layout, it is mainly induced by non-orthogonal reflections, stray light and bad alignment. Another target was to estimate the influence of drifts of an optical element on the interferometer output.

Commercial software for optical calculation is available. However none of them corresponded to the specific requests, in particularly polarization and frequency mixing, but they also provide only limited configuration and batch possibilities to simulate the long range displacement of the retro reflectors during the calibration. Access to intermediate data is hardly available. Documentation about the calculation methods and numerical precision are sometimes poor.

A.2.1 Program hierarchy and principles of the algorithm

Therefore a Monte-Carlo simulation was written from scratch in the languages "C++" and "perl". The highly speed optimised C++ core-part uses a single text file as input for the configuration. This describes one static situation of the full interferometer. Several millions of photons are then simulated and the result is put to one or several text files

which describe the signal in the photo detectors. The highly flexible perl part modifies the configuration file such that e.g. the rotation of an interferometer arm is pictured in several steps and each of them the C++ program is called. The perl program will also collect and combine the resulting output files.

As the perl program is only a manipulation of text files including some rotation and translation of three-dimensional coordinates, the following description applies to the C++ program. This simulation provides one or several light sources at which photons are generated randomly according to a given spatial and angular distribution. For each photon the path through the interferometer is calculated. At each collision with an optical surface that would split the light, randomly only one of the possible paths is followed in the calculation. At the detector all photons are summed up according to their phase or other properties.

The algorithm determines automatically which element is hit next. However, for each element a set of exclusive successors can be defined to reduce computing time. This can be abused to disable parts of the interferometer if other parts need to be investigated with higher statistics.

The polarization is stored as a unity vector perpendicular to the current direction of the photon. At each interaction point it may change according to the rules described below. The wavelength is attributed to the photon at its generation in the light source. The heterodyne frequency split is realistically implemented by a slightly different wavelength. The optical refractive index of any material will influence the actual value of the wavelength. The phase of the optical wave is calculated from the path length and the actual wavelength. The phase value at the collision point with the detector is most crucial as it is used for calculating the signal intensity. This is done by summing the complex amplitude. Usually this is done per detector pixel. It can be done also separated by wavelength, and thus frequency to reconstruct the time shape of the detector signal.

A.2.2   Available optical elements

The simulation provides different types of optical elements which can be freely positioned and oriented in space. Depending on their physical meaning some of them have parameters. Each element is simplified as a planar surface with a circular diameter. A solid object, like an optical flat, must be described by at least two elements: an entry and an exit surface.

laser generate photons with a specified space- and divergence-profile. Wavelength, phase and polarization can be specified.

passive surface usually indicates the surface of a massive object and hence the change of the refractive index, as for a mirror or an optical flat, including any coating. Two different reflective indexes may be specified for two orthogonal directions in the surface plane. Each element may accept an overruling transmission and reflection probability.

active surfaces are used for functional complex objects which would occupy high computing time when build from basic passive elements. Such functions can be as simple as polarizer and retarders or as complex as an AOM for wavelength shifting.

detector several types of detectors are available and can be combined. They store and sum the properties of the photons such as phase, travelled path, polarization and frequency.

beam dump provides a way to count photons which are lost at a particular spot, without having the full computing overhead of a "detector" element.

During the calculated path of a photon it is never split. In case of two successive light paths one is chosen according to the transmission or reflectivity probability. This choice incorporates the polarization: The polarization of a photon is stored as a vector orthogonal to its direction. Each surface can have two distinct orthogonal orientations which can react differently on the polarization of the photon. Hence, the projection of the current photon polarizations is calculated. The photon polarization is adjusted randomly to one of the surface orientations. The calculated projection is used as an amplitude of the photon to assure the normalization of the light intensity.
Of course this method neglects single photon interference effects. But in this purpose the light source can be considered as perfectly coherent. However, this indicates that many photons are necessary for an accurate result. Consequently for the sake of computation time it is useful to implement some objects as active surface instead of passive ones, e.g. retarder plates as active surface rudely re-orienting the polarization vector.

The numerical precision of most computer programs is 15 decimal digits provided by a usual 64 bit `double` data type. The required accuracy comes quite close to this limit. To avoid numerical artefacts the `C++` code uses 80 bit `long double` variables providing a precision of 19 decimal bit. All values are stored in full SI units as metres or seconds without any prefix.

On a Pentium-4 single core processor at 3.2 GHz the calculation takes per photon about 1.3 ms when simulating the full interferometer. For precision of $\lambda/14000$ considering a curved wave front about 20 million events and thus 7 hours are necessary.

A.2.3 Lacks of the simulation code

The simulation does not consider any diffraction. The effect of diaphragms could be simulated by the implementation of another type of active surface. However, this has not been implemented as analytical calculations showed no effect for *Gams6* interferometer. Inhomogeneities of materials cannot be considered. Apart from diffraction this could be implemented, but would increase the computing time unacceptably. Furthermore, studies of the influence of the non-homogeneity of individual elements justify this approximation. The refractive tensor of materials is not implemented. Currently the two projections of the tensor which are affecting the beam have to calculated by hand. Yet, this is not such a drawback, as most material specifications doe not provide the full tensor. Similarly, light absorption in material is not implemented. This is acceptable as heterodyne interferometry is amplitude independent.

The simulation is restricted to flat optics which have a circular boundary. This is sufficient for the *Gams6* purpose. A little programming effort would make arbitrary boundary shapes possible, or even spherical surfaces, however, on the cost of computing time.

A.3 Autocollimator

The autocollimator returns voltage Ψ which depends highly on the angel of the facing mirror, and thus, on the goniometer angle Φ. In a small range (< 10 µrad), when a polygon mirror is almost perpendicular to the optical axis of the autocollimator, this response function is very linear.

The principle of the autocollimator is based on a 6 µm wide slit that masks light source and detector. The slit is placed in the focal plane of a lens (focal length 171 mm). In front of the lens the polygon surfaces are passing by. Only when a polygon mirror is orthogonal to the optical axis, the light is reflected back to the detector. To increase the sensitivity of the system, the light between lens and slit is routed over an oscillating mirror, as illustrated in Figure A.5. Hence the detector signal is modulated with the mirror oscillation frequency, as shown in Figure A.6. Using a lock-in amplifier as demodulator, a precise information about the polygon mirror angle can be obtained.
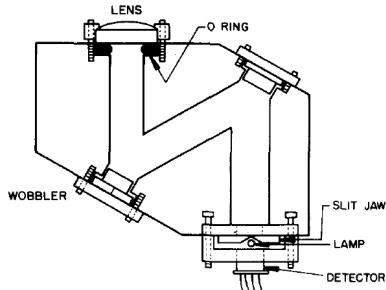
Figure A.5:   Autocollimator scheme. Drawing from [LDT84].

The geometry of the autocollimator leads to the mathematical description:

$$M(t) = M_0 \sin(\omega t) \tag{A.2}$$

$$L(x, x_0) = L_0\, e^{-\frac{(x-x_0)^2}{2\,s^2}} \tag{A.3}$$

$$D(x) = \Theta(x + b/2) \times \Theta(-x + b/2)/b \tag{A.4}$$

$$x_0(t, \Phi) = (2M(t) + \theta) \times f \tag{A.5}$$

$$S(t, \Phi) = \int D(x) \times L(x, x_0(t, \Phi))\ \mathrm{d}x \tag{A.6}$$

$$\Psi(\Phi) = \int_{-\infty}^{0} \sin(\omega t) \times S(t, \Phi) \times e^{-t/T}\, \mathrm{d}t\ , \tag{A.7}$$

with the mechanical parameters: light slit width[†] s, detector slit width b, and focal length f. The functions oscillation mirror angle M, source light distribution L, detector slit function D, centre of reflected beam x_0, detector signal S, and lock-in amplifier response Ψ depend on the variables time t, distance from slit centre x or polygon mirror angle Φ. The parameters mirror oscillation frequency ω, mirror oscillation amplitude M_0, light source intensity L_0, and integration time T can be adjusted to optimize the sensitivity of the system.

A rather high frequency $\frac{\omega}{2\pi} = 1.155\,\mathrm{kHz}$ was chosen in order to allow a small integration time $T = 300\,\mathrm{ms}$. The latter must be sufficiently longer than an oscillation period. A long integration time would require a longer waiting time at a certain position before the voltage acquisition can be started. Additionally, it would average over fast axis oscillations. This would not allow an coincident event-mode data acquisition of autocollimator and interferometer. For *Gams6* it depends on the actual level of vibrations whether event-

---

[†]The set-up constrains $s = b$, where S and D could be better described by a single slit diffraction pattern. However, the model used here – especially the Heaviside step function $\Theta()$ – is computationally much lighter and agrees with the experimental data.
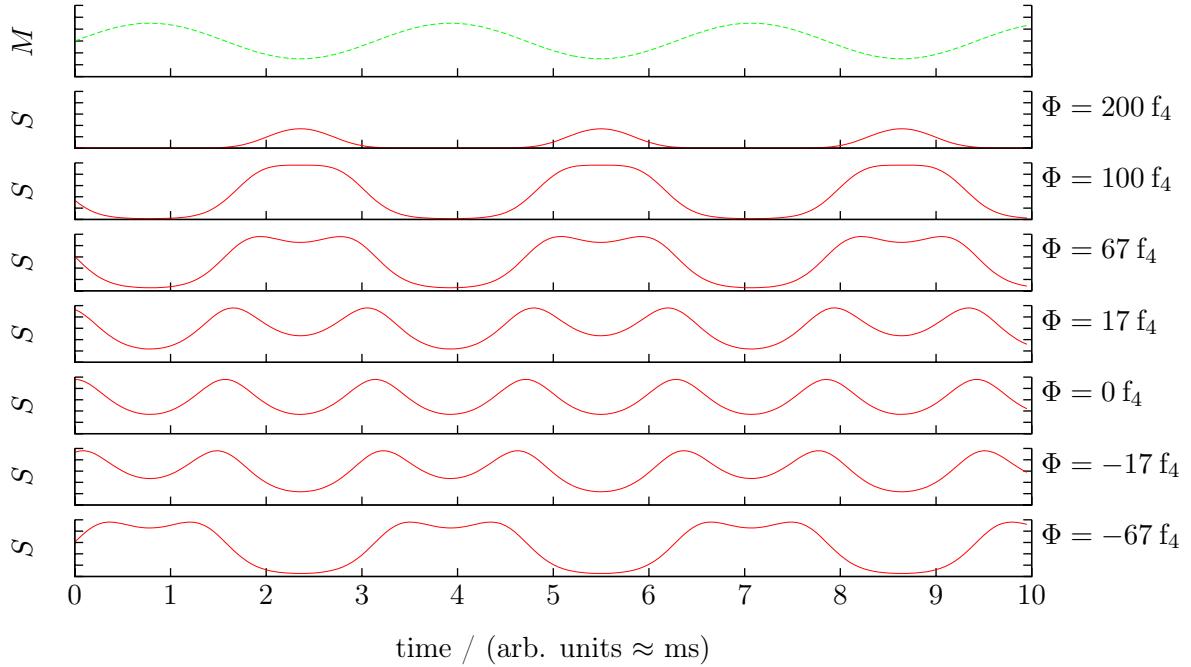
Figure A.6: Autocollimator signal – calculated from theory. The topmost graph shows the induced wobbler mirror oscillation, below are the detector signal on different angles of the polygon mirror. Note the increase of the signal in the far approach ($\Phi \approx 200\,\mathrm{f}_4$). Important for the position sensitivity is the phase change at $\Phi = 0\,\mathrm{f}_4$. All axes are in arbitrary scale.
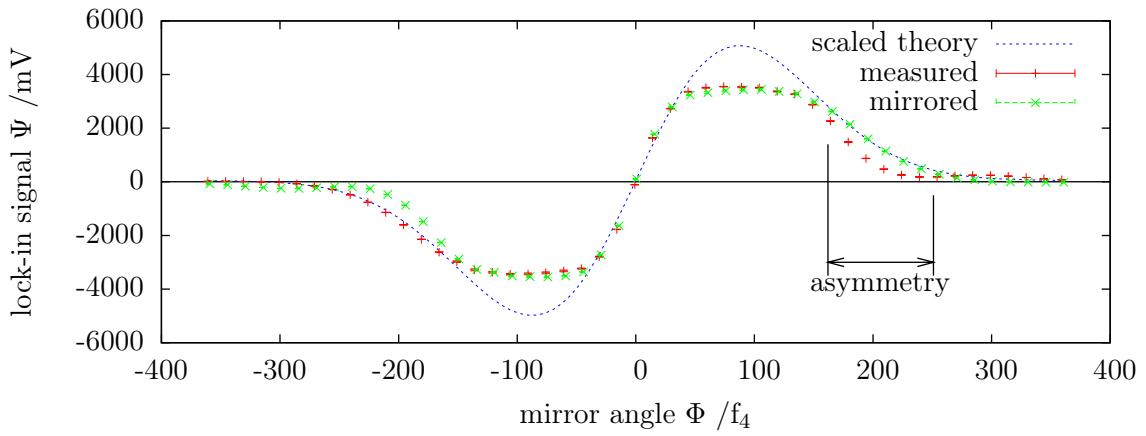
Figure A.7: Autocollimator asymmetry and comparison with theory. A copy of the data is mirrored at the origin to illustrate the asymmetry in the region around $+200\,\mathrm{f}_4$. The theory was scaled to the data by fitting to the data range -380 to $+40\,\mathrm{f}_4$. The discrepancy at high signal may be due to saturation of the photo detector or the lock-in amplifier and was not further investigated. The signal was measured without amplification, and is thus about 10 times smaller than usual. For better comparison, it was scaled back. The reason to do so is the saturation limit of 10 V of lock-in amplifier and analogue-to-digital converter.

mode or time-averaged data-acquisition is most favourable. From the current experience a time-averaged approach seems to be necessary.

At *Gams4* the vibration level of the axis was measured on 18/12/2008 to be 19 $f_{4,rms}$. Considering the autocollimator slope of 1098 mV/f_4 at this time, one would expect a voltage vibration of 21 mV$_{rms}$. The measured value was 38 mV$_{rms}$. While a 1.155 kHz oscillation of 6 mV$_{rms}$ could be identified. The latter is caused by the finite integration time.

At this occasion it was also found that the outer parts of the function are not symmetric. The "drop" marked in Figure A.7 appears for all polygon mirrors which indicates that it is most likely not due to polygon surface imperfection. It might be caused by a dark spot on the lens or a similar asymmetric defect in the autocollimator housing. It will influence the central section of Ψ. However, the effect seems to be constant over time. It is small enough so that the central part of Ψ is still sufficiently linear for a good fit. Even though the resulting effects are estimated to be negligible for *Gams4*, it is necessary to study the autocollimator function for each polygon mirror at each phasing angle (asymmetric calibration) carefully with *Gams6*. The new instrument is much faster, so the autocollimator can be studied extensively, and thermal instabilities of the interferometer have much less impact. Moreover, *Gams6* will be equipped with two autocollimators in parallel, allowing further systematic checks.

Appendix B

Units & conversion

The following units are frequently in use at *Gams*:

radian SI-unit for a plane angle. Often used as micro radian (µrad), nano radian (nrad), or pico radian (prad).

as or $1''$ Arcsecond, a unit for small plane angles, frequently used in optics. $1'' = 1/1000$ degree ≈ 0.48 µrad. At *Gams* used when referring to the alignment of optics or mechanics.

µas Microarcsecond. Unit for even smaller plane angles.

f Fringe. The natural unit of the interferometer. Corresponds to four times the interferometer lever arm length in units of laser wavelength. May have a low index to indicate at which instrument it was obtained to respect the different calibration constants.

f₄ Fringe on *Gams4*, also called electronic fringe. The old analogue acquisition system required to multiply the number of optical fringes by four in order to distinguish between movements in positive and negative directions, and to assign sub fringe information (phase) to the integer information correctly.
$1 \, f_4 \approx 1.948 \times 10^{-7}$ rad $\approx 0.040''$. Which correspond to a corner cube distance of about 8 inch.

f₅ Fringe on *Gams5*, never used in this work. *Gams5* has a corner cube length of 25 cm. Before 2006 a "electronic" multiplication by four was used, similar to *Gams4*.

f₆ Fringe on *Gams6*. $1 \, f_6 \approx 5.3 \times 10^{-7}$ rad $\approx 0.11''$.

Torr pressure unit used for the refractive index of air calculations.
1 Torr = (101 325/760) Pa.

date The British date format is used, that is $dd/mm/yy$.

Appendix C

List of abbreviations

Symbols

$u_{\mathrm{a}}(X)$ absolute uncertainty of the quantity X

$u_{\mathrm{r}}(X)$ relative uncertainty of the quantity X, $u_{\mathrm{r}}(X) = u_{\mathrm{a}}(X)/X$

$x\,\mathrm{unit}_{\mathrm{rms}}$ the index "rms" indicates that the preceding value x is the root mean square of a vibration or oscillation around an unspecified average value.

$\approx$ approximate

$\sim$ in the order of

Abbreviations

Gams *gam*ma-*s*pectrometer, several generations of high-resolution double-crystal γ-spectrometers, hosted at ILL

Gams4 a spectrometer with two flat crystals, provides possibility to absolute calibration in operation since 1980

Gams5 a spectrometer with two flat or bent crystals, in operation since 1998

Gams6 the successor of *Gams4*, scheduled to be in operation in 2011

AOM acousto-optic modulator

CTE coefficient of thermal expansion

SI international system of units (système international)

XRCD X-ray crystal density method (Section 1.1.6)

Institutes and organizations

BIPM Bureau International des Poids et Mesures in Sèvres, France

ILL Institut Laue-Langevin hosts a high-flux neutron source in Grenoble, France

INRIM L'Istituto Nazionale di Ricerca Metrologica in Turin, Italy

NIST National Institute for Standards and Technology, Gaithisburg/Boulder, USA

PTB Physikalisch-Technische Bundesanstalt in Braunschweig, Germany

CIPM Comité international des poids et mesures

CODATA Committee on Data for Science and Technology

CGPM Conférence Générale des Poids et Mesures

Bibliography

[AD90]   W. Augustyn and P. Davis. "An analysis of polarization mixing errors in distance measuring interferometers". In: *J. Vac. Sci. Technol. B* 8.6 (1990), pp. 2032–2036. DOI: 10.1116/1.584868.

[And+10]   B. Andreas et al. "An accurate determination of the Avogadro constant by counting the atoms in a ^{28}Si crystal". In: *arXiv:physics.atom-ph* (2010). URL: http://arxiv.org/abs/1010.2317.

[Aud+03]   G. Audi et al. "The evaluation of nuclear and decay properties". In: *Nuclear Physics A* 729.1 (2003). The 2003 NUBASE and Atomic Mass Evaluations, pp. 3–128. ISSN: 0375-9474. DOI: 10.1016/j.nuclphysa.2003.11.001.

[BÖ5]   H. Börner. *private communications*. Institut Laue-Langevin, 2005.

[Bar+09]   N. Barrière et al. "Experimental and theoretical study of the diffraction properties of various crystals for the realization of a soft gamma-ray Laue lens". In: *Journal of Applied Crystallography* 42.5 (Oct. 2009), pp. 834–845. DOI: 10.1107/S0021889809023218.

[Bas+89]   G. Basile et al. "Progress at IMGC in the absolute determination of the silicon $d(220)$ lattice spacing". In: *Instrumentation and Measurement, IEEE Transactions on* 38.2 (Apr. 1989), pp. 210–216. DOI: 10.1109/19.192274.

[BC64]   B. W. Batterman and H. Cole. "Dynamical diffraction of X-rays by perfect crystals". In: *Rev. Mod. Phys.* 36.3 (July 1964), pp. 681–717. DOI: 10.1103/RevModPhys.36.681.

[BCM93]   A. Bergamin, G. Cavagnero, and G. Mana. "A displacement and angle interferometer with subatomic resolution". In: *Review of Scientific Instruments* 64.11 (1993), pp. 3076–3081. DOI: 10.1063/1.1144362.

[BD93]   K. P. Birch and M. J. Downs. "An updated Edlén equation for the refractive index of air". In: *Metrologia* 30.3 (1993), pp. 155–162. URL: http://stacks.iop.org/0026-1394/30/155.

[BD94]   K. P. Birch and M. J. Downs. "Correction to the updated Edlén equation for the refractive index of air". In: *Metrologia* 31.4 (1994), p. 315. URL: http://stacks.iop.org/0026-1394/31/i=4/a=006.

[Bec08]   P. Becker. "Towards an atomic realization of the kilogram: The measurements of N_A and $N_A h$". In: *Eur. Phys. J. Special Topics* 163 (Oct. 2008), pp. 127–139. DOI: 10.1140/epjst/e2008-00815-7.

[Bec+81]   P. Becker et al. "Absolute measurement of the (220) lattice plane spacing in a silicon crystal". In: *Phys. Rev. Lett.* 46.23 (June 1981), pp. 1540–1543. DOI: 10.1103/PhysRevLett.46.1540.

[BG06]   P. Becker and M. Gläser. "Primary mass standard based on atomic masses". In: *International Journal of Mass Spectrometry* 251.2-3 (2006), pp. 220–230. ISSN: 1387-3806. DOI: 10.1016/j.ijms.2006.01.041.

[BGM07]   M. Borys, M. Gläser, and M. Mecke. "Mass determination of silicon spheres used for the Avogadro project". In: *Measurement* 40.7-8 (2007), pp. 785 – 790. ISSN: 0263-2241. DOI: 10.1016/j.measurement.2006.08.006.

[BIP06]   BIPM, ed. *Le Système international d'unités (SI)*. 8e édition. Pavillon de Breteuil, F-92312 Sèvres Cedex France: STEDI Media, Paris, 2006. ISBN: 92-822-2213-6. URL: http://www.bipm.org/en/si/si_brochure/.

[BJN76]   J. W. Berthold, S. F. Jacobs, and M. A. Norton. "Dimensional stability of fused silica, Invar, and several ultralow thermal expansion materials". In: *Appl. Opt.* 15.8 (Aug. 1976), pp. 1898–1899. DOI: 10.1364/AO.15.001898.

[Bla06]   K. Blaum. "High-accuracy mass spectrometry with stored ions". In: *Physics Reports* 425.1 (2006), pp. 1–78. ISSN: 0370-1573. DOI: 10.1016/j.physrep.2005.10.011.

[Bob93]   N Bobroff. "Recent advances in displacement measuring interferometry". In: *Measurement Science and Technology* 4.9 (1993), pp. 907–926. URL: http://stacks.iop.org/0957-0233/4/907.

[Bog10]   J. Bogenstahl. "Interferometry for the space mission LISA Pathfinder". UID: glathesis:2010-1696. PhD thesis. University of Glasgow, 2010. URL: http://theses.gla.ac.uk/1696/.

[Bus+05]   I Busch et al. "Oxide layer characterization of a ^{28}Si sphere for the international Avogadro project". In: *Conf. Digest (CPEM 2006)*. 2005, pp. 88–89. ISBN: 88-7992-228-9.

[CIP06]   CIPM. *Procès-verbaux des séances du Comité International des Poids et Mesures, 94th meeting (2005)*. 2006. URL: http://www.bipm.org/en/committees/cipm/publications_cc.html.

[CoData02] P. J. Mohr and B. N. Taylor. "CODATA recommended values of the fundamental physical constants: 2002". In: *Rev. Mod. Phys.* 77.1 (Mar. 2005), pp. 1–107. DOI: 10.1103/RevModPhys.77.1.

[CoData06] P. J. Mohr, B. N. Taylor, and D. B. Newell. "CODATA recommended values of the fundamental physical constants: 2006". In: *Reviews of Modern Physics* 80.2, 633 (2008), p. 633. DOI: 10.1103/RevModPhys.80.633.

[CoData98] P. J. Mohr and B. N. Taylor. "CODATA recommended values of the fundamental physical constants: 1998". In: *Rev. Mod. Phys.* 72.2 (Apr. 2000), pp. 351–495. DOI: 10.1103/RevModPhys.72.351.

[DB73]   P. Duenner and D Becker. *Entwicklungsarbeiten zum ITR-Brennstoff-Moderator*. Tech. rep. IA-ITB – 73.42. Bergisch-Gladbach (Germany): INTERATOM GmbH, 1973. URL: http://www.iaea.org/inisnkm/nkm/aws/fnss/knk2/fulltext/34087419.pdf.

[Dew+06]   M. S. Dewey et al. "Precision measurement of the ^{29}Si, ^{33}S, and ^{36}Cl binding energies". In: *Physical Review C (Nuclear Physics)* 73.4, 044303 (2006), p. 044303. DOI: 10.1103/PhysRevC.73.044303.

[DG70]   J. N. Dukes and G. B. Gordon. "A two-hundred-foot yardstick with graduations every microinch". In: *Hewlett Packard Journal* (Aug. 1970). URL: http://www.hpl.hp.com/hpjournal/pdfs/IssuePDFs/1970-08.pdf.

[DH73]   R. D. Deslattes and A. Henins. "X-ray to visible wavelength ratios". In: *Phys. Rev. Lett.* 31.16 (Oct. 1973), pp. 972–975. DOI: 10.1103/PhysRevLett.31.972.

[DiF+94]   F. DiFilippo et al. "Accurate atomic masses for fundamental metrology". In: *Phys. Rev. Lett.* 73.11 (Sept. 1994), pp. 1481–1484. DOI: 10.1103/PhysRevLett.73.1481.

[Dol+00]   C. Doll et al. "Gams5". In: *J. Res. Natl. Inst. Stand. Technol.* 105.1 (2000), pp. 167–171. URL: http://nvl.nist.gov/pub/nistpubs/jres/105/1/j51dol.pdf.

[Dud+02]   J. Dudek et al. "Nuclear tetrahedral symmetry: possibly present throughout the periodic table". In: *Phys. Rev. Lett.* 88.25 (June 2002), p. 252502. DOI: 10.1103/PhysRevLett.88.252502.

[Ein05a]   A. Einstein. "Ist die Trägheit eines Körpers von seinem Energieinhalt abhängig?" In: *Annalen der Physik* 323.13 (1905), pp. 639–643. DOI: 10.1002/andp.19053231314.

[Ein05b]   A. Einstein. "Zur Elektrodynamik bewegter Körper". In: *Annalen der Physik* 322.10 (1905), pp. 891–921. DOI: 10.1002/andp.19053221004.

[Ell+05]   E. J. Elliffe et al. "Hydroxide-catalysis bonding for stable optical systems for space". In: *Classical and Quantum Gravity* 22.10 (2005), S257–S267. URL: `http://stacks.iop.org/0264-9381/22/S257`.

[Est98]   W. Estler. "Uncertainty analysis for angle calibrations using circle closure". English. In: *Journal of Research of the National Institute of Standards and Technology* 103.2 (MAR-APR 1998), pp. 141–151. ISSN: 1044-677X. URL: `http://nvl.nist.gov/pub/nistpubs/jres/103/2/j32est.pdf`.

[FMM08]   L. Ferroglio, G. Mana, and E. Massa. "Si lattice parameter measurement by centimeter X-ray interferometry". In: *Opt. Express* 16.21 (2008), pp. 16877–16888. DOI: `10.1364/OE.16.016877`.

[Fuj+05]   K. Fujii et al. "Present state of the Avogadro constant determination from silicon crystals with natural isotopic compositions". In: *Instrumentation and Measurement, IEEE Transactions on* 54 (2 2005), pp. 854–859. ISSN: 0018-9456. DOI: `10.1109/TIM.2004.843101`.

[Gir94]   G Girard. "The third periodic verification of national prototypes of the kilogram (1988-1992)". In: *Metrologia* 31.4 (1994), pp. 317–336. URL: `http://stacks.iop.org/0026-1394/31/317`.

[Hab+08]   D. Habs et al. "Dense laser-driven electron sheets as relativistic mirrors for coherent production of brilliant X-ray and γ-ray beams". In: *Applied Physics B: Lasers and Optics* 93 (2 2008), pp. 349–354. ISSN: 0946-2171. DOI: `10.1007/s00340-008-3239-4`.

[Hab+10]   D. Habs et al. "Neutron halo isomers in stable nuclei and their possible application for the production of low energy, pulsed, polarized neutron beams of high intensity and high brilliance". In: *Applied Physics B: Lasers and Optics* (2010), pp. 1–15. ISSN: 0946-2171. DOI: `10.1007/s00340-010-4276-3`.

[HFG08]   D. Hanneke, S. Fogwell, and G. Gabrielse. "New measurement of the electron magnetic moment and the fine structure constant". In: *Physical Review Letters* 100.12, 120801 (2008), p. 120801. DOI: `10.1103/PhysRevLett.100.120801`.

[HJ01]   T. Hauschild and M. Jentschel. "Comparison of maximum likelihood estimation and chi-square statistics applied to counting experiments". In: *Nuclear Instruments and Methods in Physics Research Section A: Accelerators, Spectrometers, Detectors and Associated Equipment* 457.1-2 (2001), pp. 384–401. ISSN: 0168-9002. DOI: `10.1016/S0168-9002(00)00756-7`.

[HK10]   D. Habs and U. Köster. "Production of medical radioisotopes with high specific activity in photonuclear reactions with γ-beams of high intensity and large brilliance". In: *Applied Physics B: Lasers and Optics* (2010), pp. 1–19. ISSN: 0946-2171. DOI: `10.1007/s00340-010-4278-1`.

[Hug09]   C. Hugenschmidt. *private communications*. Technische Universität München, 2009.

[ILL09]   ILL. *private communication*. Scientific communication office, 2009.

[Jay03]   E. T. Jaynes. *Probability theory: The logic of science*. Cambridge University Press, Apr. 2003. ISBN: 9780521592710. DOI: `10.2277/0521592712`.

[Jay68]   E. Jaynes. "Prior probabilities". In: *Systems Science and Cybernetics, IEEE Transactions on* 4 (3 1968), p. 227. ISSN: 0536-1567. DOI: `10.1109/TSSC.1968.300117`.

[Jen07]   M. Jentschel. *private communication*. Institut Laue-Langevin, 2007.

[Jen+10]   M. Jentschel et al. "Ultrahigh-resolution γ-ray spectroscopy of ^{156}Gd: A test of tetrahedral symmetry". In: *Phys. Rev. Lett.* 104.22 (June 2010), p. 222502. DOI: `10.1103/PhysRevLett.104.222502`.

[Jen10]   M. Jentschel. *private communication*. Institut Laue-Langevin, 2010.

[JKM09]   M. Jentschel, J. Krempel, and P. Mutti. "A validity test of $E = mc^2$". In: *Eur. Phys. J. Special Topics* 172.1 (June 2009), pp. 353–362. ISSN: 1951-6355. DOI: `10.1140/epjst/e2009-01060-4`.

[Kes+01]   E. G. Kessler et al. "The GAMS4 flat crystal facility". In: *Nuclear Instruments and Methods in Physics Research Section A: Accelerators, Spectrometers, Detectors and Associated Equipment* 457.1-2 (2001), pp. 187–202. ISSN: 0168-9002. DOI: `10.1016/S0168-9002(00)00753-1`.

[Kes+85]   E. G. Kessler et al. "Gamma-ray energies from the reaction ^{35}Cl(n,γ)". In: *Phys. Rev. C* 32.2 (Aug. 1985), pp. 374–378. DOI: `10.1103/PhysRevC.32.374`.

[Kes+94]   E. G. Kessler et al. "Precision comparison of the lattice parameters of silicon monocrystals". In: *Journal of Research of the National Institute of Standards and Technology* 99.1 (January–February 1994), pp. 1–18. URL: `http://nvl.nist.gov/pub/nistpubs/jres/099/1/V99-1.pdf`.

[Kes+99]   E. G. Kessler et al. "The deuteron binding energy and the neutron mass". In: *Physics Letters A* 255.4-6 (1999), pp. 221–229. ISSN: 0375-9601. DOI: `10.1016/S0375-9601(99)00078-X`.

[KFB05]   R. Koening, J. Fluegge, and H. Bosse. "Characterizing the performance of the PTB line scale interferometer by measuring photoelectric incremental encoders". In: *Recent developments in traceable dimensional measurements III*. Ed. by J. E. Decker and G.-S. Peng. Vol. 5879. San Diego, CA, USA: SPIE, 2005, p. 587908. DOI: `10.1117/12.616332`.

[Kib75]   B. P. Kibble. "" In: *Atomic masses and fundamental constants*. Ed. by J. H. Sanders and A. H. Wapstra. Vol. 5. New York: Plenum, 1975, pp. 545–551.

[KJM06]   J. Krempel, M. Jentschel, and G. Mana. "A new double axes angular optical interferometer". In: *CPEM 2006 Conf. Digest.* Torino, Italy, July 2006, pp. 288–289. ISBN: 88-7992-228-9.

[Kre+08] J. Krempel et al. "Progress on the Gams-6 double crystal γ-spectrometer". In: *CPEM 2008 Conf. Digest.* Broomfield, Colorado, USA, June 2008, pp. 634–635. ISBN: 978-1-4244-2399-6. DOI: `10.1109/CPEM.2008.4574939`.

[Kri09]   A. Kriesch. *Drawing of a schematic Penning trap.* Retrieved on 27/08/2009 from `http://de.wikipedia.org/wiki/Penning-Falle`. 2009.

[LaCoste] LaCoste. *Micro-g – Absolute Gravimeters.* Retrieved on 11/08/2010 from `http://www.lacosteromberg.com/absolutemeters.htm`, 2010.

[Law04]   J. Lawall. "Interferometry for accurate displacement metrology". In: *Opt. Photon. News* 15.10 (2004), pp. 40–45. URL: `http://www.osa-opn.org/abstract.cfm?URI=OPN-15-10-40`.

[LDT84]   G. G. Luther, R. D. Deslattes, and W. R. Towler. "Single axis photoelectronic autocollimator". In: *Review of Scientific Instruments* 55.5 (1984), pp. 747–750. DOI: `10.1063/1.1137810`.

[Lis94]   K.-D. Liß. "Strukturelle Charakterisierung und Optimierung der Beugungseigenschaften von $Si_{1-x}Ge_x$ Gradientenkristallen, die aus der Gasphase gezogen wurden". PhD thesis. RWTH Aachen, 1994. URL: `http://darwin.bth.rwth-aachen.de/opus3/volltexte/2001/222/`.

[LK00]   J. Lawall and E. Kessler. "Michelson interferometry with 10 pm accuracy". In: *Review of Scientific Instruments* 71.7 (2000), pp. 2669–2676. DOI: `10.1063/1.1150715`.

[Luo+03] J. Luo et al. "New experimental limit on the photon rest mass with a rotating torsion balance". In: *Phys. Rev. Lett.* 90.8 (Feb. 2003), p. 081801. DOI: `10.1103/PhysRevLett.90.081801`.

[Man09]   G. Mana. *private communication.* Istituto Nazionale di Ricerca Metrologica, 2009.

[Mas+09] E Massa et al. "Measurement of the lattice parameter of a silicon crystal". In: *New Journal of Physics* 11.5 (2009), 053013 (12pp). DOI: `10.1088/1367-2630/11/5/053013`.

[Mas+10] E. Massa et al. "Calibration of a silicon crystal for absolute nuclear spectroscopy". In: *Journal of Applied Crystallography* 43.2 (Apr. 2010), pp. 293–296. DOI: `10.1107/S0021889810001652`.

[McS53]   H. J. McSkimin. "Measurement of elastic constants at low temperatures by means of ultrasonic waves – data for silicon and germanium single crystals, and for fused silica". In: *Journal of Applied Physics* 24.8 (1953), pp. 988–997. DOI: `10.1063/1.1721449`.

[Mil+05]   I. M. Mills et al. "Redefinition of the kilogram: a decision whose time has come". In: *Metrologia* 42.2 (2005), pp. 71–80. URL: `http://stacks.iop.org/0026-1394/42/71`.

[Mil+06]   I. M. Mills et al. "Redefinition of the kilogram, ampere, kelvin and mole: a proposed approach to implementing CIPM recommendation 1 (CI-2005)". In: *Metrologia* 43.3 (2006), pp. 227–246. URL: `http://stacks.iop.org/0026-1394/43/227`.

[MKF10]   G. Mana, J. Krempel, and L. Ferroglio. "Estimation of the centre of a diffraction peak by triggering the goniometer-angle readings *via* photon detection". In: *Journal of Applied Crystallography* 43.1 (Feb. 2010), pp. 83–88. DOI: `10.1107/S0021889809046548`.

[MNH79]   N. A. Massie, R. D. Nelson, and S. Holly. "High-performance real-time heterodyne interferometry". In: *Appl. Opt.* 18.11 (1979), pp. 1797–1803. DOI: `10.1364/AO.18.001797`.

[Mye07]   E. Myers. *private communications.* Florida State University, 2007.

[NB05]   R. A. Nicolaus and G Bonsch. "Absolute volume determination of a silicon sphere with the spherical interferometer of PTB". In: *Metrologia* 42.1 (2005), pp. 24–31. URL: `http://stacks.iop.org/0026-1394/42/24`.

[Nic09]   R. A. Nicolaus. *private communication.* Physikalisch-Technische Bundesanstalt, 2009.

[Nye57]   J. Nye. *Physical properties of crystals.* Oxford University Press, 1957. ISBN: 9780198511656.

[PA06]   M. Pisani and M. Astrua. "Angle amplification for nanoradian measurements". In: *Appl. Opt.* 45.8 (Mar. 2006), pp. 1725–1729. DOI: `10.1364/AO.45.001725`.

[Pec48]   E. R. Peck. "Theory of the corner-cube interferometer". In: *J. Opt. Soc. Am.* 38.12 (1948), pp. 1015–1015. DOI: `10.1364/JOSA.38.001015`.

[Pic06]   A Picard. "Mass determinations of a 1 kg silicon sphere for the Avogadro project". In: *Metrologia* 43.1 (2006), pp. 46–52. URL: `http://stacks.iop.org/0026-1394/43/46`.

[Qui89]   T. J. Quinn. "News from the BIPM". In: *Metrologia* 26.1 (1989), pp. 69–74. URL: `http://stacks.iop.org/0026-1394/26/69`.

[Rai+05]   S. Rainville et al. "World year of physics: A direct test of $E = mc^2$". In: *Nature* 438 (7071 2005), pp. 1096–1097. DOI: 10.1038/4381096a.

[RK07]   I. A. Robinson and B. P. Kibble. "An initial measurement of Planck's constant using the NPL Mark II watt balance". In: *Metrologia* 44.6 (2007), pp. 427–440. URL: http://stacks.iop.org/0026-1394/44/427.

[RTP04]   S. Rainville, J. K. Thompson, and D. E. Pritchard. "An ion balance for ultra-high-precision atomic mass measurements". In: *Science* 303.5656 (2004), pp. 334–338. DOI: 10.1126/science.1092320.

[Sch65]   H. W. Schnopper. "Spectral measurements with aligned and misaligned two-crystal spectrometers. I. Theory of the geometrical window". In: *Journal of Applied Physics* 36.4 (1965), pp. 1415–1423. DOI: 10.1063/1.1714321.

[Sch78]   W. Schwitz. "Precision of curved crystal spectrometers I. Large angle laser interferometer". In: *Nuclear Instruments and Methods* 154.1 (1978), pp. 95–104. ISSN: 0029-554X. DOI: 10.1016/0029-554X(78)90667-5.

[SNW05]   R. Steiner, D. Newell, and E. Williams. "Details of the 1998 Watt balance experiment determining the Planck constant". In: *Journal of Research of the National Institute of Standards and Technology* 110.1 (January–February 2005), pp. 1–26. URL: http://nvl.nist.gov/pub/nistpubs/jres/110/1/j110-1ste.pdf.

[SS06]   D. Sivia and J. Skilling. *Data analysis: A bayesian tutorial.* Oxford University Press, June 2006. ISBN: 978-0-19-856831-5.

[Ste+07] R. L. Steiner et al. "Uncertainty improvements of the NIST electronic kilogram". In: *Instrumentation and Measurement, IEEE Transactions on* 56 (2 2007), pp. 592–596. DOI: 10.1109/TIM.2007.890590.

[Sut87]   C. M. Sutton. "Non-linearity in length measurement using heterodyne laser Michelson interferometry". In: *Journal of Physics E: Scientific Instruments* 20.10 (1987), pp. 1290–1292. URL: http://stacks.iop.org/0022-3735/20/1290.

[TL56]   A. M. Thompson and D. G. Lampard. "A new theorem in electrostatics and its application to calculable standards of capacitance". In: *Nature* 177 (4515 1956). DOI: 10.1038/177888a0.

[WD98]   C.-M. Wu and R. D. Deslattes. "Analytical modeling of the periodic nonlinearity in heterodyne interferometry". In: *Appl. Opt.* 37.28 (1998), pp. 6696–6700. URL: http://ao.osa.org/abstract.cfm?URI=ao-37-28-6696.

[Wea71]   R. C. Weast, ed. *Handbook of chemistry and physics 52th edition.* Boca Raton, FL 33487, USA: CRC Press, 1971.

[Wil+89]   E. Williams et al. "A low field determination of the proton gyromagnetic ratio in water". In: *Instrumentation and Measurement, IEEE Transactions on* 38 (2 1989), pp. 233–237. DOI: 10.1109/19.192278.

[Wu03]   C.-M. Wu. "Periodic nonlinearity resulting from ghost reflections in heterodyne interferometry". In: *Optics Communications* 215.1-3 (2003), pp. 17–23. ISSN: 0030-4018. DOI: 10.1016/S0030-4018(02)02203-4.

[Zac45]   W. H. Zachariasen. *Theory of X-ray diffraction in crystals.* John Wiley and Sons, New York, 1945.

Appendix D

Acknowledgement

Curriculum Vitae

Jochen Krempel, born on 6th of August 1978 in Heidelberg, Germany.
Nationality: German. Currently living in Obersiggenthal, Switzerland.
E-mail: krempel@gmx.net

EDUCATION

2005 – 2010 PhD-thesis in physics at *Ludwig-Maximilians-Universität* in Munich. The experiment is sited at the *Institut Laue-Langevin* in Grenoble.

1999 – 2004 Diplom in physics at the *Ruprecht-Karls-Universität* in Heidelberg.

1989 – 1998 Abitur at the *Kurpfalz-Gymnsasium* in Schriesheim.

1985 – 1989 *Martin-Stöhr Schule* in Hirschberg.

PROFESSIONAL EXPERIENCE

since September 2010 Employed by Paul Scherrer Institut, in Villigen, Switzerland. Working in the ultracold neutron physics group on the neutron electric dipole moment project.

2005 – 2010 Responsible for the design, construction and installation of the new instrument Gams6 at the ILL. Employed by the Institut Laue-Langevin (Grenoble) and the Physikalisch-Technische Bundesanstalt (Braunschweig).

2003 – 2004 Diploma thesis *Beta-Asymmetry in the Decay of Polarized Neutrons.*

2000 – 2003 Software engineer at *Verivox GmbH* www.verivox.de.

1998 – 1999 Mandatory military service.

VOLUNTEERING ACTIVITY

2006 – 2007 Student representative at ILL.

1996 – 1998 Student speaker in high-school.

AWARDS

2008 (CPEM Boulder) Early Career Award.

1998 (Abitur) Best performance in physics, mathematics and overall result.

Appendix E

List of Publications

1. J. Krempel. "Optimierung und Durchführung einer Beta-Asymmetriemessung im Zerfall polarisierter Neutronen". MA thesis. Universität Heidelberg, 2004. `http://www.physi.uni-heidelberg.de/Publications/dipl_krempel.pdf`.

2. H. Abele et al. "The Beta-, Neutrino- and Proton-Asymmetry in Neutron Beta-Decay". In: J. Res. Natl. Inst. Stand. Technol. 110.4 (July-August 2005), pp. 377–381. `http://nvl.nist.gov/pub/nistpubs/jres/110/4/j110-4abe.pdf`.

3. M. Jentschel et al. "Precision Measurement of the Molar Planck's Constant". In: CPEM 2006 Conf. Digest. Torino, Italy, July 2006, pp. 90–91. isbn : 88-7992-228-9.

4. J. Krempel, M. Jentschel, and G. Mana. "A New Double Axes Angular Optical Interferometer". In: CPEM 2006 Conf. Digest. Torino, Italy, July 2006, pp. 288–289. ISBN: 88-7992-228-9.

5. M. Schumann et al. "Measurement of the Neutrino Asymmetry Parameter B in Neutron Decay". In: Physical Review Letters 99.19 (2007), p. 191803. `DOI:10.1103/PhysRevLett.99.191803`.

6. M. Jentschel et al. "Measurement of the Neutron Binding Energy of ^{36}Cl for a Determination of $N_\mathrm{A}h$". In: CPEM 2008 Conf. Digest. Broomfield, Colorado, USA, June 2008, pp. 632–633. ISBN: 978-1-4244-2399-6.

7. J. Krempel et al. "Progress on the Gams-6 double crystal γ-spectrometer". In: CPEM 2008 Conf. Digest. Broomfield, Colorado, USA, June 2008, pp. 634–635. ISBN: 978-1-4244-2399-6. `DOI:10.1109/CPEM.2008.4574939`.

8. M. Schumann et al. "Measurement of the Proton Asymmetry Parameter in Neutron Beta Decay". In: Physical Review Letters 100.15 (2008), p. 151801. `DOI:10.1103/PhysRevLett.100.151801`.

9. R. Frahm et al. "Positron-Electron Pair Creation Near Threshold". In: American Institute of Physics Conference Series. Ed. by J. Jolie et al. Jan. 2009, pp. 554–558. `DOI:10.1063/1.3087084`.

10. R. Frahm et al. "The Miracle of the Electron-Positron Pair Production Threshold". In: Synchrotron Radiation News 22.3 (May 2009), pp. 28–31. `DOI:10.1080/08940880902959775`.

11. M. Jentschel, J. Krempel, and P. Mutti. "A validity test of $E = mc^2$". In: Eur. Phys. J. Special Topics 172.1 (June 2009), pp. 353–362. issn : 1951-6355. `DOI:10.1140/epjst/e2009-01060-4`.

12. W. Urban et al. "Isomers in Fission Fragments". In: American Institute of Physics Conference Series. Ed. by J. Jolie et al. Jan. 2009, pp. 494–501. `DOI:10.1063/1.3087072`.

13. M. Jentschel et al. "Ultrahigh-Resolution γ-Ray Spectroscopy of ^{156}Gd: A Test of Tetrahedral Symmetry". In: Phys. Rev. Lett. 104.22 (June 2010), p. 222502. `DOI:10.1103/PhysRevLett.104.222502`.

14. G. Mana, J. Krempel, and L. Ferroglio. "Estimation of the centre of a diffraction peak by triggering the goniometer-angle readings via photon detection". In: Journal of Applied Crystallography 43.1 (Feb. 2010). `DOI:10.1107/S0021889809046548`.